UNIVERSITÀ DEGLI STUDI DI MILANO

PhD course in Veterinary and Animal Science – XXXVI cycle

Department of Veterinary Medicine and Animal Sciences (DIVAS)

Doctoral Thesis

# Impact of aging on mammalian intra- and exra-cellular environments

VET-01

Dr. **Teresina De Iorio**

Registration ID: **R12975**

Tutor: Prof. **Georgia Pennarossa**

Co-Tutor: **Prof. Tiziana AL Brevini**

PhD Coordinator: Prof. **Fabrizio Ceciliani**

A.A. 2022/2023

To those who have always been there.

To those who believed in me from the beginning,
and until the end.

To you, who, more than anyone else,
would have wanted to be there.

# Summary

# English abstract

Aging is a physiological process characterized by a gradual decline in cell, tissue, and organ functions. Although a significant amount of information is available on the senescence-related processes that take place in the cellular compartment, little is known about the role of the extracellular matrix (ECM) and its changes. Given the close relationship between the ECM and the cells residing within it, as well as the well-known ability of cells to interact with the surrounding matrix, it can be hypothesized that age-related modifications in the extracellular microenvironment might compromise cell behaviour, affecting tissue homeostasis and causing organ dysfunctions. This thesis has the specific aims to:

- study the role of the ECM in cell differentiation.
- identify age-related ECM changes.
- generate age-specific ECM-based bio-scaffolds.
- assess whether age-related ECM modifications may influence cell behaviour.
- take advantage of ECM-derived biomechanical cues to develop/support novel rejuvenating strategies.

I adopted the porcine ovary as experimental model, based on its complex microanatomy and heterogenous architecture, and used a decellularization protocol previously developed in the Laboratory hosting my PhD activities to generate ECM-based bio-scaffolds. These were then repopulated with different sets of cells, namely a) freshly isolated porcine ovarian cells, b) high-plasticity cells and c) cells previously rejuvenated with soluble factors.

The obtained results demonstrate that aging directly impact on the ovarian ECM that shows significant changes in its composition and organization with collagen, glycosaminoglycans, and laminins significantly incremented, and elastin, as well as fibronectin, decreased. This is accompanied by a dynamic response in the expression levels of key ECM and protease-related genes, suggesting a direct impact of aging on the transcriptional machinery. The ECM-based 3D bio-scaffolds generated preserved the structural changes occurring *in vivo* demonstrating their ability to act as a powerful high predictive *in vitro* model for reproductive aging and its prevention. When ECM-based scaffolds were repopulated, they were able to properly drive the differentiation, fate and viability of all cells tested. In particular, aged cells previously rejuvenated with miRNA or young cell-derived factors stably maintained the newly acquired phenotype when engrafted onto young ECM-based scaffolds. This suggests that an adequate young environment is able to stabilize miRNA and EV-mediated rejuvenation and implies a synergistic interaction among molecular effectors and ECM-derived bio-mechanical stimuli.

Altogether, these data indicate that the experimental model here developed may represent a useful tool to finely dissect the several biochemical and biomechanical cues driving tissue and organ aging.

# Italian Abstract

L'invecchiamento è un processo fisiologico caratterizzato da un graduale declino delle funzioni di cellule, tessuti e organi. Sebbene sia disponibile una quantità significativa di informazioni sui processi legati alla senescenza del compartimento cellulare, si sa poco sul ruolo della matrice extracellulare (ECM) e sui suoi cambiamenti. Data la stretta relazione tra la matrice extracellulare e le cellule che risiedono al suo interno, nonché la nota capacità delle cellule di interagire con la matrice circostante, si può ipotizzare che le modifiche legate all'età del microambiente extracellulare potrebbero compromettere il comportamento cellulare, influenzando l'omeostasi dei tessuti e causando disfunzioni d'organo. Pertanto, questa tesi ha gli obiettivi specifici di:

- Studiare il ruolo della ECM nel differenziamento cellulare.
- Identificare i cambiamenti dell'ECM legati all'età.
- Generare bio-scaffold a base di ECM età-specifici.
- Valutare se le modifiche dell'ECM legate all'età possono influenzare il comportamento cellulare.
- Sfruttare gli stimoli biomeccanici derivati dall'ECM per sviluppare/supportare nuove strategie di ringiovanimento.

Ho adottato l'ovaio suino come modello sperimentale, per la sua complessa micro-anatomia e per la sua architettura eterogenea. Ho adottato un protocollo di decellularizzazione, precedentemente sviluppato nel laboratorio che ospita le mie

attività di dottorato, per generare bio-scaffold a base di ECM. Questi sono state poi ripopolati con diversi tipi cellulari: a) cellule ovariche suine appena isolate, b) cellule altamente plastiche e c) cellule precedentemente ringiovanite con fattori solubili.

I risultati ottenuti dimostrano un forte impatto dell'invecchiamento sulla ECM ovarica, che mostra cambiamenti significativi nella sua composizione e organizzazione, con un significativo aumento di collagene, glicosamminoglicani e laminine, associato ad una diminuzione di elastina e fibronectina. Ciò è accompagnato da una risposta dinamica nei livelli di espressione dei geni chiave legati all'ECM e alle proteasi, suggerendo un impatto diretto dell'invecchiamento sul meccanismo trascrizionale. I bio-scaffold creati hanno preservato i cambiamenti strutturali che si verificano in vivo, dimostrando la loro capacità di agire come un potente modello *in vitro* altamente predittivo per studiare l'invecchiamento riproduttivo. Quando gli scaffold basati sull'ECM sono stati ripopolati, sono stati in grado di guidare adeguatamente la differenziazione, il destino e la vitalità di tutte le cellule testate. In particolare, le cellule invecchiate precedentemente ringiovanite con miRNA, o con l'utilizzo di fattori solubili derivati da cellule giovani, mantenevano stabilmente il fenotipo appena acquisito quando seminate su scaffold giovani. Ciò suggerisce che un ambiente giovane adeguato è in grado di stabilizzare il ringiovanimento, mediato dai miRNA e da fattori solubili, ed implica un'interazione sinergica tra effettori molecolari e stimoli biomeccanici derivati dall'ECM.

Nel complesso, questi dati indicano che il modello sperimentale qui sviluppato può rappresentare uno strumento utile per analizzare con precisione i numerosi segnali biochimici e biomeccanici che guidano l'invecchiamento dei tessuti e degli organi.

# 1. Introduction

## 1.1. Aging

In the past century, improvements in public health and medical care led to the increasing of human expected lifespan (United Nation, Department of Economic and Social affairs, 2022). Consequently, according to recent projections, by the year 2050 the number of people aged 60 and over will increment significantly, while the grow rate will fall (Leslie et al., 2015; Chen, 2022; United Nation, Department of Economic and Social affairs, 2022) (Figure 1).

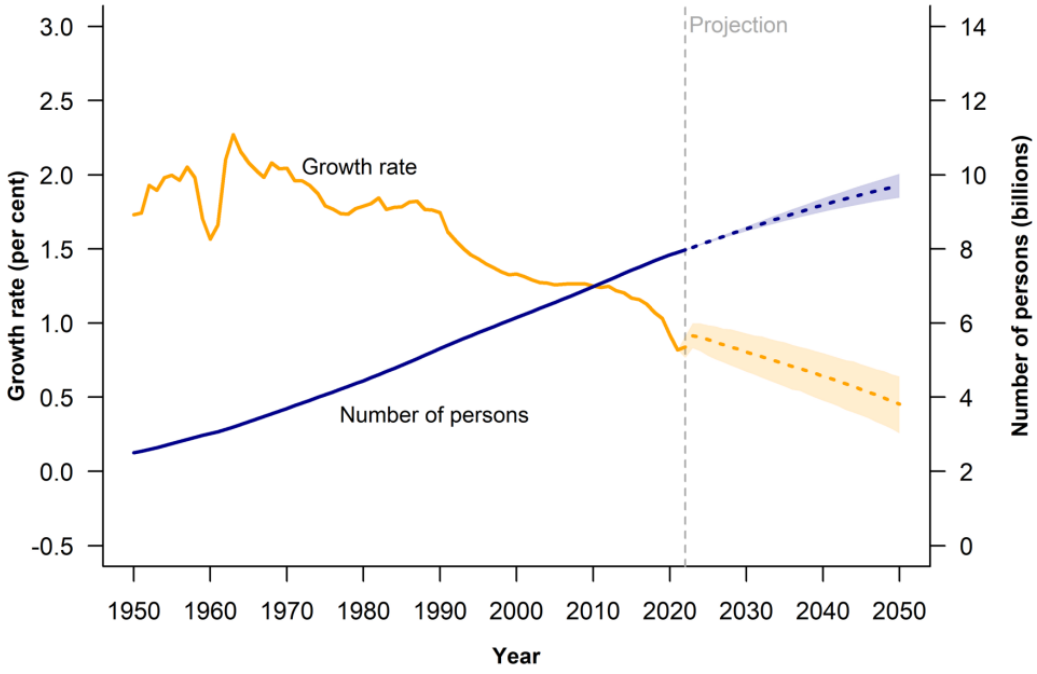


Figure 1: Graphic representation of United Nation world population prospects (United Nation, Department of Economic and Social affairs, 2022).

Aging is defined as a physiological degenerative process consisting of progressive accumulation of changes with time, concerning all living organisms. This process is responsible to an increase of susceptibility to several diseases and pathologies

(Harman, 1981; Dziechciaż et al., 2014; Guo et al., 2022). Consequently, the age-related effects on the organism have been receiving particular interest. From a biological point of view, aging is associated to the accumulation of molecular and cellular modifications that occur in tissues with advancing age. These changes are related to the increased risk of death and diseases such as cancer, stroke, diabetes, and chronic cardiovascular and neurodegenerative diseases (Tosato et al., 2007; Guo et al., 2022). Therefore, aging is generally described as a gradual loss of functional activities and is associated with significant changes, affecting not only the cellular compartment, but also the extracellular microenvironment (Birch et al., 2018; Hebisch et al., 2023).

### *1.1.1. Cellular aging*

Cell senescence is an irreversible cell cycle arrest caused by a wide variety of factors, such as oxidative damage, mitochondrial dysfunctions, chromosome aberrations, epigenetic alterations, oncogenes activation or telomere shortening (Hernandez-Segura et al., 2018). In 2013, Lopez-Otin and his colleagues tried to define and collect the main biological markers of aging, proposing twelve aging hallmarks, namely genomic instability, telomere attrition, epigenetic alterations, loss of proteostasis, dysregulation of nutrient sensing, mitochondrial dysfunctions, cellular senescence, tissue stem cells exhaustion, and altered intercellular communication (Figure 2) (Lopez-Otin et al., 2013).

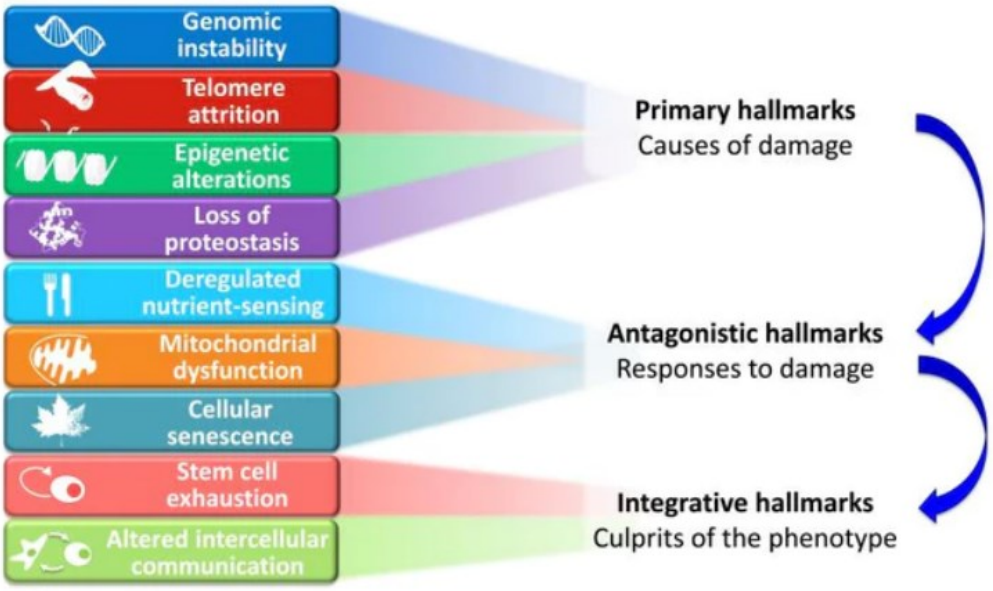


Figure 2: Schematical representation of the aging hallmarks and their connections (https://biohackercenter.com/blogs/biohacking-guides/91-hallmarks-aging-reverse-them; Lopez-Otin et al., 2013).

In agreement with this, cells increase the production of reactive oxygen species (ROS), which are the main cause of oxidative damage and mitochondrial dysfunctions, that lead to the increase electron leakage, and the reduction of ATP production. An intensified ROS production can cause further mitochondrial decline, and cellular damage (López-Otín et al, 2013). In parallel, ROS can provoke DNA damage ranging from small point mutations to large chromosome breaks and translocations. These effects lead to a wide variety of outcomes including silent mutations, the activation of oncogenes and the silencing of tumour-suppressor genes (Aunan et al, 2016). In addition, one of the most common and better characterized senescence inductors is telomere attrition (Casagrande et al., 2019).

Telomeres represent chromosome ends and are constituted by repeated sequences, which differ between species in length and base sequence, and shorten at each cell division (Srinivas et al, 2020; Chakravarti et al 2021). In pluripotent and cancer cells, telomere length is restored by telomerases, ribonucleic enzymes, which can counteract replication-related telomere attrition (Rossiello et al., 2022). However, senescence and telomere shortening do not only represent a disadvantage, since the progressive shortening of telomeres may lead not only to senescence, apoptosis, but also to oncogenic transformation of somatic cells. Indeed, these mechanisms play an essential role in protecting the organism from the effects of damaged cells, also contributing to tissue remodelling and repair (Dodig et al, 2019; Vaiserman et al., 2021).

In the recent years, most of the researchers working on improving the first aging hallmarks description and propose new hallmarks, including compromised autophagy, microbiome disturbance, inflammation, splicing dysregulation, and the alteration of tissue mechanical properties (Figure 3) (Lopez-Otin et al., 2013; Schmauck-Medina et al., 2022).

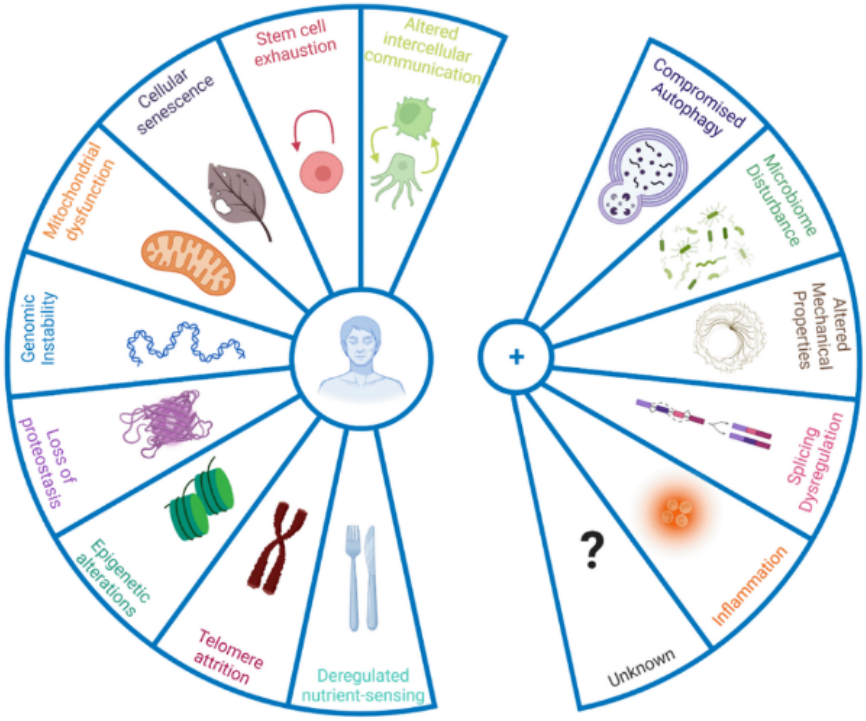


Figure 3: Scheme representing newly proposed aging hallmarks (Schmauck-Medina et al., 2022).

### *1.1.2. Extra-cellular matrix aging*

ECM

Cells arrange within tissues following a specific architecture which ensures both functional and biochemical characteristics of the organs. This cell organization is allowed by an appropriate structural support, provided by the ECM (Yue et al., 2014; Bandzerewicz et al, 2022). The ECM is a network of multiple macromolecules, including fibrous proteins and proteoglycans, essential to provide a three-dimensional (3D) guidance for cell adhesion (O'Connor et al, 2020; Zhang et al., 2021) (Figure 4).

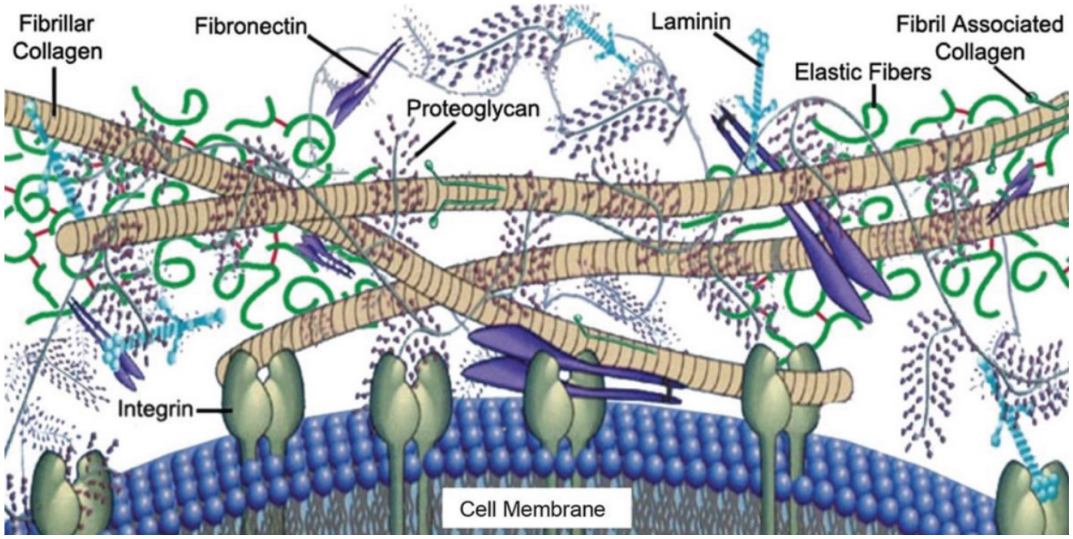


Figure 4: Schematical representation of cell interaction with ECM network (Acosta et al., 2020).

Not only does it provides an essential physical scaffolding for cells, but it also gives the transmission of biochemical and biomechanical signals that are crucial for tissue morphogenesis, differentiation, and homeostasis (Frantz et al., 2010; Pompili et al., 2021). The main proteins that characterize ECM are:

- Collagen: most abundant constituent within the body. It is found within the ECM of connective tissues, such as tendons and skin, and is mainly produced by fibroblasts, but also by epithelial and endothelial cells. Once synthesized, it is organized into fibrils that provide the necessary structural integrity to the tissues (Kular et al., 2014; Zhang et al., 2021). It provides tensile strength, regulates cell adhesion and supports chemotaxis and cell migration (Rozario & DeSimone, 2010).

- Elastin: a structural protein which provides the tissue with the ability of recovering from stretching (Kular et al., 2014; Karamanos et al., 2021). Elastin is a highly hydrophobic protein, secreted in the form of a monomer called "tropoelastin", which is polymerized by the lysyl-oxidase enzyme (LOX) through an irreversible cross-linking (Levi et al., 2020). Indeed, this allows it to self-assemble, forming, together with fibrillin, elastic fibers, which are stable and have a low turnover (Theocharis et al., 2016).
- Fibronectin: one of the main adhesive proteins, ubiquitously expressed in the ECM of all organs and tissues (Pankov & Yamada, 2002). It is mainly located within the basement membrane of the ECM, and it is organized in a network of fibrils that allows cell adhesion through the bond with integrins. It has also been determined that it has a key role in the wound healing response to injury (Smith et al., 2007; Kular et al., 2014; Parisi et al., 2020).
- Laminins: represent the major component of basal lamina membrane (Durbeej, 2010). In vertebrates five $\alpha$, three $\beta$ and three $\gamma$ chains have been identified (Theocharis et al., 2016). Laminins are expressed by many different cell types (including muscle and epithelial cells), and they are essential for cell adhesion, playing a vital role in several processes, including migration and differentiation (Kular et al., 2014; Li et al., 2021).
- Proteoglycans: the most important structural and functional biomacromolecules within tissues (Richter et al., 2018). They are pivotal in maintaining the right tissue viscosity (Mattson et al., 2017; Salbach-Hirsch

et al., 2021). They consist of a protein core to which one or more glycosaminoglycan (GAG) chains are covalently attached (Frantz et al., 2010; Theocharis et al., 2016).

Interaction between cells and matrix occurs through surface receptors, such as integrins (Ouyang et al., 2021). They bind ECM fibrils in the extracellular compartment, while actin filaments through cytoskeletal linker proteins in the intracellular environment (Schwartz, 2010). Each of these components is able to transmit forces, that may derive from either the intra or extracellular milieu (LaFoya et al., 2018).

During the last years, it has been demonstrated that ECM regulates other processes such as cell polarization, adhesion, migration, differentiation, proliferation, and apoptosis (Varshney et al., 2015; Mahon et al., 2021). It is synthesized and secreted by all cell types, under the control of multiple signals (Theocharis et al., 2016). In particular, every tissue possesses its specific matrix, with unique topology and composition that are generated during tissue development through a dynamic and reciprocal dialogue between the various cellular components and the surrounding microenvironment (Frantz et al., 2010; Pompili et al., 2021). Moreover, the ECM is subjected to continuous turnover, undergoing remodelling mediated by different matrix-degrading enzymes, namely metalloproteinases (MMPs), under normal and pathological conditions (Theocharis et al., 2016; Musale et al., 2023). Their activity is relatively low in physiological circumstances, maintaining the correct balance

between the ECM components as well as the release of biologically active molecules, such as growth factors (Rozario and De Simone, 2010). Contrarily they are upregulated during tissue repair process and/or in pathological conditions (Bonnans et al., 2015).

Age-related ECM alterations

During the last years, several research groups demonstrated that the ECM pattern reflect the tissue-resident cellular status, including healthy or pathologic conditions as well as aging. More in details, the cells and the ECM are in constant, mutual, and bi-directional dialogue. Indeed, diseased cells dysregulate ECM components as well as the alteration in ECM composition leads to the alteration of cell functions. For instance, some cancer types can be classified according to the distinctive ECM pattern they produce (Pompili et al., 2021; Sacher et al, 2021). On the other hand, ECM changes contribute to the onset of pathological conditions or failure in tissue regeneration.

Aging progression significantly affects the ECM, inducing extensive modifications of its composition and architecture. Collagen synthesis is altered during aging, producing important changes in the amount of this protein in the ECM (Ouni et al., 2020; Pennarossa et al., 2022). In agreement with this, aging is often associated with collagen overexpression and accumulation, defined as fibrosis (Wynn et al., 2008). This latter occurs when collagen synthesis exceeds the rate in which it is degraded, leading to its accumulation (Karsdal et al.,

2017). Moreover, this protein can be subjected to advanced glycation end products (AGEs) accumulation, which affects its susceptibility to degradation (Jo et al, 2021). In parallel, elastin-degrading enzymes are over-expressed during aging, leading to the loss of elasticity in tissues like skin and arteries (Fleenor et al., 2013; Baumann et al., 2021). Aging also affects mechanical and structural properties of elastic fibres. In addition, laminin, fibronectin and hyaluronic acid are subjected to age-related modifications (Levi et al, 2020; Jo et al, 2021). ECM integrity declines through the accumulation of damage caused by oxidation, glycation, crosslinking, fragmentation, and protein aggregation, causing decreased ECM dynamics and loss of organ function (Levi et al, 2020; Baumann et al., 2021; Jo et al, 2021). These changes in ECM compliance have also been associated with diseases like atherosclerosis, diabetes, and cancer (Ewald, 2019). Age-dependent modifications in ECM composition and organization are also the main cause of altered mechanical properties in cardiovascular, musculoskeletal, and skin tissues (McCabe et al., 2020). For instance, the stiffness of vascular smooth muscle in aged rats is caused by collagen deposition paralleled by enhanced elastin degradation (Bajpai et al, 2021).

## 1.2. Strategies to counteract aging

For many centuries, differentiation process was considered as unidirectional. Indeed, in 1957 cell differentiation events were represented as a ball rolling down from the top of a hill (Waddington, 1957). In this scenario, the ball on the top of the hill represents a stem cell and the valley corresponds to the series of differentiation step leading to a fully differentiated phenotype. Thus, cell fate is strictly controlled and becomes progressively restricted (Waddington, 1957). The process is driven by several extrinsic and intrinsic factors, inducing an epigenetic controls of gene expression that gradually limit the cell potency to a restricted transcription pattern (Brevini et al., 2015). These epigenetic modifications, such as histone acetylation or DNA methylation, regulate the accessibility of genetic material without any permanent loss of DNA, and are responsible to the adult cell restricted phenotype called "epigenetic memory" (Fischer et al., 2022; Gandolfi et al, 2019). Dysregulation of epigenetic machinery is often associated with aging (Fischer et al., 2014; Camillo and Quinlan, 2021).

In the last decades, several researchers focused their attention on trying to reverse aging hallmarks. A first attempt was realized through somatic cell nuclear transfer (SCNT), able to confer totipotency to an adult differentiated cell by transferring the nucleus of a somatic cell into an enucleated oocyte (Matoba et al., 2018). It is firstly achieved in sheep (Wilmut et al, 1997) and subsequently in mice (Mizutani et al, 2008) and demonstrated the possibility to generate mammalian embryo genetically identical to the donor cell (Simpson et al., 2021). These experiments indicated that the oocyte environment can modify the epigenetic pattern of an adult somatic cell,

suggesting that aging may be reversible (Wilmut et al, 1997; Mizutani et al, 2008; Singh and Newman, 2018; Wu et al., 2019).

In 2006, Takahashi and Yamanaka induced a pluripotent state in terminally differentiated cell (iPSCs) by forcing the expression of four defined transcription factors: Oct3/4, Sox2, c-Myc, and Klf4 (OSKM) (Takahashi and Yamanaka, 2006). OSKM factors bind to chromatin, inducing its remodelling and activating the expression of repressed gene. This strategy is able to de-differentiate an adult somatic cell in a stem-like state. These achievements indicate that the Waddington's landscape may be rearranged, and that the differentiation process is reversible, converting a differentiated cell to a pluripotent state (Simpson et al., 2021; Chondronasiou et al., 2022).

### *1.2.1. Epigenetic erasing*

More recent evidence demonstrated that cell epigenetic pattern can be also reverted without the use of SCNT or the forced expression of OSKM factors, by using chemical molecules, called erasers (Pennarossa et al., 2013; Gillette et al., 2015; Biswas et al, 2018; Gandolfi et a., 2019; Wang et al., 2020; Gruhn et al., 2023).

Among the several methods proposed, a promising strategy is represented by epigenetic modifications (Pennarossa et al., 2013; Pennarossa et al., 2014; Brevini et al., 2014; Brevini et al., 2016; Manzoni et al., 2016; Gandolfi et al., 2019; Pennarossa et al., 2020; Basu et al., 2021; Pennarossa et al., 2021). Indeed, it is an efficient and robust alternative method for cell reprogramming (Gailhouste et al., 2018; Manzoni

et al., 2018; Pennarossa et al., 2018; Pennarossa et al., 2021; Gandolfi et al., 2019; Pennarossa et al., 2021). Chen and his colleagues reported the first work demonstrating the possibility of using small molecules to increase cell plasticity, inducing committed myoblasts to become multipotent mesenchymal progenitor cells (Chen et al., 2004). Subsequently, several works have demonstrated that an exposure to demethylating agents or to histone deacetylase inhibitors is sufficient to erase cell original phenotype, inducing a high plasticity state in terminal differentiated somatic cells (Pennarossa et al., 2013; Pennarossa et al., 2014; Brevini et al., 2014; Lee et al., 2014; Brevini et al., 2016; Manzoni et al., 2016; Gailhouste et al., 2018; Pennarossa et al., 2018; Pennarossa et al., 2019; Pennarossa et al., 2020; Basu et al., 2021; Pennarossa et al., 2021). More in detail, it has been shown that specific chemical compounds can push cells to a transient less committed state, increasing cell plasticity for a relative short time-window, sufficient to re-address an adult mature cell into another differentiated cell type (De Coppi et al., 2007; Harris et al., 2011; Pennarossa et al., 2013; Pennarossa et al., 2014; Brevini et al., 2014 Mirakhori et al., 2015; Chandrakanthan et al., 2016; Hore et al., 2016). For instance, the 5-Azacytidine (5-aza-CR), which is a chemical analogue of cytidine, is demonstrated to be able to chemically erase epigenetic marks in human (Pennarossa et al, 2013; Gailhouste et al., 2018), murine (Cao et al., 2014; Zhou et al., 2016), porcine (Arcuri et al, 2021), and canine (Brevini et al, 2016) dermal fibroblasts, acting as an epigenetic eraser.

### *1.2.2. Micro-RNAs*

miRNAs are small non-coding RNAs, 21-24 nucleotides in length, that play pivotal role in regulating gene expression. miRNAs interact with their targets through complementary base-pairing and influence the translation or the stability of their target transcripts, usually leading to their downregulation (O'Brien et al., 2018). Indeed, they are demonstrated to be involved in several physiological and pathological processes, including the epithelial-to-mesenchymal (EMT) transition. EMT is a reversible process observed in embryonic development during gastrulation and the establishment of the neural crest, as well as in the formation of other tissues and organs (Amack et al., 2021; Ismagulov et al., 2021). It has been demonstrated that the equilibrium between EMT-suppressing miRNAs and the EMT-related transcription factors determines the epithelial cellular plasticity (Gollavilli et al, 2021). More in details, miRNA-200 (miR-200) family is highly expressed in embryonic stem cells (ESCs), as well as in iPSCs, and it has been demonstrated to influence pluripotency (Balzano et al., 2018). Indeed, when EMT is inhibited, miR-200 family members were upregulated by BMP factor, which sustains the self-renewal of ESCs, acting in a synergistic manner with the pluripotency-related genes Oct4, Klf4, C-Myc and Sox2 (Wang et al., 2013). Furthermore, miR-200b and miR200c were demonstrated to stimulate mesenchymal-to-epithelial (MET) transition, promoting cell reprogramming in mice (Samavarchi-Tehrani et al, 2010; Zhang et al, 2020). In parallel, the knockdown of miR-200c induce the downregulation of Nanog and C-Myc expression, inhibiting ESC renewal (Anastasiadou et al, 2021). This implies that this miRNA has a crucial

role in the maintenance of stem cell pluripotency and self-renewal properties. Moreover, miR-200 family has been demonstrated to be downstream of the TET enzymes' pathway, being activated through demethylation processes by these enzyme family, and inducing a high plasticity state in cells (Balzano et al, 2018). Interestingly, miRNAs, together with other signalling molecules, were delivered to other cells by extracellular vesicles.

### *1.2.3. Extracellular vesicles*

Extracellular vesicles (EVs) are lipid bound small vesicles secreted by cells into the extracellular space (Doyle et al., 2019). EVs can be classified in several subclasses, differing by size, biogenesis, release, content, and function. However, they are classically subdivided based on their biogenesis, identifying three principal groups (Raposo and Stoorvogel, 2013; Sheta et al., 2023):

- Exosomes: ranging between 50 and 150 nm, produced from multivesicular bodies.
- Microvesicles: ranging between 50 nm and 1 μm, originated from membrane budding (Raposo and Stoorvogel, 2013) (Figure 5).

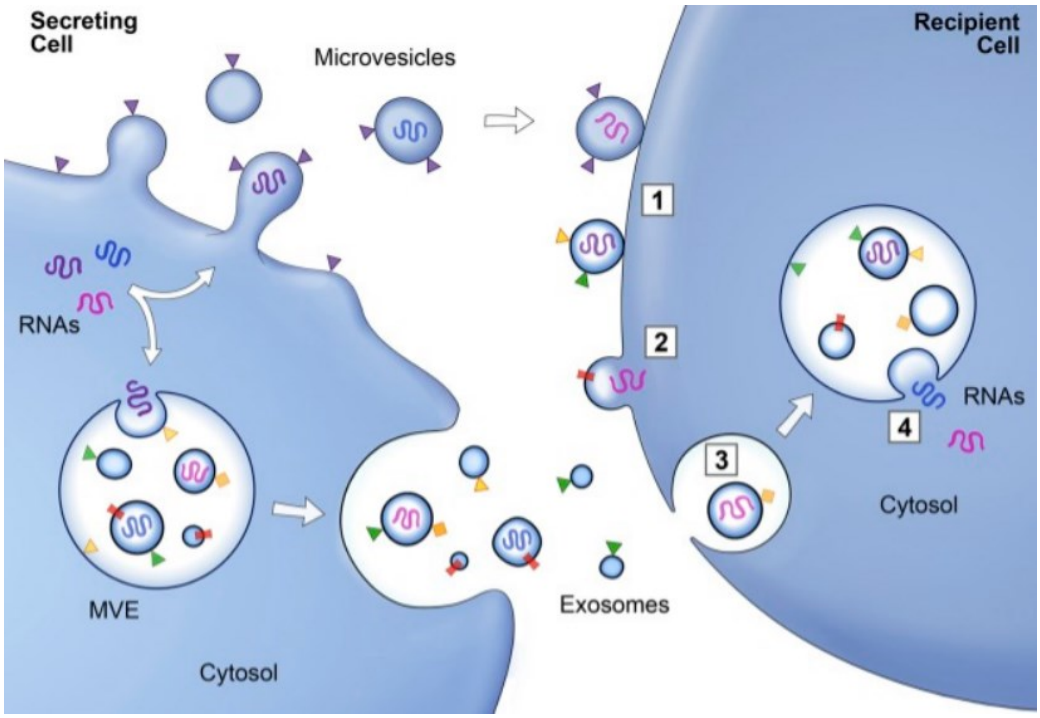


Figure 5: Schematic representation of exosomes and microvesicles-mediated RNA and protein transfer between cells. Microvesicles and exosomes may anchor to the plasma membrane of a target cell and the bound vesicles can either directly fuse with the plasma membrane or be endocytosed. The endocytosed vesicles may then fuse with the delimiting membrane of an endocytic compartment (Raposo and Stoorvogel, 2013).

EVs are demonstrated to cargo lipids, nucleic acids and proteins, both cytosolic and membrane-associated (Doyle et al., 2019; O'Brien et al., 2020; Veziroglu et al., 2020).

They are produced by almost all cell types and strictly mirror the physio-pathological state of the secreting cells (Doyle et al., 2019; Villata et al, 2020). These vesicles are also pivotal for cell communication, by transporting several different molecules, such as lipids, proteins, and nucleic acids, including miRNAs (Kwok et

al., 2021; O'Brien et al., 2020; Villata et al, 2020). Furthermore, the same cell may release subpopulations of EVs with different cargo compositions, exerting distinct effects on target cells. EVs are able to modify the target cell phenotype, by directly mediating the transfer of bioactive materials among cells, thus leading to different signalling cascades (Vogel et al, 2018; Kwok et al., 2021). EVs can be purified from several body fluids, like blood (Qi et al, 2021), plasma (Wahlgren et al, 2012), saliva (Comfort et al, 2021) and milk (De la Torre Gomez et al, 2018). In the last decades, many EV purification methods have been proposed, including differential ultracentrifugation, membrane affinity, and size exclusion chromatography (Gardiner et al, 2016; Monguió-Tortajada et al, 2019; Veerman et al, 2021). Interestingly, EV content can be easily engineered through two different approaches: passive or active encapsulation (Villata et al., 2020). In the passive mechanism, vesicles are co-incubated with the target that is spontaneously encapsulated. The active process consists in physically or chemically mediated uptake, such as sonication, electroporation, or chemical-based transfection.

## 1.3. 3D culture systems

To date, in vitro two-dimensional (2D) cell culture systems have been extensively used to study cell biology and diseases (Kapałczyńska et al., 2018; Jensen et al., 2020 Pennarossa et al, 2021). Nevertheless, cell plated onto 2D plastic surfaces tend to lose their original phenotype, due to the lack of biomechanical and biochemical signals proper of their original tissue (Baker et al, 2012; King et al., 2021). Indeed, cells derived from organs and cultured onto stiff and flat plastic supports have been demonstrated to modify their specific phenotype, due to alterations and loss of cell-to-cell and cell-to-matrix interactions. This leads to dramatic changes in cell functions, including their morphology, polarity, differentiation, proliferation, as well as their ability to react to stimuli (Pampaloni et al, 2007 Kapałczyńska et al., 2018; Hardt et al., 2023), making them unable to completely reflect crucial aspects of cell phenotype and their native milieu (Ravi et al, 2015).

During the last decades, evidence demonstrated that 3D culture systems allow researchers to *in vitro* recreate the natural cellular environment (Cacciamali et al., 2022; Ajjarapu et al., 2023). The ideal model must provide not only the 3D architecture, but also bio-chemical and bio-mechanical cues specific of their native organ, thus promoting cell adhesion, proliferation, and colonization (Pennarossa et al, 2021; Cacciamali et al., 2022; Ajjarapu et al., 2023). Nowadays, several different 3D models, both synthetic or biological, are available including hydrogels, micro-bioreactors, 3D printed and decellularized scaffolds (Pennarossa et al, 2021).

### *1.3.1. Synthetic vs biological scaffolds*

Several materials have been used for the generation of 3D scaffolds, ranging from natural, to synthetic, and composite ones. Synthetic polymers are represented by polyanhydrides, inorganics (like hydroxyapatite), and hydrophobic materials, including $\alpha$-hydroxy acid family, namely poly(lactic) acid (PLA), poly(L-lactic) acid (PLLA), poly(glycolic) acid (PGA), and poly(lactic-co-glycolic) acid (PLGA) (Kohane and Langer, 2008; Santoro et al., 2016; Victor Perez-Puyana et al., 2020). Each of these materials must possess specific bio-chemical (e.g. biocompatibility), bio-physical (e.g. porosity, degradation) and bio-mechanical (e.g. stiffness) properties (Nikolova et al, 2019). The adequate material should be chosen to realize the scaffold in order to re-create organ specific macromolecular structure and rearrangement (Reddy et al, 2021). Synthetic scaffolds can be easily produced with standardized physical and mechanical properties such as tensile strength, elastic modulus, and degradation rate (Nikolovski et al., 2000; He et al., 2016; Williams et al., 2019; Amini et al., 2021). However, they lack cell recognition sites, leading to a dramatic reduction in cell adhesion, proliferation, resulting in poor scaffold colonization (Bacáková et al., 2004; Bolle et al., 2016; Kamatar et al., 2020). On the other hand, synthetic materials can be engineered with biological molecules in order to improve cell homing (Kesireddy et al., 2016; Kamatar et al., 2020; Amini et al., 2021). In parallel, biological materials, such as collagen, proteoglycans, alginate-based substrates, and chitosan, have been used in the production of scaffolds for tissue engineering (Jenkins et al., 2019; Krishani et a., 2023). Natural polymers are highly bio-compatible and promote excellent cell adhesion and growth (Jenkins et

al., 2019; Amini et al., 2021; Krishani et a., 2023). Furthermore, they are also biodegradable and allow to host cells, to produce their own extracellular matrix and to synthesize new ECM molecules to replace the degraded scaffold (O'Brien et al., 2011; Echeverria Molina et al., 2021).

### *1.3.2. Decellularized ECM-based scaffolds*

Among the existing 3D culture system, particular attention has been given to decellularized ECM-based scaffolds. The decellularization is a strategy that allow for the creation of organ-specific scaffolds, able of providing the optimal microenvironment for cell growth and differentiation (Pennarossa et al., 2020; Pennarossa et al., 2021; Neishabouri et al., 2022). Moreover, decellularized tissues should preserve the integrity of all ECM macromolecules such as collagen, elastin, fibronectin, laminin, and proteoglycans (Zhang et al., 2022).

The decellularization protocol involve the use of chemical, enzymatic, and physical agents, with the common aim of removing cells and DNA from tissues, while preserving the organ structural proteins (Fernández-Pérez et al., 2019; Nikolova et al, 2019; Pennarossa et al., 2021; Narciso et al., 2022). Physical methods comprise agitation, sonication, mechanical pressure, or freeze-thaw procedures (Gilpin and Yang, 2017). These approaches are often related to high preservation of ECM constituents but are not able to completely remove nuclear material (Ott et al., 2008; Merna et al., 2013; Gilpin and Yang, 2017). Chemical treatments use ionic and non-ionic detergents and chemical agents, like acids or bases, to disrupt cell-to-cell and cell-to-ECM bonds and remove overall cell components (Andrée et al., 2014).

Among detergents, sodium dodecyl sulphate (SDS) is highly effective in lysing cells but may alter the microarchitecture of the ECM-based scaffold created (Keane et al., 2015; Tan et al., 2022; Narciso et al., 2022). Contrarily, Triton X-100 is less efficient in clearing DNA remnants but is able to preserve unaltered ECM composition and its mechanical properties (Gilpin and Yang, 2017; Narciso et al., 2022). Another compound widely used in chemical decellularization is the sodium deoxycholate (SD), an anionic detergent demonstrated to be highly effective in eliminating nuclear material, while preserving intact ECM (McCrary et al., 2019; Narciso et al., 2022). Alternatively, it is also possible to use enzymatic treatments with several enzymes, such as trypsin, dispase, or nuclease (Hinderer et al., 2016). However, these methods are usually aggressive and can cause damages to the ECM constituents (Zhang et al, 2022).

To date, different decellularization protocols have been successfully used to obtain scaffolds from different organs, such as heart (Rajabi-Zeleti et al., 2014; Taylor et al., 2020), lung (Lecht et al., 2014; Skolasinski et al., 2018), liver (Lee et al., 2017; Dai et al., 2022), muscle (Aulino et al., 2015; Philips et al., 2022), kidney (Yu et al., 2014; Kim et al., 2022), urinary tissue (Singh et al., 2018), oesophagus (Sjöqvist et al., 2014; Mallis et al., 2019), trachea (Baiguera et al., 2014; Batioglu-Karaaltin et al., 2019) and ovary (Pennarossa et al., 2020, Pennarossa et al., 2021) (Figure 6).

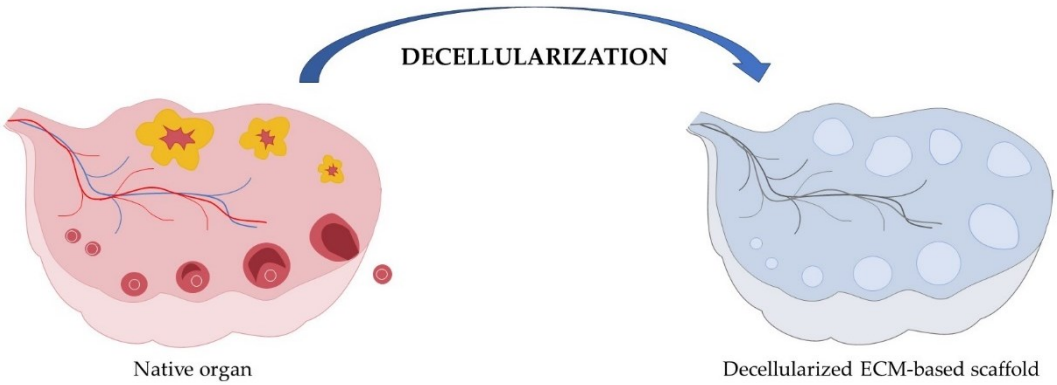


Figure 6: Schematical representation of ovarian bio-scaffold, generated through decellularization protocol (modified by Pennarossa et al., 2021).

### *1.3.3. Repopulation of decellularized ECM-based scaffolds*

Repopulation of acellular ECM scaffolds has been performed using organ-specific cell types or stem cells, with the attempt to recreate organ microanatomy and its specific functions. The preservation of the organ-specific ECM components promotes an optimal scaffold colonization, providing cells a guide for rearrangement and growth (Batchelder et al., 2015; Park et al., 2016; Hillebrandt et al., 2019).

Recellularization is typically performed through two different approaches: cell co-culture with the decellularized scaffold, or perfusion via the vascular network (Napierala et al., 2017; Kojima et al., 2018). Potential applications of decellularized matrixes in tissue engineering have been demonstrated for a number of tissues, including the liver (Booth et al., 2012), kidneys (Nakayama et al., 2010), pancreas (Goh et al., 2012), bladder (Yang et al., 2010), oesophagus (Dahl et al., 2013), and

trachea (Kutten et al., 2015). Moreover, evidence of successfully implanted repopulated kidney (Song et al, 2013), lung (Ott et al, 2010) and liver (Uygun et al, 2010) are available. Overall, this strategy appears to be very promising in order to reconstruct organ-like structures able to provide a suitable environment for cell growth, offering an optimal niche for the complex and dynamic organ milieu (Seetapun et al, 2017; Sefat et al., 2019; Zhang et al., 2020).

# 2. Aim of the work

Aging is a pathophysiological process characterized by a gradual decline of cellular, tissue and organ functions. While a considerable body of information is available on age-related processes taking place in the cellular compartment, less is known on the role of ECM and its modifications during senescence. Given the tight relationship between the ECM and the cells residing within it, and the well-known cell ability to interact with its surrounding matrix, it may be hypothesized that age-associated organ decline may involve ECM changes, beside the modifications already described in cells.

The specific aims of my PhD project were:

- To study the role of the ECM in cell differentiation.
- To identify age-related ECM changes.
- To generate age-specific ECM-based bio-scaffolds.
- To assess whether age-related ECM modifications may influence cell behaviour.
- To take advantage of ECM-derived biomechanical cues to develop/support novel rejuvenating strategies.

The experimental animal used was the porcine based on its anatomical and physiological similarities with the human. The ovary was selected as a model since it is the first organ that undergoes to age. Moreover, its complex microanatomy and heterogenous architecture may provide different mechanotransducive cues, allowing us to better characterize ECM influence on cell differentiation, proliferation and metabolism as well as to identify the main mechanisms by which physical forces are translated into the activation of local intracellular pathways.

A decellularization protocol previously established in the Laboratory hosting my PhD activities was exploited to create whole-ovary ECM-based bio-scaffolds. The latter was used in repopulation studies with freshly isolated porcine ovarian cells to investigate whether the derived bio-matrix provides an optimal microenvironment for ovarian cell growth and maintenance. The same protocol was then be carried out using high-plasticity cells to investigate scaffold ability to properly drive cell differentiation, fate, and viability.

In parallel, decellularization protocol was applied to ovaries with different age, to investigate age-related changes in ECM and to generate 3D ECM-based bio-scaffolds that preserve the distinctive age-specific features. Their repopulation with cells of different age was then used to assess the possibility that senescence-related ECM modifications may influence cell behaviour.

Finally, in the last part of my study, I developed strategies that may result in cell rejuvenation, both using biomechanical-related cues derived from the ECM, as well as soluble factors of cellular origin.

Altogether, this work has the final aim to better understand the regulatory mechanisms tuning senescence in mammalian tissues and, in particular, in the porcine ovary. Moreover, the information acquired provide new strategies to prevent, slow and counteract age progression. More in detail, the strategy here proposed allow for the generation of a suitable 3D platform to investigate solutions for hormone and fertility restoration, toxicological and drug testing, as well as transplantation studies. In addition, the model obtained represent a useful tool to better characterize these

complex regulations and to allow a fine dissection of the multiple and concurring biochemical and biomechanical stimuli driving the aging process.

# 3. Published works

## 3.1. Ovarian decellularized bio-scaffold provide an optimal microenvironment for cell growth and differentiation *in vitro*

Published in Cells on 18th August 2021.

DOI: 10.3390/cells10082126.

The first study was addressed to study the role of ECM in cell differentiation.

To this purpose, ECM was isolated through a decellularization protocol previously established in the Laboratory hosting my PhD activities, leading to the generation of whole-ovary ECM-based bio-scaffolds. The isolated matrixes were used in repopulation studies carried out using high-plasticity cells in order to investigate scaffold ability to properly drive cell differentiation, fate, and viability.

The data reported in the following manuscript agree and expand previously reported data, demonstrating that the ECM-based scaffold niche may provide inputs to repopulating cells that drive the transcription machinery at work in the native tissue. This indicates the possibility of using the generated decellularized bio-matrixes for high-plasticity cell differentiation, implying bio-matrixes ability to properly drive erased cell differentiation *in vitro*.

*Article*

# Ovarian Decellularized Bioscaffolds Provide an Optimal Microenvironment for Cell Growth and Differentiation In Vitro

**Georgia Pennarossa [1], Teresina De Iorio [1], Fulvio Gandolfi [2] and Tiziana A.L. Brevini [1,*]**

[1] Laboratory of Biomedical Embryology, Department of Health, Animal Science and Food Safety and Center for Stem Cell Research, Università degli Studi di Milano, 20133 Milan, Italy; georgia.pennarossa@unimi.it (G.P.); teresina.deiorio@unimi.it (T.D.I.); tiziana.brevini@unimi.it (T.A.L.B.)

[2] Laboratory of Biomedical Embryology, Department of Agricultural and Environmental Sciences - Production, Landscape, Agroenergy, Università degli Studi di Milano, 20133 Milan, Italy; fulvio.gandolfi@unimi.it

* Correspondence: tiziana.brevini@unimi.it; Tel.: +39 02 5031 7970

**Abstract:** Ovarian failure is the most common cause of infertility. Although numerous strategies have been proposed, a definitive solution for recovering ovarian functions and restoring fertility is currently unavailable. One innovative alternative may be represented by the development of an "artificial ovary" that could be transplanted in patients for re-establishing reproductive activities. Here, we describe a novel approach for successful repopulation of decellularized ovarian bioscaffolds in vitro. Porcine whole ovaries were subjected to a decellularization protocol that removed the cell compartment, while maintaining the macrostructure and microstructure of the original tissue. The obtained bioscaffolds were then repopulated with porcine ovarian cells or with epigenetically erased porcine and human dermal fibroblasts. The results obtained demonstrated that the decellularized extracellular matrix (ECM)-based scaffold may constitute a suitable niche for ex vivo culture of ovarian cells. Furthermore, it was able to properly drive epigenetically erased cell differentiation, fate, and viability. Overall, the method described represents a powerful tool for the in vitro creation of a bioengineered ovary that may constitute a promising solution for hormone and fertility restoration. In addition, it allows for the creation of a suitable 3D platform with useful applications both in toxicological and transplantation studies.

**Keywords:** whole-ovary decellularization; ECM-based scaffold repopulation; epigenetically erased cells; porcine; human; fibroblasts; bioprosthetic ovary; ovarian reconstruction

## 1. Introduction

Premature ovarian failure (POF) is a common endocrine disease that leads to early menopause and infertility. It has an incidence of 0.1% in women under 20 years of age and increases to 1.0–1.5% in subjects younger than 40 years [1–3]. Radiotherapy, chemotherapy, viral infections, environmental factors, metabolic and autoimmune disorders, and genetic alterations represent some of the potential causes identified so far. The clinical features displayed by affected patients are hypoestrogenism or estrogen deficiency, increased gonadotropin levels, and amenorrhea [4]. POF also impacts the overall quality-of-life, since alterations in ovarian hormone levels are responsible for different side effects on other organs and tissues, which lead to both medical and psychological problems, such as osteoporosis, cardiovascular disease, and depression [5–7]. Although several researchers have been working on the development of different strategies to allow fertility restoration, the prevention and treatment of POF are currently limited. Indeed, to date, several options have been proposed to overcome this challenging issue, including cryopreservation and transplantation of oocytes, embryos, and autologous ovarian fragments, as well as hormone replacement therapies [8–10]. However, all of these strategies present limitations and are not fully effective in a complete recovery of the ovarian function [4]. The development of novel and efficient therapeutic alternatives is therefore urgently needed.

In this context, the generation of a bioprosthetic ovary has been proposed as a promising strategy. During the last few years, the "artificial ovary" has received great attention, and many studies have been focusing on the creation of transplantable bioengineered ovaries using different natural polymers and biological materials, such as alginate, collagen, and fibrin three-dimensional matrices [11–14]. More recently, the extracellular matrix (ECM) has been exploited as the material of choice in the field of tissue engineering and regenerative medicine. ECM-based scaffolds are obtained by decellularization processes, wherein the living cells of an organ are removed, while the ECM components are preserved. This allows for the obtainment of 3D scaffolds that retain the biomechanical and biochemical cues of the native tissue, as well as its ultrastructural architecture, while eliminating immunoreactivity [15]. In contrast to the biological and synthetic matrices previously used, decellularized ECM-based scaffolds are therefore able to recreate in vitro the complex in vivo milieu, promoting the necessary interactions between cells and their surrounding microenvironment, as well as ensuring the correct cell growth, differentiation, and function [2,16,17]. Based on these advantages, decellularization techniques have been applied to a large variety of organs, including the heart [18], lung [19], liver [20], kidney [21], muscle [22], trachea [23], esophagus [24], urinary tissues [25], arteries [26], derma [16], and vagina [27].

Whole-ovary decellularization was recently carried out in bovine [28] and porcine species [2,29], leading to the successful production of 3D bioscaffolds for the generation of a bioprosthetic ovary. It must be noted that, to create in vitro an artificial functional organ, we need a recellularization step in which the ECM-based scaffolds are repopulated using suitable cells.

In the present work, we produced porcine whole-ovary decellularized ECM-based scaffolds. We repopulated them with porcine ovarian cells (pOCs) to investigate whether the generated scaffold may constitute a suitable niche for ex vivo culture of ovarian cells. In addition, we engrafted the generated ECM-based matrixes with both porcine and human epigenetically erased cells to explore whether the decellularized scaffolds are able to properly drive cell differentiation, fate, and viability.

## 2. Materials and Methods

All reagents were purchased from Thermo Fisher Scientific unless otherwise indicated.

### *2.1. Ethical Statement*

Human skin biopsies were obtained from healthy female individuals undergoing surgical interventions, after written informed consent and approval of the Ethical Committee of the Ospedale Maggiore Policlinico, Milan, Italy. All methods were carried out in accordance with the approved guidelines.

### *2.2. Collection of Porcine Ovaries*

Twenty ovaries were collected from gilts weighing approximately 120 kg at the local slaughterhouse and transported to the laboratory in cold sterile PBS containing 2% antibiotic/antimycotic solution (Sigma). Fifteen out of twenty ovaries were subjected to the decellularization protocol for the creation of ovarian ECM-based scaffolds (Figure 1). The remaining 5 ovaries were used as native control tissue. Half of each was immediately fixed in 10% buffered formalin for histological evaluations; the remaining half was subjected to DNA quantification analysis or immersed in RNA later solution (Sigma) for gene expression studies.

### *2.3. Creation of Decellularized Ovarian ECM-Based Scaffolds*

ECM-based scaffolds were obtained by subjecting 15 porcine ovaries to the whole-organ decellularization protocol previously described by Pennarossa et al. [2,29]. Briefly, ovaries were frozen at –80 °C for at least 24 h, thawed at 37 °C in a water bath for 30 min, immersed in 0.5% sodium dodecyl sulfate (SDS; Bio-Rad) in deionized water (DI-$H_2O$) for 3 h, and incubated overnight in 1% Triton X-100 (Sigma) in DI-$H_2O$. This step was followed by a wash in DI-$H_2O$ for 9 h and a subsequent treatment with 2% deoxycholate (Sigma) in DI-$H_2O$ for 12 h. Decellularized whole ovaries were then extensively washed in DI-H2O for 6 h and sterilized with 70% ethanol

and 2% antibiotic/antimycotic solution in sterile $H_2O$ for 30 min. All the steps described were performed using an orbital shaker at 200 rpm.

Before repopulation, half of each decellularized ovary was subjected to histological analysis, DNA quantification, and the MTT test to evaluate the efficiency of the decellularization process (see Figure 1). The remaining decellularized hemi-ovaries were cut into 9 fragments each of 7 mm in diameter and 1 mm in thickness and repopulated with (A) freshly isolated pOCs, (B) epigenetically erased porcine adult dermal fibroblasts (pEpiE), or (C) epigenetically erased human adult dermal fibroblasts (hEpiE) (Figure 1).

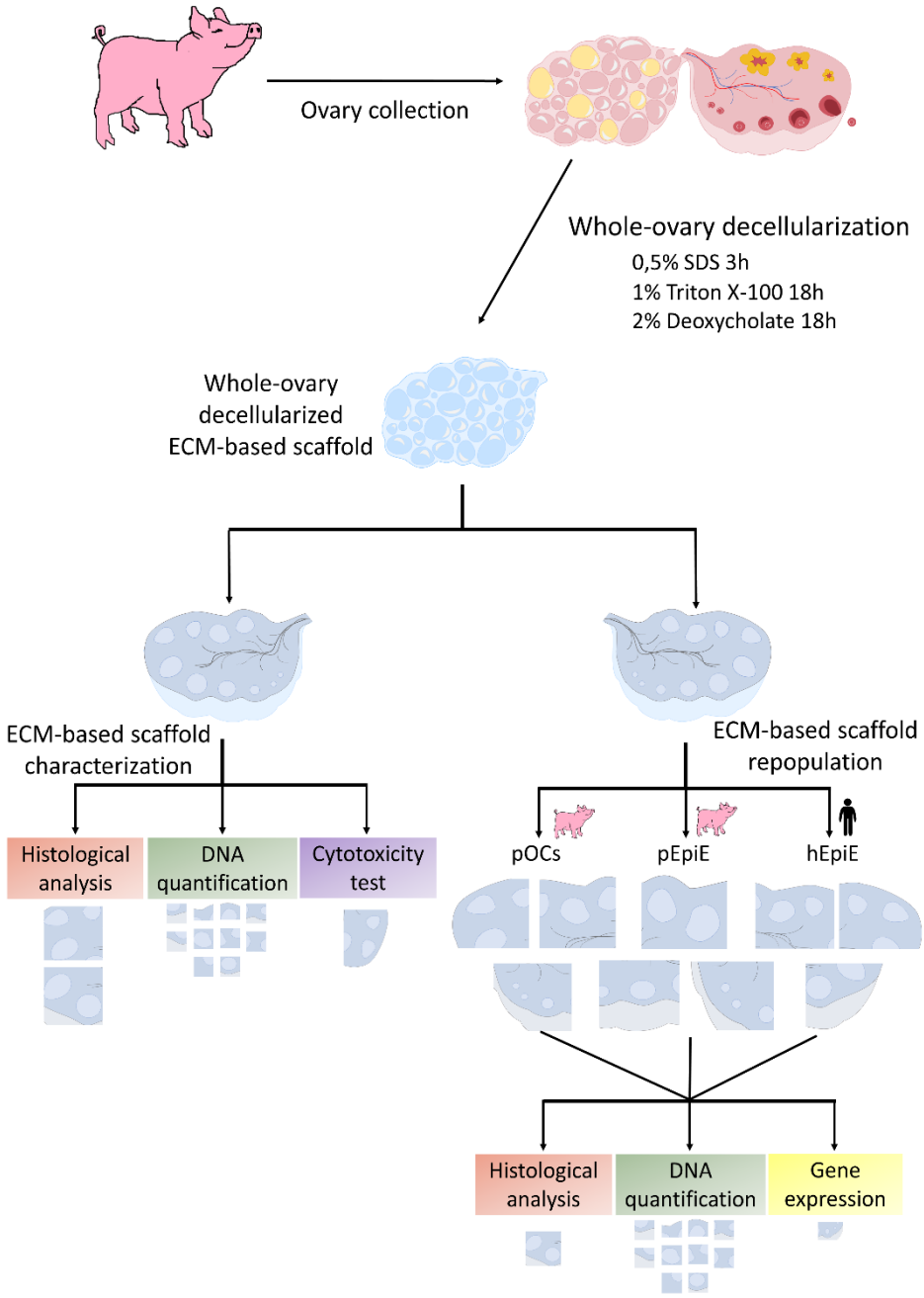


**Figure 1.** Scheme showing overall experimental design.

*2.4. Repopulation of Decellularized Ovarian ECM-Based Scaffolds with pOCs*

pOCs were isolated immediately prior to seeding onto decellularized ovarian ECM-based scaffolds.

2.4.1. Collection of Porcine Ovaries and Isolation of pOCs

Five ovaries were collected from gilts weighing approximately 120 kg at the local slaughterhouse and transported to the laboratory in cold sterile PBS containing 2% antibiotic/antimycotic solution (Sigma). The ovarian cortex was sliced in ~1 $mm^3$ fragments and digested with 1 mg/mL type IV collagenase in HBSS for 45 min, followed by a treatment with 0.25% trypsin/EDTA solution for 15 min. Digested tissues were centrifuged and resuspended in Dulbecco's Modified Eagle Medium (DMEM) supplemented with 10% fetal bovine serum (FBS), 2 mM glutamine (Sigma), and 1% antibiotic/antimycotic solution (Sigma).

2.4.2. Repopulation of Decellularized Ovarian ECM-based Scaffolds

The pOC suspension was dispersed by pipetting, filtered with a 40 μm cell strainer, and seeded onto ECM-based scaffold fragments (7 mm in diameter and 1 mm in thickness). The repopulation process was carried out for 7 days at 37 °C in 5% $CO_2$. Half of the medium volume was refreshed every other day. Cultures were arrested after 24 and 48 h and at Day 7, as previously described [2]. Samples were subjected to histological evaluations, DNA quantification, the TUNEL assay, and gene expression analysis.

*2.5. Repopulation of Decellularized Ovarian ECM-Based Scaffolds with Epigenetically Erased Porcine Adult Dermal Fibroblasts*

2.5.1. Collection of Porcine Skin Tissues

Porcine skin tissues were collected from 5 gilts weighing approximately 120 kg at the local slaughterhouse. Specifically, 5 skin specimens of 5 $cm^2$ were obtained from an avascular area of the abdomen. Tissues were immersed in sterile PBS containing 2% antibiotic/antimycotic solution (Sigma), transported to the laboratory, and used for adult porcine dermal fibroblast isolation.

2.5.2. Isolation and Culture of Porcine Adult Dermal Fibroblasts

Adult dermal fibroblasts were isolated from fresh skin biopsies obtained from 5 gilts. Tissues were cut into small fragments of ~ 2$mm^3$ and transferred into 35 $mm^2$ Petri dishes (Sarstedt) previously coated with 0.1% gelatin (Sigma). Droplets of DMEM supplemented with 20% FBS, 2 mM glutamine (Sigma), and 2% antibiotic/antimycotic solution (Sigma) were added onto each fragment. Culture dishes were transferred in a 5% $CO_2$ incubator at 37 °C in humidified chambers. After 6 days of culture, porcine dermal fibroblasts started to grow out of the original fragments, and the latter were carefully removed. Cells were cultured using the medium described above, grown in 5% $CO_2$ at 37 °C, and passaged twice a week at a 1:3 ratio. The porcine primary cell lines obtained from each individual were used in triplicate in 3 independent experiments.

2.5.3. Epigenetic Erasing of Porcine Adult Dermal Fibroblasts With 5-aza-CR and Repopulation of Decellularized Ovarian ECM-based Scaffolds

Porcine adult dermal fibroblasts were plated onto 0.1% gelatin (Sigma) precoated T75 flasks at a concentration of $7.8 \times 10^4$ cells/$cm^2$. Then, 24 h after seeding, cells were exposed to the epigenetic eraser 5-aza-cytidine (5-aza-CR; Sigma) at a 1μM concentration for 18 h. The concentration and time of exposure were selected based on our previous studies [30–37]. At the end of 5-aza-CR exposure, epigenetically erased porcine adult dermal fibroblasts (pEpiE) were used to repopulate the decellularized ovarian ECM-based scaffolds.

To this purpose, $7 \times 10^6$ pEpiE were resuspended in 300 μL of DMEM supplemented with 10% FBS, 2 mM glutamine (Sigma), and 1% antibiotic/antimycotic solution (Sigma) and seeded onto scaffold fragments (7 mm in diameter and 1 mm in thickness), which were then cultured in 5% CO2 at 37 °C for 7 days. Half of the medium volume was refreshed every other day. Cultures were arrested after 24 and 48 h and after 7 days. Samples were subjected to histological evaluations, DNA quantification, the TUNEL assay, and gene expression analysis. pEpiE plated in standard plastic 4-well multidishes (Nunc) and cultured in DMEM supplemented with 10% FBS, 2 mM glutamine (Sigma), and 1% antibiotic/antimycotic solution (Sigma) were used as the control.

*2.6. Repopulation of Decellularized Ovarian ECM-Based Scaffolds with Epigenetically Erased Human Adult Dermal Fibroblasts*

2.6.1. Collection of Human Skin Tissues

Human skin biopsies were collected from 5 healthy women undergoing surgical interventions. Samples were transported to the laboratory in sterile PBS containing 2% antibiotic/antimycotic solution (Sigma) and used for adult human dermal fibroblast isolation.

2.6.2. Isolation and Culture of Human Adult Dermal Fibroblasts

Human adult dermal fibroblasts were isolated from skin biopsies freshly collected from 5 healthy women. Samples were cut into ~ $2mm^3$ fragments and transferred into 0.1% gelatin (Sigma) precoated 35 $mm^2$ Petri dishes (Sarstedt). Droplets of DMEM supplemented with 20% FBS, 2 mM glutamine (Sigma), and 2% antibiotic/antimycotic solution (Sigma) were added onto each fragment. Culture was carried out in humidified chambers using a 5% $CO_2$ incubator at 37 °C. After 6 days of culture, human dermal fibroblasts grew out of the original tissues, which were carefully removed. Fibroblasts were cultured using the medium described above, grown in 5% $CO_2$ at 37 °C and passaged twice a week at a 1:3 ratio. The human primary cell lines obtained from each individual were used in triplicate in 3 independent experiments.

2.6.3. Epigenetic Erasing of Human Adult Dermal Fibroblasts with 5-aza-CR and Repopulation of Decellularized Ovarian ECM-Based Scaffolds

Human fibroblasts were seeded onto T75 flasks previously coated with 0.1% gelatin (Sigma) at a concentration of $7.8 \times 10^4$ cells/$cm^2$. Then, 24 h after plating, cells were exposed to the epigenetic eraser 5-aza-CR (Sigma) at a 1μM concentration for 18 h [30–37]. At the end of 5-aza-CR exposure, $7 \times 10^6$ epigenetically erased human dermal fibroblasts (hEpiE) were resuspended in 300 μL of DMEM supplemented with 10% FBS, 2 mM glutamine (Sigma), and 1% antibiotic/antimycotic solution (Sigma) and seeded onto scaffold fragments to repopulate the decellularized ovarian ECM-based scaffolds. Cell repopulation was performed in 5% $CO_2$ at 37 °C for 7 days. Half of the medium volume was refreshed every other day. Cultures were arrested after 24 and 48 h and at Day 7. Samples were subjected to histological evaluations, DNA quantification, the TUNEL assay, and gene expression analysis. hEpiE plated in standard plastic 4-well multidishes (Nunc) and cultured in DMEM supplemented with 10% FBS, 2 mM glutamine (Sigma), and 1% antibiotic/antimycotic solution (Sigma) were used as the control.

*2.7. Histological Analysis*

Samples were fixed in 10% buffered formalin for 24 h at room temperature, dehydrated in graded alcohols, cleared with xylene, and embedded in paraffin. Serial microtome sections (5 μm thick) were cut, dewaxed, rehydrated, and stained with hematoxylin and eosin (H&E, BioOptica) to evaluate the general morphological aspects. ECM components were analyzed with Masson Trichrome staining (Bio-optica) for the detection of collagen, Mallory Trichrome staining (Bio-optica) for collagen and elastic fibers, Gomori's aldehyde-fuchsin (Bio-optica) for elastic fibers alone, and Alcian blue (pH 2.5; Bio-optica) for the total glycosaminoglycan (GAGs) content. The efficient cell removal was confirmed with 4',6-diamidino-2-phenylindole (DAPI), and the cell density was measured. Samples were analyzed under an Eclipse E600 microscope (Nikon) equipped with a digital camera (Nikon). Pictures were acquired with NIS-Elements Software (Version 4.6; Nikon). Native ovaries were used as the control.

*2.8. Stereological Analysis*

Volume density (Vv) estimation of collagen, elastin, and GAG was performed on Masson Trichrome, Gomori's aldehyde-fuchsin, and Alcian blue-stained (pH 2.5) vertical sections, respectively, according to the general Delesse principle. Briefly, the relative volume of each area of interest was estimated from the fractional area of the structure of interest (e.g., collagen) and the total area of the reference compartment (e.g., whole section). Systematic uniform random sampling was applied, and images were captured and superimposed with a point-count stereologic grid with

equally distant test points. The points hitting the structure of interest and the respective reference compartment were counted, and the relative volume of each region of interest was then calculated from the respective quotient of points hitting these structures. Vv expressed as percentages was calculated as follows:

$$Vv_{(\text{analyzed compartment, reference compartment})} = [\sum P_{(\text{analyzed compartment})} / \sum P_{(\text{reference compartment})}] \times 100$$

where $\sum P_{(\text{analyzed compartment})}$ is the number of points hitting the compartment under study and $\sum P_{(\text{reference compartment})}$ is the number of points hitting the relevant structure.

*2.9. Cell Density*

The cell number was counted in 5 DAPI-stained tissue sections obtained from each sample. Then, 5 randomly selected fields, at 100× total magnification, were analyzed for each section. Images were acquired with constant exposure parameters and analyzed with ImageJ software (http://rsbweb.nih.gov/ij/index. html), using the Automated Cell Counter tool and following the provider's instructions. Briefly, 8 bit images were generated, and threshold adjustments were applied. Images were subsequently segmented with a thresholding algorithm in order to highlight areas occupied by the nuclei and to remove the background. Collected data were transformed in binary form. Size and circularity parameters were set, and nuclei were automatically counted. Cell density is expressed per mm2 of tissue.

*2.10. DNA Quantification*

Ten fragments, ranging from 10 to 24 mg, were cut from each decellularized ovarian ECM-based scaffold and from each repopulated one. Genomic DNA was extracted from each fragment with the PureLink® Genomic DNA Kit, following the manufacturer's instructions. The DNA concentration was measured with NanoDrop 8000 and normalized against the fragment weights previously annotated. Native ovarian tissues were used as the control.

*2.11. TUNEL Assay*

Apoptotic cell death was evaluated with the terminal deoxynucleotidyl transferase-mediated dUTP nick end-labeling (TUNEL) assay. Dewaxed and rehydrated sections were digested with 10 μg/mL proteinase-K (Roche) for 30 min at 37°C and labelled with the in situ Cell Death Detection Kit, TMR red (Sigma), according to the manufacturer's instructions. Prior to the labelling procedure, positive controls were treated with DNase I recombinant (50 U/mL in 50 mM Tris–HCl, pH 7.5, and 1 mg/mL BSA) for 10 min at 25 °C, to induce DNA strand breaks. For negative controls, TDT was omitted from the reaction mixture. All samples were counterstained with DAPI and mounted with ProLong™ Gold Antifade Mountant. Slides were observed under a Nikon Eclipse 600 microscope. Native tissue was used as the control. TUNEL-positive cells were counted, and their numbers are expressed as a percentage of the total cell counted.

*2.12. Cytotoxicity Assessment*

Decellularized ovarian ECM-based scaffold cytotoxicity was assessed by performing the 3(4,5-dimethylthiazole-2-yl)-2,5-diphenyltetrazolium-bromide (MTT, Roche) assay. Briefly, both porcine and human fibroblasts were plated onto 96-well multidishes at a seeding density of $5 \times 10^3$ cells/mL. After 24 h, 20 mg of each generated decellularized scaffold was added to cells and cocultured for 1, 3, and 7 days. The, 10 μL of MTT solution was added to the culture media and incubated for 4 h. Formazan salt crystals were dissolved in 100 μL of 10% SDS in 0.01 M HCl overnight. Optical density (OD) was measured at 550 nm. In the control culture (CTR), porcine and human fibroblasts were plated at the same seeding density ($5 \times 10^3$ cells/mL), and the addition of decellularized whole-ovary fragments was omitted. All experiments were performed in triplicate.

*2.13. Gene expression Analysis*

RNA was extracted using the TaqManGene Expression Cells to Ct kit (Applied Biosystems) following the manufacturer's instruction. DNase I was added in lysis solution at a 1:100 concentration. Quantitative PCR was performed on a CFX96 Real-Time PCR (Bio-Rad) using predesigned gene-specific primers and probe sets from TaqManGene Expression Assays (see Table 1 for the primer information). ACTB and GAPDH were used as internal reference genes. CFX Manager software (Bio-Rad) was used for target gene quantification. Gene expression levels are reported with the highest expression set to 1 and the others relative to this.

**Table 1.** List of primers used for quantitative PCR analysis.

| Gene | Species | Description | Cat. N. |
|---|---|---|---|
| ACTB | Sus scrofa | Actin, beta | Ss03376563_uH |
| ACTB | Homo sapiens | Actin, beta | Hs99999903_m1 |
| AMH | Sus scrofa | Anti-Mullerian hormone | Ss03383931_u1 |
| AMH | Homo sapiens | Anti-Mullerian hormone | Hs00174915_m1 |
| CYP11A1 | Sus scrofa | Cytochrome P450 family 11 subfamily A member 1 | Ss03384849_u1 |
| CYP11A1 | Homo sapiens | Cytochrome P450 family 11 subfamily A member 1 | Hs00167984_m1 |
| CYP19A1 | Sus scrofa | Cytochrome P450 family 19 subfamily a member 1 | Ss03384876_u1 |
| CYP19A1 | Homo sapiens | Cytochrome P450 family 19 subfamily a member 1 | Hs00903411_m1 |
| FSHR | Sus scrofa | Follicle-stimulating hormone receptor | Ss03384581_u1 |
| FSHR | Homo sapiens | Follicle-stimulating hormone receptor | Hs01019695_m1 |
| GAPDH | Sus scrofa | Glyceraldehyde-3-phosphate dehydrogenase | Ss03375629_u1 |
| GAPDH | Homo sapiens | Glyceraldehyde-3-phosphate dehydrogenase | Hs02786624_g1 |
| LHCGR | Sus scrofa | Luteinizing hormone/choriogonadotropin receptor | Ss03384991_u1 |
| LHCGR | Homo sapiens | Luteinizing hormone/choriogonadotropin receptor | Hs00174885_m1 |
| NANOG | Sus scrofa | Nanog homeobox | Ss04245375_s1 |
| NANOG | Homo sapiens | Nanog homeobox | Hs02387400_g1 |
| OCT4 | Sus scrofa | POU Class 5 Homeobox 1 | Ss03389800_m1 |
| OCT4 | Homo sapiens | POU Class 5 Homeobox 1 | Hs00999632_g1 |
| REX1 | Sus scrofa | ZFP42 zinc finger protein | Ss03373622_g1 |
| REX1 | Homo sapiens | ZFP42 zinc finger protein | Hs01938187_s1 |
| SOX2 | Sus scrofa | SRY-Box Transcription Factor 2 | Ss03388002_u1 |
| SOX2 | Homo sapiens | SRY-Box Transcription Factor 2 | Hs04234836_s1 |
| STAR | Sus scrofa | Steroidogenic acute regulatory protein | Ss03381250_u1 |
| STAR | Homo sapiens | Steroidogenic acute regulatory protein | Hs00986559_g1 |
| THY1 | Sus scrofa | Thy-1 cell surface antigen | Ss03376963_u1 |
| THY1 | Homo sapiens | Thy-1 cell surface antigen | Hs00174816_m1 |
| VIM | Sus scrofa | Vimentin | Ss04330801_gH |
| VIM | Homo sapiens | Vimentin | Hs05024057_m1 |

### *2.14. Statistical Analysis*

Statistical analysis was performed using one-way ANOVA (SPSS 19.1; IBM). Data are presented as the mean ± the standard deviation (SD). Differences of $p \leq 0.05$ were considered significant and are indicated with different superscripts.

## 3. Results

### *3.1. ECM-based Scaffold Evaluation*

#### 3.1.1. Whole-Organ Decellularization Protocol Eliminates Cellular Components and Maintains Ovarian Macro-Architecture

Macroscopic observations revealed that, during the decellularization process, the color of the ovaries turned from red to white, while the shape and the homogeneity were well preserved, without any deformation (Figure 2a).

H & E and DAPI staining showed that the decellularization process was successful and the obtained ECM-based scaffolds were devoid of cells. In particular, basophilic and DAPI staining were absent in decellularized scaffolds (scaffold), while cell nuclei were clearly visible in native

ovaries (native), used as the control (Figure 2b). Cell density analysis confirmed a significantly lower number of nuclei in ECM-based scaffolds (scaffold), compared to untreated tissues (native; Figure 2c). In addition, the DNA quantification assay demonstrated a drastic decrease in the DNA content after the whole-organ decellularization process. Specifically, 0.05 ± 0.03 µg DNA/mg of tissue was measured in ECM-based scaffolds (scaffold), while native ovaries contained 1.55 ± 0.21 µg DNA/mg of tissue (native; Figure 2d).

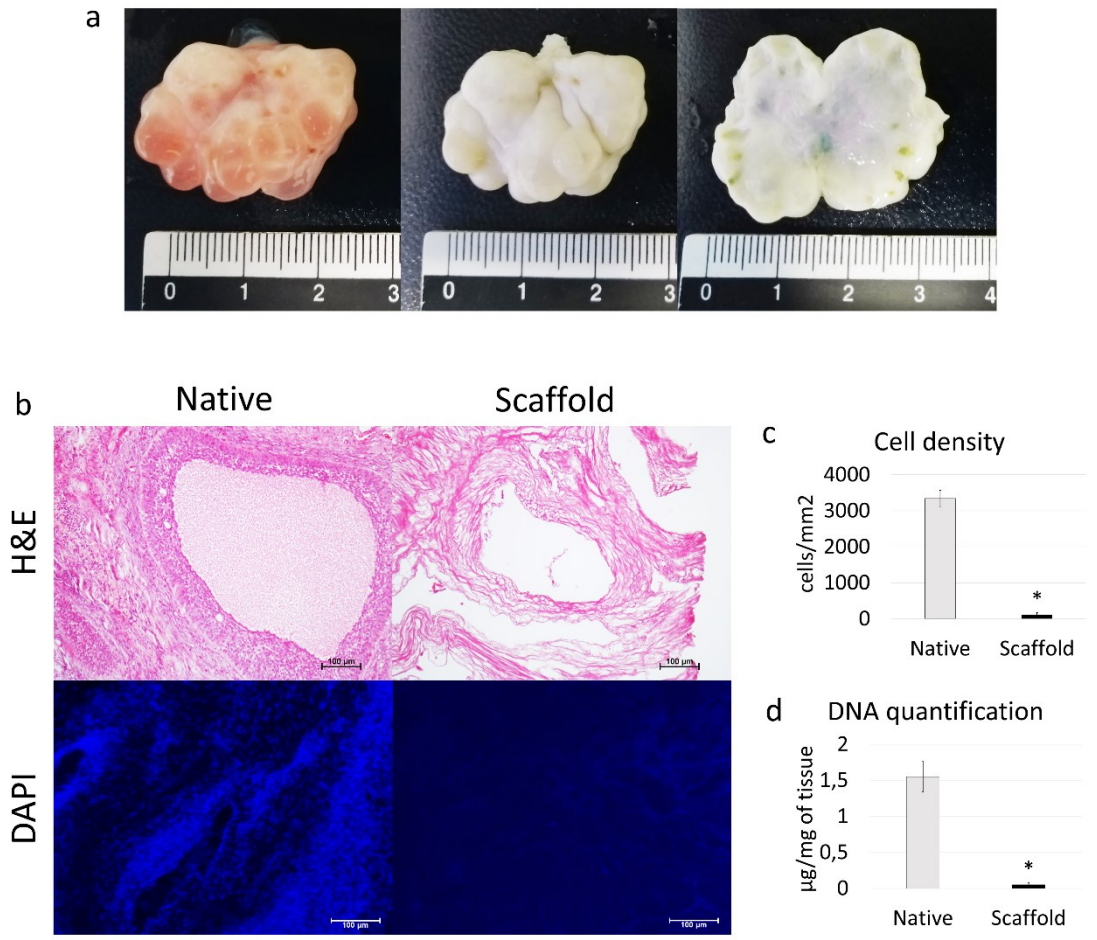


**Figure 2.** Macroscopic and microscopic evaluations of ECM-based scaffolds and DNA quantification. (**a**) Native (left panel) and decellularized (middle and right panels) ovaries display comparable shapes and homogeneity, while the color turns from red (left panel) to white (middle and right panels); (**b**) H & E staining shows the presence of both basophilic (cell nuclei) and eosinophilic (cell cytoplasm and ECM) staining in the control tissue (native), while cell nuclei and the related basophilic staining are absent in the decellularized ECM-based scaffolds (scaffold). DAPI staining displays the presence of nuclei in native ovaries (native), which disappeared after the decellularization process (scaffold). Scale bars = 100 µm; (**c**) Cell density demonstrated a significantly lower number of nuclei in the decellularized ECM-based scaffolds (scaffold) compared to the untreated tissues (native); data are expressed as the mean ± the standard error of the mean (SEM), *$p < 0.05$; (**d**) DNA quantification analysis showed a significant decrease in the DNA content of the decellularized ECM-based scaffolds (scaffold) compared to the native tissue (native). Data are expressed as the mean ± the standard error of the mean (SEM), *$p < 0.05$.

3.1.2. Whole-Organ Decellularization Protocol Preserves Ovarian ECM Components

Histochemical assessments demonstrated the preservation of the major structural components of the ECM after the whole-organ decellularization process. Both Masson and Mallory Trichrome staining showed the persistence of collagen (blue), which displayed a comparable distribution between ECM-based scaffolds (scaffold) and native tissues (native) (Figure 3a). In addition,

Mallory Trichrome staining indicated the maintenance of elastic fibers (red magenta) after the decellularization process (scaffold) (Figure 3a). This was also confirmed by Gomori's aldehyde-fuchsin staining, demonstrating that the elastic fibers scattered throughout the decellularized ovarian tissues (scaffold), similar to what was detected in native ovaries (native, Figure 3a). Alcian blue staining revealed GAG retention in ECM-based scaffolds (scaffold; Figure 3a). The morphological observations were also confirmed by stereological quantifications, which demonstrated no differences in collagen (Figure 3b), elastin (Figure 3c), and GAGs (Figure 3d) between the ECM-based scaffolds (scaffold) and the native tissue (native).

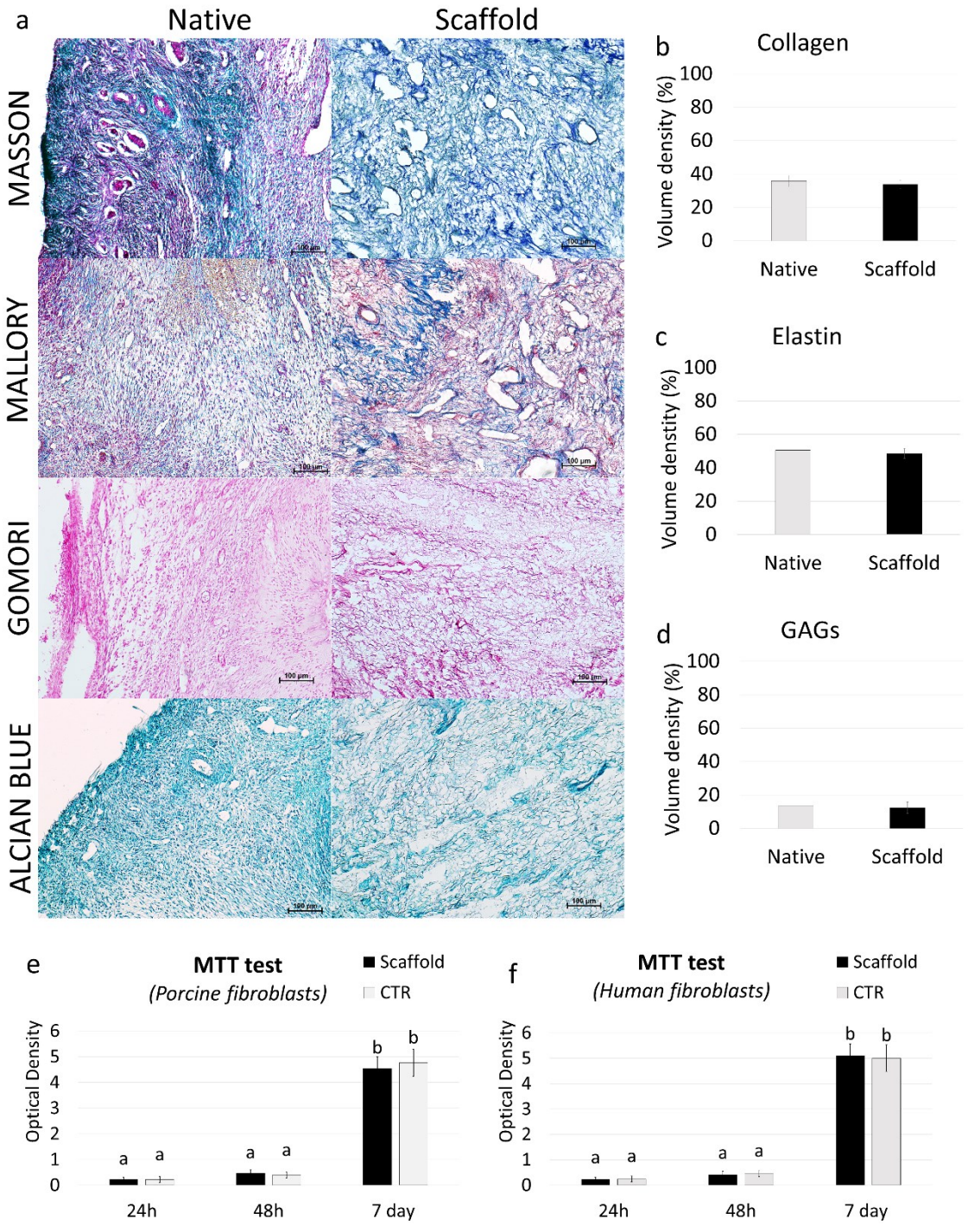


**Figure 3.** ECM microarchitecture and composition in ECM-based scaffolds and cytotoxicity assessment. (**a**) Masson's Trichrome staining showed the persistence of collagen fibers (blue) and their comparable

distribution between the native ovaries (native) and the decellularized tissues (scaffold). Mallory's Trichrome staining demonstrated the maintenance of intact collagen (blue) and elastic fibers (red magenta) after the decellularization process (scaffold). Gomori's aldehyde-fuchsin staining confirmed that ECM-based scaffolds (scaffold) retained the elastic fibers scattered throughout the decellularized ovary, similar to what was visible in untreated ovaries (native). Alcian blue staining revealed GAG retention in the decellularized scaffolds (scaffold). Scale bars = 100 μm. (**b–d**) Stereological quantifications demonstrated no significant differences between untreated ovaries (native) and the decellularized ECM-based scaffolds (scaffold) in collagen (**b**), elastin (**c**), and GAG (**d**) contents. Data are expressed as the mean ± the standard error of the mean (SEM) ($p > 0.05$). (**e–f**) MTT assays demonstrated no significant differences in the OD values of porcine (**e**) and human (**f**) adult dermal fibroblasts cocultured with ECM-based scaffold fragments and those identified in control cultures (CTR) at all the different time points analyzed. Data are expressed as the mean ± the standard error of the mean (SEM) ($p > 0.05$). a and b indicate statistically significant differences ($p < 0.05$).

#### 3.1.3. ECM-based Scaffolds Show No Cytotoxicity In Vitro

ECM-based scaffold cytocompatibility was determined by the MTT assay, performed using both porcine and human adult dermal fibroblasts. The results obtained demonstrated that the decellularized scaffold exerted no cytotoxic effects. In particular, the OD values detected in porcine (Figure 3e) and human cells (Figure 3f), cocultured with ECM-based scaffolds, were comparable with those obtained in control cultures (CTR), where scaffold fragments were omitted. More in detail, all experimental groups displayed analogous viabilities after 24 and 48 h of culture (Figure 3e,f). In addition, even protracted exposure (seven days) to the decellularized matrix did not induce any cytotoxic response, confirming the efficient removal of the residual chemicals from the ECM-based scaffolds (Figure 3e,f).

### *3.2. pOCs Recellularize the ECM-Based Scaffold In Vitro*

Freshly isolated pOCs (Figure 4a) were able to adhere and gradually migrate into the decellularized ECM-based ovarian scaffolds (Figure 4b).

H & E and DAPI staining demonstrated the presence of pOCs in the scaffolds after 24 h of coculture (Figure 4c,d). The histological observations were confirmed by cell density analysis, which showed an increasing number of cells along the culture period (Figure 4e). The TUNEL assay demonstrated the survival of the engrafted cells and showed pOC viability even after seven days of culture (Figure 4 g,h).

In agreement with the morphological data, DNA quantification studies indicated an increase in DNA content. In particular, 0.61 ± 0.05, 1.12 ± 0.1, and 1.34 ± 0.1µg of DNA/mg of tissue were detected after 24 and 48 h and at Day 7 of culture, respectively (Figure 4f).

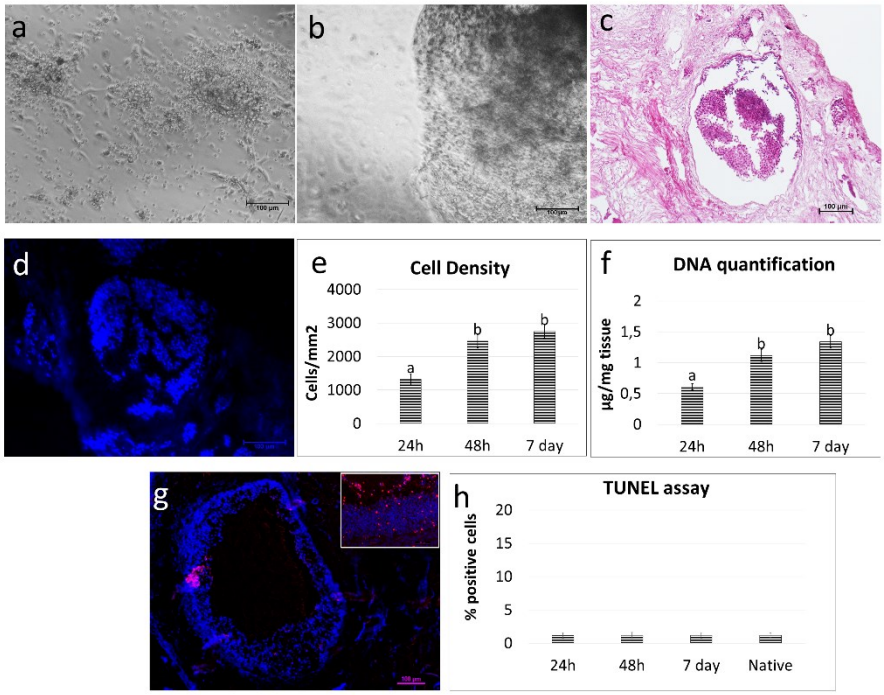


**Figure 4.** Repopulation of decellularized ovarian ECM-based scaffolds with pOCs. (**a**) Image illustrating freshly isolated pOCs. Scale bar = 100 µm. (**b**) pOCs adhered and migrated into the decellularized ECM-based ovarian scaffolds. Representative image after 7 days of culture. Scale bar = 100 µm. (**c**) H & E staining demonstrated the presence of pOCs in the ECM-based scaffolds. Scale bar = 100 µm. (**d**) DAPI staining confirmed the positivity for nuclei. Scale bar = 100 µm. (**e**) Cell density analysis showed ECM-based scaffolds' repopulation after 24 h, with a higher number of cells after 48h and 7 days of coculture. Data are expressed as the mean ± the standard error of the mean (SEM). a and b indicate statistically significant differences ($p < 0.05$). (**f**) DNA quantification demonstrated the presence of pOCs into the ECM-based scaffolds after 24 h, with an increasing cell number at 48h, which was steadily maintained at Day 7. Data are expressed as the mean ± the standard error of the mean (SEM). a and b indicate statistically significant differences ($p < 0.05$). (**g**) Representative picture of the TUNEL assay showing positive cells in red. Nuclei were stained with DAPI (blue). Scale bars = 100 µm and 50 µm. (**h**) TUNEL-positive cell rates detected 24- 48 hours and 7 days postseeding were comparable to those identified in the native tissues (native). Data are expressed as the mean ± the standard error of the mean (SEM).

Gene expression analysis revealed active transcription of the genes specific to the principal active cells of connective tissue, namely VIM and THY1, as well as the markers classically associated with granulosa cells, namely STAR, CYP11A1, CYP19A1, AMH, FSHR, and LHR (Figure 5). Interestingly, the expression levels detected for all the selected genes were comparable between those measured in native tissue (T0) and in repopulated ECM-based scaffolds at all time points considered (Figure 5).

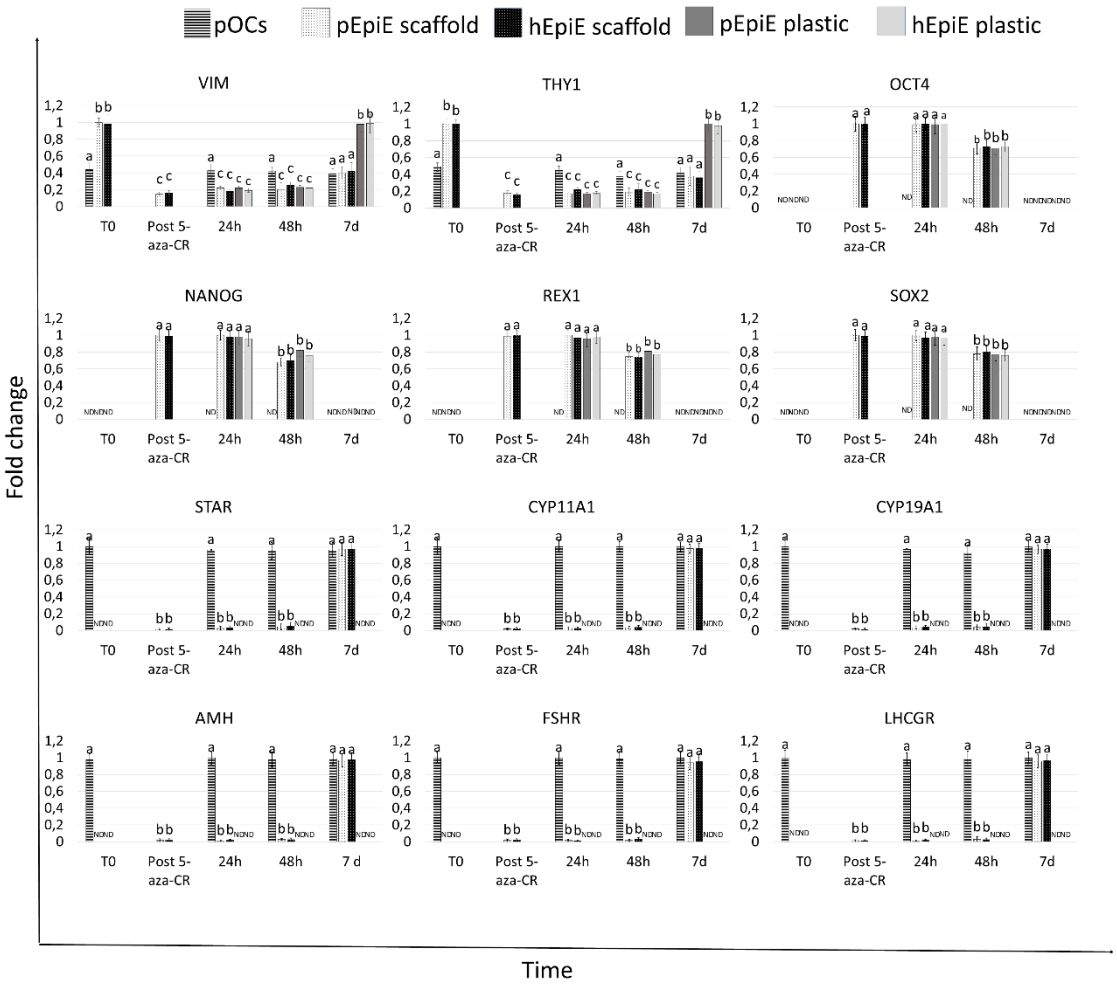


**Figure 5.** Gene expression changes in pOCs (line bars), pEpiE (white with black dots bars), and hEpiE (black with white dots bars) during the ECM-based scaffold repopulation process. Expression pattern of fibroblast-specific (VIM, and THY1), pluripotency-related (OCT4, NANONG, REX1, and SOX2), and granulosa-cell-associated (STAR, CYP11A1, CYP19A1, AMH, FSHR, and LHCGR) markers in freshly isolated pOCs and porcine and human untreated fibroblasts (T0), in fibroblasts exposed to 5-aza-CR (post 5- aza-CR), and at different time points of ECM-based scaffold repopulation (24 and 48 h and 7 days). a, b, and c indicate statistically significant differences ($p < 0.05$).

### *3.3. ECM-Based Scaffolds Induce pEpiE and hEpiE Differentiation Towards Ovarian Fate*

After epigenetic erasing with 5-aza-CR, porcine and human cells changed their phenotype; the typical fibroblast elongated morphology was replaced by an oval or round shape. Erased cells became smaller with larger nuclei and granular and vacuolated cytoplasm. These changes were functionally accompanied by the onset of the transcription of the pluripotency-related genes OCT4, NANOG, REX1, and SOX2, originally undetectable in untreated fibroblasts (T0; Figure 5c). In parallel, both pEpiE and hEpiE significantly downregulated the typical fibroblast markers VIM and THY (Figure 5).

Both porcine and human erased cells were able to repopulate the decellularized ovaries and adhered and gradually migrated into the ECM-based scaffolds. H&E and DAPI staining demonstrated the presence of cells after 24 h of coculture (Figure 6d,e,j,k). Cell density analysis showed an increasing number of cells during the period of culture (Figure 6a). In addition, the TUNEL assay revealed the survival of the engrafted cells and showed pEpiE and hEpiE viability even after seven days of culture (Figure 6f,l). The morphological data were supported by DNA quantification analysis, indicating an increase in DNA content. In particular, 0.57 ± 0.07, 1.01 ± 0.08,

and 1.19 ± 0.09 µg of DNA/mg of tissue were detected after 24 and 48 h and at Day 7 of pEpiE coculture with the ECM-based scaffolds and 0.56 ± 0.05, 1.06 ± 0.09, and 1.21 ± 0.11 µg of DNA/mg of tissue at the same time points using hEpiE (Figure 5b).

Gene expression analysis revealed the onset of the genes specifically associated with granulosa cells, namely STAR, CYP11A1, CYP19A1, AMH, FSHR, and LHR, which were induced, although at low levels, 24 and 48 h postseeding and picked by Day 7 of coculture with levels comparable to those detected in pOC repopulation experiments (Figure 5). Similarly, VIM and THY1 expression values at Day 7 were significantly lower than those identified in untreated fibroblasts (T0), but showed comparable expression levels to those detected when pOCs were used to repopulate. These changes were also paralleled by downregulation of the pluripotency-related genes OCT4, NANOG, REX1, and SOX2. In contrast, when pEpiE and hEpiE were plated onto standard plastic dishes, cells progressively reverted to their original phenotype, and after seven days of culture, the expression of the pluripotency-related genes was completely downregulated, while the VIM and THY1 levels returned comparable to those of untreated fibroblasts (Figure 5).

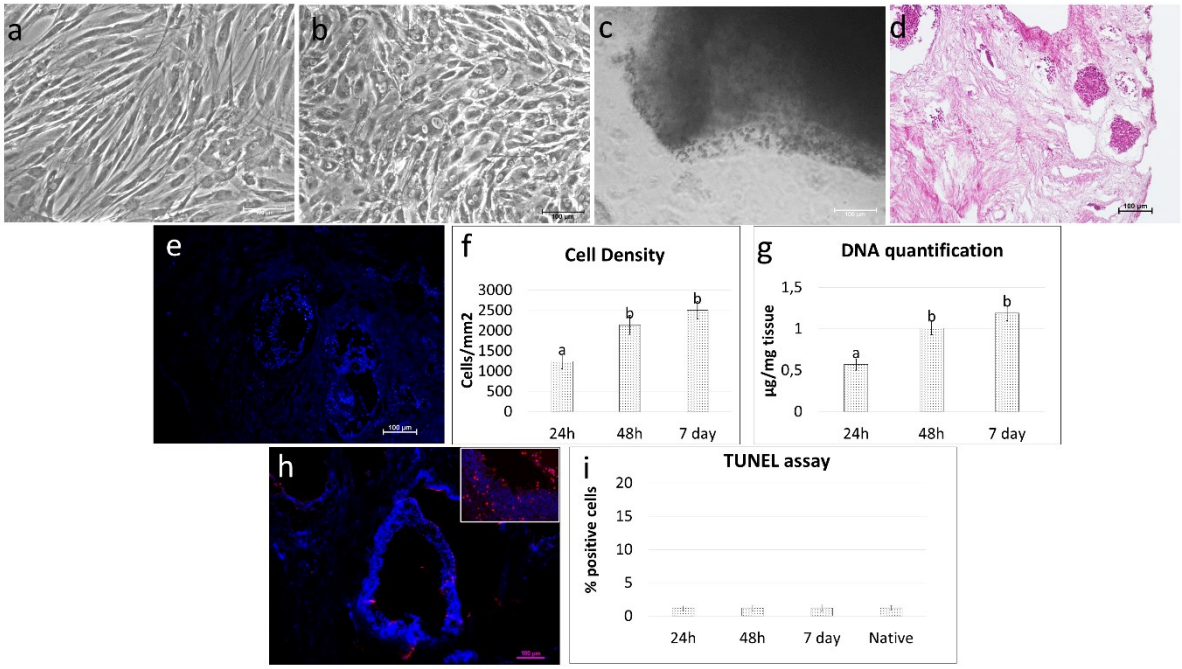


**Figure 6.** Repopulation of decellularized ovarian ECM-based scaffolds with pEpiE. (**a**) Representative image of porcine untreated fibroblasts showing the typical elongated shape. Scale bar = 100 µm. (**b**) After 18 h of exposure to 5-aza-CR, the cells displayed a round epithelioid aspect and became smaller in size with larger nuclei and granular cytoplasm. Scale bar = 100 µm. (**c**) pEpiE adhered and migrated to the decellularized ECM-based ovarian scaffolds. Representative image after 7 days of culture. Scale bar = 100 µm. (**d**) H & E staining demonstrated the presence of pEpiE in the ECM-based scaffolds. Scale bar = 100 µm. (**e**) DAPI staining confirmed the positivity for nuclei. Scale bar = 100 µm. (**f**) Cell density analysis showed ECM-based scaffolds' repopulation after 24 h, with a higher number of cells after 48 h and 7 days of coculture. Data are expressed as the mean ± the standard error of the mean (SEM). a and b indicate statistically significant differences ($p < 0.05$). (**g**) DNA quantification demonstrated the presence of pEpiE in the ECM-based scaffolds after 24 h, with an increasing number of cells at 48 h, which was steadily maintained at Day 7. Data are expressed as the mean ± the standard error of the mean (SEM). a, and b indicate statistically significant differences ($p < 0.05$). (**h**) Representative picture of the TUNEL assay showing positive cells in red. Nuclei were stained with DAPI (blue). Scale bars = 100 µm and 50 µm. (**i**) TUNEL-positive cell rates detected 24–48 h and 7 days after seeding were comparable to those identified in the native tissues (native). Data are expressed as the mean ± the standard error of the mean (SEM).

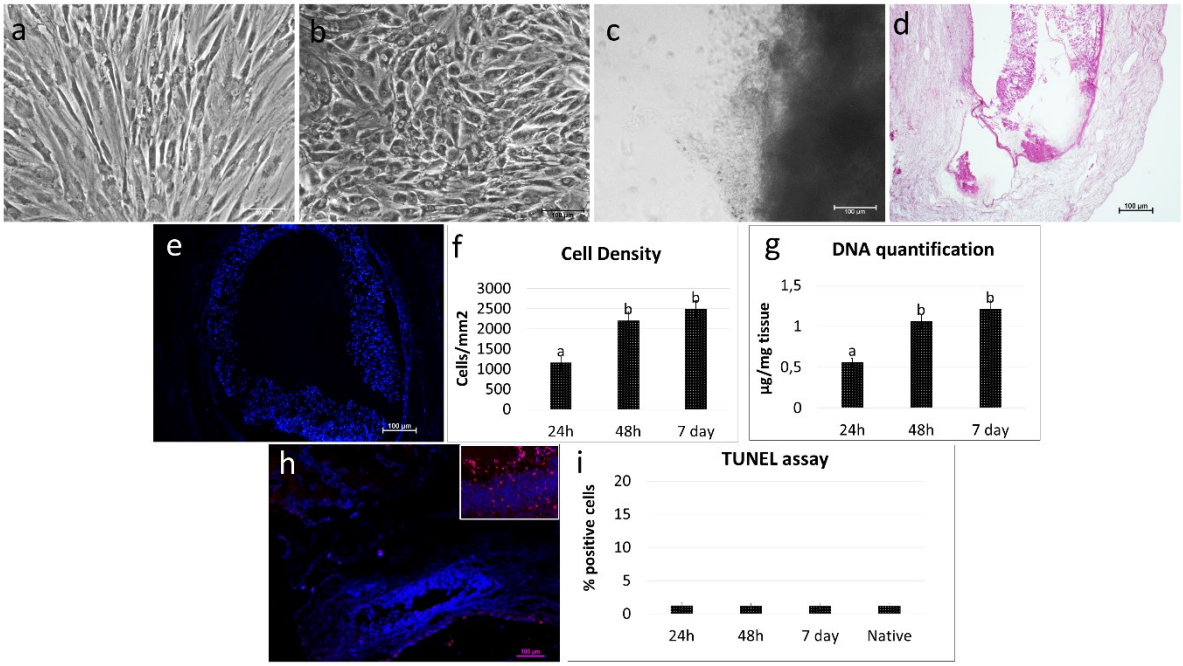


**Figure 7.** Repopulation of decellularized ovarian ECM-based scaffolds with hEpiE. (**a**) Representative image of human untreated fibroblasts showing the typical elongated shape. Scale bar = 100 µm. (**b**) After 18 h of exposure to 5-aza-CR, cells displayed a round epithelioid aspect and became smaller in size with larger nuclei and granular cytoplasm. Scale bar = 100 µm. (**c**) hEpiE adhered and migrated into the decellularized ECM-based ovarian scaffolds. Representative image after 7 days of culture. Scale bar = 100 µm. (**d**) H & E staining demonstrated the presence of hEpiE in the ECM-based scaffolds. Scale bar = 100 µm. (**e**) DAPI staining showed the positivity for nuclei. Scale bar = 100 µm. (**f**) Cell density analysis indicated ECM-based scaffolds' repopulation after 24 h, with a higher number of cells after 48h and 7 days of coculture. Data are expressed as the mean ± the standard error of the mean (SEM). a and b indicate statistically significant differences ($p < 0.05$). (**g**) DNA quantification confirmed the presence of hEpiE in the ECM-based scaffolds after 24 h, with an increasing number of cells at 48h, which was steadily maintained at Day 7. Data are expressed as the mean ± the standard error of the mean (SEM). a and b indicate statistically significant differences ($p < 0.05$). (**h**) Representative picture of the TUNEL assay showing positive cells in red. Nuclei were stained with DAPI (blue). Scale bars = 100 µm and 50 µm. (**i**) TUNEL-positive cell rates detected 24–48 hours and 7 days after seeding were comparable to those identified in the native tissues (native). Data are expressed as the mean ± the standard error of the mean (SEM).

## 4. Discussion

Assisted reproduction techniques and hormone replacement therapies presently adopted for the management of POF-affected patients are not fully effective in recovering ovarian functions and do not provide a definitive solution for female fertility restoration. There is therefore an urgent need for novel and efficient therapeutic alternatives, and among the possible strategies, the development of an "artificial ovary" may represent a promising and safe approach to obtain transplantable "structures" that can be used in patients, from childhood to adult age, for restoring endocrine dysfunctions and re-establishing reproductive activities.

In the present study, we described a novel approach to generate porcine decellularized ovarian ECM-based scaffolds and demonstrated their ability to support cell survival and growth and drive cell differentiation. Ovarian ECM-based scaffolds were obtained through the use of a four-step decellularization protocol previously developed in our laboratory. In particular, this involved a freeze–thaw cycle, followed by sequential incubations with SDS, Triton X-100, and deoxycholate, which was previously shown, and here confirmed, for its ability to successfully remove cells, cellular debris, and nuclear material from whole ovaries, while maintaining the macrostructure and microstructure of the original tissue, preserving the shape and homogeneity, and showing no

deformation at the end of the process [2,29]. In addition, similar to what was described by Liu et al. [5] and Hassanpour et al. [38], who applied a decellularization protocol to porcine and human ovarian fragments, respectively, the color of the organs turned from red to white, suggesting the ability of the protocol adopted here to induce a significant reduction in cellular components, even when applied to whole ovaries. This was also confirmed by the histological analysis and the DNA quantifications presented in our manuscript, which demonstrated a significant decrement in cell number and DNA content, respectively.

Parallel with the effective removal of the cellular compartment, a key aspect for the quality of the produced bioscaffolds is the preservation of the ovarian microstructures and its ECM components post-decellularization. The histochemical analysis performed here demonstrated the maintenance of intact collagen and elastic fibers, as well as the persistence of an unaltered distribution of GAGs. This was also confirmed by stereological quantifications, which revealed no differences between native and decellularized ovaries for collagen, elastin, and GAG content, in agreement with what was recently reported by Henning et al., who demonstrated comparable matrisome protein quantities and distributions in porcine decellularized ovaries and the related native tissue [7].

Detergent residuals within the decellularized ECM-based scaffolds are also a critical point that needs to be carefully addressed, since this may impair the subsequent scaffold biocompatibility, both in vitro and in vivo, as well as its subsequent recellularization [39]. In this respect, the cytotoxicity assay performed post-decellularization revealed no significant differences between the MTT values detected in porcine and human fibroblasts cocultured with ECM-based scaffolds and those scored in control cultures, even when exposures were protracted up to seven days. To our understanding, this suggests that any toxic effect exerted by the decellularized ovaries is very unlikely.

Altogether, these findings support and expand previous results obtained through the use of decellularization techniques applied to ovarian tissue fragments [5,28] and demonstrate, to our understanding, the possibility to successfully extend the protocol to the whole ovary, leading to the production of ECM-based matrixes suitable for tissue bioengineering.

In this perspective, decellularized ECM-based scaffold quality was tested in repopulation experiments. More in detail, when freshly isolated pOCs were seeded onto the generated biomatrices, cells rapidly adhered and gradually migrated into the bioscaffolds within the first 24 h. The cell homing ability was confirmed both by H&E and DAPI staining, as well as by cell density analysis, which demonstrated an increase in cell number along the culture period. In parallel, the TUNEL assay showed the repopulating cell viability as being stably maintained in culture, with apoptotic indices comparable to those scored in the native tissue. These observations suggested the decellularized ECM-based scaffolds' ability to support ovarian cell survival in vitro for a protracted culture period, as demonstrated by DNA quantification studies, which showed an increase in DNA content with $0.61 \pm 0.05$, $1.12 \pm 0.1$, and $1.34 \pm 0.1$ μg of DNA/mg of tissue after 24 h and 48 h and at Day 7 of culture, respectively. These data are in full agreement and further expand previous studies reporting the ability of decellularized ovarian fragments to successfully support murine and human ovarian cell engraftment in vitro [5,17,38]. In addition, they demonstrated the possibility to use whole-ovary decellularized ECM-based scaffolds as suitable niches for pOC ex vivo culture.

Molecular evaluations of engrafted pOCs demonstrated active and steady transcription for the main ovary-specific genes. In particular, we could detect the expression of genes specifically associated with granulosa cells, namely STAR, CYP11A1, CYP19A1, AMH, FSHR, and LHR, as well as connective tissue markers, such as VIM and THY1. Interestingly, the results obtained indicated that the relative expression levels of each specific gene vs. all the other genes considered was maintained for all of the engrafting period. Although further studies are needed to better elucidate this aspect, it is tempting to speculate that, different from what was reported for 2D culture systems where a poor correlation with in vivo conditions was detected [40,41], the decellularized ECM-based scaffold niche may provide repopulating cells with inputs that preserve the transcription regulatory mechanisms at work in their native tissue, offering an adequate 3D microenvironment driving repopulating cells. This hypothesis found further support in the results obtained when ECM-based scaffolds were repopulated with epigenetically erased cells obtained

through epigenetic erasing [30–37,43–48]. Similar to what was observed when pOCs were used, both pEpiE and hEpiE rapidly adhered and migrated into the bioscaffolds, suggesting the ability of the decellularized ECM-based scaffolds to provide a suitable environment and support epigenetically erased cell attachment, migration, and growth. Notably, gene expression analysis showed striking changes in the transcription pattern, with downregulation of the pluripotency-related genes OCT4, NANOG, REX1, and SOX2 and the onset of the main genes specifically associated with granulosa cells, namely STAR, CYP11A1, CYP19A1, AMH, FSHR, and LHR, which were originally undetectable in repopulating cells. In particular, the expression levels of the above-mentioned genes, which have been commonly used for tracking ESC differentiation into mature and functional granulosa cells [49,50], were detectable after 24 and 48 h and reached values comparable with those detected in pOC repopulation experiments at Day 7 of culture, indicating ECM-based scaffolds' ability to properly address and drive erased cell differentiation in vitro

## 5. Conclusions

The results described in this manuscript demonstrated that decellularized ECM-based scaffolds may provide an optimal 3D microenvironment for ex vivo culture of ovarian cells, supporting the maintenance of the original expression pattern. Furthermore, they are able to properly drive epigenetically erased cell differentiation, fate, and viability in vitro, encouraging repopulating cells to adopt a transcriptional shift in response to the scaffold environment. Overall, the strategy proposed here allows for the creation of a suitable 3D platform to investigate solutions for hormone and fertility restoration, toxicological and drug testing, as well as transplantation studies.

**Author Contributions:** Investigation, G.P. and T.D.I.; data curation, G.P. and T.D.I.; writing—original draft preparation, G.P. and T.A.L.B; writing—review and editing, G.P., F.G., and T.A.L.B; funding acquisition, G.P. and T.A.L.B. All authors read and agreed to the published version of the manuscript.

**Funding:** This research was funded by Carraresi Foundation, PSR2017 and PSR2020. This research is part of the project "MIND FoodS HUB (Milano Innovation District Food System Hub): Innovative concept for the eco-intensification of agricultural production and for the promotion of dietary patterns for human health and longevity through the creation in MIND of a digital Food System Hub", cofunded by POR FESR 2014-2020_BANDO Call HUB Ricerca e Innovazione, Regione Lombardia.

**Institutional Review Board Statement:** The study was conducted according to the guidelines of the Declaration of Helsinki and approved by the Ethics Committee of the University of Milan and of the Ospedale Maggiore Policlinico, Milan, Code 479_2016.

**Informed Consent Statement:** Informed consent was obtained from all subjects involved in the study.

**Data Availability Statement:** The data presented in this study are available on request from the corresponding author.

**Acknowledgments:** The authors are members of the COST Action CA16119 In vitro 3-D total cell guidance and fitness (CellFit) and of the Trans-COST Actions Task-Force on COVID-19.

**Conflicts of Interest:** The authors declare no conflict of interest.

## References

1. Lin, D.; Quan, H.; Chen, K.; Lin, L.; Lin, L.; Ji, Q. An adolescent girl with premature ovarian failure, Graves' disease, and chronic urticaria: A case report. *J. Med. Case Rep.* **2020**, *14*, 1–5, doi:10.1186/s13256-020-02491-w.
2. Pennarossa, G.; Ghiringhelli, M.; Gandolfi, F.; Brevini, T.A.L. Whole-ovary decellularization generates an effective 3D bioscaffold for ovarian bioengineering. *J. Assist. Reprod. Genet.* **2020**, 1–11, doi:10.1007/s10815-020-01784-9.
3. Gandolfi, F.; Ghiringhelli, M.; Brevini, T.A.L.; Gandolfi, F.; Ghiringhelli, M.; Brevini, T.A.L. Bioengineering the ovary to preserve and reestablish female fertility. *Anim. Reprod.* **2019**, *16*, 45–51, doi:10.21451/1984-3143-AR2018-0099.
4. Fu, Y.X.; Ji, J.; Shan, F.; Li, J.; Hu, R. Human mesenchymal stem cell treatment of premature ovarian failure: New challenges and opportunities. *Stem Cell Res. Ther.* **2021**, *12*, 1–13.
5. Liu, W.-Y.; Lin, S.-G.; Zhuo, R.-Y.; Xie, Y.-Y.; Pan, W.; Lin, X.-F.; Shen, F.-X. Xenogeneic decellularized scaffold: A novel platform for ovary regeneration. *Tissue Eng. Part., C. Methods* **2017**, *23*, 61–71, doi:10.1089/ten.TEC.2016.0410.

6. Eivazkhani, F.; Abtahi, N.S.; Tavana, S.; Mirzaeian, L.; Abedi, F.; Ebrahimi, B.; Montazeri, L.; Valojerdi, M.R.; Fathi, R. Evaluating two ovarian decellularization methods in three species. *Mater. Sci. Eng. C.* **2019**, *102*, 670–682, doi:10.1016/J.MSEC.2019.04.092.
7. Henning, N.F.; LeDuc, R.D.; Even, K.A.; Laronda, M.M. Proteomic analyses of decellularized porcine ovaries identified new matrisome proteins and spatial differences across and within ovarian compartments. *Sci. Rep.* **2019**, *9*, 20001, doi:10.1038/s41598-019-56454-3.
8. Donnez, J.; Dolmans, M.-M.; Pellicer, A.; Diaz-Garcia, C.; Sanchez Serrano, M.; Schmidt, K.T.; Ernst, E.; Luyckx, V.; Andersen, C.Y. Restoration of ovarian activity and pregnancy after transplantation of cryopreserved ovarian tissue: A review of 60 cases of reimplantation. *Fertil. Steril.* **2013**, *99*, 1503–1513, doi:10.1016/J.FERTNSTERT.2013.03.030.
9. Diaz-Garcia, C.; Domingo, J.; Garcia-Velasco, J.A.; Herraiz, S.; Mirabet, V.; Iniesta, I.; Cobo, A.; Remohí, J.; Pellicer, A. Oocyte vitrification versus ovarian cortex transplantation in fertility preservation for adult women undergoing gonadotoxic treatments: A prospective cohort study. *Fertil. Steril.* **2018**, *109*, 478–485, doi:10.1016/j.fertnstert.2017.11.018.
10. Moravek, M.B.; Confino, R.; Smith, K.N.; Kazer, R.R.; Klock, S.C.; Lawson, A.K.; Gradishar, W.J.; Pavone, M.E. Long-term outcomes in cancer patients who did or did not pursue fertility preservation. *Fertil. Steril.* **2018**, *109*, 349–355, doi:10.1016/j.fertnstert.2017.10.029.
11. Xu, M.; Barrett, S.L.; West-Farrell, E.; Kondapalli, L.A.; Kiesewetter, S.E.; Shea, L.D.; Woodruff, T.K. In vitro grown human ovarian follicles from cancer patients support oocyte growth. *Hum. Reprod.* **2009**, *24*, 2531–2540, doi:10.1093/humrep/dep228.
12. Luyckx, V.; Dolmans, M.M.; Vanacker, J.; Legat, C.; Fortuño Moya, C.; Donnez, J.; Amorim, C.A. A new step toward the artificial ovary: Survival and proliferation of isolated murine follicles after autologous transplantation in a fibrin scaffold. *Fertil. Steril.* **2014**, *101*, 1149–1156, doi:10.1016/j.fertnstert.2013.12.025.
13. Amorim, C.A.; Shikanov, A. The artificial ovary: Current status and future perspectives. *Futur. Oncol.* **2016**, *12*, 2323–2332.
14. Vanacker, J.; Dolmans, M.-M.; Luyckx, V.; Donnez, J.; Amorim, C.A. First transplantation of isolated murine follicles in alginate. *Regen. Med.* **2014**, *9*, 609–619, doi:10.2217/rme.14.33.
15. Hoshiba, T.; Chen, G.; Endo, C.; Maruyama, H.; Wakui, M.; Nemoto, E.; Kawazoe, N.; Tanaka, M. Decellularized extracellular matrix as an in vitro model to study the comprehensive roles of the ECM in stem cell differentiation. *Stem Cells Int.* **2016**, *2016*, 6397820, doi:10.1155/2016/6397820.
16. Gilpin, A.; Yang, Y. Decellularization strategies for regenerative medicine: From processing techniques to applications. *Biomed. Res. Int.* **2017**, *2017*, 9831534, doi:10.1155/2017/9831534.
17. Pors, S.E.; Ramløse, M.; Nikiforov, D.; Lundsgaard, K.; Cheng, J.; Andersen, C.Y.; Kristensen, S.G. Initial steps in reconstruction of the human ovary: Survival of pre-antral stage follicles in a decellularized human ovarian scaffold. *Hum. Reprod.* **2019**, *34*, 1523–1535, doi:10.1093/humrep/dez077.
18. Rajabi-Zeleti, S.; Jalili-Firoozinezhad, S.; Azarnia, M.; Khayyatan, F.; Vahdat, S.; Nikeghbalian, S.; Khademhosseini, A.; Baharvand, H.; Aghdami, N. The behavior of cardiac progenitor cells on macroporous pericardium-derived scaffolds. *Biomaterials* **2014**, *35*, 970–982, doi:10.1016/J.BIOMATERIALS.2013.10.045.
19. Lecht, S.; Stabler, C.T.; Rylander, A.L.; Chiaverelli, R.; Schulman, E.S.; Marcinkiewicz, C.; Lelkes, P.I. Enhanced reseeding of decellularized rodent lungs with mouse embryonic stem cells. *Biomaterials* **2014**, *35*, 3252–3262, doi:10.1016/j.biomaterials.2013.12.093.
20. Lee, H.; Han, W.; Kim, H.; Ha, D.-H.; Jang, J.; Kim, B.S.; Cho, D.-W. Development of liver decellularized extracellular matrix bioink for three-dimensional cell printing-based liver tissue engineering. *Biomacromolecules* **2017**, *18*, 1229–1237, doi:10.1021/acs.biomac.6b01908.
21. Yu, Y.L.; Shao, Y.K.; Ding, Y.Q.; Lin, K.Z.; Chen, B.; Zhang, H.Z.; Zhao, L.N.; Wang, Z.B.; Zhang, J.S.; Tang, M.L.; et al. Decellularized kidney scaffold-mediated renal regeneration. *Biomaterials* **2014**, *35*, 6822–6828.
22. Aulino, P.; Costa, A.; Chiaravalloti, E.; Perniconi, B.; Adamo, S.; Coletti, D.; Marrelli, M.; Tatullo, M.; Teodori, L. Muscle extracellular matrix scaffold is a multipotent environment. *Int. J. Med. Sci.* **2015**, *12*, 336–340, doi:10.7150/ijms.10761.
23. Baiguera, S.; Del Gaudio, C.; Kuevda, E.; Gonfiotti, A.; Bianco, A.; Macchiarini, P. Dynamic decellularization and cross-linking of rat tracheal matrix. *Biomaterials* **2014**, *35*, 6344–6350, doi:10.1016/J.BIOMATERIALS.2014.04.070.
24. Sjöqvist, S.; Jungebluth, P.; Lim, M.L.; Haag, J.C.; Gustafsson, Y.; Lemon, G.; Baiguera, S.; Burguillos, M.A.; Del Gaudio, C.; Rodríguez, A.B.; et al. Experimental orthotopic transplantation of a tissue-engineered oesophagus in rats. *Nat. Commun.* **2014**, *5*, 3562, doi:10.1038/ncomms4562.
25. Singh, A.; Bivalacqua, T.J.; Sopko, N. Urinary Tissue engineering: challenges and opportunities. *Sex. Med. Rev.* **2018**, *6*, 35–44, doi:10.1016/J.SXMR.2017.08.004.
26. Kajbafzadeh, A.-M.; Khorramirouz, R.; Kameli, S.M.; Hashemi, J.; Bagheri, A. Decellularization of human internal mammary artery: Biomechanical properties and histopathological evaluation. *Biores. Open Access* **2017**, *6*, 74–84, doi:10.1089/biores.2016.0040.

27. Zhang, J.-K.; Du, R.-X.; Zhang, L.; Li, Y.-N.; Zhang, M.-L.; Zhao, S.; Huang, X.-H.; Xu, Y.-F. A new material for tissue engineered vagina reconstruction: Acellular porcine vagina matrix. *J. Biomed. Mater. Res. Part. A.* **2017**, *105*, 1949–1959, doi:10.1002/jbm.a.36066.
28. Laronda, M.M.; Jakus, A.E.; Whelan, K.A.; Wertheim, J.A.; Shah, R.N.; Woodruff, T.K. Initiation of puberty in mice following decellularized ovary transplant. *Biomaterials* **2015**, *50*, 20–29, doi:10.1016/j.biomaterials.2015.01.051.
29. Pennarossa, G.; Ghiringhelli, M.; Gandolfi, F.; Brevini, T.A.L. Creation of a bioengineered ovary: Isolation of female germline stem cells for the repopulation of a decellularized ovarian bioscaffold. *Methods Mol. Biol.* **2021**, *2273*, 139–149, doi:10.1007/978-1-0716-1246-0_9.
30. Pennarossa, G.; Maffei, S.; Campagnol, M.; Tarantini, L.; Gandolfi, F.; Brevini, T.A.L. Brief demethylation step allows the conversion of adult human skin fibroblasts into insulin-secreting cells. *Proc. Natl. Acad. Sci. U.S.A.* **2013**, *110*, 8948–8953, doi:10.1073/pnas.1220637110.
31. Pennarossa, G.; Maffei, S.; Campagnol, M.; Rahman, M.M.; Brevini, T.A.L.; Gandolfi, F. reprogramming of pig dermal fibroblast into insulin secreting cells by a brief exposure to 5-aza-cytidine. *Stem Cell Rev. Reports* **2014**, *10*, 31–43, doi:10.1007/s12015-013-9477-9.
32. Brevini, T.A.L.; Pennarossa, G.; Rahman, M.M.; Paffoni, A.; Antonini, S.; Ragni, G.; deEguileor, M.; Tettamanti, G.; Gandolfi, F. Morphological and Molecular changes of human granulosa cells exposed to 5-azacytidine and addressed toward muscular differentiation. *Stem Cell Rev. Reports* **2014**, *10*, 633–642 doi:10.1007/s12015-014-9521-4.
33. Manzoni, E.F.M.; Pennarossa, G.; DeEguileor, M.; Tettamanti, G.; Gandolfi, F.; Brevini, T.A.L. 5-azacytidine affects TET2 and histone transcription and reshapes morphology of human skin fibroblasts. *Sci. Rep.* **2016**, *6*, 37017, doi:10.1038/srep37017.
34. Pennarossa, G.; Ledda, S.; Arcuri, S.; Gandolfi, F.; Brevini, T.A.L. A two-step strategy that combines epigenetic modification and biomechanical cues to generate mammalian pluripotent cells. *J. Vis. Exp.* **2020**, 162, doi:10.3791/61655.
35. Pennarossa, G.; Manzoni, E.F.M.; Ledda, S.; DeEguileor, M.; Gandolfi, F.; Brevini, T.A.L. Use of a PTFE micro-bioreactor to promote 3D cell rearrangement and maintain high plasticity in epigenetically erased fibroblasts. *Stem Cell Rev. Reports* **2019**, *15*, 82–92, doi:10.1007/s12015-018-9862-5.
36. Pennarossa, G.; Santoro, R.; Manzoni, E.F.M.; Pesce, M.; Gandolfi, F.; Brevini, T.A.L. Epigenetic erasing and pancreatic differentiation of dermal fibroblasts into insulin-producing cells are boosted by the use of low-stiffness substrate. *Stem cell Rev. Reports* **2018**, *14*, 398–411, doi:10.1007/s12015-017-9799-0.
37. Brevini, T.A.L.; Pennarossa, G.; Acocella, F.; Brizzola, S.; Zenobi, A.; Gandolfi, F. Epigenetic conversion of adult dog skin fibroblasts into insulin-secreting cells. *Vet. J.* **2016**, *211*, 52–56, doi:10.1016/j.tvjl.2016.02.014.
38. Hassanpour, A.; Talaei-Khozani, T.; Kargar-Abarghouei, E.; Razban, V.; Vojdani, Z. Decellularized human ovarian scaffold based on a sodium lauryl ester sulfate (SLES)-treated protocol, as a natural three-dimensional scaffold for construction of bioengineered ovaries. *Stem Cell Res. Ther.* **2018**, *9*, 252, doi:10.1186/S13287-018-0971-5.
39. Morris, A.H.; Stamer, D.K.; Kyriakides, T.R. The host response to naturally-derived extracellular matrix biomaterials. *Semin. Immunol.* **2017**, *29*, 72–91, doi:10.1016/J.SMIM.2017.01.002.
40. Healy, M.W., Dolitsky, S.N., Villancio-Wolter, M., Raghavan, M., Tillman, A.R., Morgan, N.Y., DeCherney, A.H., Park, S., Wolff, E.F. Creating an artificial 3-Dimensional ovarian follicle culture system using a microfluidic system. *Micromachines* **2021**, *12*, 1–15, doi:10.3390/MI12030261.
41. Desai, N., Alex, A., AbdelHafez, F., Calabro, A., Goldfarb, J., Fleischman, A., Falcone, T. Three-dimensional in vitro follicle growth: Overview of culture models, biomaterials, design parameters and future directions. *Reprod. Biol. Endocrinol.* **2010**, *8*, 119, doi:10.1186/1477-7827-8-119.
42. Brevini, T.A.L.; Manzoni, E.F.M.; Ledda, S.; Gandolfi, F. Use of a Super-hydrophobic Microbioreactor to Generate and Boost Pancreatic Mini-organoids. *Methods Mol. Biol.* **2017**, *1576*, 291–299.
43. Mirakhori, F.; Zeynali, B.; Kiani, S.; Baharvand, H. Brief azacytidine step allows the conversion of suspension human fibroblasts into neural progenitor-like cells. *Cell J.* **2015**, *17*, 153–158, doi:10.22074/cellj.2015.522.
44. Tan, S.J.; Fang, J.Y.; Wu, Y.; Yang, Z.; Liang, G.; Han, B. Muscle tissue engineering and regeneration through epigenetic reprogramming and scaffold manipulation. *Sci. Rep.* **2015**, *5*, 16333, doi:10.1038/srep16333.
45. Diomede, F.; Zini, N.; Pizzicannella, J.; Merciaro, I.; Pizzicannella, G.; D'Orazio, M.; Piattelli, A.; Trubiani, O. 5-Aza exposure improves reprogramming process through embryoid body formation in human gingival stem cells. *Front. Genet.* **2018**, *9*, doi:10.3389/fgene.2018.00419.
46. Brevini, T.A.L.; Pennarossa, G.; Manzoni, E.F.M.; Gandolfi, F. Safety and efficacy of epigenetically converted human fibroblasts into insulin-secreting cells: A preclinical study. *Springer Cham* **2018**; 151–162.
47. Brevini, T.A.L.; Pennarossa, G.; Maffei, S.; Zenobi, A.; Gandolfi, F. Epigenetic conversion as a safe and simple method to obtain insulinsecreting cells from adult skin fibroblasts. *J. Vis. Exp.* **2016**, *2016*, doi:10.3791/53880.

48. Chandrakanthan, V.; Yeola, A.; Kwan, J.C.; Oliver, R.A.; Qiao, Q.; Kang, Y.C.; Zarzour, P.; Beck, D.; Boelen, L.; Unnikrishnan, A.; et al. PDGF-AB and 5-Azacytidine induce conversion of somatic cells into tissue-regenerative multipotent stem cells. *Proc. Natl. Acad. Sci. U.S.A.* **2016**, *113*, E2306, doi:10.1073/pnas.1518244113.
49. Lan, C.W., Chen, M.J., Jan, P.S., Chen, H.F., Ho, H.N. differentiation of human embryonic stem cells into functional ovarian granulosa-like cells. *J. Clin. Endocrinol. Metab.* **2013**, *98*, 3713–3723, https://doi.org/10.1210/jc.2012-4302.
50. Woods, D.C., White, Y.A.R., Niikura, Y., Kiatpongsan, S., Lee, H.J., Tilly, J.L. embryonic stem cell–derived granulosa cells participate in ovarian follicle formation in vitro and in vivo. *Reprod. Sci.* **2013,** *20*, 524–535.

## 3.2. Impact of Aging on the Ovarian Extracellular Matrix and Derived 3D Scaffolds

Published in Nanomaterials on 21th January 2022.

DOI: 10.3390/nano12030345.

The second study is addressed to investigate the main ovarian age-related changes in ECM and to the generation of 3D ECM-based bio-scaffolds, that preserve the distinctive age-specific features. To this aim, ECM major components were quantified in young and aged ovaries, spanning from the structural network to gene expression modifications. In addition, the production of 3D ECM-based biological scaffolds, that mimic the senescent ovarian microstructure, is described for the first time.

In this manuscript we describe the main age-related changes in ovarian ECM, that include altered concentrations of the main structural molecules, such as collagen, elastin, laminins, and fibronectin, parallelled by altered gene expression that closely reflects the post-transcriptional variations. The typical aging phenotype is preserved after decellularization with the creation of decellularized ECM-based scaffolds, that maintain intact ECM framework and well-connected and oriented fibers, while preserving age-associated modifications.

Altogether, this represents an innovative tool to better characterize ovarian aging in a complex and physiologically relevant environment, providing the opportunity to carry out *in vitro* studies aimed at the identification of novel therapeutic targets against ovarian senescence, as well as potential anti-aging molecules.

*Article*

# Impact of aging on the ovarian extracellular matrix and derived 3D scaffolds

**Georgia Pennarossa[1, †, *], Teresina De Iorio[1,†], Fulvio Gandolfi[2], and Tiziana A.L. Brevini[1]**

[1] Laboratory of Biomedical Embryology, Department of Health, Animal Science and Food Safety and Center for Stem Cell Research, Università degli Studi di Milano, Milan, 20133, Italy; teresina.deiorio@unimi.it, georgia.pennarossa@unimi.it, tiziana.brevini@unimi.it.

[2] Laboratory of Biomedical Embryology, Department of Agricultural and Environmental Sciences - Production, Landscape, Agroenergy, Università degli Studi di Milano, Milan, 20133, Italy; fulvio.gandolfi@unimi.it

* Correspondence: tiziana.brevini@unimi.it ; georgia.pennarossa@unimi.it

† These authors contributed equally

**Abstract:** Advances in medical care, improvements in sanitation, and rising living standards contribute to increased life expectancy. Although this reflects positive human development, it also poses new challenges. Among these, reproductive aging is gradually becoming a key health issue because the age of menopause has remained constant at ~50 years, leading women to live longer in suboptimal endocrine conditions. An adequate understanding of ovarian senescence mechanisms is essential to prevent age-related diseases and to promote wellbeing, health, and longevity in women. We here analyze the impact of aging on ovarian extracellular matrix (ECM), and we demonstrate significant changes in its composition and organization with collagen, glycosaminoglycans, and laminins significantly incremented, and elastin as well as fibronectin decreased. This is accompanied by a dynamic response in gene expression levels of the main ECM- and protease-related genes, indicating a direct impact of aging on the transcription machinery. Furthermore, in order to study the mechanisms driving aging and identify possible strategies to counteract ovarian tissue degeneration, we here described the successful production of a 3D ECM-based biological scaffold that preserves the structural modifications taking place in vivo and that represents a powerful high predictive in vitro model for reproductive aging and its prevention.

**Keywords:** reproductive aging; senescence; extracellular matrix; whole-ovary decellularization; ECM-based bio-scaffold; porcine.

## 1. Introduction

In mammals, the female reproductive system is the first to show signs of physiological aging [1], with fertility decline and hormonal disfunctions that can, in turn, affect overall health. This leads to multiple medical and psychosocial problems, such as osteoporosis, cardio- vascular disease, autoimmune disorders, and depression [2,3]. Although medical care advances and rising living standards have contributed to increase lifespan, the age of menopause has remained constant at the age of ~50 years, leading women to live longer in suboptimal endocrine conditions [4]. The reproductive aging has therefore gradually become a key health issue and an adequate understanding of its mechanisms is essential in order to prevent age-related diseases and to promote health and longevity in women [5].

Aging is generally described as a complex, multifaceted process, characterized by a progressive accumulation of macroscopic and microscopic modifications, accompanied by molecular and cellular damages that can affect organs, tissues, cells, and subcellular organelles, causing severe biological degenerations and a gradual loss of organ functions [6]. Recent studies also suggest that the non-cellular compartment of the tissues, the extracellular matrix (ECM), may play a key role in

aging progression [7]. Indeed, during the last years, it has been clearly demonstrated that ECM contributes not only to physical scaffolding and structural support, but also provides biochemical and biomechanical stimuli directly influencing cell behaviour [8]. Cells are indeed able to respond to physical and mechanical cues exerted by the surrounding environment modifying their own morphology, polarity, adhesion, migration, growth, gene expression and functions [9–13]. However, cell ability to sense changes in ECM compliance (mechanosensation) and to transduce these stimuli into biochemical signals (mechanotransduction) are negatively affected by aging progression [6]. In addition, recent studies also suggested that aging may induce critical alterations in ECM composition and organization [14,15], resulting in biomechanical and biochemical ECM property modifications [6,16], that impact on cell-to-matrix interactions as well as on cell fate and behaviour.

Reproductive biology addressed growing interest to ovarian mechanobiology in the last decade and, in particular, the dynamic reciprocity that exists between ovarian cells and their microenvironment is currently under investigation [17,18]. In this contest, follicles and oocyte developmental quality have been demonstrated to be strongly influenced by biochemical cues [19] as well as by physical ovarian microenvironment [20–22]. However, at present, only scattered information is available in the literature regarding aging mechanobiology of the reproductive tissues, where several aspects still need to be elucidated.

In the present study, we adopted the porcine as a model, based on its anatomical and physiological similarities with the human and we analyzed the impact of aging on ovarian ECM. In particular, we characterized and quantified the major ECM components, namely collagen, elastin, glycosaminoglycans, fibronectin and laminins, in young and aged ovaries. We analysed the ECM-related gene expression pattern in the two groups. Lastly, we generated 3D ECM-based biological scaffolds that preserve the age-specific ovarian milieu.

To the best of our knowledge, this is the first study reporting with great details the changes taking place in the ECM of senescent ovary, spanning from the structural remodeling to gene expression modifications. In addition, for the first time, the production of 3D ECM-based biological scaffolds that mimic the senescent ovarian micro-structure is described and represent an innovative tool to better characterize ovarian aging in a complex and physiologically relevant environment. This will in turn allow to carry out in vitro studies aimed to the identification of novel therapeutic targets against ovarian senescence as well as potential anti-aging agents.

## 2. Materials and Methods

All reagents were purchased from Thermo Fisher Scientific (Milan, Italy) unless otherwise indicated.

### *2.1. Ovary collection*

60 porcine ovaries were collected at the local slaughterhouse and transported to the laboratory in sterile cold PBS. Organs from individuals ranging from 2 to 6 months of age were considered "young" (n=30), while those from 3-5 years old animals were identified as "aged" (n=30).

### *2.2. Histological Analysis*

Young and aged ovaries were fixed in 10% buffered formalin for 24 h at room temperature, dehydrated in graded alcohols, cleared with xylene, and embedded in paraffin. Serial microtome sections of 5 μm in thickness were cut, dewaxed, rehydrated, and stained with hematoxylin and eosin (H&E, BioOptica, Milan, Italy), in order to evaluate the general morphological aspects.

### *2.3. Histochemical Analysis*

Collagen, elastin, and GAGs were analyzed using Masson Trichrome (Bio-optica, Milan, Italy), Gomori's aldehyde-fuchsin (Bio-optica), and Alcian blue (pH 2.5; Bio-optica, Milan, Italy) staining, respectively. Microtome sections (5 μm thick) were dewaxed, rehydrated, and stained following

the manufacturer's instructions. Samples were analyzed under an Eclipse E600 microscope (Nikon, Amsterdam, Netherlands), equipped with a digital camera (Nikon, Amsterdam, Netherlands). Pictures were acquired with NIS-Elements Software (Version 4.6; Nikon).

*2.4. Immunohistochemical Analysis*

Laminin subunit alpha 3 (LAMA3), laminin subunit beta 1 (LAMB1), and fibronectin 1 (FN1) were characterized by indirect immunohistochemistry using the Vectastain ABC Elite KIT (Burlingame, CA, USA). Laminin antigen retrieval was carried out in 10 mM sodium citrate buffer containing 0.05% Tween20 (pH 6) at sub-boiling temperature for 10 min. Tris-Base solution containing 0.05% Tween20 (pH 9) in pressure cooker for 5 min was used for FN1 unmasking. After cooling for 20 min, sections were rinsed and immersed in 3% $H_2O_2$ for 15 min to quench the endogenous peroxidase. Aspecific sites were blocked with Normal Serum for 30 min. Sections were then incubated with 1:100 LAMA3 (SantaCruz Biotechnology, CM6, California, USA), 1:500 LAMB1 (SantaCruz Biotechnology, LT3, California, USA), and 1:100 FN1 (Abcam, Cambridge, UK) antibodies diluted in 4% BSA in PBS, for 60 min in a humidified chamber. The appropriate biotinylated secondary antibody was added for 30 min. Lastly, tissues were stained with avidin-biotinylated horseradish peroxidase (HRP) complex for 30 min and with HRP substrate solution ImmPACT DAB substrate (Vector Laboratories, Burlingame, CA, USA). Sections were counterstained with Mayer's hematoxylin, dehydrated and permanently mounted (Bio-Optica, Milano, Italy). Secondary antibody controls were performed omitting the primary antibodies. All the procedures were carried out at room temperature unless otherwise indicated.

*2.5. Stereological Analysis*

Volume density (Vv) estimation of the ECM components was carried out on histochemical and immunohistochemical stained vertical sections, according to the general Delesse principle. In detail, the relative volume of each area of interest was calculated from the fractional area of the structure of interest (e.g., collagen) and the total area of the reference compartment (e.g., whole section). Systematic uniform random sampling was applied, and images were captured and superimposed with a point-count stereologic grid with equally distant test points. The points hitting the structure of interest and the respective reference compartment were counted, and the relative volume of each region of interest was then calculated from the respective quotient of points hitting these structures. Vv expressed as percentages was calculated as follows:

$$Vv_{(\text{analysed compartment, reference compartment})} = [\sum P_{(\text{analysed compartment})} / \sum P_{(\text{reference compartment})}] \times 100$$

where $\sum P_{(\text{analysed compartment})}$ is the number of points hitting the compartment under study, and $\sum P_{(\text{reference compartment})}$ is the number of points hitting the relevant structure.

*2.6. ELISA test*

Quantifications of ECM components were carried out through ELISA tests using specific porcine ELISA kits (see Table 1). 400-500 mg of tissue were homogenized with Polytron (Kinematica AG, Malters, Switzerland), centrifuged at 3000 rpm for 20 min and supernatants were collected. Assays were carried out following the manufacture instructions and, at the end of the procedures, collagen content was measured at 560 nm. Elastin, GAGs, LAMA3, LAMB1, and FN1 were quantified at 450 nm. Standard curves were constructed by plotting the mean absorbance (y-axis) against the protein concentration (x-axis) and the best fit line was determined by regression analyses. Absolute quantifications were then calculated.

**Table 1.** ELISA kits used to quantify the different ECM components.

| Protein | Description | Cat.N. |
|---|---|---|
| Collagen | Total Collagen Assay Kit (Bio-Techne SRL, Milano, Italy) | NBP2-59748 |

| | | |
|---|---|---|
| Elastin | Porcine Elastin,ELN ELISA Kit (BT Lab, Shanghai, China) | E0504Po-96T |
| GAGs | Porcine Glycosaminoglycans,GAGs ELISA Kit (BT Lab, Shanghai, China) | E0503Po-96T |
| LAMA3 | Porcine Epiligrin ELISA Kit (MyBioSource, San Diego, CA, USA) | MBS019792 |
| LAMB1 | Porcine Laminin subunit beta-1 (LAMB1) ELISA Kit (MyBioSource, San Diego, CA, USA) | MBS2613645 |
| FN1 | Fibronectin (FN), ELISA Kit (MyBioSource, San Diego, CA, USA) | MBS2700851 |

*2.7. Gene Expression Analysis*

Young and aged ovary RNA was extracted using the TaqManGene Expression Cells to Ct kit (Applied Biosystems, Milan, Italy) and following the manufacturer's instruction. DNase I was added in lysis solution at a 1:100 concentration. Quantitative PCR was performed on a CFX96 Real-Time PCR (Bio-Rad, Milan, Italy) using predesigned gene-specific primers and probe sets from TaqManGene Expression Assays (see Table 2 for the primer information). ACTB and GAPDH were used as internal reference genes. Target gene quantification was carried out with CFX Manager software 18450000 (Bio-Rad, Milan, Italy). Gene expression levels are reported with the highest expression set to 1 and the others relative to this.

**Table 2.** List of primers used for quantitative PCR analysis.

| Gene | Description | Cat.N. |
|---|---|---|
| ACTB | Actin, beta | Ss03376563_uH |
| GAPDH | Glyceraldehyde-3-phosphate dehydrogenase | Ss03375629_u1 |
| COL1A1 | Collagen type I alpha 1 chain | Ss03373341_g1 |
| COL3A1 | Collagen type III alpha 1 chain | Ss04323772_g1 |
| COL4A2 | Collagen type IV alpha 2 chain | Ss06936852_mH |
| ELN | Elastin | Ss04955050_m1 |
| FN1 | Fibronectin 1 | Ss03373883_m1 |
| EMILIN1 | Elastin microfibril interfacer 1 | Ss06869485_m1 |
| LAMA3 | Laminin subunit alpha 3 | Ss06874585_g1 |
| LAMB1 | Laminin subunit beta 1 | Ss03375563_u1 |
| VCAN | Versican | Ss04323138_m1 |
| HSPG2 | Heparan sulfate proteoglycan 2 | Ss06878501_m1 |
| CSPG4 | Chondroitin sulfate proteoglycan 4 | Ss03374044_m1 |
| ELANE | Elastase, neutrophil expressed | Ss06915973_gH |
| MMP1 | Matrix metallopeptidase 1 | Ss04245657_g1 |
| MMP2 | Matrix metallopeptidase 2 | Ss04955620_m1 |
| MMP3 | Matrix metallopeptidase 3 | Ss03375473_u1 |
| MMP9 | Matrix metallopeptidase 9 | Ss03392100_m1 |
| MMP12 | Matrix metallopeptidase 12 | Ss03386225_u1 |
| MMP14 | Matrix metallopeptidase 14 | Ss03394427_m1 |

*2.8. Whole-ovary decellularization*

Young and aged whole-ovaries were decellularized according to the protocol previously developed in our laboratory [23–25]. Briefly, the entire organs were frozen at − 80 °C for at least 24 h. They were then thawed at 37 °C in a water bath for 30 min, followed by an incubation with 0.5% sodium dodecyl sulfate (SDS; Bio-Rad, Milan, Italy) in deionized water (dd-$H_2O$) for 3 h. Ovaries were then treated overnight with 1% Triton X-100 (Sigma, Milan, Italy) in dd-$H_2O$, extensively

washed in dd-$H_2O$ for 9 h and, subsequently, immersed in 2% deoxycholate in dd-$H_2O$ (Sigma, Milan, Italy) for 12 h. Lastly, decellularized whole-ovaries were washed in dd-$H_2O$ for 6 h, with changes every 2 h. All steps were carried out at room temperature using an orbital shaker at 200 rpm.

At the end of the decellularization process, age-specific ovarian ECM-based scaffolds obtained were subjected to histological (please see 2.2. section) and histochemical analyses (please see 2.3. section), ELISA tests (as described above in 2.4. section), cell density analysis, and DNA quantification studies.

### *2.9. Cell Density*

Efficient cell removal from the decellularized whole-ovaries was assessed by staining serial microtome sections with 40 ,6-diamidino-2-phenylindole (DAPI). Cell number was counted in 15 DAPI-stained tissue sections obtained from each decellularized ovarian scaffold. A total of 5 randomly selected fields at × 100 total magnifications were analysed for each section. Images were acquired with constant exposure parameters and analysed using the Automated Cell Counter tool of ImageJ software (http://rsbweb.nih.gov/ij/index. html), following the provider's instructions. Briefly, 8-bit images were generated, and threshold adjustments were applied. Subsequently, in order to remove the background and highlight the area occupied by nuclei, the images were segmented with a thresholding algorithm. The data obtained were then transformed in binary form and size and circularity parameters were set in order to automatically counted nuclei. Cell density was expressed per $mm^2$ of tissue.

### *2.10. DNA Quantification*

Ten fragments, ranging from 10 to 24 mg, were cut from each decellularized ovarian ECM-based scaffold and their weights were annotated. Genomic DNA was then extracted from each fragment with the PureLink® Genomic DNA Kit, following the manufacturer's instructions. The DNA concentration was measured with NanoDrop 8000 and normalized against the fragment weights previously recorded.

### *2.11. Statistical Analysis*

Statistical analyses were performed using one-way and two-way ANOVA (SPSS 19.1; IBM). Data are presented as the mean ± the standard error of the mean (SEM). Differences of $p \leq 0.05$ were considered significant and were indicated with different superscripts.

## 3. Results

### *3.1. Macroscopic and microscopic analysis of young and aged ovaries*

Macroscopic evaluation revealed the typical morphology of young and adult ovaries with numerous follicles ranging from 3- to 8- mm in diameter (Figure 1 a). As expected, smaller follicle size, 3- 4- mm, were more abundant than larger ones (5- 8- mm) in both young and aged ovaries. However, the rate of 3- 4-mm follicles was higher in young ovaries, while a higher proportion of 5- 8-mm follicles was found in aged ovaries (Figure 1 b).

In order to evaluate the general morphological aspect of young and aged ovaries, H&E staining were carried out. The analyzed tissues showed the typical ovarian tissue architecture consisting of primordial, growing, and antral follicles, ovarian stroma and vasculature in both young and aged tissues. However, aged ovaries displayed a denser and more compact stromal compartment compared to the young ones (Figure 1c).

a

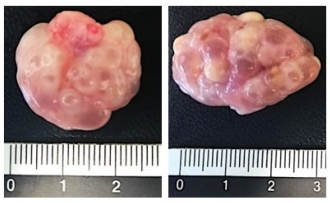


b

| Follicle diameter (mm) | Young ovaries | Aged ovaries |
|---|---|---|
| 3- 4- | 89.7 ± 3.1 % | 77.3 ± 2.7 %*** |
| 5- 8- | 10.3 ± 1.2 % | 22.7 ± 2.1 %*** |

c

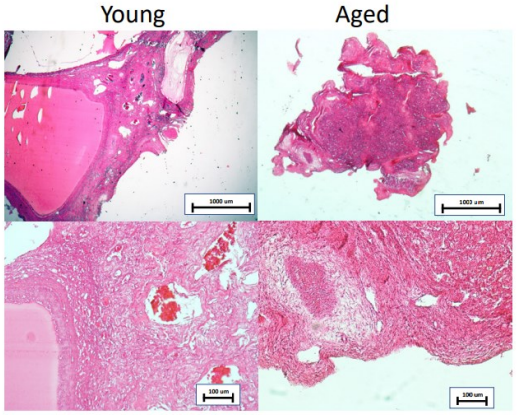


**Figure 1.** Macroscopic and histological evaluations of young and aged ovaries. **(a)** Representative macroscopic images illustrating young (left panel) and aged ovaries (right panels); **(b)** 3- 4- mm and 5- 8- mm follicle rate observed in young and aged ovaries, ***p<0.001; **(c)** H & E staining showed the typical ovarian tissue architecture with primordial, growing and antral follicles, ovarian stroma and vasculature in both young and aged tissues. Scale bars = 100 μm.

*3.2 Aging effects on ovarian extracellular matrix composition*

In order to characterize the major ECM components, we selected specific histological and immuno-staining. In addition, a quantitative evaluation was carried out through stereological analysis and ELISA tests.

More in detail, Masson trichrome showed a robust blue staining in aged ovaries, indicating an increment in collagen content (Figure 2 a). This was also confirmed by stereological analysis (Figure 2 b) as well as ELISA quantifications (Figure 2 c) that demonstrated significantly higher concentrations of collagen fibers in aged ovaries compared to their young counterpart.

Elastin specific staining Gomori's Aldehyde Fuchsin demonstrated a decrease in elastic fiber content in aged samples (Figure 2 d). This is further supported by stereological analysis (Figure 2 e) and ELISA quantifications (Figure 2 f), that indicated a significant decrease in elastic fiber volume density in aged ovaries.

In contrast, Alcian blu staining (Figure 2 g) and stereological analysis (Figure 2 h) demonstrated an increased quantity of GAGs in aged ovaries compared to the young ones. This was also confirmed by ELISA tests that indicated significantly higher concentration of GAG content in aged ovaries (Figure 2 i).

Immunohistochemical characterization demonstrated higher amount of LAMA3 and LAMB1 in aged ovaries compared to the young group (Figure 2 j, m). This was confirmed by stereological (Figure 2 k, n) and ELISA quantifications (Figure 2 l, o). On the other hand, FN1 staining (Figure 2 p), stereological analysis (Figure 2 q) and ELISA tests (Figure 2 r) indicated a decreased fibronectin quantity in aged ovaries.

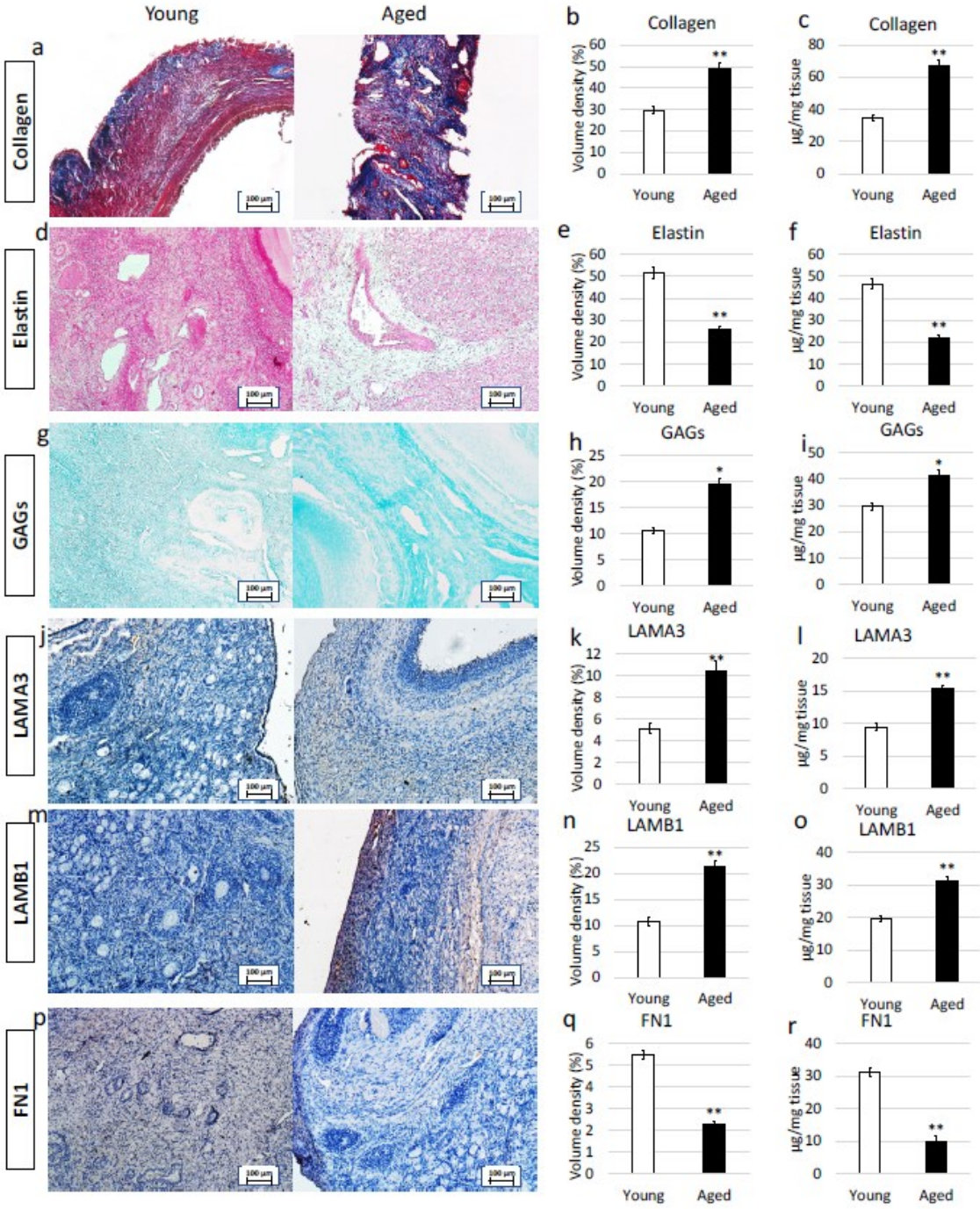


**Figure 2.** Histochemical and immunohistochemical analysis, stereological quantification, and ELISA tests in young and aged ovaries. **(a)** Masson's trichrome staining showed the presence of collagen (blue) and elastic (magenta) fibers in both young and aged ovaries. Scale bars = 100 µm; **(b)** Stereological analysis demonstrated a significant increase of collagen fibers in aged ovaries compared to the young ones. Data are expressed as the mean. Error bars represent the standard error of the mean (SEM), **p<0.01; **(c)** ELISA quantifications indicated a significant increase of the collagen content in aged ovaries compared the young ones. Data are expressed as the mean. Error bars represent the standard error of the mean (SEM), **p<0.01; **(d)** Gomori's Aldehyde Fuchsin staining revealed the presence elastic fibers in both young and aged ovaries. Scale bars = 100 µm; **(e)** Stereological analysis displayed a significant decrease of elastic fibers in aged ovaries compared to the young ones. Data are expressed as the mean. Error bars represent the standard error of the mean (SEM), **p<0.01; **(f)** ELISA quantifications confirmed a significant decrease of the elastin content in aged ovaries compared the young ones. Data are expressed as the mean. Error bars represent the standard error of the mean (SEM), **p<0.01; **(g)** Alcian blue staining showed the presence of GAGs in both young and aged ovaries. Scale bars = 100 µm; **(h)** Stereological

analysis indicated a significant increase of GAGs in aged ovaries compared to the young ones. Data are expressed as the mean. Error bars represent the standard error of the mean (SEM), *p<0.05; **(i)** ELISA quantifications confirmed a significant increase of the GAG content in aged ovaries compared the young ones. Data are expressed as the mean. Error bars represent the standard error of the mean (SEM), *p<0.05; **(j)** Immunohistochemical staining of young and aged ovaries for LAMA3. Scale bars = 100 μm; **(k)** Stereological analysis demonstrated a significant increase of LAMA3 in aged ovaries compared to the young ones. Data are expressed as the mean. Error bars represent the standard error of the mean (SEM), **p<0.01; **(l)** ELISA quantifications showed a significant increase of the LAMA3 content in aged ovaries compared the young ones. Data are expressed as the mean. Error bars represent the standard error of the mean (SEM), **p<0.01; **(m)** Immunohistochemical staining of young and aged ovaries for LAMB1. Scale bars = 100 μm; **(n)** Stereological analysis revealed a significant increase of LAMB1 in aged ovaries compared to the young ones. Data are expressed as the mean. Error bars represent the standard error of the mean (SEM), **p<0.01**; (o)** ELISA quantifications displayed a significant increase of the LAMB1 content in aged ovaries compared the young ones. Data are expressed as the mean. Error bars represent the standard error of the mean (SEM), **p<0.01; **(p)** Immunohistochemical staining of young and aged ovaries for FN1. Scale bars = 100 μm; **(q)** Stereological analysis indicated a significant decrease in FN1 content in aged ovaries compared to the young ones. Data are expressed as the mean. Error bars represent the standard error of the mean (SEM), **p<0.01; **(r)** ELISA quantifications showed a significant increase of the LAMB1 content in aged ovaries compared the young ones. Data are expressed as the mean. Error bars represent the standard error of the mean (SEM), **p<0.01.

*3.3. Aging effects on extracellular matrix-related gene expression*

To confirm the morphological data revealing ECM composition changes with aging progression, we profiled expression patterns and levels of ECM-related genes (Figure 3). While no significant modifications in expression patterns was detected, we could assess a very dynamic response in the transcription levels of the genes considered. In particular, we were able to demonstrate a significant increased expression levels of collagens (COL1A1, COL3A1, COL4A2), EMILIN1 glycoprotein, laminins (LAMA3, LAMB1), and proteoglycans (VCAN, HSPG2, CSPG4) in aged ovaries compared to the young ones. In contrast, down regulation of elastin (ELN)and fibronectin (FN1) accompanied the aging process which also caused a decreased expression of various proteases that hydrolyze the different ECM components, namely ELANE, MMP1, MMP2, MMP3, MMP9, and MMP14. Interestingly, the matrix metalloproteinase involved in elastin degradation, the MMP12, was upregulated in aged ovaries.

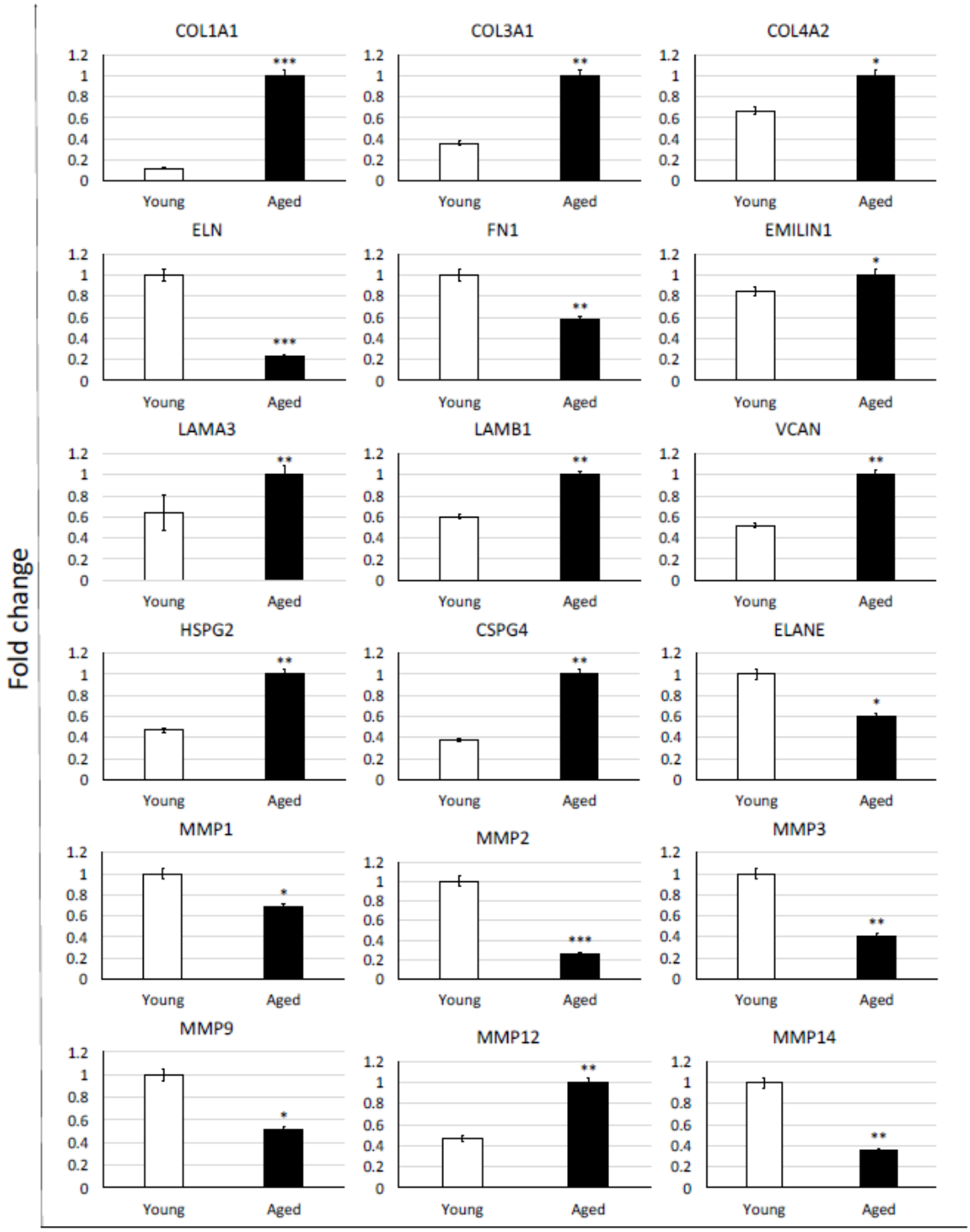


**Figure 3.** Gene expression changes of extracellular matrix-related genes in young (white bars) and aged ovaries (black bars). Expression levels of collagens (COL1A1, COL3A1, COL4A2), elastin (ELN), fibronectin (FN1), glycoprotein (EMILIN1), laminins (LAMA3, LAMB1), proteoglycans (VCAN, HSPG2, CSPG4), and proteases (ELANE, MMP1, MMP2, MMP3, MMP9, MMP12, and MMP14). Data are expressed as the mean. Error bars represent the standard error of the mean (SEM), *p<0.05, **p<0.01, ***p<0.001.

*3.4. Whole-ovary decellularization protocol sucessufully removes cell compartment and preserves age-specific ovarian architecture*

In order to assess the efficacy of the whole-organ decellularization protocol, macroscopic evaluations were carried out along the decellularization process. The results obtained demonstrated that both young and aged ovaries preserved their original shape and homogeneity,

without any deformation and maintained the age-related morphological differences already detectable in the native organs. In addition, comparable changes in whole organ color, turning from red to white, were visible in both the experimental groups (Figure 4 a).

In addition, H&E staining were performed to evaluate the general morphological aspect of the decellularized whole-ovaries. The data obtained demonstrated the successful removal of the cellular compartment and the maintenance of general structure in both young and aged decellularized ovaries. More in detail, the basophilic staining, clearly visible in the native tissues, was absent after the decellularization processes in all sample analyzed, regardless of age (Figure 4 b). In agreement with this, DAPI staining (Figure 4 c) and cell density evaluations (Figure 4 d) showed a significantly lower number of cell nuclei in both young and aged decellularized ovaries compared to the untreated tissues. This is also confirmed by DNA quantification studies indicating a 98.07% and a 98.22% decrease in young and aged decellularized ovaries, respectively. In particular, a content of 36.36±4.54 ng DNA/mg and 31.75±2.29 ng DNA/mg of tissue was measured in young and aged decellularized tissues vs. 1890.28±257.37 ng DNA/mg and 1789.96±313.55 ng DNA/mg of tissue in young and aged native controls (Figure 4 e).

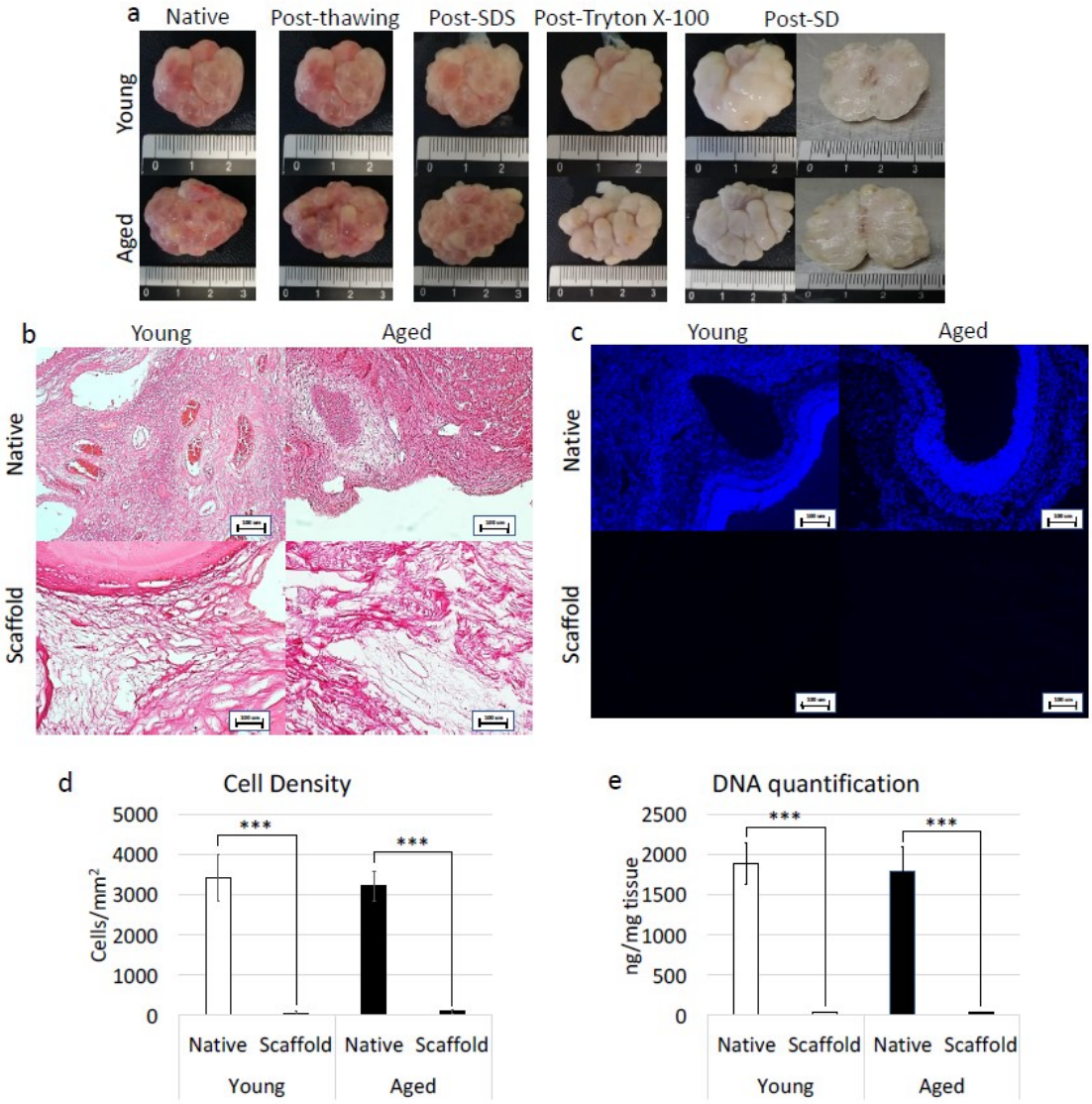


**Figure 4.** Macroscopic and microscopic evaluations of young and aged ECM-based scaffolds, cell density and DNA quantification. **(a)** Chronological macroscopic images illustrating the decellularization process in young (upper panel) and aged ovaries (lower panels). Native and decellularized organs displayed comparable

shapes and homogeneity, while their color turns from red to white along the process; **(b)** H & E staining showed the presence of both basophilic (cell nuclei) and eosinophilic (cell cytoplasm and ECM) staining in the control tissues (Young Native and Aged Native), while cell nuclei and the related basophilic staining were absent in the decellularized ECM-based scaffolds (Young Scaffold and Aged Scaffold). Scale bars = 100 μm; **(c)** DAPI staining displayed the presence of nuclei in native ovaries (Young Native and Aged Native), which disappeared after the decellularization process (Young Scaffold and Aged Scaffold). Scale bars = 100 μm; **(d)** Cell density demonstrated a significantly lower number of nuclei in both young and aged decellularized ECM-based scaffolds (Scaffold) compared to the untreated tissues (Native). Data are expressed as the mean. Error bars represent the standard error of the mean (SEM), ***p<0.001; **(e)** DNA quantification analysis showed a significant decrease in the DNA content of young and aged decellularized ECM-based scaffolds (Scaffold) compared to the native tissue (Native). Data are expressed as the mean. Error bars represent the standard error of the mean (SEM), ***p<0.001.

### *3.5. Whole-ovary decellularization protocol maintains unaltered aged-specific extracellular matrix composition*

#### 3.5.1. Histochemical characterization

Maintenance of age specific ECM composition and organization after decellularization was investigated using specific histochemical staining for collagen, elastin and GAGs were characterized.

More in detail, Masson trichrome staining showed the persistence of collagen fibers in both young and aged decellularized ovaries, with comparable distribution between decellularized and native tissues belonging to the same age. In agreement with this, at the end of the decellularization processes, collagen fibers maintained the age-specific organization detected in the native tissues (Figure 5 a). These morphological observations were also confirmed by stereological analysis, where no significant differences were detected between native and decellularized tissues of the same age (Figure 5 b). In agreement with this, the age-related differences originally identified in the native tissues were maintained after the decellularization process (Figure 5 b). These data were further supported by ELISA tests indicating comparable collagen content in young native and decellularized ovaries (35.1±4.1 μg/mg and 32.3±3.9 μg/mg of tissue) as well as in aged native and decellularized tissues (67.1±9.1 μg/mg and 63.2±8.9 μg/mg of tissue; Figure 5 c).

Gomori's aldehyde-fuchsin staining demonstrated that decellularized tissues preserved elastic fibers scattered throughout the ovary, regardless of age. Consistently, decellularized young and aged ovaries displayed the same differences observed in the native organs (Figure 5 d). This was further supported by stereological analysis displaying no significant differences between young decellularized and native tissue as well as between aged decellularized and native ovaries (Figure 5 e). Similarly, elastin quantification studies showed comparable amount of elastin before and after the decellularization process in young (46.5±3.12 μg/mg and 44.85±2.32 μg/mg) and aged (21.87±3.34 μg/mg and 20.09±2.01 μg/mg) tissues (Figure 5 f).

Alcian blue staining revealed GAG retention in both young and aged tissues, preserving the age-specific distributions visible in the native ovaries (Figure 5 g). These morphological observations were confirmed by both stereological analysis (Figure 5 h) and ELISA quantification studies (Figure 5 i), that, as seen for the others ECM components, displayed no significant GAG reduction after the decellularization.

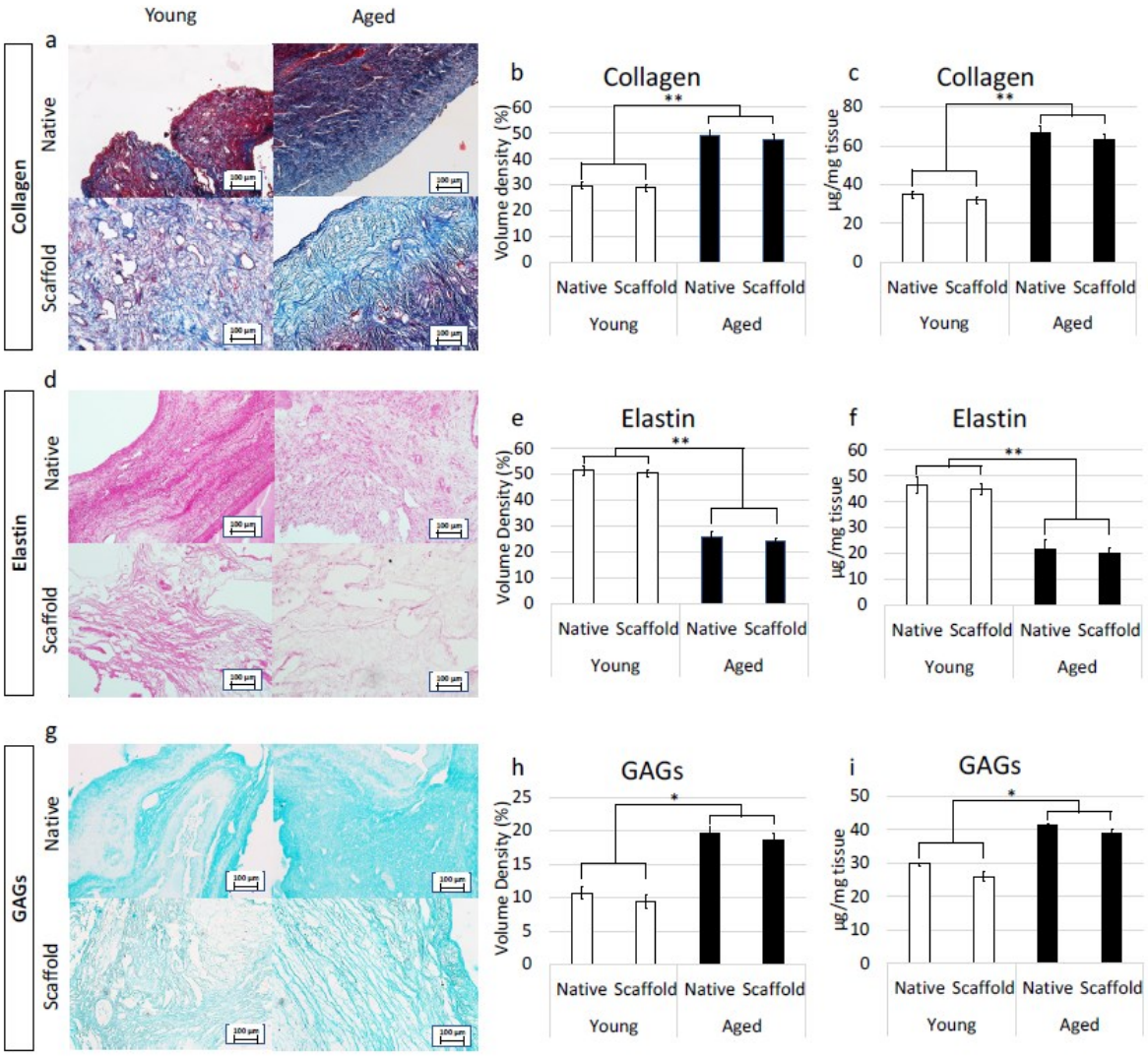


**Figure 5.** ECM microarchitecture and composition in young and aged ECM-based scaffolds. (**a**) Masson's Trichrome staining showed the persistence of collagen fibers (blue) and their comparable distribution between native (native) and decellularized ovaries (scaffold) belonging to the same age. (**b-c**) Stereological (**b**) and ELISA quantifications (**c**) demonstrated no significant differences between native ovaries (native) and the decellularized ECM-based scaffolds (scaffold) in collagen content. Data are expressed as the mean. Error bars represent the standard error of the mean (SEM), **p<0.01; (**d**) Gomori's aldehyde-fuchsin staining indicated that ECM-based scaffolds (scaffold) retained the elastic fibers scattered throughout the decellularized ovary, similar to what was visible in untreated young and aged ovaries (native). (e-f) Stereological (**e**) and ELISA quantifications (**f**) confirmed no significant differences between native ovaries (native) and the decellularized ECM-based scaffolds (scaffold) in elastin content. Data are expressed as the mean. Error bars represent the standard error of the mean (SEM), **p<0.01; (**g**) Alcian blue staining revealed GAG retention in young and aged decellularized scaffolds (scaffold). Scale bars = 100 µm; (h-i) Stereological (**h**) and ELISA quantifications (**i**) demonstrated no significant differences between native ovaries (native) and the decellularized ECM-based scaffolds (scaffold) in GAG content. Data are expressed as the mean. Error bars represent the standard error of the mean (SEM), *p<0.05.

### 3.5.2. Immunohistochemical characterization

Preservation of LAMA3, LAMB1, and FN1 in the produced bio-scaffold was investigated using immunohistochemical analysis. The results obtained demonstrated that decellularized ovaries maintained unaltered distribution of LAMA3, LAMB1, and FN1 compared to the untreated native tissues (Figure 6 a, d, g). This was confirmed by stereological analysis indicating significantly lower volume densities of LAMA3 (Figure 6 b) and LAMB1 (Figure 6 e) in both native and decellularized young tissues compared to their aged counterparts. In contrast, FN1 content was higher in young

samples as displayed by immunohistochemical staining (Figure 6 g) and stereological analysis (Figure 6 h). These evaluations were also supported by ELISA quantifications demonstrating higher amount of LAMA3 (Figure 6 c) and LAMB1 (Figure 6 f) in aged native and decellularized tissues and lower content of FN1 (Figure 6 i).

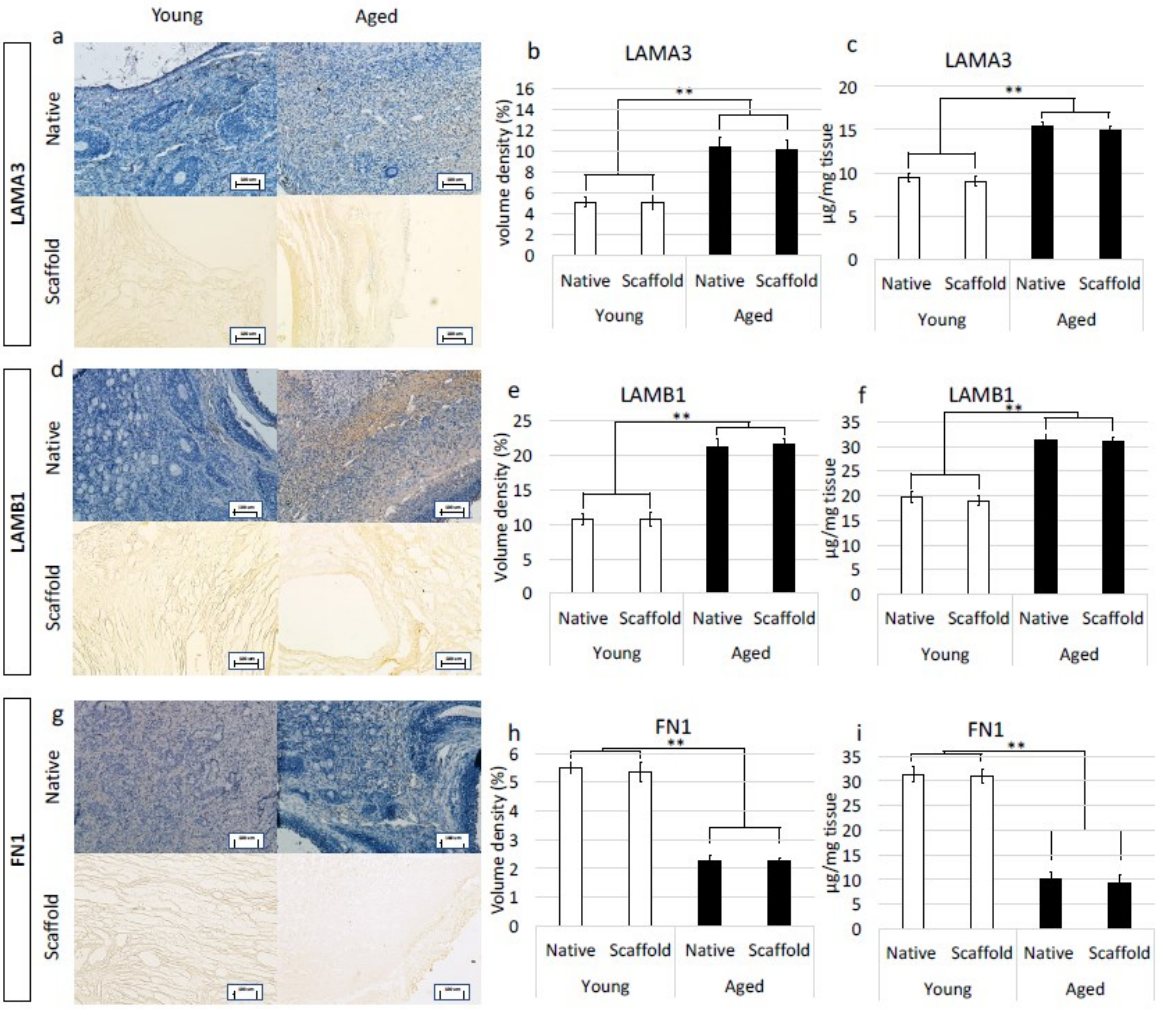


**Figure 6.** Immunohistochemical characterizations of young and aged ECM-based scaffolds. (**a**) LAMA3 immunostaining displayed the persistence of the fibers after decellularization in both young and aged tissues; Stereological analysis (**b**) and ELISA quantifications **(c)** demonstrated no significant differences between native (native) and decellularized (scaffold) ovaries in LAMA3 content. Data are expressed as the mean. Error bars represent the standard error of the mean (SEM), **p<0.01; (**d**) LAMB1 immunostaining showed the maintenance of the fibers at the end of the process in both young and aged organs; Stereological analysis (**e**) and ELISA tests (**f**) indicated no significant differences between native (native) and decellularized tissues (scaffold) in LAMB1 content. Data are expressed as the mean. Error bars represent the standard error of the mean (SEM), **p<0.01; **(g)** FN1 immunostaining revealed fiber retainment in both young and aged decellularized tissues; Stereological (**h**) and ELISA analysis (**i**) showed no significant differences between native (native) and decellularized samples (scaffold) in FN1 content. Data are expressed as the mean. Error bars represent the standard error of the mean (SEM), **p <0.01.

## 4. Discussion

In the present work, we characterize the impact of aging on ovarian ECM and report the possibility to successfully apply a whole-organ decellularization technique to produce for the first time ECM-based scaffolds that preserve the structural modifications taking place in the senescent ovary.

Macroscopic and microscopic evaluations of aged ovaries reveal distinctive morphological features, when compared to the young counterparts. A significantly lower number of small follicles (3- 4- mm) and higher number of larger ones (5- 8- mm) are scored in aged ovaries. This appears to be strictly correlated with the age of the animals and as previously described in several mammalian species, ranging from mouse [26] and cow [27] to the human [28], is likely to be associate with age-related infertility. A fundamental difference of aged ECM structure is also represented by the presence of a denser and more compact stromal compartment, which suggests the possibility of distinct matrix re-arrangements taking place during the aging process. This hypothesis is further confirmed by the histochemical results that indicate, both with Masson trichrome staining and stereological analysis, an increase in collagen fibers. A significantly higher quantity of collagen is also demonstrated by ELISA tests, comparing aged ovaries vs. young ones. These data are in agreement with recent studies, carried out on reproductively old mouse models, reporting a quantitative increase in ovarian stiffness due to collagen deposition [1,7,22]. It is interesting to remember that accumulation of collagen is an important event contributing to tissue fibrosis that is usually identified as one of the most common aging-associated hallmarks, exhibited by a wide range of tissues, including liver [29,30], heart [31,32], and lung [15], and that, in turn, induces tissue architecture disruption and affects organ biomechanics and functions [33]. In addition, it has also been demonstrated that stiffness increase may also be correlated with age- associated tumor development, facilitating ovarian cancer cell proliferation and aggregation [34]. Senescence-specific increment in matrix rigidity has been also accounted for alterations in collagen-to-elastin ratio and/or a general decrease in elastin content [35,36]. This fully fits with the results presented here, showing a significant decrease of elastic fibers in aged ovaries, both by Gomori's Aldehyde Fuchsin staining and stereological analysis, and clearly displaying a significantly lower number of elastic fibers in aged tissues compared to the young ones. These observations are consistent with the dramatic fall in elastin levels detected in menopausal women perifollicular ECM [20] and is well in agreement with the unbalanced collagen/elastin ratio here demonstrated with ELISA quantification studies in senescent ovaries. Altogether, this suggests that, similarly to what described in other tissues [37–39], ovarian aging can be associated with a progressive elasticity reduction and, therefore, with a general decrement in mechanical resilience and durability. However, the increase in GAG content, demonstrated in the present study, indicates that these molecules may act to buffer the altered collagen/elastin balance, therefore, suggesting the existence of compensative mechanisms, possibly mitigating the decrease in tissue elasticity.

Interestingly enough, the changes described above are accompanied by a significant increase of the laminins LAMA3 and LAMB1 in aged samples. Although only few data are available on laminin-matrix deposition mechanisms, the signaling pathways involved and the role in specifying cell behaviors [40], it must be noted that several studies reported high laminin contents in senescent cells isolated from fibrotic tissues, including aorta [41], lung [42], and skin [43]. We may therefore speculate that laminin deposition may be correlated and/or contribute to age-related ECM modifications [44] and further studies are needed in other to better clarify these aspects and the related mechanisms. The increase in laminins is also paralleled by a significant reduction in FN1 content. This is in line with Schnabl et al. and Krizhanovsky et al. that reported a reduction in FN expression levels in liver fibrosis [45,46]. On the other hand, an opposite trend was described by other Authors that showed FN transcription upregulation in different organs [44,47,48]. We have no clear explanation for such discrepancies, but we may hypothesize that the different results obtained may be related to cell type-specific differences and/or tissue-specific responses.

A very dynamic variation in gene transcription levels, closely reflecting the morphological data described above, accompanies ECM reorganization in senescent ovary, with higher expression levels of collagens (COL1A1, COL3A1, COL4A2), glycoprotein (EMILIN1), laminins (LAMA3, LAMB1), proteoglycans (VCAN, HSPG2, CSPG4), and downregulation of elastin (ELN) and fibronectin (FN1). Interestingly, all the protease-related genes analyzed, namely ELANE, MMP1, MMP2, MMP3, MMP9, and MMP14, show significantly lower expression levels in aged ovaries, suggesting that ECM degradation and remodeling activities may decrease during senescence, while protein deposition mechanisms are kept active, resulting in fiber accumulation. In contrast to all the protease analyzed, MMP12 transcription is significantly increased in senescent ovaries.

Since this gene encode for a matrix metalloproteinase involved in elastin degradation, its upregulation may well explain the significant reduction in elastic fiber content described above. In our understanding the molecular results here reported demonstrate a fine tuning in gene expression activity that orchestrates ECM composition changes characterizing the aging process and that suggests a direct impact of senescence on the transcription machinery.

When a whole-organ decellularization protocol, previously developed in our laboratory, [23–25] was applied to aged ovaries, we were able to derive 3D ECM-based biological scaffolds that represent a viable alternative to the use of synthetic matrix such as hydrogels [49].The decellularized scaffolds preserve all the changes that are described above and that are distinctive of the senescent organ. Both histochemical and immunohistochemical staining demonstrate indeed the preservation and the quantities of collagen, elastin, GAGs, laminins, and fibronectin detected in aged native tissues, thus basically confirming the maintenance of the original aged organ. These observations suggest that the generated scaffold maintains an intact basement membrane complex after the decellularization process, that has been previously demonstrated to play a key role in modulating in vitro cell growth patterns [50] . This is, to our knowledge, the first attempt to create a biological matrix that mimics the senescent ovarian micro-structure and offers an exciting opportunity to better characterize ovarian aging in vitro in a complex and physiologically relevant environment.

## 5. Conclusions

Significant changes take place in the aged ovarian ECM. These include altered concentrations of the main structural molecules, such as collagen, elastin, laminins, and fibronectin, that lead to tissue architecture remodeling, increment of fibrosity and reduced elasticity. Interestingly, age-related modifications are not only the results of post-transcriptional processes, but rather has a direct impact on gene expression.

The typical aging phenotype is preserved after decellularization, with the creation of an ECM-based scaffold that mimics the senescent ovarian micro-structure and offers an exciting opportunity to better characterize ovarian aging in vitro in a complex and physiologically relevant environment. This, in turn, constitutes an alternative high predictive in vitro model for the research in the aging field, allowing for a reduction of the number of experimental animals used. At the same time, the bio-scaffold will in due time implement the production of an "aging ovary in a dish" model to further study the mechanisms driving aging and, when coupled with non-cytotoxic nanovehicles [51], may lead to the identification of possible strategies to counteract tissue degeneration.

**Author Contributions:** Investigation, G.P., T.D.I.; data curation, G.P., T.D.I.; writing—original draft preparation, G.P., T.A.L.B; writing—review and editing, G.P., F.G., T.A.L.B; funding acquisition, G.P., T.A.L.B. All authors have read and agreed to the published version of the manuscript.

**Funding:** This research was funded by Carraresi Foundation, PSR2017 and PSR2020. This research is part of the project "MIND FoodS HUB (Milano Innovation District Food System Hub): Innovative concept for the eco-intensification of agricultural production and for the promotion of dietary patterns for human health and longevity through the creation in MIND of a digital Food System Hub", cofunded by POR FESR 2014-2020_BANDO Call HUB Ricerca e Innovazione, Regione Lombardia.

**Data Availability Statement:** The data presented in this study are available on request from the corresponding author.

**Acknowledgments:** Authors are members of the COST Action CA16119 In vitro 3-D total cell guidance and fitness (CellFit) and of the Trans-COST Actions Task-Force on Covid-19.

**Conflicts of Interest:** The authors declare no conflict of interest.

## References

1. Amargant, F.; Manuel, S.L.; Tu, Q.; Parkes, W.S.; Rivas, F.; Zhou, L.T.; Rowley, J.E.; Villanueva, C.E.; Hornick, J.E.; Shekhawat, G.S.; et al. Ovarian Stiffness Increases with Age in the Mammalian Ovary and Depends on Collagen and Hyaluronan Matrices. *Aging cell* **2020**, *19*, doi:10.1111/ACEL.13259.

2. Trinh, X.-B.; Peeters, F.; Tjalma, W.A.A. The Thoughts of Breast Cancer Survivors Regarding the Need for Starting Hormone Replacement Therapy. *European Journal of Obstetrics & Gynecology and Reproductive Biology* **2006**, *124*, 250–253, doi:10.1016/J.EJOGRB.2005.07.013.

3. Broekmans, F.J.; Soules, M.R.; Fauser, B.C. Ovarian Aging: Mechanisms and Clinical Consequences. *Endocrine reviews* **2009**, *30*, 465–493, doi:10.1210/ER.2009-0006.

4. Gold, E.B. The Timing of the Age at Which Natural Menopause Occurs. *Obstetrics and gynecology clinics of North America* **2011**, *38*, 425–440, doi:10.1016/J.OGC.2011.05.002.

5. Li, C.J.; Lin, L. te; Tsai, H.W.; Chern, C.U.; Wen, Z.H.; Wang, P.H.; Tsui, K.H. The Molecular Regulation in the Pathophysiology in Ovarian Aging. *Aging and Disease* **2021**, *12*, 934, doi:10.14336/AD.2020.1113.

6. Phillip, J.M.; Aifuwa, I.; Walston, J.; Wirtz, D. The Mechanobiology of Aging. *Annual review of biomedical engineering* **2015**, *17*, 113, doi:10.1146/ANNUREV-BIOENG-071114-040829.

7. Briley, S.M.; Jasti, S.; McCracken, J.M.; Hornick, J.E.; Fegley, B.; Pritchard, M.T.; Duncan, F.E. Reproductive Age-Associated Fibrosis in the Stroma of the Mammalian Ovary. *Reproduction (Cambridge, England)* **2016**, *152*, 245–260, doi:10.1530/REP-16-0129.

8. Brevini, T.A.L.; Pennarossa, G.; Gandolfi, F. A 3D Approach to Reproduction. *Theriogenology* **2020**, *150*, doi:10.1016/j.theriogenology.2020.01.020.

9. Discher, D.E.; Mooney, D.J.; Zandstra, P.W. Growth Factors, Matrices, and Forces Combine and Control Stem Cells. *Science* **2009**, *324*, 1673–1677, doi:10.1126/science.1171643.

10. Jaalouk, D.E.; Lammerding, J. Mechanotransduction Gone Awry. *Nature Reviews Molecular Cell Biology* **2009**, *10*, 63–73, doi:10.1038/nrm2597.

11. Mammoto, A.; Ingber, D.E. Cytoskeletal Control of Growth and Cell Fate Switching. *Current Opinion in Cell Biology* **2009**, *21*, 864–870, doi:10.1016/J.CEB.2009.08.001.

12. Wozniak, M.A.; Chen, C.S. Mechanotransduction in Development: A Growing Role for Contractility. *Nature Reviews Molecular Cell Biology* **2009**, *10*, 34–43, doi:10.1038/nrm2592.

13. Frantz, C.; Stewart, K.M.; Weaver, V.M. The Extracellular Matrix at a Glance. *Journal of Cell Science* **2010**, *123*, 4195, doi:10.1242/JCS.023820.

14. Biernacka, A.; Frangogiannis, N.G. Aging and Cardiac Fibrosis. *Aging and Disease* **2011**, *2*, 158.

15. Giménez, A.; Duch, P.; Puig, M.; Gabasa, M.; Xaubet, A.; Alcaraz, J. Dysregulated Collagen Homeostasis by Matrix Stiffening and TGF-B1 in Fibroblasts from Idiopathic Pulmonary Fibrosis Patients: Role of FAK/Akt. *International journal of molecular sciences* **2017**, *18*, doi:10.3390/IJMS18112431.

16. Urbanczyk, M.; Layland, S.L.; Schenke-Layland, K. The Role of Extracellular Matrix in Biomechanics and Its Impact on Bioengineering of Cells and 3D Tissues. *Matrix biology : journal of the International Society for Matrix Biology* **2020**, *85–86*, 1–14, doi:10.1016/J.MATBIO.2019.11.005.

17. Thorne, J.T.; Segal, T.R.; Chang, S.; Jorge, S.; Segars, J.H.; Leppert, P.C. Dynamic Reciprocity between Cells and Their Microenvironment in Reproduction. *Biology of reproduction* **2015**, *92*, doi:10.1095/BIOLREPROD.114.121368.

18. Woodruff, T.K.; Shea, L.D. A New Hypothesis Regarding Ovarian Follicle Development: Ovarian Rigidity as a Regulator of Selection and Health. *Journal of assisted reproduction and genetics* **2011**, *28*, 3–6, doi:10.1007/S10815-010-9478-4.

19. Hsueh, A.J.W.; Kawamura, K.; Cheng, Y.; Fauser, B.C.J.M. Intraovarian Control of Early Folliculogenesis. *Endocrine Reviews* **2015**, *36*, 1, doi:10.1210/ER.2014-1020.

20. Ouni, E.; Bouzin, C.; Dolmans, M.M.; Marbaix, E.; Pyr Dit Ruys, S.; Vertommen, D.; Amorim, C.A. Spatiotemporal Changes in Mechanical Matrisome Components of the Human Ovary from Prepuberty to Menopause. *Human reproduction (Oxford, England)* **2020**, *35*, 1391–1410, doi:10.1093/HUMREP/DEAA100.

21. Wood, C.D.; Vijayvergia, M.; Miller, F.H.; Carroll, T.; Fasanati, C.; Shea, L.D.; Catherine Brinson, L.; Woodruff, T.K. Multi-Modal Magnetic Resonance Elastography for Noninvasive Assessment of Ovarian Tissue Rigidity in Vivo. *Acta biomaterialia* **2015**, *13*, 295–300, doi:10.1016/J.ACTBIO.2014.11.022.

22. Hirshfeld-Cytron, J.E.; Duncan, F.E.; Xu, M.; Jozefik, J.K.; Shea, L.D.; Woodruff, T.K. Animal Age, Weight and Estrus Cycle Stage Impact the Quality of in Vitro Grown Follicles. *Human reproduction (Oxford, England)* **2011**, *26*, 2473–2485, doi:10.1093/HUMREP/DER183.

23. Pennarossa, G.; Ghiringhelli, M.; Gandolfi, F.; Brevini, T.A.L.L. Creation of a Bioengineered Ovary: Isolation of Female Germline Stem Cells for the Repopulation of a Decellularized Ovarian Bio-Scaffold. *Methods in molecular biology (Clifton, N.J.)* **2021**, *2273*, 139–149, doi:10.1007/978-1-0716-1246-0_9.

24. Pennarossa, G.; Ghiringhelli, M.; Gandolfi, F.; Brevini, T.A.L. Whole-Ovary Decellularization Generates an Effective 3D Bioscaffold for Ovarian Bioengineering. *Journal of Assisted Reproduction and Genetics* **2020**, 1–11, doi:10.1007/s10815-020-01784-9.

25. Pennarossa, G.; de Iorio, T.; Gandolfi, F.; Brevini, T.A.L. Ovarian Decellularized Bioscaffolds Provide an Optimal Microenvironment for Cell Growth and Differentiation In Vitro. *Cells* **2021**, *10*, doi:10.3390/CELLS10082126.

26. Lliberos, C.; Liew, S.H.; Zareie, P.; la Gruta, N.L.; Mansell, A.; Hutt, K. Evaluation of Inflammation and Follicle Depletion during Ovarian Ageing in Mice. *Scientific Reports 2021 11:1* **2021**, *11*, 1–15, doi:10.1038/s41598-020-79488-4.

27. Mossa, F.; Walsh, S.W.; Butler, S.T.; Berry, D.P.; Carter, F.; Lonergan, P.; Smith, G.W.; Ireland, J.J.; Evans, A.C.O. Low Numbers of Ovarian Follicles ≥3 Mm in Diameter Are Associated with Low Fertility in Dairy Cows. *Journal of Dairy Science* **2012**, *95*, 2355–2361, doi:10.3168/JDS.2011-4325.

28. Scheffer, G.J.; Broekmans, F.J.M.; Looman, C.W.N.; Blankenstein, M.; Fauser, B.C.J.M.; DeJong, F.H.; te Velde, E.R. The Number of Antral Follicles in Normal Women with Proven Fertility Is the Best Reflection of Reproductive Age. *Human reproduction (Oxford, England)* **2003**, *18*, 700–706, doi:10.1093/HUMREP/DEG135.

29. Chen, K.; Ma, J.; Jia, X.; Ai, W.; Ma, Z.; Pan, Q. Advancing the Understanding of NAFLD to Hepatocellular Carcinoma Development: From Experimental Models to Humans. *Biochimica et biophysica acta. Reviews on cancer* **2019**, *1871*, 117–125, doi:10.1016/J.BBCAN.2018.11.005.

30. Acharya, P.; Chouhan, K.; Weiskirchen, S.; Weiskirchen, R. Cellular Mechanisms of Liver Fibrosis. *Frontiers in Pharmacology* **2021**, *12*, 1072, doi:10.3389/FPHAR.2021.671640/BIBTEX.

31. Biernacka, A.; Frangogiannis, N.G. Aging and Cardiac Fibrosis. *Aging and disease* **2011**, *2*, 158–173.

32. Meschiari, C.A.; Ero, O.K.; Pan, H.; Finkel, T.; Lindsey, M.L. The Impact of Aging on Cardiac Extracellular Matrix. *GeroScience* **2017**, *39*, 7–18, doi:10.1007/S11357-017-9959-9.

33. Wynn, T.A.; Ramalingam, T.R. Mechanisms of Fibrosis: Therapeutic Translation for Fibrotic Disease. *Nature medicine* **2012**, *18*, 1028–1040, doi:10.1038/NM.2807.

34. Guo, Z.; Zhang, T.; Chen, X.; Fang, K.; Hou, M.; Gu, N. The Effects of Porosity and Stiffness of Genipin Cross-Linked Egg White Simulating Aged Extracellular Matrix on Proliferation and Aggregation of Ovarian Cancer Cells. *Colloids and Surfaces A: Physicochemical and Engineering Aspects* **2017**, *520*, 649–660, doi:10.1016/J.COLSURFA.2017.02.031.

35. Blair Dodson, R.; Rozance, P.J.; Fleenor, B.S.; Petrash, C.C.; Shoemaker, L.G.; Hunter, K.S.; Ferguson, V.L. Increased Arterial Stiffness and Extracellular Matrix Reorganization in Intrauterine Growth–Restricted Fetal Sheep. **2013**, doi:10.1038/pr.2012.156.

36. Zhang, J.; Zhao, X.; Vatner, D.E.; McNulty, T.; Bishop, S.; Sun, Z.; Shen, Y.T.; Chen, L.; Meininger, G.A.; Vatner, S.F. Extracellular Matrix Disarray as a Mechanism for Greater Abdominal Versus Thoracic Aortic Stiffness with Aging in Primates. *Arteriosclerosis, Thrombosis, and Vascular Biology* **2016**, *36*, 700–706, doi:10.1161/ATVBAHA.115.306563.

37. Sherratt, M.J. Age-Related Tissue Stiffening: Cause and Effect. *Advances in Wound Care* **2013**, *2*, 11, doi:10.1089/WOUND.2011.0328.

38. Sherratt, M.J. Tissue Elasticity and the Ageing Elastic Fibre. *Age (Dordrecht, Netherlands)* **2009**, *31*, 305–325, doi:10.1007/S11357-009-9103-6.

39. Frances, C.; Branchet, M.C.; Boisnic, S.; Lesty, C.L.; Robert, L. Elastic Fibers in Normal Human Skin. Variations with Age: A Morphometric Analysis. *Archives of Gerontology and Geriatrics* **1990**, *10*, 57–67, doi:10.1016/0167-4943(90)90044-7.

40. Hamill, K.J.; Kligys, K.; Hopkinson, S.B.; Jones, J.C.R. Laminin Deposition in the Extracellular Matrix: A Complex Picture Emerges. *Journal of cell science* **2009**, *122*, 4409–4417, doi:10.1242/JCS.041095.

41. Augustin-Voss, H.G.; Voss, A.K.; Pauli, B.U. Senescence of Aortic Endothelial Cells in Culture: Effects of Basic Fibroblast Growth Factor Expression on Cell Phenotype, Migration, and Proliferation. *Journal of cellular physiology* **1993**, *157*, 279–288, doi:10.1002/JCP.1041570210.

42. Chilosi, M.; Carloni, A.; Rossi, A.; Poletti, V. Premature Lung Aging and Cellular Senescence in the Pathogenesis of Idiopathic Pulmonary Fibrosis and COPD/Emphysema. *Translational research : the journal of laboratory and clinical medicine* **2013**, *162*, 156–173, doi:10.1016/J.TRSL.2013.06.004.

43. Natarajan, E.; Omobono, J.D.; Guo, Z.; Hopkinson, S.; Lazar, A.J.F.; Brenn, T.; Jones, J.C.; Rheinwald, J.G. A Keratinocyte Hypermotility/Growth-Arrest Response Involving Laminin 5 and P16INK4A Activated in Wound Healing and Senescence. *The American journal of pathology* **2006**, *168*, 1821–1837, doi:10.2353/AJPATH.2006.051027.

44. Levi, N.; Papismadov, N.; Solomonov, I.; Sagi, I.; Krizhanovsky, V. The ECM Path of Senescence in Aging: Components and Modifiers. *The FEBS journal* **2020**, *287*, 2636–2646, doi:10.1111/FEBS.15282.

45. Schnabl, B.; Purbeck, C.A.; Choi, Y.H.; Hagedorn, C.H.; Brenner, D.A. Replicative Senescence of Activated Human Hepatic Stellate Cells Is Accompanied by a Pronounced Inflammatory but Less Fibrogenic Phenotype. *Hepatology (Baltimore, Md.)* **2003**, *37*, 653–664, doi:10.1053/JHEP.2003.50097.

46. Krizhanovsky, V.; Yon, M.; Dickins, R.A.; Hearn, S.; Simon, J.; Miething, C.; Yee, H.; Zender, L.; Lowe, S.W. Senescence of Activated Stellate Cells Limits Liver Fibrosis. *Cell* **2008**, *134*, 657–667, doi:10.1016/J.CELL.2008.06.049.

47. Murano, S.; Thweatt, R.; Shmookler Reis, R.J.; Jones, R.A.; Moerman, E.J.; Goldstein, S. Diverse Gene Sequences Are Overexpressed in Werner Syndrome Fibroblasts Undergoing Premature Replicative Senescence. *Molecular and cellular biology* **1991**, *11*, 3905–3914, doi:10.1128/MCB.11.8.3905-3914.1991.

48. Dumont, P.; Burton, M.; Chen, Q.M.; Gonos, E.S.; Frippiat, C.; Mazarati, J.B.; Eliaers, F.; Remacle, J.; Toussaint, O. Induction of Replicative Senescence Biomarkers by Sublethal Oxidative Stresses in Normal Human Fibroblast. *Free radical biology & medicine* **2000**, *28*, 361–373, doi:10.1016/S0891-5849(99)00249-X.

49. Ganguly, S.; Das, P.; Maity, P.P.; Mondal, S.; Ghosh, S.; Dhara, S.; Das, N.C. Green Reduced Graphene Oxide Toughened Semi-IPN Monolith Hydrogel as Dual Responsive Drug Release System: Rheological, Physicomechanical, and Electrical Evaluations. *Journal of Physical Chemistry B* **2018**, *122*, 7201–7218, doi:10.1021/ACS.JPCB.8B02919/SUPPL_FILE/JP8B02919_SI_001.PDF.

50. Brown, B.; Lindberg, K.; Reing, J.; Stolz, D.B.; Badylak, S.F. The Basement Membrane Component of Biologic Scaffolds Derived from Extracellular Matrix. *Tissue engineering* **2006**, *12*, 519–526, doi:10.1089/TEN.2006.12.519.

51. Ganguly, S.; Das, P.; Itzhaki, E.; Hadad, E.; Gedanken, A.; Margel, S. Microwave-Synthesized Polysaccharide-Derived Carbon Dots as Therapeutic Cargoes and Toughening Agents for Elastomeric Gels. *ACS Applied Materials and Interfaces* **2020**, *12*, 51940–51951, doi:10.1021/ACSAMI.0C14527/SUPPL_FILE/AM0C14527_SI_005.AVI.

## 3.3. Synergistic Effect of miR-200 and Young Extracellular Matrix-based Bio-scaffolds to Reduce Signs of Aging in Senescent Fibroblasts

Published in Stem Cell Reviews and Reports on 27th august 2022.

DOI: 10.1007/s12015-022-10438-5.

The third study is focused on the influence of ECM age-related modifications on cell behaviour, taking the advantage of ECM-derived biomechanical cues to develop/support novel rejuvenating strategies. In this context, young bio-matrixes ability to recreate an age-specific microenvironment was exploited to examine whether these bio-scaffolds are able to boost, and properly maintain, the rejuvenated phenotype acquired by cells after miR-200 exposure.

To this purpose, the high-plasticity state induced by miR-200b/c exposure was firstly assessed, also analysing the transcription of the main aging hallmarks. In addition, the miR-200-treated cells were used in repopulation studies to investigate the role of age-associated ECM modifications in cellular senescence.

The data reported in the following manuscript agree and expand previously reported data, indicating a significant reduction of aging hallmarks in miR-200b/c-treated cells. Interestingly, the rejuvenated phenotype acquired was stably retained only when cells were engrafted onto young 3D ECM-based scaffolds, contrarily to what observed in standard 2D culture systems, as well as aged bio-matrixes. These results point out to the possibility that a young microenvironment may exert a supporting effect to stably maintain the rejuvenated phenotype induced by miR-200b/c exposure, which would otherwise be transient and reversible.

*Article*

# Synergistic effect of miR-200 and young extracellular matrix-based bio-scaffolds to reduce signs of aging in senescent fibroblasts

**Georgia Pennarossa[1], Teresina De Iorio[1], Sharon Arcuri[1], Fulvio Gandolfi[2], and Tiziana A.L. Brevini[1,*]**

[1] Laboratory of Biomedical Embryology, Department of Health, Animal Science and Food Safety and Center for Stem Cell Research, Università degli Studi di Milano, Milan, 20133, Italy; teresina.deiorio@unimi.it, georgia.pennarossa@unimi.it, tiziana.brevini@unimi.it.
[2] Laboratory of Biomedical Embryology, Department of Agricultural and Environmental Sciences - Production, Landscape, Agroenergy, Università degli Studi di Milano, Milan, 20133, Italy; fulvio.gandolfi@unimi.it
* Correspondence: tiziana.brevini@unimi.it

**Abstract**

Aging is defined as a complex, multifaceted degenerative process that causes a gradual decline of physiological functions and a rising mortality risk with time. Stopping senescence or even rejuvenating the body represent one of the long standing human dreams. Somatic cell nuclear transfer as well as cell reprogramming have suggested the possibility to slow or even reverse signs of aging.

We exploited miR-200 ability to induce a transient high plasticity state in fibroblasts isolated from old individuals and we investigated whether this ameliorates cellular and physiological hallmarks of senescence. In addition, based on the assumption that extracellular matrix (ECM) provides biomechanical stimuli directly influencing cell behavior, we examine whether ECM-based bio-scaffolds obtained from young animals stably maintain the rejuvenated phenotype acquired by cells after miR-200 exposure. The results show the existence of multiple factors that cooperate to control a unique program, driving the cell clock. In particular, miR-200 family directly regulates the molecular mechanisms erasing cell senescence. However, this effect is transient, reversible, and quickly lost. On the other hand, the use of an adequate young microenvironment stabilizes the miR-200-mediated rejuvenating effects, suggesting that synergistic interactions occur among molecular effectors and ECM-derived biomechanical stimuli. The model here described is a useful tool to better characterize these complex regulations and to finely dissect the multiple and concurring biochemical and biomechanical cues driving the cell biological clock.

**Keywords:** Aging, cellular rejuvenation, ECM-based bio-scaffolds, micro-RNA, miR-200 family, cell senescence

## Introduction

Advances in medical care, improvements in sanitation, and rising living standards contribute to increase life expectancy. Although this reflects positive human development, it also poses new important challenges that will aggravate in the years to come. Among them, aging is one of the most critical and emerging problems in public health, due to the exponential increase of elderly patients suffering with chronic age-onset diseases, often with multiple co-morbidities. Aging is indeed defined as a complex, multifaceted process characterized by a progressive accumulation of macroscopic and microscopic modifications that are accompanied by molecular and cellular damages, negatively affecting organ, tissue, cell, and subcellular organelle functions [1, 2]. These senescence processes are influenced by environmental factors as well as by genetic and epigenetic dysregulations that induce a gradual organism decline [3]. In agreement with this, several studies have described a link between DNA methylation and aging [4–7], demonstrating that around 29% of the methylation sites in the genome is modified with increasing age, thus reflecting the natural development of age-related phenotypes and diseases, such as diabetes, autoimmune and cardiovascular disorders [8].

The possibility to reverse aging hallmarks was suggested, for the first time, by the generation of sheep and mouse offspring with a normal lifespan, after adult somatic cell nuclear transfer (SCNT) [9–11]. Subsequently, the induced pluripotent stem cell (iPSC) technique [12] was used to reprogram senescent and centenarian cells and re-differentiate them into fully rejuvenated cells [13]. During the last years, parallel studies reported the possibility to induce a transient high plasticity state by using a brief exposure to the demethylating agent 5-azacytidine (5-aza-CR) [14–24]. Interestingly, 5-aza-CR treated cells displayed a significant decrease in global DNA methylation, paralleled by an increment in formylcytosine (5fC) and 5-carboxylcytosine (5caC), thus indicating that 5-aza-CR induces both direct and indirect demethylating events [18]. Direct demethylation is known to be driven by the TET enzyme family enzymes that play a crucial role during cellular reprogramming, removing the epigenetic blocks and re-activating previously silenced genes [25–28]. Recent studies demonstrated that TET-mediated activation of the miR-200 family promotes a transient high plasticity state and helps fibroblasts to overcome the mesenchymal-epithelial transition (MET) barrier, facilitating iPSC generation [29]. Consistent with this, all members of miR-200 family, namely miR-200a, miR-200b, miR-200c, miR-141 and miR-429, are highly expressed in both ESCs and iPSCs, thus suggesting their involvement in pluripotency induction and maintenance [29].
In the present work, we exploit miR-200 ability to induce a transient high plasticity state in cells isolated from old individuals. We investigate whether this is able to ameliorate cellular and physiological hallmarks of aging in senescent cells. Furthermore, we examine whether extracellular matrix (ECM)-based scaffolds obtained from young animals are able to boost and properly maintain the rejuvenated phenotype acquired by cells after miR-200 exposure.

**Materials and methods**
All reagents were purchased from Thermo Fisher Scientific unless otherwise indicated.

*Ethics statement*
Human cells were purchased from the NIGMS Human Genetic Cell Repository at the Coriell Institute for Medical Research (USA). Ethical approval was not required for this study because it did not involve living animals. All the methods in our study were carried out in accordance with the approved guidelines.

*Culture of human fibroblasts obtained from young and aged individuals*
Fibroblast cell lines obtained from 29-32 years old donors (Young, n=3) and from 82-92 years old individuals (Aged, n=3) were purchased from the NIGMS Human Genetic Cell Repository at the Coriell Institute for Medical Research (USA). Cells were grown in fibroblast culture medium (FCM) consisting of Eagle's Minimum Essential Medium (MEM) supplemented with 15% Foetal Bovine Serum (FBS), 2mM glutamine (Sigma-Aldrich), 1% antibiotic/antimycotic solution (Sigma-Aldrich), and maintained in 5% CO2 at 37°C. All experiments were carried out in triplicates at least three times.

*Fibroblast exposure to miR-200b/c*
Cells were plated at a concentration of 2.1 x 104 cells/cm2. After 24 h, they were exposed to 100nM of miR-200b/c (predesigned mirVANA Mimics) using RNAi-MAX in Opti-MEMTM medium, following the manufacturer's instructions, and incubated in 5% CO2 at 37°C for 48h.

*Culture of miR-200b/c treated fibroblasts onto 2D systems*
At the end of miRNA exposure, cells were returned to FCM and maintained in standard plastic dishes (2D) for 10 days. Cell morphology was monitored daily using an Eclipse TE200 inverted microscope (Nikon), connected to a Digital Sight camera (Nikon). Cultures were arrested at day 2, 5, 7 and 10 and analysed as described below.

*Culture of miR-200b/c treated fibroblasts onto 3D ECM-based bio-scaffolds*
Generation of Young and Aged ECM-based bio-scaffolds
18 ovaries from 6-month (n=9, Young) and 5 years old (n=9, Aged) swine were collected at the local abattoir and subjected to whole-organ decellularization protocol [2, 30–32]. Briefly, organs were frozen at −80 °C for at least 24 h, thawed in a 37 °C water bath for 30 min, treated with 0.5% sodium dodecyl sulfate (SDS; Bio-Rad) for 3 h, and immersed overnight in 1% Triton X-100 (Sigma-Aldrich). Ovaries were then washed in deionized water (DI-H2O) for 9 h and incubated with 2% deoxycholate (Sigma-Aldrich) for 12 h. At the end of the decellularization protocol, the ovarian bio-scaffold generated were extensively washed in DI-

H2O for 6 h and sterilized with 70% ethanol and 2% antibiotic/antimycotic solution (Sigma-Aldrich) for 30 min. All the steps described were performed at room temperature using an orbital shaker at 300 rpm. A fragment from each bio-scaffold was collected and analysed for evaluating the efficacy of the decellularization process (data not shown).

Seeding and culture of miR-200b/c treated fibroblasts onto Young and Aged ECM-based bio-scaffolds

miR-200b/c treated fibroblasts were seeded onto Young and Aged ECM-based bio-scaffolds (3D) at a concentration of 6.9 × 106 cells per 7 mm x 1 mm fragment, in 300 μL of FCM and maintained in a 5% CO2 incubator at 37 °C. Half medium volume was changed every other day. Cultures were arrested at day 2, 5, 7, and 10, and analysed as described below.

*Cell growth curve*

Growth curve was assessed by plating 2.5 x 104 cells/cm2 in 4-well multidishes (Nunc). Cell number was counted using Hycor KOVA TM Glasstic TM (Sentinel Diagnostic) and cell viability was determined by trypan blue dye exclusion assay (Sigma-Aldrich). Each time point was assessed in triplicate.

*Cell proliferation index*

Cell proliferation index was evaluated by proliferating cell nuclear antigen (PCNA) immuno-staining. Cells were fixed in methanol at -20 °C for 15 min, while paraffin-embedded tissues were treated with 10mM Sodium citrate solution (pH 6) containing 0,05% Tween-20 (Sigma-Aldrich) to unmask antigens. Samples were incubated in blocking solution containing 10% Goat Serum (Sigma-Aldrich) in PBS for 30 min. Primary antibody (1:200, Sigma-Aldrich) was incubated for 1 h, followed by a suitable secondary antibody exposure (1:250, Alexa FluorTM) for 1 h. Nuclei were counterstained with 4′,6-diamidino-2-phenylindole (DAPI, Sigma-Aldrich). Samples were observed under the Eclipse TE200 microscope (Nikon). All steps were performed at room temperature, unless otherwise indicated. The number of immuno-positive cells was counted in 10 randomly selected fields at 100× total magnification. A minimum of 500 cells were scored in three independent replicates. The number of PCNA positive cells was expressed as a percentage of the total cell counted.

*Reactive oxygen species (ROS) and β-galactosidase (β-GAL) activity*

ROS and β-GAL activities were analysed using human reactive oxygen species (MyBioSource, MBS166870) and Galactosidase beta ELISA kits (MyBioSource, MBS721441). Samples were sonicated at 20kHz in ice for 20 min, homogenates were centrifuged at 3000 rpm for 20 min and supernatants were collected. Assays were carried out following the manufacturer's instructions and, at the end of the procedures, total ROS and β-GAL contents were quantified at 450 nm using a Multiskan FC. Standard curves were designed by plotting the absorbance means (y-axis) against the relative concentrations (x-axis) and the best fit line was determined by regression analyses. Absolute quantifications were then calculated.

*Gene expression analysis*

Quantitative PCR was performed using CFX96 Real-Time PCR detection system (Bio-Rad Laboratories). Total RNA was extracted using the TaqManGene Expression Cells to Ct kit (Applied Biosystems) and DNase I was added in lysis solutions at 1:100 concentration, as indicated by the manufacturer's instructions. Target genes were analysed using predesigned primers and probe sets from TaqManGene Expression Assays (Table 1). GAPDH and ACTB were used as reference genes. Gene expression levels were quantified with CFX Manager software (Bio-Rad Laboratories) and here reported with the highest expression set to 1 and the other relative to this.

*DNA quantification*

Genomic DNA was extracted from fragments, ranging from 10 to 24 mg, with the PureLink® Genomic DNA Kit (Invitrogen), following the provider's instructions. DNA concentrations were measured with NanoDrop 8000 and normalized against the previously annotated fragment weights.

*Histological analysis*

Repopulated bio-scaffolds were fixed in 10% buffered formalin for 24 h, dehydrated in graded alcohols, cleared with xylene, and embedded in paraffin. Serial microtome sections (5 μm thick) were cut, dewaxed, rehydrated, and stained with hematoxylin and eosin (H&E, BioOptica).

*Cell density*

5-µm-thick sections were stained with DAPI and observed under an Eclipse E600 microscope (Nikon) equipped with a digital camera (Nikon). Pictures were acquired with NIS-Elements Software (Version 4.6; Nikon), using constant exposure parameters. Five randomly selected fields at 100X magnification were examined for each section and analysed using the Automated Cell Counter tool (ImageJ software version 1.53j). Briefly, 8-bit images were created and segmented with a thresholding algorithm to eliminate the background and to highlight areas occupied by the nuclei. Collected data were transformed in binary form. Nuclei were automatically counted using previously set size and circularity parameters. Cell density is expressed per mm2 of tissue.

Statistical analysis

Statistical analysis was performed using two-way ANOVA (SPSS 19.1; IBM). Data are presented as the mean ± the standard deviation (SD). Differences of $p \leq 0.05$ were considered significant and are indicated with different superscripts.

**Results**

*miR-200b/c exposure induces high plasticity and erase signs of senescence in fibroblasts isolated from aged individuals*

After miR-200b/c exposure, fibroblasts isolated from aged patients showed considerable phenotype changes. More in detail, the typical elongated shape, visible in untreated fibroblasts (T0, Figure 1a), was replaced by a stem-cell-like morphology with cells smaller in size, granular and vacuolated cytoplasm, and larger nuclei. In addition, miR-2020b/c treated fibroblasts rearranged in a reticular pattern and tended to form distinguishable aggregates (Post miR-200b/c, Figure 1a). Morphological changes were also accompanied by a significant increment in cell proliferation (Post miR-200b/c, Figure 1b). In agreement with this, Post miR-200b/c aged cells showed a growth curve comparable to that of untreated fibroblasts isolated from young individuals (Young, Figure 1b). PCNA immunocytochemical analysis confirmed these data (Figure 1c) and, in particular, its quantitative evaluation demonstrated a significantly higher PCNA positive cell rate after miR-200b/c exposure (Post miR-200b/c, Figure 1d).

These changes were paralleled by a significant decrease in β-galactosidase (β-GAL) activity (Post miR-200b/c, Figure 1e) and reactive oxygen species (ROS) levels (Post miR-200b/c, Figure 1f), with values post-treatment comparable to those young cells (Young, Figure 1e, f).

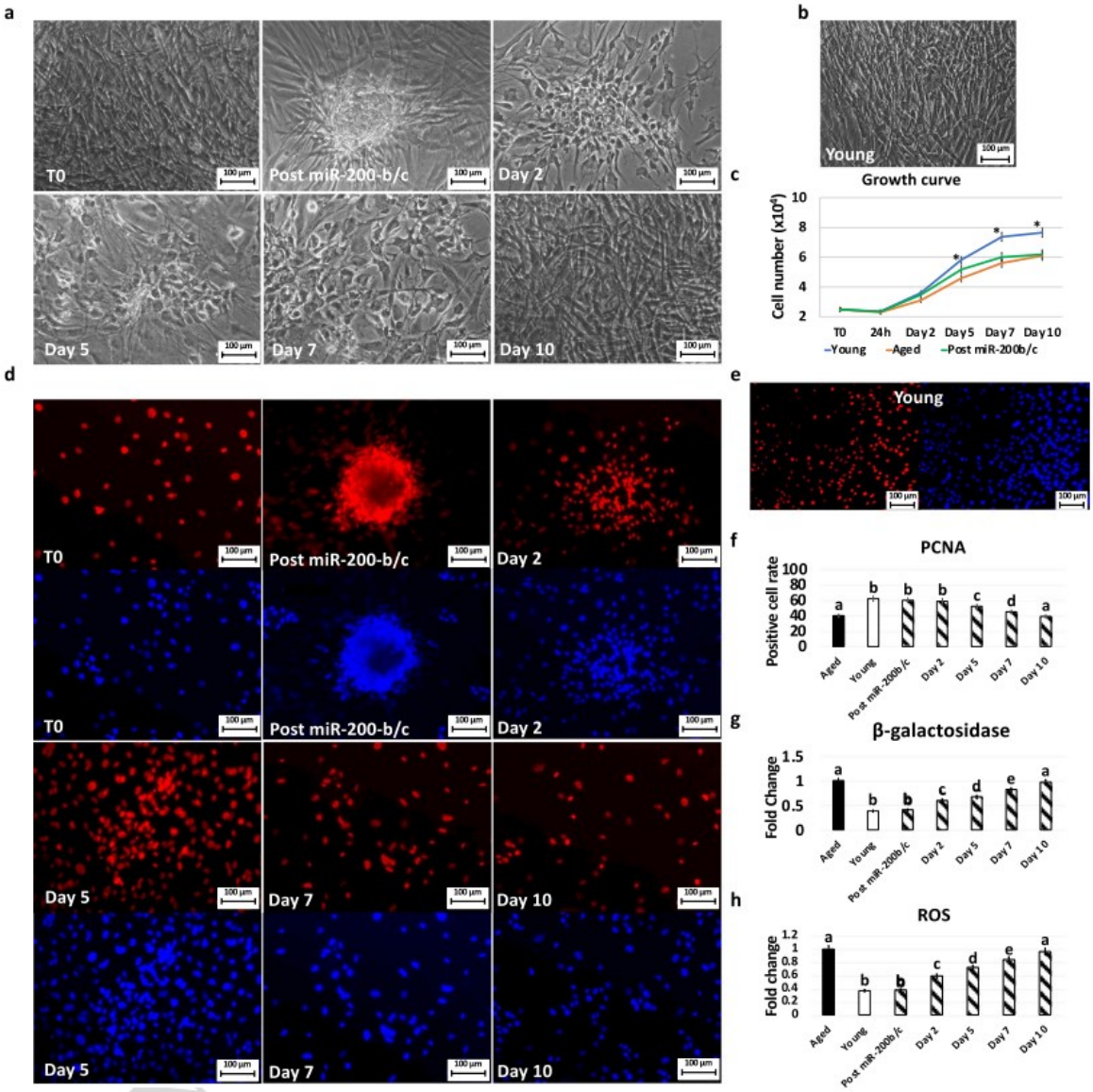


**Figure 1.** Morphology, growth curve, PCNA immunostaining/positive cell rate, β-GAL and ROS activity quantification in miR-200b/c treated aged fibroblasts cultured in 2D systems. (a) After miR-200b/c exposure, fibroblasts isolated from aged individuals loss their typical elongated shape (T0) and become smaller in size with granular, vacuolated cytoplasm, larger nuclei and form distinguishable aggregates (Post miR-200b/c). When fibroblasts returned to FCM progressively reverted to the original phenotype (Day 2, day 5 and day 7) and, by day 10, exhibited small central nuclei and an elongated spindle shape. Scale bars: 100 ⊚m (b) miR-200b/c exposed cells (Post miR-200b/c, green line) increment proliferation rate immediately after treatment and gradually return comparable to untreated aged cells (Aged, orange line). Data are expressed as the mean. Error bars represent the standard error of the mean (SEM). *$p < 0.05$. (c) PCNA (upper panels) and DAPI (lower panels) immunocytochemical staining in untreated fibroblasts isolated from aged (T0), at the end of 48h miR-200b/c exposure (Post miR-200b/c) and at day 2, 5, 7, and 10 of culture in 2D systems. Scale bars: 100 ⊚m. (d) PCNA quantitative evaluation in untreated fibroblasts isolated from aged (Aged, black bar) and young individuals (Young, white bars), at the end of 48h miR-200b/c exposure (Post miR-200b/c) and at day 2, 5, 7, and 10 of culture in 2d systems. Data are expressed as the mean. Error bars represent the standard error of the mean (SEM). Different superscripts indicate $p < 0.05$. (e) β-GAL activity and (f) ROS levels in untreated fibroblasts isolated from aged (Aged, black bars) and young individuals (Young, white bars), at the end of 48h miR-200b/c exposure (Post miR-200b/c) and at day 2, 5, 7, and 10 of culture in 2d systems. Data are expressed as the mean. Error bars represent the standard error of the mean (SEM). *$p < 0.05$.

Gene expression analysis were consistent with the morphological observations and indicated the onset of the pluripotency-related genes OCT4, NANOG, REX1, and SOX2 (Post miR200b/c, Figure 2), which were originally undetectable in untreated fibroblasts (Aged, Young; Figure 2).

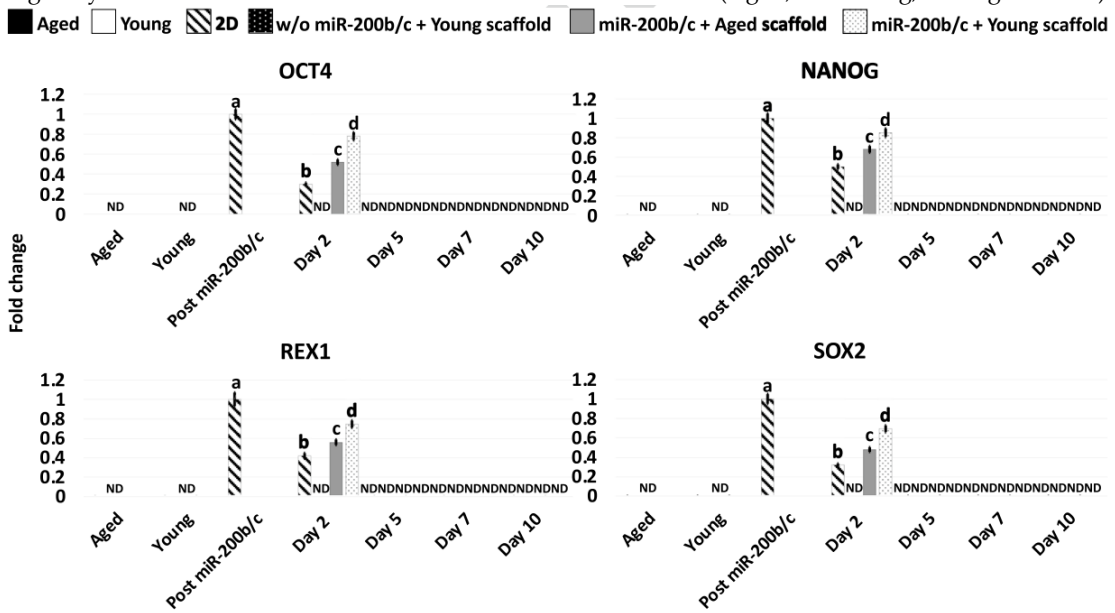


**Figure 2.** Gene expression levels of pluripotency-related (OCT4, NANOG, REX1, SOX2) genes in untreated fibroblasts isolated from aged (Aged, black bars) and young individuals (Young, white bars), at the end of miR-200b/c exposure, in miR-200b/c treated aged fibroblasts cultured in 2D systems (2D, striped bars), untreated aged fibroblasts cultured onto young 3D ECM-based bio-scaffolds (w/o miR-200b/c+Young scaffold, dotted black bars), miR-200b/c treated aged fibroblasts cultured onto aged 3D ECM-based bio-scaffolds (miR-200b/c+Aged scaffold, grey bars), and miR-200b/c treated aged fibroblasts cultured onto young 3D ECM-based bio-scaffolds (miR-200b/c+Young scaffold, dotted white bars). Data are expressed as the mean. Error bars represent the standard error of the mean (SEM). Different superscripts indicate $p<0.05$.

Furthermore, Post miR-200b/c significantly increased their expression of the cell proliferation marker MKI67 (figure 3), and the mitochondrial activity-related genes TFAM, PDHA1, and COX4I1 (Figure 4), picking to values comparable to young cells (Young; Figure 3 and 4).

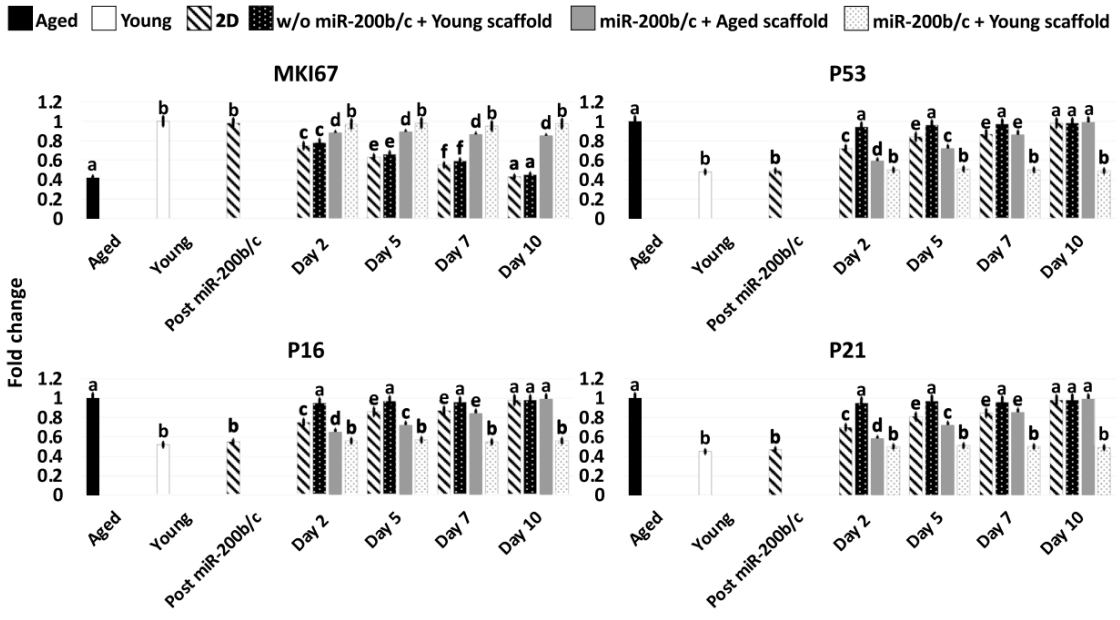

**Figure 3.** Gene expression levels of cell proliferation (MKI67) and senescence-related (P53, P16, P21) genes in untreated fibroblasts isolated from aged (Aged, black bars) and young individuals (Young, white bars), at the end of miR-200b/c exposure, in miR-200b/c treated aged fibroblasts cultured in 2D systems (2D, striped bars), untreated aged fibroblasts cultured onto young 3D ECM-based bio-scaffolds (w/o miR-200b/c+Young scaffold, dotted black bars), miR-200b/c treated aged fibroblasts cultured onto aged 3D ECM-based bio-scaffolds (miR-200b/c+Aged scaffold, grey bars), and miR-200b/c treated aged fibroblasts cultured onto young 3D ECM-based bioscaffolds (miR-200b/c+Young scaffold, dotted white bars). Data are expressed as the mean. Error bars represent the standard error of the mean (SEM). Different superscripts indicate $p<0.05$.

Transcription levels of the reactive oxygen species modulator ROMO1 (Figure 4) and of the senescence-related markers, P53, P16 and P21 (Figure 3), significantly decreased to levels distinctly of young cells (Young; Figure 3 and 4).

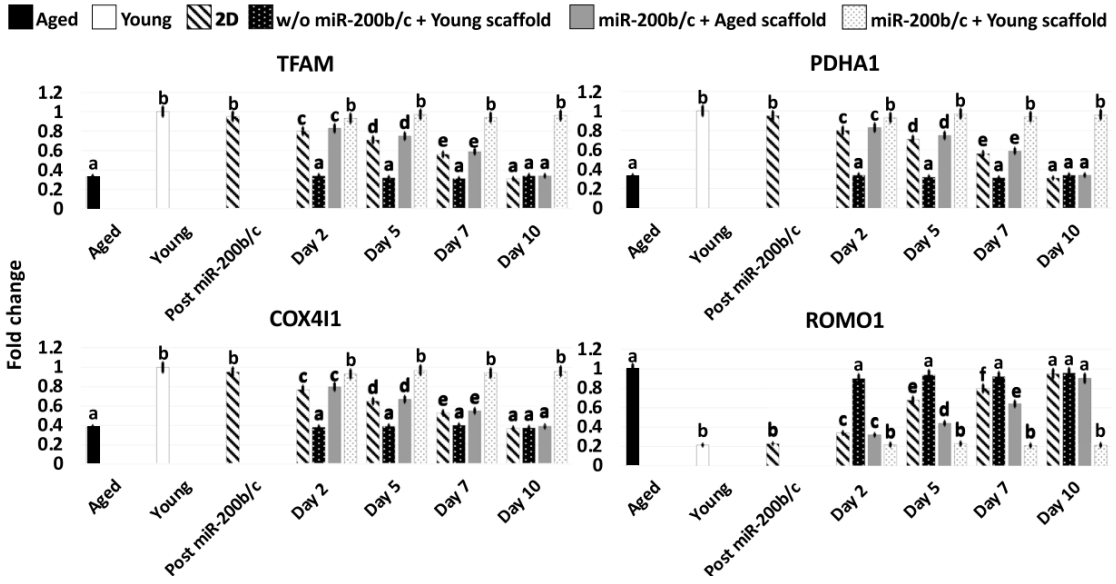


**Figure 4.** Gene expression levels of mitochondrial activity (TFAM, PDHA1, COX4I1) and reactive oxygen species modulator (ROMO1) genes in untreated fibroblasts isolated from aged (Aged, black bars) and young individuals (Young, white bars), at the end of miR-200b/c exposure, in miR-200b/c treated aged fibroblasts cultured in 2D systems (2D, striped bars), untreated aged fibroblasts cultured onto young 3D ECM-based bio-scaffolds (w/o miR-200b/c+Young scaffold, dotted black bars), miR-200b/c treated aged fibroblasts cultured onto aged 3D ECM-based bio-scaffolds (miR-200b/c+Aged scaffold, grey bars), and miR-200b/c treated aged fibroblasts cultured onto young 3D ECM-based bio-scaffolds (miR-200b/c+Young scaffold, dotted white bars). Data are expressed as the mean. Error bars represent the standard error of the mean (SEM). Different superscripts indicate $p < 0.05$.

*miR-200b/c treated fibroblasts cultured in 2D systems revert to their original phenotype*

Fibroblasts returned to FCM, after removal of miR-200b/c, progressively reverted to the original phenotype (Day 2, day 5 and day 7; Figure 1a) and, by day 10, exhibited small central nuclei and an elongated spindle shape, comparable to those of untreated aged fibroblasts (T0, Figure 1a). The morphological changes were also paralleled by a decrement in cell proliferation (Figure 1b). This was also supported by PCNA positive cell rate values that slowly decreased, returning statistically comparable to those of aged fibroblasts by day 10 of culture (Figure 1c, d). Consistently, β-GAL activity (Figure 1e) and ROS levels (Figure 1f) gradually incremented during the culture period, up to day 10, when the values detected were statistically comparable to those observed in untreated aged cells (Aged).

Molecular analysis confirmed these data, with pluripotency-related gene OCT4, NANOG, REX1, and SOX2 expression undetectable by day 5 of culture in FCM. Moreover, by day 10 ROMO1, P53, P16, and P21 gene transcription returned statistically comparable to that of untreated aged cells (Aged; Figure 2, 3

and 4). By day 10 MKI67, TFAM, PDHA1, COX4I1 genes displayed expression levels comparable to those detected in untreated aged cells (Aged; Figure 3 and 4).

*miR-200b/c treated fibroblasts repopulate 3D ECM-based bio-scaffolds, but maintain a rejuvenated phenotype only on young ECM*

H & E (Figure 5a) and DAPI staining (Figure 5b) demonstrated a comparable repopulating ability in miR-200b/c treated cells as well as in untreated fibroblasts (w/o miR-200b/c), indicating that miR-200b/c treatment does not affect cell engrafting ability. Moreover, cell density analyses showed an increasing number of cells along the culture period in all the experimental groups (Figure 5c). Nevertheless, significant differences among the experimental groups were detected. Specifically, starting from day 2 of co-culture and onward, cell number was significantly higher in young decellularized bio-scaffolds repopulated with miR-200b/c exposed fibroblasts (miR-200b/c + Young scaffold) compared to miR-200b/c + Aged scaffold and the control group (w/o miR-200b/c + Young scaffold, Figure 5c). These observations were also confirmed by DNA quantification (Figure 5d).

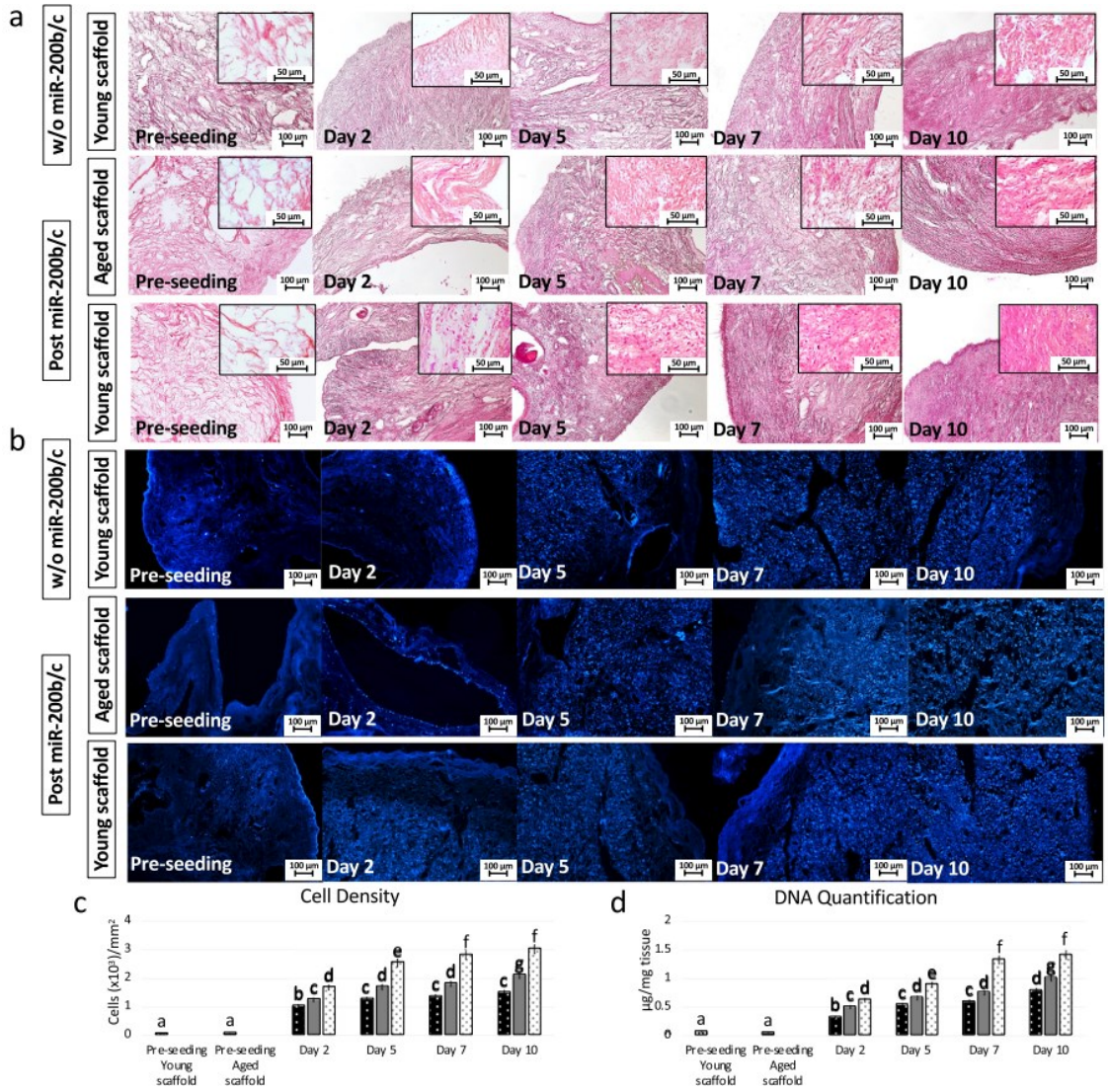


**Figure 5.** H&E, DAPI staining, cell density and DNA quantification in miR-200b/c treated aged fibroblasts cultured onto 3D ECM-based bio-scaffolds. (a) H & E and (b) DAPI staining before cell seeding (Pre-seeding), in untreated aged fibroblasts (w/o miR-200b/c) plated onto young 3D ECM-based bio-scaffolds (Young scaffold) and in miR-200b/c treated aged fibroblasts (Post miR-200b/c) plated onto aged (Aged scaffold) or onto young 3D ECM-based bio-scaffolds (Young scaffold) at day 2, 5, 7, and 10 of culture. Scale bars: 100 ⊙m. (c) Cell density analyses before cell seeding in aged (Pre-seeding aged scaffold, vertical stripped bars) and young scaffolds (Pre-seeding young scaffold, horizontal stripped bars), in untreated aged fibroblasts plated onto young 3D ECM-based bio-scaffolds (w/o miR-200b/c + Young scaffold, dotted

black bars) and in miR-200b/c treated aged fibroblasts plated onto aged (miR-200b/c + Aged scaffold, grey bars) or onto young 3D ECM-based bio-scaffolds (Young scaffold) at day 2, 5, 7, and 10 of culture. Data are expressed as the mean. Error bars represent the standard error of the mean (SEM). Different superscripts indicate $p < 0.05$. (d) DNA quantification before cell seeding in aged (Pre-seeding aged scaffold, vertical stripped bars) and young scaffolds (Pre-seeding young scaffold, horizontal stripped bars), in untreated aged fibroblasts plated onto young 3D ECM-based bio-scaffolds (w/o miR-200b/c + Young scaffold, dotted black bars) and in miR-200b/c treated aged fibroblasts plated onto aged (miR-200b/c + Aged scaffold, grey bars) or onto young 3D ECM-based bio-scaffolds (Young scaffold) at day 2, 5, 7, and 10 of culture. Data are expressed as the mean. Error bars represent the standard error of the mean (SEM). Different superscripts indicate $p < 0.05$.

PCNA staining reveled immuno-positivity in all groups considered (Figure 6a). However, significantly high number of PCNA positive cells were scored in young scaffolds repopulated with miR-200b/c treated fibroblasts (miR-200b/c + Young scaffold, Figure 6b). This is coherent with β-GAL (Figure 6c) and ROS (Figure 6d).

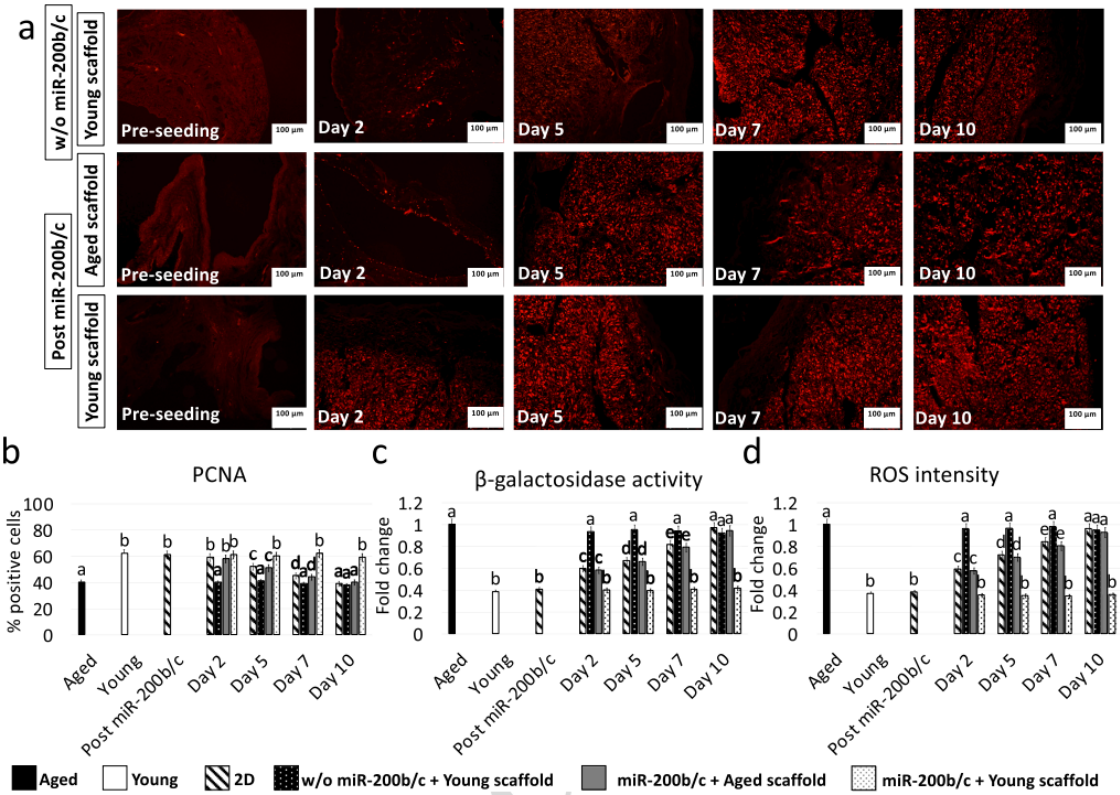


**Figure 6.** PCNA immunostaining/positive cell rate, β-GAL and ROS activity quantification in miR-200b/c treated aged fibroblasts cultured onto 3D ECM-based bio-scaffolds. (a) PCNA immunocytochemical staining before cell seeding (Pre-seeding), in untreated aged fibroblasts (w/o miR-200b/c) plated onto young 3D ECM-based bio-scaffolds (Young scaffold) and in miR-200b/c treated aged fibroblasts (Post miR-200b/c) plated onto aged (Aged scaffold) or onto young 3D ECM-based bio-scaffolds (Young scaffold) at day 2, 5, 7, and 10 of culture. Scale bars: 100 ⊚m. (b) PCNA quantitative evaluation in untreated fibroblasts isolated from aged (Aged, black bars) and young individuals (Young, white bars), at the end of 48h miR-200b/c exposure (Post miR-200b/c), in untreated aged fibroblasts plated onto young 3D ECM-based bio-scaffolds (w/o miR-200b/c + Young scaffold, dotted black bars) and in miR-200b/c treated aged fibroblasts plated onto aged (miR-200b/c + Aged scaffold, grey bars) or onto young 3D ECM-based bio-scaffolds (Young scaffold) at day 2, 5, 7, and 10 of culture. Data are expressed as the mean. Error bars represent the standard error of the mean (SEM). Different superscripts indicate $p < 0.05$. (e) β-GAL activity and (f) ROS levels in untreated fibroblasts isolated from aged (Aged, black bars) and young individuals (Young, white bars), at the end of 48h miR-200b/c exposure (Post miR-200b/c), in untreated aged fibroblasts plated onto young 3D ECM-based bio-scaffolds (w/o miR-200b/c + Young scaffold, dotted black bars) and in miR-200b/c treated aged fibroblasts plated onto aged (miR-200b/c + Aged scaffold, grey bars) or onto young 3D

ECM-based bio-scaffolds (Young scaffold) at day 2, 5, 7, and 10 of culture. Data are expressed as the mean. Error bars represent the standard error of the mean (SEM). Different superscripts indicate $p < 0.05$.

Gene panel evaluation indicated the loss of the pluripotency-related genes by day 5 of co-culture, as expected and previously demonstrated [15, 16, 18–21, 33, 34]. In addition, transcription of MKI67, TFAM, PDHA1, COX4I1, ROMO1, P53, P16, and P21 genes was maintained at levels statistically comparable to those distinctive of young cells only in miR-200b/c + Young scaffold (Figure 2, 3 and 4).

**Discussion**

In the present study, we provide evidence that the use of miR-200b/c induces a transient high plasticity state and ameliorate cellular and physiological hallmarks of aging in senescent cells. In addition, we demonstrate that the rejuvenated phenotype is stably maintained when exposure to miR-200b/c is coupled with engrafting onto young ECM-based bio-scaffolds.

More in detail, exposure to miR-200b/c induces significant changes in fibroblasts isolated from aged patients that acquire morphological and molecular features distinctive of pluripotent cells. Fibroblast standard elongated shape is replaced by a round or oval one. Cells become smaller in size with granular, vacuolated cytoplasm and rearrange in distinguishable aggregates. All these aspects closely resemble those previously described for human ESCs [35] and iPSCs [36], which show a typical round morphology and are able to form compact colonies, with distinct borders and well-defined edges [35–39]. In addition, senescent cells exposed to miR-200b/c display larger nuclei with less cytoplasm, an aspect usually correlated to the relaxed and accessible chromatin structure typically exhibited by pluripotent cells [40–43]. All these observations suggest that the use of miR-200b/c may encourage the appearance of morphological properties previously described in both native and induced high plasticity cells, which is also supported by the molecular analyses performed, demonstrating the onset of the pluripotency-related genes, OCT4, NANOG, REX1, and SOX2, in response to miR-200b/c exposure. Overall, these data confirm and further expand previous studies indicating that overexpression of miR-200 supports Nanog active transcription and ESC self-renewal, while inhibiting embryoid body formation and repressing the expression of ectoderm, endoderm, and mesoderm markers [44, 45].

Interestingly, the morphological changes described above are paralleled by significant reduction of aging hallmarks. In particular, miR-200b/c exposure causes an increment in cellular growth curve values, in proliferation rates and PCNA immune-positive cell number. These results suggest cell-cycle re-activation and the reestablishment of a robust cell division in senescent cells challenged with miR-200b/c. Consistent with this, recent pilot works described the possibility to achieve a young phenotype after restoration of a vigorous cell growth in non-dividing quiescent and senescent cells [46, 47], pointing to a scenario where proliferation is an essential requirement for cellular rejuvenation [48].

Reduction of senescence-associated markers after miR-200b/c exposure is also demonstrated by a significant decrease in β-GAL and ROS activities and is in line with a recent study, showing miR-200 treatment ability to induce a decrement in β-GAL levels as well as in P53 and P21 gene transcription [49]. Consistent with this, our molecular data indicate that miR-200b/c treated cells display a downregulation of P53 and P21 as well as P16 genes. In addition, physiological signs of aging are damped by reducing the oxidative stress (ROMO1), promoting cell proliferation (MKI67) and increasing mitochondrial activity (TFAM, PDHA1, and COX4I1). Altogether these observations confirm the key role played by the miR-200 family, not only to promote and maintain high plasticity [29, 44, 50], but also to reduce signs of cellular senescence and to encourage the acquisition of a young phenotype. It is however important to note that when miR-200b/c are removed from cultures and cells are returned to FCM, they gradually revert to their original phenotype, exhibiting all morphological and molecular signs distinctive of aged cells by day 10 of culture. Specifically, cells increase their size, appear longer with elongated shape, and decrease both their proliferation indexes and PCNA positive rates. The reacquisition of a senescent phenotype is also confirmed by an increased β-GAL and ROS activities and by changes in the transcription levels of MKI67, TFAM, PDHA1, COX4I1, ROMO1, P53, P16, and P21 genes, that returned statistically comparable to those of untreated aged cells. In our understanding, these results demonstrate not only an evident cell rejuvenation induced by miR-200b/c treatment, but also that this effect is transient and reversible.

In contrast, the rejuvenated state appears to be stably retained when cells are engrafted onto young 3D ECM-based bio-scaffolds. Indeed, following miR-200b/c removal, cells adhere and colonize the bio-scaffolds stably maintaining all the hallmarks typical of young cells, namely high number of PCNA positive cells, low values of β-GAL and ROS activities, high transcription levels for the genes involved in

cell proliferation (MKI67), mitochondrial activity (TFAM, PDHA1, and COX4I1) and low transcription for the genes associated to cell senescence, such as ROMO1, P53, P16, and P21. These results point to the possibility that a young microenvironment may exert a supporting effect to stably maintain the rejuvenated phenotype induced by miR-200b/c treatment, which would otherwise be transient and quickly lost.

**Conclusion**

In conclusion, the data presented in this manuscript show that multiple factors cooperate to control a unique program, driving the cell clock. In particular, molecular mechanisms regulated by miR200 are directly involved in erasing cellular senescence, however, an adequate microenvironment is required to stabilize the rejuvenating effects, suggesting the involvement of synergistic interactions among molecular effectors and microenvironment-derived biomechanical cues. The model here developed represent, in our understanding, a useful tool to better characterize these complex regulations and to allow a fine dissection of the multiple and concurring biochemical and biomechanical stimuli driving the process.

**Declarations**

Ethical Approval: Human cells were purchased from the NIGMS Human Genetic Cell Repository at the Coriell Institute for Medical Research (USA). Ethical approval was not required for this study because it did not involve living animals. All the methods in our study were carried out in accordance with the approved guidelines.

Authors Contributions: TALB and FG designed the study. GP, TDI and SA performed the literature reviewing and performed the experiments. GP, TALB and FG wrote the manuscript and all authors read, edited, and approved the final manuscript.

Funding: This research was funded by Carraresi Foundation and PSR2020, PSR2021. It is part of the project "MIND FoodS HUB (Milano Innovation District Food System Hub): Innovative concept for the eco-intensification of agricultural production and for the promotion of dietary patterns for human health and longevity through the creation in MIND of a digital Food System Hub", cofunded by POR FESR 2014-2020_BANDO Call HUB Ricerca e Innovazione, Regione Lombardia. Authors are members of the Trans-COST Actions Task-Force on Covid-19.

Competing Interests: The authors declare that they have no conflict of interest.

Availability of data and materials: The data presented in this study are available on request from the corresponding author.

**References**

1. Phillip, J. M., Aifuwa, I., Walston, J., & Wirtz, D. (2015). The Mechanobiology of Aging. Annual review of biomedical engineering, 17, 113. https://doi.org/10.1146/ANNUREV-BIOENG-071114-040829
2. Pennarossa, G., de Iorio, T., Gandolfi, F., & Brevini, T. A. L. (2022). Impact of Aging on the Ovarian Extracellular Matrix and Derived 3D Scaffolds. Nanomaterials (Basel, Switzerland), 12(3), 345. https://doi.org/10.3390/NANO12030345
3. McHugh, D., & Gil, J. (2018). Senescence and aging: Causes, consequences, and therapeutic avenues. The Journal of Cell Biology, 217(1), 65-77. https://doi.org/10.1083/JCB.201708092
4. Garagnani, P., Bacalini, M. G., Pirazzini, C., Gori, D., Giuliani, C., Mari, D., et al. (2012). Methylation of ELOVL2 gene as a new epigenetic marker of age. Aging cell, 11(6), 1132–1134. https://doi.org/10.1111/ACEL.12005
5. Johnson, A. A., Akman, K., Calimport, S. R. G., Wuttke, D., Stolzing, A., de Magalhães, J. P. (2012). The role of DNA methylation in aging, rejuvenation, and age-related disease. Rejuvenation research, 15(5), 483–494. https://doi.org/10.1089/REJ.2012.1324
6. Teschendorff, A. E., Menon, U., Gentry-Maharaj, A., Ramus, S. J., Weisenberger, D. J., Shen, H., et al. (2010). Age-dependent DNA methylation of genes that are suppressed in stem cells is a hallmark of cancer. Genome research, 20(4), 440–446. https://doi.org/10.1101/GR.103606.109
7. Horvath, S., Zhang, Y., Langfelder, P., Kahn, R. S., Boks, M. P. M., van Eijk, K., et al. (2012). Aging effects on DNA methylation modules in human brain and blood tissue. Genome biology, 13(10), R97. https://doi.org/10.1186/GB-2012-13-10-R97
8. Johansson, Å., Enroth, S., & Gyllensten, U. (2013). Continuous Aging of the Human DNA Methylome Throughout the Human Lifespan. PloS one, 8(6). https://doi.org/10.1371/JOURNAL.PONE.0067378

9. Mizutani, E., Ono, T., Li, C., Maki-Suetsugu, R., Wakayama, T. (2008). Propagation of senescent mice using nuclear transfer embryonic stem cell lines. Genesis (New York, N.Y. : 2000), 46(9), 478–483. https://doi.org/10.1002/DVG.20420
10. Chung, Y. G., Eum, J. H., Lee, J. E., Shim, S. H., Sepilian, V., Hong, S. W., et al. (2014). Human somatic cell nuclear transfer using adult cells. Cell stem cell, 14(6), 777–780. https://doi.org/10.1016/J.STEM.2014.03.015
11. Wilmut, I., Schnieke, A. E., McWhir, J., Kind, A. J., Campbell, K. H. S. (1997). Viable offspring derived from fetal and adult mammalian cells. Nature, 385(6619), 810–813. https://doi.org/10.1038/385810A0
12. Takahashi, K., & Yamanaka, S. (2006). Induction of pluripotent stem cells from mouse embryonic and adult fibroblast cultures by defined factors. Cell, 126(4), 663–676. https://doi.org/10.1016/j.cell.2006.07.024
13. Lapasset, L., Milhavet, O., Prieur, A., Besnard, E., Babled, A., Ät-Hamou, N., et al. (2011). Rejuvenating senescent and centenarian human cells by reprogramming through the pluripotent state. Genes & development, 25(21), 2248–2253. https://doi.org/10.1101/GAD.173922.111
14. Pennarossa, G., Ledda, S., Arcuri, S., Gandolfi, F., Brevini, T. A. L. (2020). A Two-Step Strategy that Combines Epigenetic Modification and Biomechanical Cues to Generate Mammalian Pluripotent Cells. Journal of visualized experiments : JoVE, (162). https://doi.org/10.3791/61655
15. Pennarossa, G., Maffei, S., Campagnol, M., Rahman, M. M., Brevini, T. A. L., Gandolfi, F. (2014). Reprogramming of Pig Dermal Fibroblast into Insulin Secreting Cells by a Brief Exposure to 5-aza-cytidine. Stem Cell Reviews and Reports, 10(1), 31-43. https://doi.org/10.1007/s12015-013-9477-9
16. Brevini, T. A. L., Pennarossa, G., Acocella, F., Brizzola, S., Zenobi, A., Gandolfi, F. (2016). Epigenetic conversion of adult dog skin fibroblasts into insulin-secreting cells. Veterinary Journal, 211(52), 6. https://doi.org/10.1016/j.tvjl.2016.02.014
17. Pennarossa, G., Manzoni, E. F. M., Ledda, S., DeEguileor, M., Gandolfi, F., Brevini, T. A. L. (2019). Use of a PTFE Micro-Bioreactor to Promote 3D Cell Rearrangement and Maintain High Plasticity in Epigenetically Erased Fibroblasts. Stem Cell Reviews and Reports, 15(1), 82–92. https://doi.org/10.1007/s12015-018-9862-5
18. Manzoni, E. F. M., Pennarossa, G., DeEguileor, M., Tettamanti, G., Gandolfi, F., Brevini, T. A. L. (2016). 5-azacytidine affects TET2 and histone transcription and reshapes morphology of human skin fibroblasts. Scientific Reports, 6, 37017. https://doi.org/10.1038/srep37017
19. Pennarossa, G., Santoro, R., Manzoni, E. F. M., Pesce, M., Gandolfi, F., Brevini, T. A. L. (2018). Epigenetic Erasing and Pancreatic Differentiation of Dermal Fibroblasts into Insulin-Producing Cells are Boosted by the Use of Low-Stiffness Substrate. Stem cell reviews and reports, 14(3), 398–411. https://doi.org/10.1007/s12015-017-9799-0
20. Pennarossa, G., Maffei, S., Campagnol, M., Tarantini, L., Gandolfi, F., & Brevini, T. A. L. (2013). Brief demethylation step allows the conversion of adult human skin fibroblasts into insulin-secreting cells. Proceedings of the National Academy of Sciences of the United States of America, 110(22), 8948–8953. https://doi.org/10.1073/pnas.1220637110
21. Brevini, T. A. L., Pennarossa, G., Rahman, M. M., Paffoni, A., Antonini, S., Ragni, G., et al. (2014). Morphological and Molecular Changes of Human Granulosa Cells Exposed to 5-Azacytidine and Addressed Toward Muscular Differentiation. Stem Cell Reviews and Reports, 10(5), 633-642. https://doi.org/10.1007/s12015-014-9521-4
22. Mirakhori, F., Zeynali, B., Kiani, S., Baharvand, H. (2015). Brief azacytidine step allows the conversion of suspension human fibroblasts into neural progenitor-like cells. Cell journal, 17(1), 153–158. https://doi.org/10.22074/cellj.2015.522
23. Chandrakanthan, V., Yeola, A., Kwan, J. C., Oliver, R. A., Qiao, Q., Kang, Y. C., et al. (2016). PDGF-AB and 5-Azacytidine induce conversion of somatic cells into tissue-regenerative multipotent stem cells. Proceedings of the National Academy of Sciences of the United States of America, 113(16), E2306-15. https://doi.org/10.1073/pnas.1518244113
24. Diomede, F., Zini, N., Pizzicannella, J., Merciaro, I., Pizzicannella, G., D'Orazio, M., et al. (2018). 5-Aza exposure improves reprogramming process through embryoid body formation in human gingival stem cells. Frontiers in Genetics, 9, 419. https://doi.org/10.3389/fgene.2018.00419
25. He, Y.-F., Li, B.-Z., Li, Z., Liu, P., Wang, Y., Tang, Q., et al. (2011). Tet-mediated formation of 5-carboxylcytosine and its excision by TDG in mammalian DNA. Science (New York, N.Y.), 333(6047), 1303–1307. https://doi.org/10.1126/science.1210944

26. Ito, S., Shen, L., Dai, Q., Wu, S. C., Collins, L. B., Swenberg, J. A., et al. (2011). Tet Proteins Can Convert 5-Methylcytosine to 5-Formylcytosine and 5-Carboxylcytosine. Science, 333(6047), 1300–1303. https://doi.org/10.1126/SCIENCE.1210597
27. Tahiliani, M., Koh, K. P., Shen, Y., Pastor, W. A., Bandukwala, H., Brudno, Y., et al. (2009). Conversion of 5-methylcytosine to 5-hydroxymethylcytosine in mammalian DNA by MLL partner TET1. Science, 324(5929), 930–935. https://doi.org/10.1126/science.1170116
28. Hu, X., Zhang, L., Mao, S. Q., Li, Z., Chen, J., Zhang, R. R., et al. (2014). Tet and TDG mediate DNA demethylation essential for mesenchymal-to-epithelial transition in somatic cell reprogramming. Cell Stem Cell, 14(4), 512–522. https://doi.org/10.1016/j.stem.2014.01.001
29. Balzano, F., Cruciani, S., Basoli, V., Santaniello, S., Facchin, F., Ventura, C., Maioli, M. (2018). MiR200 and miR302: Two Big Families Influencing Stem Cell Behavior. Molecules, 23(2), 282. https://doi.org/10.3390/MOLECULES23020282
30. Pennarossa, G., de Iorio, T., Gandolfi, F., Brevini, T. A. L. (2021). Ovarian Decellularized Bioscaffolds Provide an Optimal Microenvironment for Cell Growth and Differentiation In Vitro. Cells, 10(8), 2126. https://doi.org/10.3390/CELLS10082126
31. Pennarossa, G., Ghiringhelli, M., Gandolfi, F., Brevini, T. A. L. (2021). Creation of a bioengineered ovary: isolation of female germline stem cells for the repopulation of a decellularized ovarian bio-scaffold. Methods in molecular biology (Clifton, N.J.), 2273, 139–149. https://doi.org/10.1007/978-1-0716-1246-0_9
32. Pennarossa, G., Ghiringhelli, M., Gandolfi, F., Brevini, T. A. L. (2020). Whole-ovary decellularization generates an effective 3D bioscaffold for ovarian bioengineering. Journal of Assisted Reproduction and Genetics, 37(6), 1329-1339. https://doi.org/10.1007/s10815-020-01784-9
33. Brevini, T. A. L., Pennarossa, G., Maffei, S., Zenobi, A., Gandolfi, F. (2016). Epigenetic conversion as a safe and simple method to obtain insulinsecreting cells from adult skin fibroblasts. Journal of Visualized Experiments, 2016(109), 53880. https://doi.org/10.3791/53880
34. Pennarossa, G., Manzoni, E. F. M., Ledda, S., deEguileor, M., Gandolfi, F., Brevini, T. A. L. (2019). Use of a PTFE Micro-Bioreactor to Promote 3D Cell Rearrangement and Maintain High Plasticity in Epigenetically Erased Fibroblasts. Stem cell reviews and reports, 15(1), 82–92. https://doi.org/10.1007/S12015-018-9862-5
35. Sathananthan, H., Pera, M., Trounson, A. (2002). The fine structure of human embryonic stem cells. Reprod Biomed Online, 4(1), 56–61. doi: 10.1016/s1472-6483(10)61916-5.
36. Courtot, A. M., Magniez, A., Oudrhiri, N., Feraud, O., Bacci, J., Gobbo, E., et al. (2014). Morphological analysis of human induced pluripotent stem cells during induced differentiation and reverse programming. Biores Open Access, 3(5), 206–216. https://doi.org/10.1089/biores.2014.0028
37. Lai, D., Wang, Y., Sun, J., Chen, Y., Li, T., Wu, Y., et al. (2015). Derivation and characterization of human embryonic stem cells on human amnion epithelial cells. Sci Rep, 5, 10014. https://doi.org/10.1038/srep10014
38. Meshorer, E., Yellajoshula, D., George, E., Scambler, P. J., Brown, D. T., Misteli, T. (2006). Hyperdynamic plasticity of chromatin proteins in pluripotent embryonic stem cells. Dev Cell, 10(1), 105–116. https://doi.org/10.1016/j.devcel.2005.10.017
39. Brevini, T. A. L., Pennarossa, G., Maffei, S., Gandolfi, F. (2012). Pluripotency network in porcine embryos and derived cell lines. Reproduction in Domestic Animals, 47(SUPPL.4), 86-91. https://doi.org/10.1111/j.1439-0531.2012.02060.x
40. Niwa, H. (2007). How is pluripotency determined and maintained? Development, 134(4), 635–646. doi: 10.1242/dev.02787.
41. Meshorer, E., Misteli, T. (2006). Chromatin in pluripotent embryonic stem cells and differentiation. Nat Rev Mol Cell Biol, 7(7), 540–546. https://doi.org/10.1038/nrm1938
42. Efroni, S., Duttagupta, R., Cheng, J., Dehghani, H., Hoeppner, D. J., Dash, C., et al. (2008). Global transcription in pluripotent embryonic stem cells. Cell Stem Cell, 2(5), 437–447. https://doi.org/10.1016/j.stem.2008.03.021
43. Liang, G., Zhang, Y. (2013). Embryonic stem cell and induced pluripotent stem cell: an epigenetic perspective. Cell Res, 23(1), 49–69. https://doi.org/10.1038/cr.2012.175
44. Huang, H. N., Chen, S. Y., Hwang, S. M., Yu, C. C., Su, M. W., Mai, W., et al. (2014). miR-200c and GATA binding protein 4 regulate human embryonic stem cell renewal and differentiation. Stem Cell Research, 12(2), 338–353. https://doi.org/10.1016/J.SCR.2013.11.009

45. Kim, Y., Kim, N., Park, S. W., Kim, H., Park, H. J., Han, Y. M. (2017). Lineage-specific Expression of miR-200 Family in Human Embryonic Stem Cells during In Vitro Differentiation. International Journal of Stem Cells, 10(1), 28–37. https://doi.org/10.15283/IJSC17013
46. Manukyan, M., Singh, P. B. (2014). Epigenome rejuvenation: HP1β mobility as a measure of pluripotent and senescent chromatin ground states. Scientific Reports 2014 4:1, 4(1), 1–8. https://doi.org/10.1038/srep04789
47. Sarkar, T. J., Quarta, M., Mukherjee, S., Colville, A., Paine, P., Doan, L., et al. (2020). Transient non-integrative expression of nuclear reprogramming factors promotes multifaceted amelioration of aging in human cells. Nature Communications 2020 11:1, 11(1), 1–12. https://doi.org/10.1038/s41467-020-15174-3
48. Simpson, D. J., Olova, N. N., Chandra, T. (2021). Cellular reprogramming and epigenetic rejuvenation. Clinical Epigenetics 2021 13:1, 13(1), 1–10. https://doi.org/10.1186/S13148-021-01158-7
49. Anastasiadou, E., Ceccarelli, S., Messina, E., Gerini, G., Megiorni, F., Pontecorvi, P., et al. (2021). MiR-200c-3p maintains stemness and proliferative potential in adipose-derived stem cells by counteracting senescence mechanisms. PloS one, 16(9), e0257070. https://doi.org/10.1371/JOURNAL.PONE.0257070
50. Wang, G., Guo, X., Hong, W., Liu, Q., Wei, T., Lu, C., et al. (2013). Critical regulation of miR-200/ZEB2 pathway in Oct4/Sox2-induced mesenchymal-to-epithelial transition and induced pluripotent stem cell generation. Proceedings of the National Academy of Sciences of the United States of America, 110(8), 2858–2863. https://doi.org/10.1073/PNAS.1212769110/-/DCSUPPLEMENTAL

## 3.4. 3D ECM-Based Scaffolds Boost Young Cell Secretome-Derived EV Rejuvenating Effects in Senescent Cells

Published in International Journal of Molecular Science on 5th May 2022.

DOI: 10.3390/ijms24098285.

The fourth study is focused on influence of ECM age-related modifications on cell behaviour, taking the advantage of ECM-derived biomechanical cues to develop and support innovative rejuvenating strategies.

To this aim, young bio-matrixes ability to recreate an age-specific milieu was exploited to examine whether these ECM-based scaffolds can boost, and properly maintain, the rejuvenated phenotype acquired by senescent cells after exposure to young cell secretome. Moreover, based on previous observations indicating the miR-200 family's ability to regulate the molecular mechanisms driving cellular senescence erasure (Moimas et al., 2019), we compare young and aged cell secretome-derived EVs for their content in miR-200b and miR-200c.

The data reported confirm that an adequate young microenvironment may stabilize and support the rejuvenated phenotype acquired by aged cells in response to anti-aging factors and suggests the involvement of synergistic interactions among soluble effectors and ECM-derived stimuli (Pennarossa et al., 2022). Moreover, young secretome possesses significantly higher amounts of miR-200b and miR-200c compared to the aged ones, suggesting the intriguing possibility that miR-200 family may be one of the paracrine effectors involved in cellular rejuvenation.

*Article*

# 3D ECM-Based Scaffolds Boost Young Cell Secretome-Derived EV Rejuvenating Effects in Senescent Cells

**Sharon Arcuri [1,†], Georgia Pennarossa [1,*,†], Teresina De Iorio [1], Fulvio Gandolfi [2] and Tiziana A. L. Brevini [1,*]**

[1] Laboratory of Biomedical Embryology and Tissue Engineering, Department of Veterinary Medicine and Animal Sciences, Center for Stem Cell Research, Università degli Studi di Milano, Via Trentacoste 2, 20134 Milan, Italy; sharon.arcuri@unimi.it (S.A.); teresina.deiorio@unimi.it (T.D.I.)

[2] Department of Agricultural and Environmental Sciences-Production, Landscape, Agroenergy, Università degli Studi di Milano, Via Celoria 2, 20133 Milan, Italy; fulvio.gandolfi@unimi.it (F.G.)

* Correspondence: georgia.pennarossa@unimi.it (G.P.); tiziana.brevini@unimi.it (T.A.L.B.); Tel.: +39-02-503-15754 (G.P.); +39-02-503-15756 (T.A.L.B.)

† These authors contributed equally to this work.

**Abstract:** Aging is a complex, multifaceted degenerative process characterized by a progressive accumulation of macroscopic and microscopic modifications that cause a gradual decline of physiological functions. During the last few years, strategies to ease and counteract senescence or even rejuvenate cells and tissues were proposed. Here we investigate whether young cell secretome-derived extracellular vesicles (EVs) ameliorate the cellular and physiological hallmarks of aging in senescent cells. In addition, based on the assumption that extracellular matrix (ECM) provides biomechanical stimuli, directly influencing cell behavior, we examine whether ECM-based bio-scaffolds, obtained from decellularized ovaries of young swine, stably maintain the rejuvenated phenotype acquired by cells after exposure to young cell secretome. The results obtained demonstrate that young cells release EVs endowed with the ability to counteract aging. In addition, comparison between young and aged cell secretomes shows a significantly higher miR-200 content in EVs produced using fibroblasts isolated from young donors. The effect exerted by young cell secretome-derived EVs is transient, but can be stabilized using a young ECM microenvironment. This finding indicates a synergistic interaction occurring among molecular effectors and ECM-derived stimuli that cooperate to control a unique program, driving the cell clock. The model described in this paper may represent a useful tool to finely dissect the complex regulations and multiple biochemical and biomechanical cues driving cellular biological age.

**Keywords:** aging; cellular rejuvenation; ECM-based bio-scaffolds; EVs; cell senescence; young; secretome

## 1. Introduction

Human life expectancy is increasing worldwide at a rapid rate thanks to improvements in medical care, healthier lifestyles, and a significant reduction in child mortality [1]. Although this reflects a positive development, it also poses new challenges that will aggravate in the coming years. Indeed, the increase in lifespans of the last decades was not paralleled with enhancements in life quality for the elderly, and the risk of chronic age-onset diseases, often with multiple co-morbidities, is steadily on the rise, thus becoming one of the most critical emerging issues in public health [2].

To overcome these problems, several recent studies focused on in-depth characterization of aging, leading to the identification of different molecular and biomechanical mechanisms that drive and/or influence senescence progression [3–10]. Based on this new knowledge, strategies to ease, stop, or counteract the accumulation of macroscopic and microscopic modifications that are distinctive of age progression and negatively affect organ, tissue, cell, and subcellular organelle homeostasis and functions are proposed [8]. Some of these methods are based on nutrient-related

pathway alterations, either through dietary restrictions [11]; pharmacological interventions employing chemical drugs, such as rapamycin, metformin, or resveratrol [12]; or the use of individual "rejuvenating" factors, such as Growth Differentiation Factor 11 (GDF11), Tissue Inhibitor of Metalloproteinases 2 (TIMP2), and Mesencephalic Astrocyte Derived Neurotrophic Factor (MANF) [12,13]. Other approaches involve the induction of a stable [14] or transient [3] pluripotent state for ameliorating cellular and physiological aging hallmarks in senescent or centenarian cells. Parallel reports also describe the possibility of reverting aging-related features in old stem cells through culturing them with young stem cell-derived conditioned medium, also referred as "secretome" [11,15–17]. This method is composed of a complex set of soluble bio-active molecules released by cells, including serum proteins, angiogenic and growth factors, hormones, cytokines, extracellular matrix proteins, and EVs [18]. EVs are lipid bound structures that contain proteins, lipids, nucleic acids, and metabolites [19,20]. They are known to facilitate intercellular communications and play a key role in a variety of physiological and pathological processes, including immuno-regulation, cell differentiation and metabolism, and cancer and autoimmune diseases [19,20].

In the present study, we investigate whether young cell secretome-derived EVs ameliorate cellular and physiological hallmarks of aging in senescent cells. Taking advantage of acellular scaffold low immunogenicity, we use decellularized bio-scaffolds obtained from young pigs to examine whether extracellular matrix (ECM)-based supports can boost and properly maintain the rejuvenated phenotype acquired by senescent cells after exposure to young cell secretome-derived EVs. In addition, based on previous observations indicating the miR-200 family's ability to regulate the molecular mechanisms driving cellular senescence erasure [3,21], we compare young and aged cell secretome-derived EVs for their content in miR-200b and miR-200c.

## 2. Results

### *2.1. Young Cell Secretome-Derived EVs Transiently Erase Signs of Senescence in Fibroblasts Isolated from Aged Individuals Cultured in 2D Systems*

After 48-hour exposure to young cell conditioned media (Post treatment yCM), fibroblasts isolated from aged patients showed phenotype changes. The elongated morphology, visible in untreated cells (Aged, Figure 1A), was replaced with a rounder and more oval shape, with cells becoming smaller in size (yCM, Figure 1A). Comparable phenotype modifications were observed when aged cells were treated with yCM-derived EVs resuspended in Eagle's Minimum Essential Medium (MEM) (Post treatment MEM + yCM-derived EVs Figure 1A). In contrast, fibroblasts maintained the original phenotype when incubated with EV-depleted yCM (Post EV-yCM, Figure 1A) or aged cell conditioned media (Post aCM, Figure 1A).

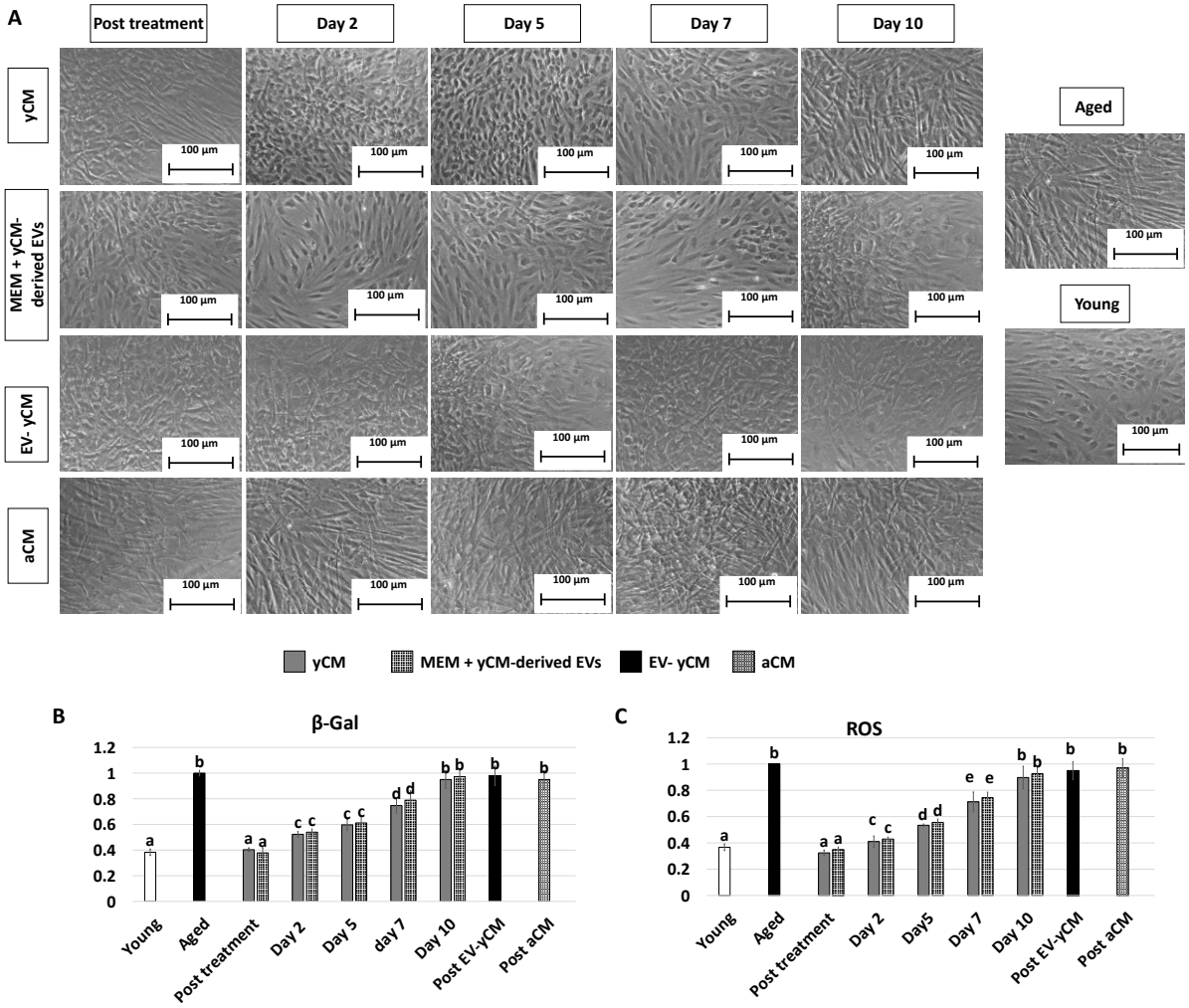


**Figure 1.** Morphology, β-GAL, and ROS activity quantifications in treated aged fibroblasts cultured onto 2D systems. (**A**) Representative images of untreated fibroblasts isolated from aged (Aged) and young donors (Young); and aged fibroblasts at the end of 48-hour exposure (post-treatment) to yCM, MEM + yCM-derived EV, and EV-depleted yCM (EV-yCM) and aCM at days 2, 5, 7, and 10 of culture. Scale bars: 100 µm. (**B**) β-GAL activity and (**C**) ROS levels in untreated fibroblasts isolated from young (Young) and aged donors (Aged); aged fibroblasts at the end of yCM and MEM + yCM-derived EV treatments (post-treatment) at days 2, 5, 7, and 10 of culture; and aged fibroblasts exposed to EV-depleted yCM (EV-yCM) and aCM for 48 h. Data are expressed as the mean. Error bars represent the standard error of the mean (SEM). Different lowercase letters indicate $p < 0.05$.

The morphological changes visible after exposure to yCM and MEM + yCM-derived EVs were accompanied with a significant decrease in β-galactosidase (β-GAL) activity (post-treatment yCM and MEM + yCM-derived EVs, Figure 1B), as well as significantly lower levels of reactive oxygen species (ROS) (post-treatment yCM and MEM + yCM-derived EVs, Figure 1C), with values comparable to those detected in young cells (Young, Figure 1B,C). In contrast, EV-yCM and aCM treatments did not induce β-GAL and ROS level changes, and their values remained statistically comparable to those of untreated aged fibroblasts (Aged, Figure 1B,C).

Gene expression analyses were consistent with the morphological observations and demonstrated a significant decrease in the transcription levels of senescence-related markers (P53, P16 and P21) and the reactive oxygen species modulator ROMO1 after 48 h of treatment with both yCM (Post treatment yCM) and MEM + yCM-derived EVs (post-treatment MEM + yCM-derived EVs, Figure 2), showing values comparable to those distinctive of cells isolated from young donors (Young). In addition, expression levels of the cell proliferation marker MKI67, as well as the mitochondrial activity-related genes TFAM, PDHA1, and COX4l1, peaked at values comparable to those of fibroblasts derived from young individuals (Young, Figure 2).

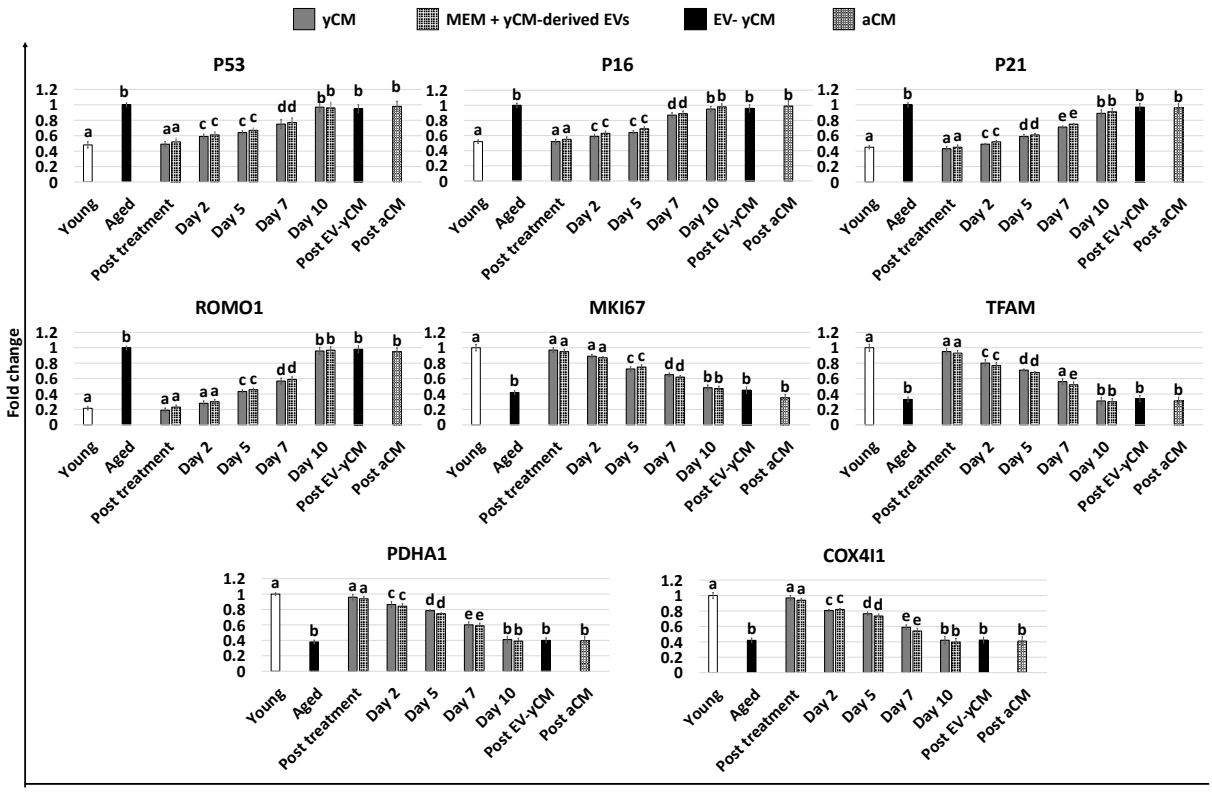


**Figure 2.** Gene expression levels of senescence-related markers (P53, P16, P21), reactive oxygen species modulator (ROMO1), cell proliferation (MKI67), and mitochondrial activity (TFAM, PDHA1, COX4I1) genes in untreated fibroblasts isolated from young (Young) and aged (Aged) individuals, at the end of yCM and MEM + yCM-derived EV exposures (Post treatment), at days 2, 5, 7, and 10 of culture, and in aged cells exposed to EV-depleted yCM (EV-yCM) and aCM for 48 h. Data are expressed as the mean. Error bars represent the standard error of the mean (SEM). Different lowercase letters indicate $p < 0.05$.

PCNA immunocytochemical analysis and its quantitative evaluation demonstrated a significantly higher PCNA positive cell rate after yCM (post-treatment yCM, Figure 3A, B) and MEM + yCM-derived EVs (post-treatment MEM + yCM-derived EVs, Figure 3A,B) exposure, while no differences were detected among untreated aged fibroblasts (Aged, Figure 3A,B) and cells incubated with EV-yCM (post-EV-yCM, Figure 3A,B) or aCM (Post aCM, Figure 3A,B).

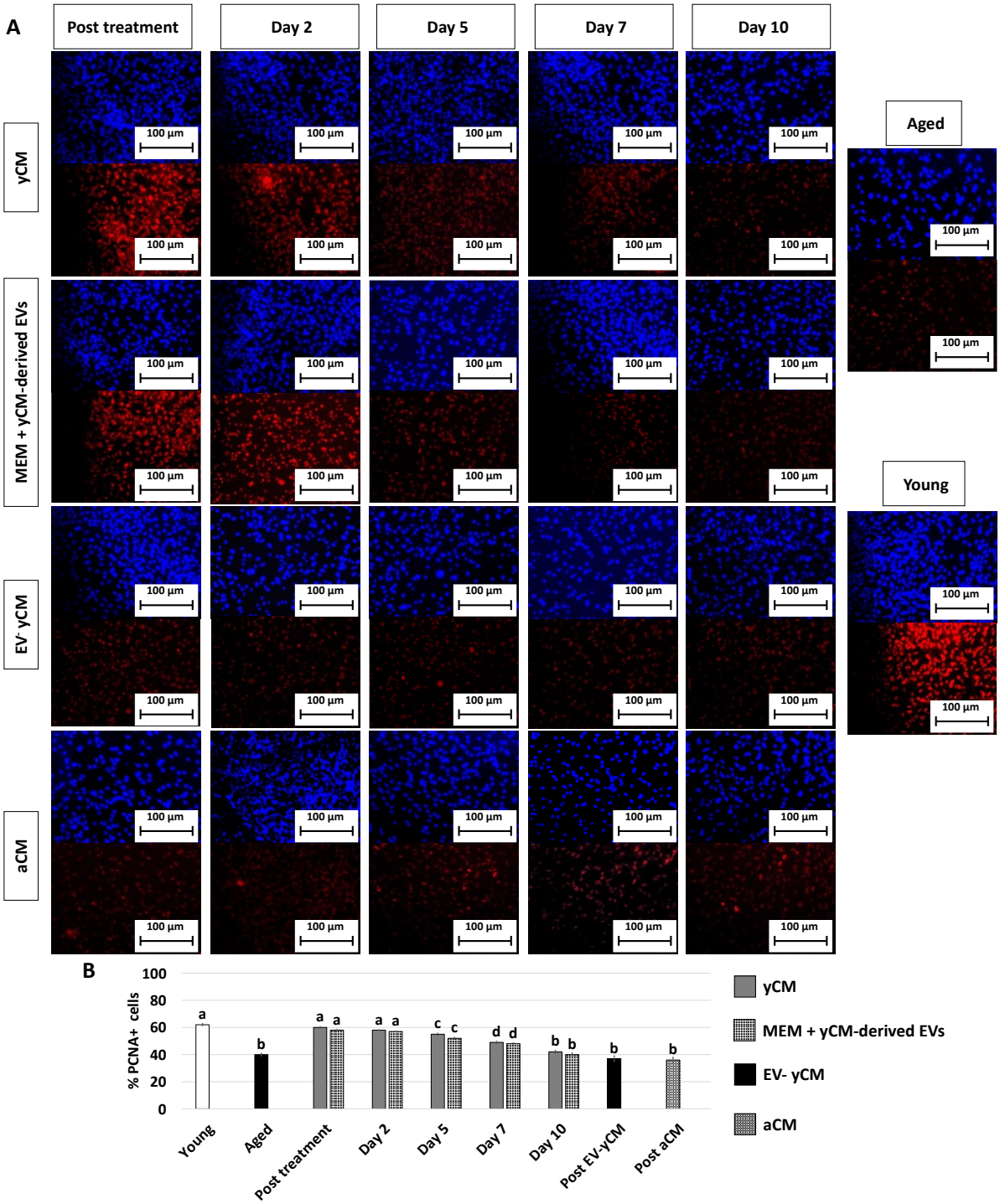


**Figure 3.** PCNA immunocytochemical staining and quantitative evaluation. (**A**) Representative images of DAPI (upper panels) and PCNA (lower panels) immunostaining in untreated fibroblasts isolated from aged (Aged) and young donors (Young), and of aged fibroblasts at the end of 48-hour exposure period (post-treatment) to yCM, MEM + yCM-derived EV, EV-depleted yCM (EV-yCM), and aCM at days 2, 5, 7 and 10 of culture. Scale bars: 100 µm. (**B**) PCNA quantitative evaluation in untreated fibroblasts isolated from young (Young) and aged individuals (Aged), at the end of yCM and MEM + yCM-derived EV exposures (post-treatment), at days 2, 5, 7, and 10 of culture, and in aged cells exposed to EV-depleted yCM (EV-yCM) and aCM for 48 h. Data are expressed as the mean. Error bars represent the standard error of the mean (SEM). Different lowercase letters indicate $p < 0.05$.

However, when yCM and MEM + yCM-derived EV treated cells were returned to fibroblast standard culture medium, they progressively reverted to their original phenotype (Day 2, day 5

and day 7; Figure 1A); by day 10, they exhibited small central nuclei and an elongated spindle shape, comparable to characteristics of untreated aged fibroblasts (Aged, Figure 1A). Consistently, β-GAL activity (Figure 1B) and ROS levels (Figure 1C) gradually incremented during the culture period up to day 10, when the values detected were statistically comparable to those observed in untreated aged cells (Aged). These changes were paralleled by P53, P16, P21, and ROMO1 gene transcription levels that gradually increased and returned results statistically comparable to those of untreated aged cells (Aged) by day 10 of culture (Figure 2). Similarly, by day 10, MKI67, TFAM, PDHA1, and COX4I1 genes decreased to expression levels comparable to those detected in aged fibroblasts (Aged, Figure 2). Immunostaining confirmed these data, with PCNA+ cell rates slowly decreasing and returning results statistically comparable to those of aged cells by day 10 of culture (Figure 3A,B).

### *2.2. Young Cell-Derived EV Rejuvenating Effects Are Boosted and Steadly Maintened in Cells Grown onto Young 3D ECM-Based Bio-Scaffolds*

Hematoxylin and eosin (H and E) and DAPI staining (Figure 4A) showed comparable engrafting ability in both yCM and EV-yCM treated cells, demonstrating that EV exposure does not affect cell repopulating ability. However, although cell density analyses indicated an increasing number of cells along the culture period in all the experimental groups, significant differences were visible (Figure 4B). Moreover, from day 2 onward, cell density was significantly higher in yCM cultured onto young decellularized bio-scaffolds (yCM + Young scaffold, Figure 4B) compared to EV-yCM engrafted onto young decellularized bio-scaffolds (EV-yCM + Young scaffold, Figure 3B) and yCM cultured onto aged decellularized bio-scaffolds (yCM + Aged scaffold, Figure 3B). These histological observations were also confirmed through DNA quantification studies, indicating comparable cell growth trends (Figure 4C).

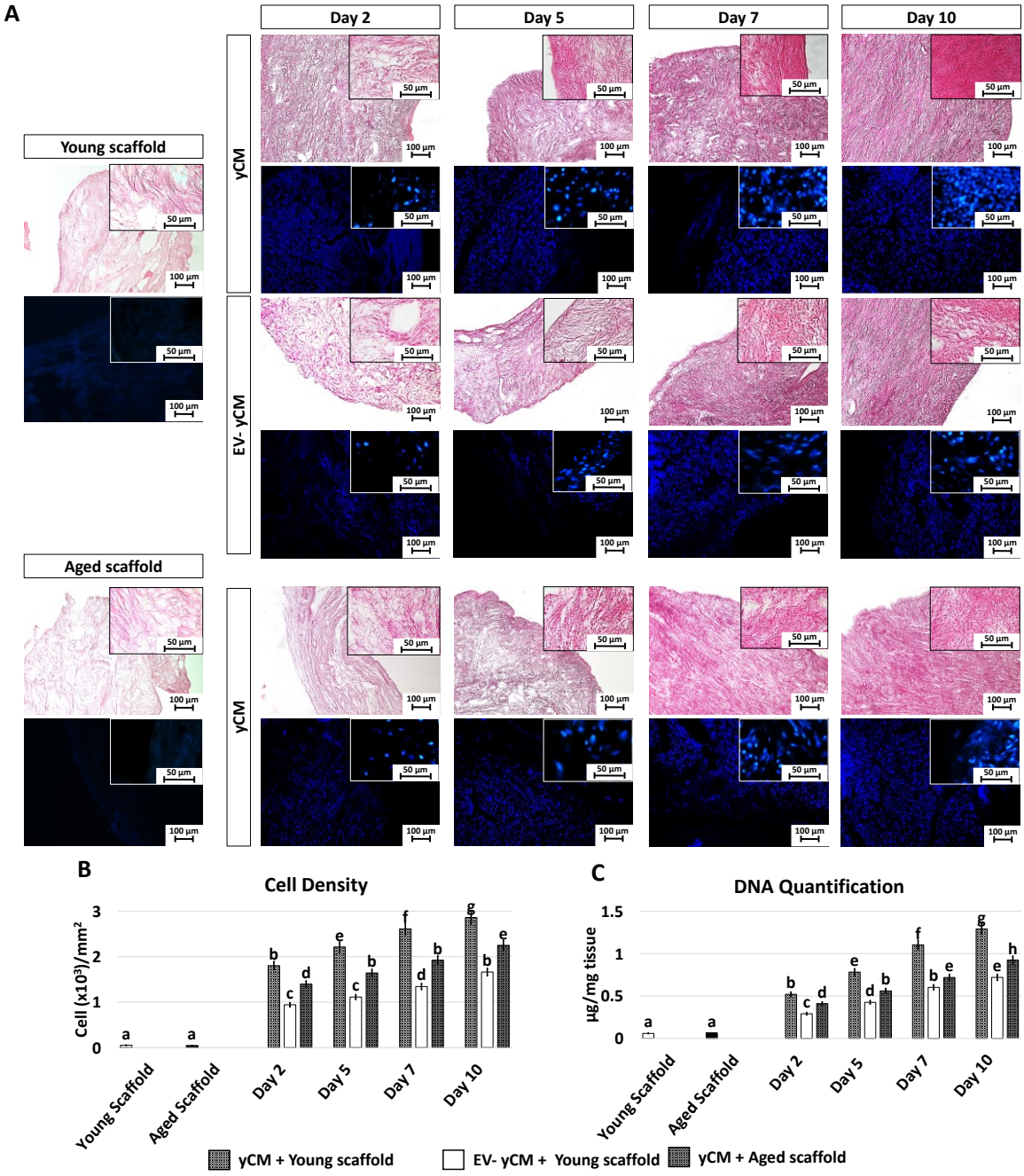


**Figure 4.** H and E, DAPI staining, cell density, and DNA quantification in treated aged fibroblasts cultured onto young and aged 3D ECM-based bio-scaffolds. (**A**) H and E (upper panels) and DAPI (lower panels) staining of young (Young scaffold) and aged ECM-based bio-scaffolds (Aged scaffold), aged fibroblasts exposed to yCM and EV-depleted yCM (EV-yCM) cultured onto young scaffold, and aged fibroblasts exposed to yCM and engrafted onto aged scaffolds at days 2, 5, 7, and 10 of culture. Scale bars: 100 µm. Insert scale bars: 50 µm. (**B**) Cell density analyses in young and aged scaffolds before cell seeding, aged fibroblasts exposed to yCM and EV-yCM cultured onto young scaffolds (yCM + Young scaffold, EV-yCM + Young scaffold), and aged fibroblasts exposed to yCM and engrafted onto aged scaffolds (yCM + Aged scaffold) at days 2, 5, 7, and 10 of culture. Data are expressed as the mean. Error bars represent the standard error of the mean (SEM). Different lowercase letters indicate $p < 0.05$. (**C**) DNA quantification in young and aged scaffolds before cell seeding, aged fibroblasts exposed to yCM and EV-yCM cultured onto young scaffolds (yCM + Young scaffold, EV-yCM + Young scaffold), and aged fibroblasts exposed to yCM and engrafted onto aged scaffolds (yCM + Aged scaffold) at days 2, 5, 7, and 10 of culture. Data are expressed as the mean. Error bars represent the standard error of the mean (SEM). Different lowercase letters indicate $p < 0.05$.

Gene expression studies indicated that the significant reductions in the transcription levels of P53, P16, P21, and ROMO1 genes detected after 48-hour exposure to yCM (Post treatment yCM, Figure 5) were steadily maintained with values statistically comparable to those distinctive of young cells (Young, Figure 5), albeit only when treated cells were engrafted onto young scaffolds (yCM + Young scaffold, Figure 5). Similarly, the increased expression values of MKI67, TFAM, PDHA1, and COX4I1 genes visible after yCM incubation (Post treatment yCM, Figure 5) remained statistically, albeit only comparable to those of young cells in the yCM + Young scaffold group (Figure 5).

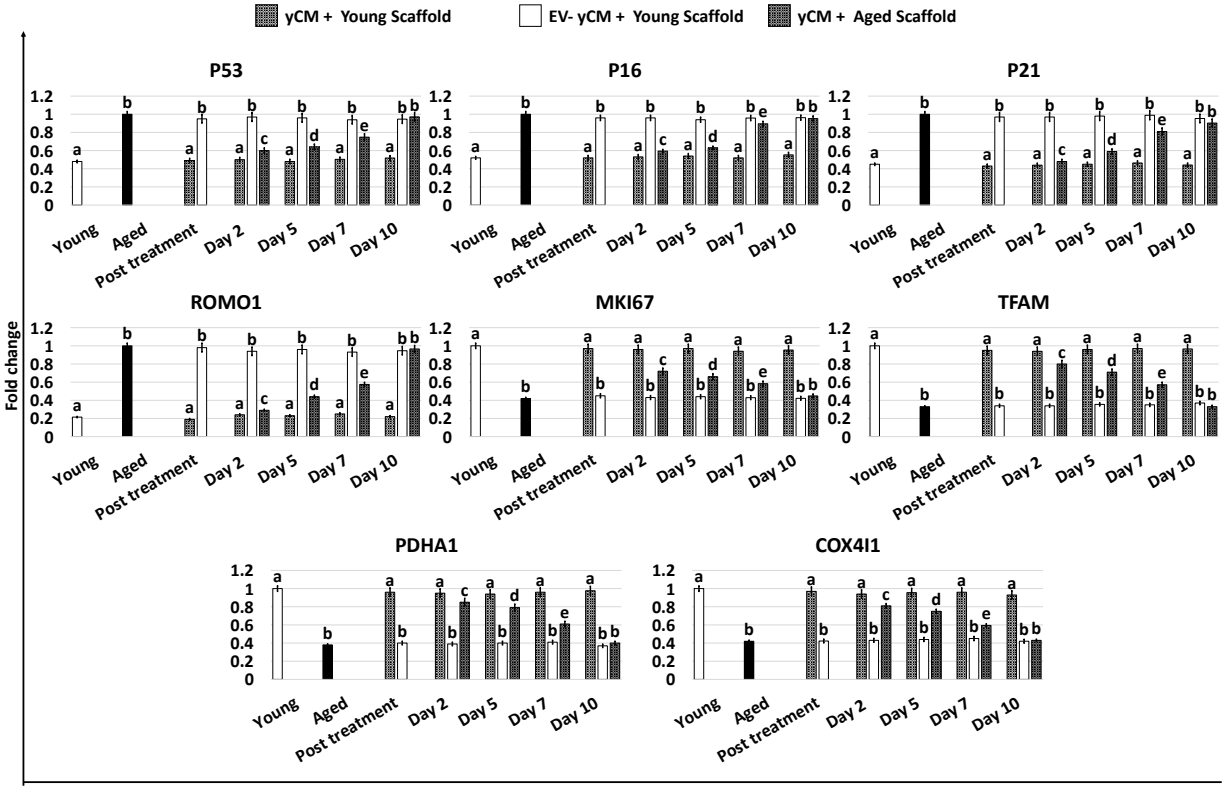


**Figure 5.** Gene expression levels of senescence-related markers (P53, P16, P21), reactive oxygen species modulator (ROMO1), cell proliferation (MKI67), and mitochondrial activity (TFAM, PDHA1, COX4I1) genes in untreated fibroblasts isolated from young (Young, white) and aged individuals (Aged, black) at the end of yCM and EV-depleted yCM (EV-yCM) treatments (post-treatment), and in yCM + Young scaffold, EV-yCM + Young scaffold, and yCM + Aged scaffold at days 2, 5, 7, and 10 of culture. Data are expressed as the mean. Error bars represent the standard error of the mean (SEM). Different lowercase letters indicate $p < 0.05$.

In agreement with this, the decreased β-GAL activity and ROS levels, which were visible after 48-hour incubation with yCM (Post treatment yCM, Figure 6A,B), remained statistically comparable to those distinctive of young cells (Young), albeit only when treated cells were cultured onto young scaffolds (yCM + Young scaffold, Figure 6A,B). In addition, PCNA staining revealed immunopositivity in all experimental groups (Figure 6C). However, a significantly higher number of PCNA+ cells was scored in young scaffolds repopulated with yCM-treated cells (yCM + Young scaffold, Figure 6D) compared to the other groups (Figure 6D).

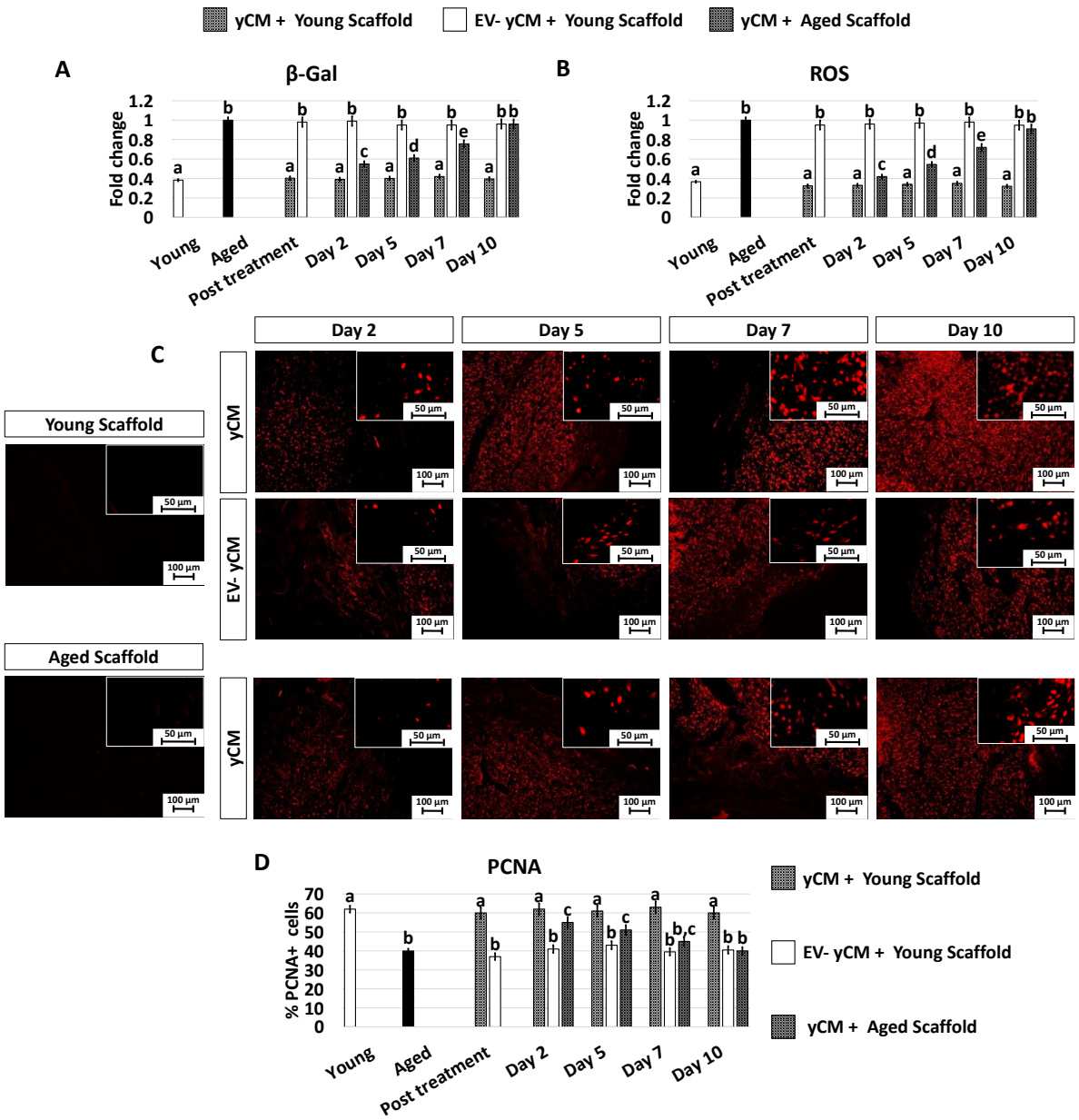


**Figure 6.** β-GAL and ROS activity quantifications, PCNA immunocytochemical staining, and quantitative evaluation in treated aged fibroblasts cultured onto young and aged 3D ECM-based bio-scaffolds. (**A**) β-GAL activity and (**B**) ROS levels in untreated fibroblasts isolated from young (Young) and aged individuals (Aged), aged fibroblasts exposed to exposed to yCM and EV-depleted yCM (EV-yCM) cultured onto young scaffolds (yCM + Young scaffold, EV-yCM + Young scaffold), and aged fibroblasts exposed to yCM and engrafted onto aged scaffolds (yCM + Aged scaffold) at days 2, 5, 7, and 10 of culture. Data are expressed as the mean. Error bars represent the standard error of the mean (SEM). Different lowercase letters indicate $p < 0.05$. (**C**) Representative images of PCNA immunocytochemical staining of young (Young scaffold) and aged ECM-based bio-scaffolds (Aged scaffold) before seeding, aged fibroblasts exposed to yCM and EV-depleted yCM (EV-yCM) cultured onto young scaffolds (yCM + Young scaffold, EV-yCM + Young scaffold), and aged fibroblasts exposed to yCM and engrafted onto aged scaffolds (yCM + Aged scaffold) at days 2, 5, 7, and 10 of culture. Scale bars: 100 µm. Insert scale bars: 50 µm. (**D**) PCNA quantitative evaluation in untreated fibroblasts isolated from young (Young) and aged individuals (Aged), aged fibroblasts exposed to exposed to yCM and EV-depleted yCM (EV-yCM) cultured onto young scaffolds (yCM + Young scaffold, EV-yCM + Young scaffold), and aged fibroblasts exposed to yCM and engrafted onto aged scaffolds (yCM + Aged scaffold) at days 2, 5, 7, and 10 of culture. Data are expressed as the mean. Error bars represent the standard error of the mean (SEM). Different lowercase letters indicate $p < 0.05$.

*2.3. Young and Aged Cell Secretome-Derived EVs*

TEM studies demonstrated the presence of polydisperse spherical structures ranging from 30 to 250 nm in size (Figure 7A) and displaying the distinctive EV cup morphology, surrounded by a lipid bilayer with variable electron density cargo content. Consistent with this result, WB analysis indicated that both yCM- and aCM-derived EVs contained the tetraspanin markers CD9, CD63, and CD81 at similar levels, when equal amounts of EV proteins were loaded (Figure 7B). However, EV quantification studies revealed that aCM contained a significantly higher amount of EVs than yCM (Figure 7C). Nevertheless, an opposite trend was observed when assessing miRNA concentrations in yCM- and aCM-derived EVs, with significantly higher amounts of miR-200b and miR-200c in yCM-derived EVs (Figure 7D).

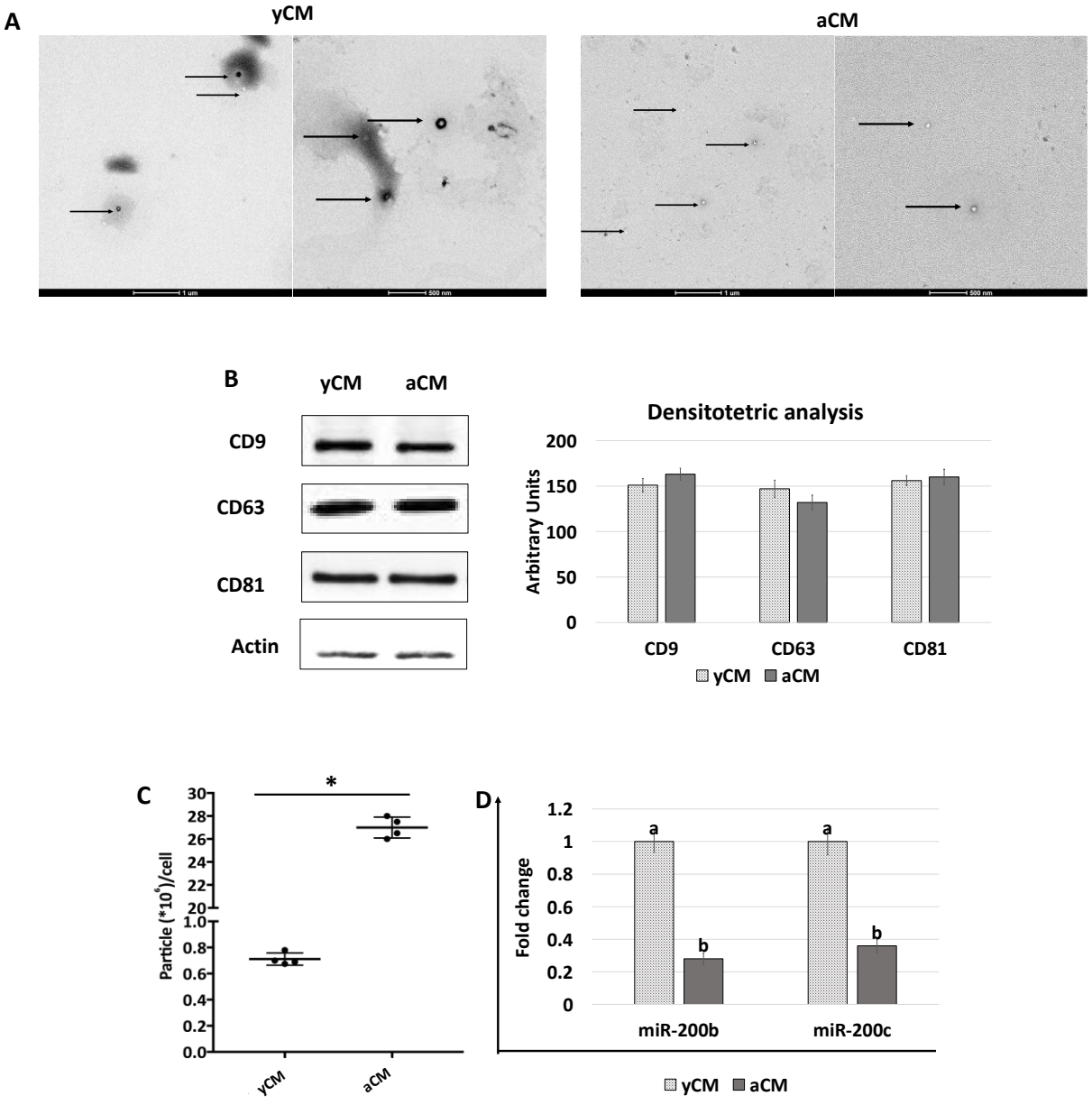


**Figure 7.** TEM, western blot, quantification, and miR200b and miR200c expression studies in yCM and aCM. (**A**) Representative images of TEM analysis of yCM- and aCM-derived EVs. Black arrows indicate spherical structures displaying the distinctive EV cup morphology, surrounded by a lipid bilayer with variable electron density cargo content. Scale bars 1 μm and 500 nm. (**B**) Western blot and densitometric analyses (arbitrary units) of EV proteins for the tetraspanin markers CD9, CD63, CD81, and beta Actin in yCM and

aCM. (**C**) Quantification of EV particles detected in yCM and CM. Data are expressed as the mean. Error bars represent the standard error of the mean (SEM). Asterisks indicate $p < 0.05$. (**D**) Expression levels of miR-200b and miR-200c in yCM- and aCM-derived EVs. Data are expressed as the mean. Error bars represent the standard error of the mean (SEM). Different lowercase letters indicate $p < 0.05$.

## 3. Discussion

In the present study, we demonstrate that young cells release EVs endowed with the ability to counteract aging. Interestingly, this effect is transient; however, it can be stabilized using the contribution derived from young ECM microenvironment. We also show that young cell secretome-derived EVs contain a significantly higher miR-200 amount, compared to those EVs isolated from aged donors.

After yCM exposure, fibroblasts obtained from aged individuals acquire morphological and molecular features distinctive of cells derived from young donors. Moreover, at the end of 48-hour treatment with yCM or MEM + yCM-derived EVs, the fibroblast elongated shape is replaced by a more compact and rounded phenotype, with cells becoming smaller in size. In contrast, when cells are exposed to EV-yCM or aCM, no changes are detected, and cell morphology remains comparable to that of untreated cells. These results clearly indicate that EVs released by young fibroblasts directly influenced cellular remodeling. Morphological observations are also supported through functional and molecular analyses, which demonstrate a significant reduction in the main age-related hallmarks in cells treated with yCM and MEM + yCM-derived EV. In particular, exposure of aged cells to young cell secretome-derived EVs induces a significant decrement in β-GAL and ROS activities, with values comparable to those detected in young cells. This result is paralleled through a statistically significant downregulation of P53, P21, P16, and ROMO1 gene trascription, and increased expression levels for the mitochondrial- (TFAM, PDHA1, and COX4I1) and proliferation-related (MKI67) genes. In contrast, EV-yCM and aCM treatments neither induce β-GAL and ROS level changes nor transcriptional activity modifications, with all values remaining statistically comparable to those of untreated aged fibroblasts. This result agrees with recent studies demonstrating young cell derived- EV ability to mediate senescence rejuvenation [11,22–24]. In particular, the authors report the possibility of reducing signs of aging in a variety of tissues in old mice [23], as well as improving wheel-running activity and extending lifespans in aged mice exposed to EVs isolated from young individuals [22]. In addition, Fafián-Labora et al. also showed that EVs isolated from primary fibroblasts of young donors ameliorate certain senescence-related biomarkers in cells derived from old and Hutchinson–Gilford progeria syndrome donors [23].

The age reversion observed in the present study is also confirmed via PCNA immunocytochemical analysis and its quantitative evaluation, which demonstrate a significantly higher PCNA+ cell rate after yCM and MEM + yCM-derived EV exposure, and no differences detected in aged cells incubated with EV-yCM or aCM. These data suggest the ability of EVs derived from young cells to re-activate cell-cycle and re-establish a robust cell division rate in senescent cells. Consistent with this result, recent pilot works described the possibility of achieving a young phenotype after restoration of a vigorous cell growth in non-dividing quiescent and senescent cells [4,5], pointing to a scenario where proliferation was an essential requirement for cellular rejuvenation [6]. Altogether, these data indicate the key role played by young cell secretome-derived EVs in reducing signs of cellular senescence and encouraging the acquisition of a young phenotype. It is, however, important to note that, when yCM or MEM + yCM-derived EVs are removed from cultures and cells are returned to fibroblast standard culture medium, a gradual reversion to the original phenotype is detected, with cells restoring all the morphological and molecular features distinctive of aged cells by day 10 of culture. Specifically, cells revert to a larger size and have an elongated shape, increased β-GAL and ROS activities, and MKI67, TFAM, PDHA1, COX4I1, ROMO1, P53, P16, and P21 transcription levels statistically comparable to those of untreated aged cells.

While the rejuvenating effect exerted through young cell secretome-derived EVs appears to be transient and reversible, it is important to note that, in combination with the use of young 3D ECM-based bio-scaffolds, it results in a stable acquisition of a young phenotype. Indeed, even

after the removal of young cell secretome-derived EVs, cells cultured in fibroblast standard culture medium continue to colonize the bio-scaffolds, and stably maintain all the distinctive features of young cells. They display low β-GAL and ROS values, a high number of PCNA+ cells, high transcription levels for cell proliferation- (MKI67) and mitochondrial activity-related genes (TFAM, PDHA1, and COX4I1), and low expression of P53, P16, P21, and ROMO1. These results confirm that an adequate young microenvironment may stabilize and support the rejuvenated phenotype acquired by aged cells in response to anti-aging factors, and suggests the involvement of synergistic interactions among soluble effectors and ECM-derived stimuli [3].

To aid our understanding, a key means of further elucidating the contribution of soluble effectors was to analyze and compare the EVs isolated from young and aged cell secretomes. TEM studies demonstrated the presence of polydisperse spherical structures with distinctive EV size and morphology in both yCM and aCM. Similarly, WB analysis indicated that the tetraspanin markers CD9, CD63, and CD81 were contained at similar levels in both the experimental groups, when equal amounts of EV proteins were loaded. This result suggests that both young and senescent cells release EVs in the culture medium. However, EV quantification studies reveal that aCM contains a significantly higher amount of EVs than yCM. Although further experiments are needed, this result is consistent with recent studies demonstrating an increase in EV secretion and a modification in their bioactive content connected with cellular aging, thus resulting in a pattern that constitutes the senescence-associated secretory phenotype (SASP) [11,25–31]. On the other hand, it is important to note that several reports have highlighted variations in EV-containing molecules in relation to cellular age [25–27]. Based on this factor and recent evidence obtained in our laboratory demonstrating the miR-200 family's ability to transiently rejuvenate senescent cells [3], we investigated miR-200 contents in young and aged cell secretome-derived EVs. The results obtained demonstrate that yCM-derived EVs have significantly higher amounts of miR-200b and miR-200c compared to aCM-derived EVs, suggesting the intriguing possibility that miR-200 family may be one of the paracrine effectors involved in cellular rejuvenation. In agreement with this hypothesis, the miR-200 family's ability to restore normal functions in different senescent cell types was previously demonstrated [3,21]. A clear example can be found in idiopathic pulmonary fibrosis, which causes downregulation of miR-200 members in alveolar epithelial cells, leading to the acquisition of a senescent phenotype [32,33]. It is, however, interesting to note that miR-200b and miR-200c transfection restores cell trans-differentiation ability, and induces a significant reduction in aging hallmarks in senescence alveolar cells [21]. Similarly, the use of miR-200b and miR-200c was shown to directly regulate the molecular mechanisms erasing cell senescence in fibroblasts isolated from old individuals [3]. Although further studies are needed to better elucidate these aspects, based on these observations, we may speculate that young cells release EVs containing high amount of miR-200s, which are required to support normal physiological cell functions, and that this ability decreases in aged and pathological cells.

In conclusion, the data reported in this study demonstrate that multiple factors cooperate to modulate the cell clock. In particular, the paracrine effectors released by young cells appear to play a fundamental role in erasing cellular senescence. However, the combination of their action with young ECM-derived stimuli boost and stabilize the anti-aging effect observed in the experimental model used, which may represent a useful tool to finely dissect the complex regulations driving cellular biological age.

## 4. Materials and Methods

All reagents were purchased from Thermo Fisher Scientific (Milan, Italy), unless otherwise indicated.

### *4.1. Ethical Statement*

Human primary skin fibroblast cell lines (GM02674, GM00495, GM08402, GM01706, GM00731, and AG09602) were obtained from the NIGMS Human Genetic Cell Repository, based at the Coriell Institute for Medical Research (New Jersey, USA). Porcine ovaries were collected

from an authorized local slaughterhouse. This study did not involve the use living humans and animals; therefore, ethical approval was not required. All the methods were carried out following the approved guidelines.

*4.2. Culture of Human Skin Fibroblasts*

Fibroblasts isolated from 29–32 years old individuals (young, $n = 3$) and from 82–96 year-old donors (aged, $n = 3$) were cultured in fibroblast standard culture medium (FCM) consisting of Eagle's Minimum Essential Medium (MEM), 15% Fetal Bovine Serum (FBS, not heat-inactivated), 2mM glutamine (Sigma-Aldrich, Milan, Italy), and 1% antibiotic/antimycotic solution (Sigma-Aldrich, Milan, Italy). Cells were maintained in 5% $CO_2$ at 37 °C and passaged twice per week at ratios of 1:3 (young) and 1:2 (aged). All experiments were performed using all 6 human fibroblast cell lines at least for three times in triplicates.

*4.3. Production of Young and Aged Cell Secretomes*

Fibroblasts isolated from young and aged individuals were seeded into Nunc™ 4-well multi-dishes (Nunc) at density of $1 \times 10^5$ cells/cm$^2$, and cultured in fibroblast standard culture medium for 24 h. On day 2, cells were extensively washed with PBS, and incubated with 0.25 mL/well of FCM without FBS in 5% $CO_2$ at 37 °C. After 48 h of culture, young (yCM) and aged secretomes/conditioned media (aCM) were collected, centrifuged twice at 1000× *g* for 10 min, filtered through 0.2 μm filters (Sarstedt, Milan, Italy), and stored at −80 °C until use.

*4.4. EV Isolation/Depletion*

EVs were purified from yCM and aCM using the qEVs 35 nm Size Exclusion Chromatography (SEC) columns (iZon, Christchurch, New Zealand), following the manufacturer's instructions. Briefly, columns were left at room temperature for 30 min, washed with 2 volumes (13.5 mL each) of filtered PBS, equilibrated with 3 volumes (13.5 mL each) of filtered MEM, and injected with 1 mL of CM. EVs were collected and used for culture experiments (See below paragraph 4.5.), or subjected to quantification analysis, transmission electron microscopy (TEM), Western Blot, and miR-200b and miR200c expression studies. EV-depleted yCM (EV-yCM) were also collected and used for the experiments described in paragraphs 4.5 and 4.7.

*4.5. Aged Fibroblast Exposure to Cell Secretomes Using 2D Systems*

Fibroblasts were seeded at a concentration of $7 \times 10^4$ cells/cm$^2$ in Nunc™ 4-well multi-dishes and allowed to attach overnight. The next day, the FCM was removed, cells were washed in PBS and exposed to yCM, and yCM-derived EVs were resuspended in fibroblast standard culture medium without FBS (MEM + yCM-derived EVs), EV-depleted yCM (EV-yCM), and aCM for 48 h. At the end of treatment, cells were returned to FCM and maintained in 5% $CO_2$ for 10 days at 37 °C. Medium was replaced every two days. Cell morphology was monitored daily using an Eclipse TE200 inverted microscope (Nikon, Tokyo, Japan), which was connected to a Digital Sight camera (Nikon, Tokyo, Japan). Cultures were arrested at days 2, 5, 7, and 10, and analyzed as described below.

*4.6. Generation of Young and Aged 3D ECM-Based Bio-Scaffolds*

Ovaries from 6-month (young, $n = 3$) and 5-year-old (aged, $n = 3$) sows were subjected to the decellularization protocol previously developed in our laboratory [34–37]. Briefly, organs were frozen for at least 24 h at −80 °C, thawed, and treated with 0.5% sodium dodecyl sulfate (Bio-Rad, Milan, Italy) for 3 h, 1% Triton X-100 (Sigma-Aldrich, Milan, Italy) for 16 h, and 2% deoxycholate (Sigma-Aldrich, Milan, Italy) overnight. At the end of the procedures, the generated bio-scaffolds were extensively washed in double-distilled water (dd$H_2O$) for 6 h, sterilized with 70% ethanol supplemented with 2% antibiotic/antimycotic solution (Sigma-Aldrich, Milan, Italy) for 30 min, and used as cell culture supports. Small fragments from each bio-scaffold were analyzed to evaluate the efficacy of the decellularization process and the composition of the model.

*4.7. Aged Fibroblast Exposure to Cell Secretomes Using Young and Aged 3D ECM-Based Bio-Scaffolds*

$7 \times 10^4$ aged fibroblasts/$cm^2$ were seeded onto young and aged 3D ECM-based bio-scaffolds and allowed to attach overnight. The next day, the FCM was removed, and cells were washed in PBS and exposed to yCM or EV-yCM for 48 h. At the end of treatment, cells were returned to standard culture medium and maintained in 5% $CO_2$ for 10 days at 37 °C. Medium was replaced every two days. EV-yCM was used as a control. Cultures were arrested at days 2, 5, 7, and 10, and embedded in paraffin for histological analyses or used for DNA quantification or gene expression studies.

*4.8. Cell Proliferation Index*

Cells cultured onto 2D systems were fixed in methanol for 15 min at −20 °C. Cells cultured onto 3D ECM-based bio-scaffolds were fixed in 10% neutral buffered formalin for 24 h, gradually dehydrated in alcohols, cleared with xylene, and embedded in paraffin. A total of 5-µm thick microtome sections were cut and rehydrated, and antigens were unmasked with 10mM Sodium citrate solution (pH 6) containing 0.05% Tween-20 (Sigma-Aldrich, Milan, Italy) at 120 °C.

Non-specific cross-reacting antigens were blocked with 10% Goat Serum (Sigma-Aldrich, Milan, Italy) in PBS for 30 min. Anti-proliferating cell nuclear antigen (PCNA) primary antibody (1:200, Sigma-Aldrich, Milan, Italy) was incubated for 1 h, followed by secondary antibody exposure (1:250, Alexa Fluor™ 594) for 30 min. Nuclei were counterstained with 1 µg/mL 4′,6-diamidino-2-phenylindole (DAPI, Sigma-Aldrich, Milan, Italy). All steps were performed at room temperature, unless otherwise specified. At the end of the immunostaining, 2D cultured samples were observed under the Eclipse TE200 microscope (Nikon, Tokyo, Japan), equipped with DS-2MBWc (Nikon, Tokyo, Japan) while paraffin-embedded tissues were analyzed through a Leica DMR microscope (Wetzlar, Germany) equipped with a DS-Fi3 digital camera (Nikon, Tokyo, Japan). Pictures were acquired using NIS-Elements Software (Version 4.6; Nikon, Tokyo, Japan). The number of PCNA+ cells was counted in 10 randomly selected fields at 100× total magnification and expressed as a percentage of the total cell counted.

*4.9. β-Galactosidase (β-GAL) and Reactive Oxygen Species (ROS) Activities*

Human human galactosidase beta (β-GAL; MyBioSource, MBS721441, San Diego, USA) and reactive oxygen species (ROS; MyBioSource, MBS166870, San Diego, USA) ELISA kits were used to detect cell activities. After 20 min of sonication at 20 kHz, samples were centrifuged at 3000 rpm for 20 min, and supernatants were collected and analyzed at 450 nm using a Multiskan FC. Standard curves were generated via plotting the target concentrations versus absorbances, linear regression analysis was computed, and β-GAL and ROS fold changes were quantified and reported with the higher expression set to 1, while the other expression was relative to this value.

*4.10. Histological Analysis and Cell Density Evaluation*

Cells cultured onto 3D ECM-based bio-scaffolds were fixed in 10% neutral buffered formalin for 24 h, gradually dehydrated in alcohols, cleared with xylene, and embedded in paraffin. In total, 5-µm thick microtome sections were cut, rehydrated, and stained with hematoxylin (Histoline, Milan, Italy) and eosin (BioOptica, Milan, Italy) or with 1 µg/mL DAPI (Sigma-Aldrich, Milan, Italy).

Cell density was estimated via analyzing 15 DAPI-stained sections (5-µm-thick) obtained from each experimental group.

All samples were visualized through a DMR microscope (Leica, Wetzlar, Germany) equipped with a DS-Fi3 digital camera (Nikon, Tokyo, Japan). Pictures were acquired using NIS-Elements Software (Version 4.6; Nikon, Tokyo, Japan) and constant exposure parameters. Five randomly selected fields for each section at 100X magnification were analyzed using the Manual Cell Counter tool (ImageJ software, version 1.53j, https://imagej.nih.gov/ij/index.html, (accessed on 4 May 2023)). Cell density was expressed as cell/$mm^2$ of tissue.

*4.11. DNA Quantification*

Genomic DNA was extracted from repopulated bio-scaffold fragments using the PureLink® Genomic DNA Kit, following the manufacturer's instructions. DNA concentrations were quantified with NanoDrop 8000 (Bio-Rad Laboratories, Milan, Italy) and normalized against the previously annotated tissue weights.

*4.12. Gene Expression Analysis*

RNA was extracted using the TaqMan™ Gene Expression Cells to Ct kit. DNase I was added in lysis solutions at 1:100 concentration. The expression of target genes was analyzed using the CFX96 Real-Time PCR detection system (Bio-Rad Laboratories, Milan, Italy) and pre-designed primers and probe sets from TaqMan™ Gene Expression Assays (Table 1). GAPDH and ACTB were used as internal reference genes. Gene expression levels were quantified with CFX Manager software 18450000 (Bio-Rad Laboratories, Milan, Italy), and reported with the highest expression set to 1, while the other expression was relative to this value.

**Table 1.** List of primers used for quantitative PCR analysis.

| Gene | Description | Cat. N. |
|---|---|---|
| ACTB | Actin, beta | Hs01060665_g1 |
| GAPDH | Glyceraldehyde-3-phosphate dehydrogenase | Hs02786624_g1 |
| MKI67 | Marker of proliferation Ki-67 | Hs04260396_g1 |
| TFAM | Transcription Factor A, Mitochondrial | Hs00273372_s1 |
| ROMO1 | Reactive oxygen species modulator 1 | Hs00603977_m1 |
| PDHA1 | Pyruvate dehydrogenase E1 subunit alpha 1 | Hs01049345_g1 |
| COX4I1 | Cytochrome C oxidase subunit 4I1 | Hs00971639_m1 |
| CDKN1 (P21) | Cyclin-dependent kinase inhibitor 1A | Hs00355782_m1 |
| CDKN2A (P16) | Cyclin-dependent kinase inhibitor 2A | Hs00923894_m1 |
| TP53 (P53) | Tumor protein p53 | Hs01034249_m1 |

*4.13. Transmission Electron Microscope Analysis*

Morphology of yCM- and aCM-derived EVs was analysed using TEM. Five microliters of EV suspensions were placed on a glow-discharged Formvar-Carbon Copper grid of 300 mesh (Sigma-Aldrich, Milan, Italy) for 2 min and stained with 2% uranyl acetate (Sigma-Aldrich, Milan, Italy) for a further 2 min. Samples were then washed with 0.1 μm filtered PBS for 1 min at room temperature. After drying, they were observed under a TEM Talos™ L120C at 120 KV. Images were acquired using a Ceta camera 4k × 4k.

*4.14. Western Blot*

yCM- and aCM-derived EVs were lysed for 30 min at 4 °C in RIPA buffer (20 nM Tris-HCl, 150 nM NaCl, 1% deoxycholate, 0.1% SDS, 1% Triton X-100, pH 7.8), supplemented with protease and phosphatase inhibitors cocktail (Sigma-Aldrich, Milan, Italy). Protein concentrations were quantified using a BCA Protein Assay Kit. A total of 10 μg of proteins were loaded, electrophoresed on precast 4–20% polyacrylamide Mini-PROTEAN TGX gels (#4561093, Bio-Rad Laboratories, Milan, Italy) at 200V for 35 min, transferred onto nitrocellulose membranes (Hybond-C Extra, GE Healthcare Life Sciences, Chicago, Illinois, USA), and probed with primary antibodies for CD9 (1:250, #555370, BD Biosciences, Franklin Lakes, New Jersey, USA), CD63 (1:1000, #ab271286, Abcam, Cambridge, United Kingdom), CD81 (1:1000, #ab79559, Abcam, Cambridge, United Kingdom) and beta Actin (1:5000, #ab6276, Abcam, Cambridge, United Kingdom). Protein bands were visualized using the WesternBreeze chemiluminescent kit, and densitometric analysis was performed using the ImageJ software (ImageJ software version 1.53j).4.15. EV Quantification

EVs isolated from yCM and aCM were quantified using the ExoCET® Exosome Quantitation Kit (System Biosciences, Palo Alto, California, USA), following the manufacturer's instructions. Briefly, EVs were lysed, centrifuged at 1500× *g* for 5 min, and the supernatants were transferred

in the microtiter plate for quantification at 405 nm using a Multiskan FC. The standard curve was obtained through plotting the target concentrations versus absorbances. Linear regression analysis was computed, and EV quantifications were calculated and reported with the highest expression set to 1, while the other expression was relative to this value.

*4.16. miR-200b and miR-200c Expression Analysis*

Small RNAs were extracted from yCM- and aCM-derived EVs using the Total Exosome RNA and Protein Isolation Kit, following the provider's instructions. miR-200b and miR-200c were selectively reverse-transcribed using TaqMan™ MicroRNA Reverse Transcription kit (Applied Biosystems™, Waltham, Massachusetts, USA) and TaqMan™ pre-designed probes (Mir200b #002251; Mir200c #002300, Applied Biosystems™, Waltham, Massachusetts, USA). RT-qPCR was performed with Universal Master Mix II (Applied Biosystems™, Waltham, Massachusetts, USA) and TaqMan™ microRNA Assay (Mir200b #002251; Mir200c #002300, Applied Biosystems™, Waltham, Massachusetts, USA), using the CFX96 Real-Time PCR detection system (Bio-Rad Laboratories, Milan, Italy). miR-200b and miR-200c contents are here reported; the highest expression was set to 1, while the other was relative to this value.

*4.17. Statistical Analysis*

Statistical analysis was performed using two-way ANOVA (SPSS 19.1; IBM). Data were reported as the mean ± standard deviation (SD). Differences of $p \leq 0.05$ were considered significant and indicated with different lowercase letters.

**Author Contributions:** Conceptualization, T.A.L.B. and F.G.; investigation, G.P., S.A. and T.D.I.; writing—original draft preparation, G.P. and T.A.L.B.; writing—review and editing, T.A.L.B. and F.G.; project administration, T.A.L.B. and F.G.; funding acquisition, T.A.L.B. All authors have read and agreed to the published version of the manuscript.

**Funding:** This research was funded by Carraresi Foundation, PSR2021, PSR2022 and HORIZON-WIDERA-2021 project *n*#101079349 (OH-Boost).

**Institutional Review Board Statement:** Not applicable. This study did not involve live humans or animals.

**Informed Consent Statement:** Not applicable.

**Data Availability Statement:** The data presented in this study are available on request from the corresponding author.

**Acknowledgments:** TALB is member of the Inter-COST Actions Task-Force on COVID-19 and the COST Action CA20140, CorEuStem.

**Conflicts of Interest:** The authors declare no conflicts of interest.

**References**

1. Crimmins, E.M. Lifespan and Healthspan: Past, Present, and Promise. *Gerontologist* **2015**, *55*, 901. https://doi.org/10.1093/GERONT/GNV130.
2. Brown, G.C. Living Too Long: The Current Focus of Medical Research on Increasing the Quantity, Rather than the Quality, of Life Is Damaging Our Health and Harming the Economy. *EMBO Rep.* **2015**, *16*, 137. https://doi.org/10.15252/EMBR.201439518.
3. Pennarossa, G.; De Iorio, T.; Arcuri, S.; Gandolfi, F.; Brevini, T.A.L. Synergistic Effect of MiR-200 and Young Extracellular Matrix-Based Bio-Scaffolds to Reduce Signs of Aging in Senescent Fibroblasts. *Stem Cell Rev. Rep.* **2022**, *19*, 417–429. https://doi.org/10.1007/S12015-022-10438-5/FIGURES/6.
4. Manukyan, M.; Singh, P.B. Epigenome Rejuvenation: HP1β Mobility as a Measure of Pluripotent and Senescent Chromatin Ground States. *Sci. Rep.* **2014**, *4*, 4789. https://doi.org/10.1038/srep04789.
5. Sarkar, T.J.; Quarta, M.; Mukherjee, S.; Colville, A.; Paine, P.; Doan, L.; Tran, C.M.; Chu, C.R.; Horvath, S.; Qi, L.S.; et al. Transient Non-Integrative Expression of Nuclear Reprogramming Factors Promotes Multifaceted Amelioration of Aging in Human Cells. *Nat. Commun.* **2020**, *11*, 1545. https://doi.org/10.1038/s41467-020-15174-3.
6. Simpson, D.J.; Olova, N.N.; Chandra, T. Cellular Reprogramming and Epigenetic Rejuvenation. *Clin. Epigenetics* **2021**, *13*, 170 . https://doi.org/10.1186/S13148-021-01158-7.

7. Anastasiadou, E.; Ceccarelli, S.; Messina, E.; Gerini, G.; Megiorni, F.; Pontecorvi, P.; Camero, S.; Onesti, M.G.; Trivedi, P.; Faenza, M.; et al. MiR-200c-3p Maintains Stemness and Proliferative Potential in Adipose-Derived Stem Cells by Counteracting Senescence Mechanisms. *PLoS ONE* **2021**, *16*, e0257070. https://doi.org/10.1371/JOURNAL.PONE.0257070.
8. Phillip, J.M.; Aifuwa, I.; Walston, J.; Wirtz, D. The Mechanobiology of Aging. *Annu. Rev. Biomed. Eng.* **2015**, *17*, 113. https://doi.org/10.1146/ANNUREV-BIOENG-071114-040829.
9. McHugh, D.; Gil, J. Senescence and Aging: Causes, Consequences, and Therapeutic Avenues. *J. Cell. Biol.* **2018**, *217*, 65. https://doi.org/10.1083/JCB.201708092.
10. Johnson, A.A.; Akman, K.; Calimport, S.R.G.; Wuttke, D.; Stolzing, A.; De Magalhães, J.P. The Role of DNA Methylation in Aging, Rejuvenation, and Age-Related Disease. *Rejuvenation Res.* **2012**, *15*, 483–494. https://doi.org/10.1089/REJ.2012.1324.
11. O'Loghlen, A. The Potential of Aging Rejuvenation. *Cell Cycle* **2022**, *21*, 111–116. https://doi.org/10.1080/15384101.2021.2013612.
12. Mahmoudi, S.; Xu, L.; Brunet, A. Turning Back Time with Emerging Rejuvenation Strategies. *Nat. Cell. Biol.* **2019**, *21*, 32–43. https://doi.org/10.1038/s41556-018-0206-0.
13. Neves, J.; Sousa-Victor, P.; Jasper, H. Rejuvenating Strategies for Stem Cell-Based Therapies in Aging. *Cell. Stem Cell.* **2017**, *20*, 161–175. https://doi.org/10.1016/J.STEM.2017.01.008.
14. Lapasset, L.; Milhavet, O.; Prieur, A.; Besnard, E.; Babled, A.; Ät-Hamou, N.; Leschik, J.; Pellestor, F.; Ramirez, J.M.; De Vos, J.; et al. Rejuvenating Senescent and Centenarian Human Cells by Reprogramming through the Pluripotent State. *Genes. Dev.* **2011**, *25*, 2248–2253. https://doi.org/10.1101/GAD.173922.111.
15. Mirsaidi, A.; Genelin, K.; Vetsch, J.R.; Stanger, S.; Theiss, F.; Lindtner, R.A.; von Rechenberg, B.; Blauth, M.; Müller, R.; Kuhn, G.A.; et al. Therapeutic Potential of Adipose-Derived Stromal Cells in Age-Related Osteoporosis. *Biomaterials* **2014**, *35*, 7326–7335. https://doi.org/10.1016/J.BIOMATERIALS.2014.05.016.
16. Fraile, M.; Eiro, N.; Costa, L.A.; Martín, A.; Vizoso, F.J. Aging and Mesenchymal Stem Cells: Basic Concepts, Challenges and Strategies. *Biology* **2022**, *11*, 1678. https://doi.org/10.3390/BIOLOGY11111678.
17. Boulestreau, J.; Maumus, M.; Rozier, P.; Jorgensen, C.; Noël, D. Mesenchymal Stem Cell Derived Extracellular Vesicles in Aging. *Front. Cell. Dev. Biol.* **2020**, *8*, 107. https://doi.org/10.3389/fcell.2020.00107.
18. Daneshmandi, L.; Shah, S.; Jafari, T.; Bhattacharjee, M.; Momah, D.; Saveh-Shemshaki, N.; Lo, K.W.H.; Laurencin, C.T. Emergence of the Stem Cell Secretome in Regenerative Engineering. *Trends Biotechnol.* **2020**, *38*, 1373. https://doi.org/10.1016/J.TIBTECH.2020.04.013.
19. Doyle, L.M.; Wang, M.Z. Overview of Extracellular Vesicles, Their Origin, Composition, Purpose, and Methods for Exosome Isolation and Analysis. *Cells* **2019**, *8*, 727. https://doi.org/10.3390/CELLS8070727.
20. Yáñez-Mó, M.; Siljander, P.R.M.; Andreu, Z.; Zavec, A.B.; Borràs, F.E.; Buzas, E.I.; Buzas, K.; Casal, E.; Cappello, F.; Carvalho, J.; et al. Biological Properties of Extracellular Vesicles and Their Physiological Functions. *J. Extracell. Vesicles* **2015**, *4*, 27066. https://doi.org/10.3402/JEV.V4.27066.
21. Moimas, S.; Salton, F.; Kosmider, B.; Ring, N.; Volpe, M.C.; Bahmed, K.; Braga, L.; Rehman, M.; Vodret, S.; Graziani, M.L.; et al. MiR-200 Family Members Reduce Senescence and Restore Idiopathic Pulmonary Fibrosis Type II Alveolar Epithelial Cell Transdifferentiation. *ERJ Open. Res.* **2019**, *00138-2019*. https://doi.org/10.1183/23120541.00138-2019.
22. Yoshida, M.; Satoh, A.; Lin, J.B.; Mills, K.F.; Sasaki, Y.; Rensing, N.; Wong, M.; Apte, R.S.; Imai, S. ichiro Extracellular Vesicle-Contained ENAMPT Delays Aging and Extends Lifespan in Mice. *Cell. Metab.* **2019**, *30*, 329–342.e5. https://doi.org/10.1016/J.CMET.2019.05.015.
23. Fafián-Labora, J.A.; Rodríguez-Navarro, J.A.; O'Loghlen, A. Small Extracellular Vesicles Have GST Activity and Ameliorate Senescence-Related Tissue Damage. *Cell. Metab.* **2020**, *32*, 71–86.e5. https://doi.org/10.1016/J.CMET.2020.06.004.
24. Zhang, Y.; Kim, M.S.; Jia, B.; Yan, J.; Zuniga-Hertz, J.P.; Han, C.; Cai, D. Hypothalamic Stem Cells Control Ageing Speed Partly through Exosomal MiRNAs. *Nature* **2017**, *548*, 52–57. https://doi.org/10.1038/nature23282.
25. Kadota, T.; Fujita, Y.; Yoshioka, Y.; Araya, J.; Kuwano, K.; Ochiya, T. Emerging Role of Extracellular Vesicles as a Senescence-Associated Secretory Phenotype: Insights into the Pathophysiology of Lung Diseases. *Mol. Asp. Med.* **2018**, *60*, 92–103. https://doi.org/10.1016/J.MAM.2017.11.005.
26. Coppé, J.P.; Patil, C.K.; Rodier, F.; Sun, Y.; Muñoz, D.P.; Goldstein, J.; Nelson, P.S.; Desprez, P.Y.; Campisi, J. Senescence-Associated Secretory Phenotypes Reveal Cell-Nonautonomous Functions of Oncogenic RAS and the P53 Tumor Suppressor. *PLoS Biol.* **2008**, *6*, e301. https://doi.org/10.1371/JOURNAL.PBIO.0060301.
27. Rodier, F.; Coppé, J.P.; Patil, C.K.; Hoeijmakers, W.A.M.; Muñoz, D.P.; Raza, S.R.; Freund, A.; Campeau, E.; Davalos, A.R.; Campisi, J. Persistent DNA Damage Signalling Triggers Senescence-Associated Inflammatory Cytokine Secretion. *Nat. Cell. Biol.* **2009**, *11*, 973–979. https://doi.org/10.1038/ncb1909.

28. Beninson, L.A.; Fleshner, M. Exosomes: An Emerging Factor in Stress-Induced Immunomodulation. *Semin. Immunol.* **2014**, *26*, 394–401. https://doi.org/10.1016/J.SMIM.2013.12.001.
29. Simpson, R.J.; Lim, J.W.E.; Moritz, R.L.; Mathivanan, S. Exosomes: Proteomic Insights and Diagnostic Potential. *Expert Rev. Proteom.* **2014**, *6*, 267–283. https://doi.org/10.1586/EPR.09.17.
30. Lehmann, B.D.; Paine, M.S.; Brooks, A.M.; McCubrey, J.A.; Renegar, R.H.; Wang, R.; Terrian, D.M. Senescence-Associated Exosome Release from Human Prostate Cancer Cells. *Cancer Res.* **2008**, *68*, 7864–7871. https://doi.org/10.1158/0008-5472.CAN-07-6538.
31. Takasugi, M.; Okada, R.; Takahashi, A.; Virya Chen, D.; Watanabe, S.; Hara, E. Small Extracellular Vesicles Secreted from Senescent Cells Promote Cancer Cell Proliferation through EphA2. *Nat. Commun.* **2017**, *8*, 15729. https://doi.org/10.1038/ncomms15728.
32. Yang, S.; Banerjee, S.; De Freitas, A.; Sanders, Y.Y.; Ding, Q.; Matalon, S.; Thannickal, V.J.; Abraham, E.; Liu, G. Participation of MiR-200 in Pulmonary Fibrosis. *Am. J. Pathol.* **2012**, *180*, 484–493. https://doi.org/10.1016/j.ajpath.2011.10.005.
33. Chilosi, M.; Caliò, A.; Rossi, A.; Gilioli, E.; Pedica, F.; Montagna, L.; Pedron, S.; Confalonieri, M.; Doglioni, C.; Ziesche, R.; et al. Epithelial to Mesenchymal Transition-Related Proteins ZEB1, β-Catenin, and β-Tubulin-III in Idiopathic Pulmonary Fibrosis. *Mod. Pathol.* **2017**, *30*, 26–38. https://doi.org/10.1038/MODPATHOL.2016.147/ATTACHMENT/00751DB3-B9C6-42C3-BE85-2953C8610D96/MMC2.ZIP.
34. Pennarossa, G.; De Iorio, T.; Gandolfi, F.; Brevini, T.A.L. Ovarian Decellularized Bioscaffolds Provide an Optimal Microenvironment for Cell Growth and Differentiation In Vitro. *Cells* **2021**, *10*, 2126. https://doi.org/10.3390/CELLS10082126.
35. Pennarossa, G.; De Iorio, T.; Gandolfi, F.; Brevini, T.A.L. Impact of Aging on the Ovarian Extracellular Matrix and Derived 3D Scaffolds. *Nanomaterials* **2022**, *12*, 345. https://doi.org/10.3390/NANO12030345.
36. Pennarossa, G.; Ghiringhelli, M.; Gandolfi, F.; Brevini, T.A.L.L. Creation of a Bioengineered Ovary: Isolation of Female Germline Stem Cells for the Repopulation of a Decellularized Ovarian Bio-Scaffold. *Methods Mol. Biol.* **2021**, *2273*, 139–149. https://doi.org/10.1007/978-1-0716-1246-0_9.
37. Pennarossa, G.; Ghiringhelli, M.; Gandolfi, F.; Brevini, T.A.L. Whole-Ovary Decellularization Generates an Effective 3D Bioscaffold for Ovarian Bioengineering. *J. Assist. Reprod. Genet.* **2020**, *37*, 1329–1339. https://doi.org/10.1007/s10815-020-01784-9.

# 4. Discussion

The first studies were addressed to assess whether the ovarian ECM-based bio-scaffolds, obtained through the decellularization protocol previously established in the Laboratory hosting my PhD activities, are able to support cell survival and growth and drive cell differentiation. The four-step protocol used involves a freeze–thaw cycle, followed by serial incubations with SDS, Triton X-100, and deoxycholate, which were previously shown, and here confirmed, for their ability to successfully remove cells, cellular debris, and nuclear material from whole ovaries, while maintaining the macrostructure and microstructure of the original tissue (Pennarossa et al., 2020; Pennarossa et al., 2021; Pennarossa et al., 2022; Pennarossa et al., 2023a; Pennarossa et al., 2023b). In addition, the generated decellularized ovaries preserve the shape and homogeneity, showing no deformation, while their colour turned from red to white, similar to what described for porcine and human decellularized ovarian fragments (Liu et al., 2017; Hassanpour et al., 2018; Alshaikh et al., 2020), thus suggesting the ability of the protocol adopted to induce a significant reduction in cellular components, even when applied to whole ovaries. This is also confirmed by histological evaluations and DNA quantification studies that demonstrated a significant decrease in cell number and DNA amount respectively.

Besides the effective removal of the cellular compartment, a fundamental aspect for the bio-scaffold quality is represented by the preservation of the ECM composition and its microstructure at the end of decellularization process. The histochemical analyses carried out show the maintenance of intact collagen and elastic fibres, accompanied by the persistence of GAGs. This is also supported by the stereological quantifications,

which reveal no significant differences between native and decellularized ovaries in collagen, elastin, and GAG contents. These data well fit with what was previously described, demonstrating comparable matrisome protein quantities and distribution in porcine decellularized ovaries and the related native tissue (Henning et al., 2019; Alshaikh et al., 2020). Another key aspect is represented by the scaffold biocompatibility, since detergent residuals may impair the subsequent repopulation, leading to cytotoxic environment for cells (Morris et al., 2017; Fernández-Pérez et al., 2019; Neishabouri et al., 2022; Sembiring et al., 2022). In this experiments, MTT assay detect no significant differences between both porcine and human fibroblasts, co-cultured with the generated bio-scaffolds and those of control cultures. This suggest that the decellularized ovaries do have any toxic effect, leading to the production of ECM-based matrixes suitable for tissue engineering.

In this respect, the generated bio-scaffolds were repopulated with freshly isolated porcine ovarian cells (pOCs) and cells adhered and migrated into the matrixes within the first 24h. This is confirmed by both H&E and DAPI staining, as well as by cell density analysis that demonstrate a cell number increase during the culture period, thus suggesting site-specific cell homing can be achieved. These data are supported by TUNEL assay that indicate a stably maintenance of cell viability, with apoptotic indexes comparable to those of the native tissue. This clearly indicate scaffold ability to support *in vitro* ovarian cell survival. Moreover, these observations are confirmed by DNA quantification studies, displaying an increase in DNA content during the culture period. These data agree and expand previously reported data, indicating the ability of decellularized ovarian fragments to encourage *in vitro* cell engraftment (Liu

et al., 2017; Hassanpuor et al., 2018; Henning et al., 2019; Pennarossa et al., 2020) and demonstrate the possibility to use ECM-based scaffolds as a suitable niche for ovarian cell *ex vivo* culture (Liu et al., 2017; Hassanpuor et al., 2018; Pors et al., 2019).

Molecular analyses of engrafted pOCs support the morphological data demonstrating active expression of the major ovarian-related genes. More in details, we are able to detect the granulosa cell gene transcription, namely STAR, CYP11A1, CYP19A1, AMH, FSHR, and LHR, paralleled by connective tissue markers, such as VIM and THY1. In addition, the data obtained indicate that their expression levels were steadily maintained when a 3D ECM-based scaffold is used. We therefore may speculate that the generated decellularized bio-matrixes represent a suitable environment for ovarian cell engraftment, preserving the typical transcription machinery, compared to the native control tissue. This hypothesis is further supported by the results obtained repopulating ECM-based scaffolds with porcine (pEpiE) and human (hEpiE) epigenetically erased cells, obtained through epigenetic erasing (Pennarossa et al., 2013; Pennarossa et al., 2014; Mirakhori et al., 2015; Manzoni et al., 2016; Diomede et al., 2018; Pennarossa et al., 2018; Pennarossa et al., 2019). Similar to pOCs, also pEpiE and hEpiE rapidly adhered and migrated into the bio-matrixes, confirming the ability of ECM-based scaffolds to offer a suitable niche for cell. Interestingly, gene expression analyses show striking changes in the transcription pattern, with downregulation of the pluripotency-related genes OCT4, NANOG, REX1, and SOX2 and the onset of the main genes specifically associated with granulosa cells, namely STAR, CYP11A1, CYP19A1, AMH, FSHR, and LHR, which were originally undetectable in repopulating cells. This is consistent with the ESCs differentiation into functional granulosa cells

(Lan et al., 2013; Woods et al., 2013; Wu et al., 2023) indicating bio-matrixes ability to properly drive erased cell differentiation *in vitro*.

In the subsequent set of experiments, we evaluate the impact of aging on the ovarian ECM. The results obtained through macroscopic and microscopic evaluations of aged ovaries reveal distinctive morphological features when compared to the young counterparts. In particular, aged ovaries display a significantly number of larger ones (5–8 mm) and a lower number of small follicles (3–4 mm) compared to young ovaries. This appears to be strictly correlated to the age of the animals and, as previously described in mouse (Lliberos et al., 2021), bovine (Mossa et al., 2012) and human (Scheffer et al., 2003), is associated with age-related infertility. This is also paralleled by the presence of a denser and more compact stromal compartment in aged ovaries, which suggest the possibility of distinct matrix re-arrangements taking place during the aging process. This hypothesis is further confirmed by the histochemical data that indicate a significant increase in collagen fibres, both with Masson trichrome staining, stereological analysis and ELISA tests. These results agree with recent studies, carried out on reproductively old mice, demonstrating a quantitative increment in ovarian stiffness due to collagen deposition (Amargant et al., 2020; Briley et al., 2016; Hirshfeld-Cytron et al., 2011). Notably, the collagen accumulation, defined as tissue fibrosis, is a crucial event that is usually considered one of the most common aging-associated hallmarks. Indeed, this is exhibited by a wide range of aged tissues, including heart (Biernacka et al., 2011; Meschiari et al., 2017), lung (Giménez et a., 2017) and liver (Chen et al., 2019; Acharya et al., 2021) and affects organ biomechanics and functions (Wynn et al., 2012). Age-specific increment in matrix stiffness has been also associated to

alterations in collagen-to-elastin ratio and/or a general decrease in elastin content (Dodson et al., 2013; Zhang et al., 2016; Selman et al., 2021). This is consistent with the data here reported, demonstrating a significant decrease of elastic fibres in aged ovaries, both by Gomori's aldehyde fuchsin staining, stereological analysis and supported by ELISA tests. These observations are in agreement with the marked decrease in elastin levels noticed in perifollicular ECM of menopausal women (Ouni et al., 2020) and confirm the different collagen/elastin ratio here demonstrated in senescent ovaries. This suggests that ovarian aging can be associated to an elasticity reduction, thus impairing tissue mechanical resilience, similar to what was described in other organs (Sherratt, 2009; Duck et al., 2013; Sherratt, 2013; Baumann et al., 2021; Heinz et al., 2021). However, elastin decrement is paralleled by an increase in GAGs content, known to be responsible to cell adhesion as well as to the maintenance of the typical viscosity (Lee et al., 2016; Wang et al., 2018), thus suggesting that these molecules may buffer the modified collagen/elastin balance. This lead to hypothesize the existence of compensative mechanisms, possibly acting to mitigate the altered tissue stiffness.

The changes described above are accompanied by a significant LAMA3 and LAMB1 increase in aged tissues. These proteins are essential for cell adhesion and are described to be highly prevalent in fibrotic samples (Augustin-Voss et al., 1993; Natarajan et al., 2006; Chilosi et al., 2013). The increase in laminins is also paralleled by a significant reduction in FN1 content, similarly to what was reported in liver fibrosis (Schnabl et al., 2003; Krizhanovsky et al., 2008), but in contrast to what happens in other organs such as heart (Hu et al., 2022) and lung (Greenwell et al., 2020). We have no explanation

for these incongruities, but we may hypothesize that these data could be related to cell type-specific differences and/or tissue-specific responses. Interestingly, a very dynamic variation in gene transcription levels is detected, closely reflecting the morphological data described above, accompanies ECM reorganisation in the senescent ovary, with higher expression of collagens (COL1A1, COL3A1, COL4A2), glycoprotein (EMILIN1), laminins (LAMA3, LAMB1), proteoglycans (VCAN, HSPG2, CSPG4), and downregulation of elastin (ELN) and fibronectin (FN1). Interestingly, all the main matrix remodelling gene enzymes analysed, namely ELANE, MMP1, MMP2, MMP3, MMP9, and MMP14, display significantly lower transcription levels in senescent samples. This suggests that the unbalance in protein deposition and ECM remodelling result in fiber accumulation. In contrast to the other proteases analysed, MMP12 expression, specifically involved in elastin degradation, increase in aged ovaries. This well fits with the significant reduction in elastin content described above. Altogether, these findings indicate the presence of a finely tuned gene transcription machinery that regulates ECM composition, suggesting the influence of senescence on the ECM-related gene expression.

Interestingly enough, when the whole-ovary decellularization protocol was applied to aged ovaries, we derived 3D ECM-based bio-scaffolds that maintain all the changes described above and that are distinctive of the senescent organ. Indeed, both histochemical and immunohistochemical studies as well as ELISA assays show the preservation of collagen, elastin, GAGs, laminins, and fibronectin quantities identified in aged native tissues. These data are in agreement with our previous studies, demonstrating an efficient removal of the cellular compartment, while preserving

intact ECM fibres (Pennarossa et al., 2020; Pennarossa et al., 2021). In addition, the decellularization protocol used allow for the maintenance of age-specific ECM microstructures, leading to the creation of bio-scaffolds that mimic the ovarian environment and offer an exciting opportunity to better characterize ovarian aging as well as to identify possible strategies to counteract tissue degeneration *in vitro*, in a complex and physiologically relevant model.

In this context, we exploited young ECM-based scaffold ability to recreate an age-specific microenvironment to boost and properly maintain rejuvenated phenotype acquired by aged cells after miR-200 exposure. In particular, we firstly demonstrated that the use of miR-200b/c induces a transient high plasticity state and ameliorates cellular and physiological hallmarks of aging in senescent cells. Indeed, in the first set of experiments we showed that exposure to miR-200b/c induces significant changes in fibroblasts isolated from aged patients that acquire morphological and molecular features distinctive of pluripotent cells. This is confirmed by morphological evaluations, indicating that the typical fibroblast elongated shape is replaced by an oval morphology. Cells become smaller in size with granular, vacuolated cytoplasm and rearrange in distinguishable aggregates. These observations are in agreement to what previously described for human ESC and iPSCs (Sathananthan et al., 2002; Courtot et al., 2014) and are possibly related to a relaxed and accessible chromatin structure, typical of pluripotent cells (Niwa et al., 2007; Efroni et al., 2008; Liang et al., 2013; Zhu et al., 2021). All these observations suggest that the use of miR-200b/c may encourage the appearance of morphological properties previously described in both native and induced high plasticity cells, which is also supported by the molecular

analyses performed, showing the onset of the pluripotency-related genes, OCT4, NANOG, REX1, and SOX2, in response to miR-200b/c exposure.

Interestingly, the morphological changes described above are paralleled by significant reduction of aging hallmarks. In particular, miR-200b/c exposure leads to an increment in cell growth and proliferation, accompanied by a significant decrease in senescence-related markers, namely β-GAL and ROS activities as well as P16, P21 and P53 gene expression levels. Consistent with this, we also detect an oxidative stress reduction (ROMO1), an increment in cell proliferation (MKI67) and mitochondrial activity (TFAM, PDHA1, and COX4I1). Altogether, these observations confirm the key role played by the miR-200 family, not only to promote and maintain high plasticity (Wang et al., 2013; Huang et al., 2014; Balzano et al., 2018), but also to reduce signs of cellular senescence and to encourage the acquisition of a young phenotype. However, it cannot be stably maintained in 2D culture systems and when miR-200b/c are removed from cultures and cells are returned to standard culture medium, they gradually revert to their original phenotype, exhibiting all morphological and molecular signs distinctive of aged cells by day 10 of culture. On the other hand, the acquired rejuvenated phenotype is stably retained when cells are engrafted onto young 3D ECM-based bio-scaffolds. In particular, after miR-200b/c removal, cells adhered and colonized the bio-scaffolds and stably maintained all the hallmarks typical of young cells. Specifically, the number of PCNA positive cells is comparable to the that detected in young fibroblasts, as well as the β-GAL and ROS activities. This is also paralleled by high expression levels for the genes involved in cell proliferation (MKI67), mitochondrial activity (TFAM, PDHA1, and COX4I1) and low transcription for the genes associated

to cell senescence (ROMO1, P16, P21 and P53). These results suggest that a specific 3D environment may exert a supporting effect to stably maintain the rejuvenated phenotype induced by the miR-200b/c treatment, which would otherwise be transient and quickly lost.

Based on these achievements and on the data reported in the literature, demonstrating the possibility to revert aging-related features in old stem cells through culturing them with young stem cell-derived conditioned medium, also referred as "secretome" (Mirsaidi et al., 2014; Boulestreau et al., 2020; O' Loghlen, 2022; Fraile et al., 2022), we combined the use of young cell secretome-derived EVs with young ECM-based scaffolds to ameliorate cellular and physiological hallmark of aging in senescent cells and stably maintain a rejuvenated phenotype.

The results obtained demonstrate that young conditioned medium (yCM) or yCM-derived EVs are able to induce aged cells to acquire morphological and molecular features distinctive of cells derived from young donors. Indeed, after yCM exposure, cells isolated from aged individuals appear more compact, with rounded phenotype, and smaller in size. These morphological observations are accompanied by a significant decrease in β-GAL and ROS activities and an increase in the proliferation marker PCNA. This is also paralleled by the downregulation of P16, P21, P53, and ROMO1 gene expression levels, and by the upregulation of the mitochondrial activity (TFAM, PDHA1, and COX4I1) and the proliferation related (MKI67) gene, reaching levels statistically comparable to those distinctive of young cells. These data are in line with recently published manuscripts reporting that young patients derived-EVs are able to revert senescence hallmarks (Yoshida et al., 2019; Fafián-Labora et al., 2020;

O'Loghlen et al., 2022), and point out to the pivotal role played by young fibroblast-derived EVs in the acquisition of young phenotype. However, similarly to what observed in the experiments described above, the EV-mediated rejuvenating effect is transient and reversible when cells are cultured in 2D standard conditions. Specifically, cells revert to a larger size and have an elongated shape, increased β-GAL and ROS activities, and MKI67, TFAM, PDHA1, COX4I1, ROMO1, P16, P21, and P53 transcription, reaching levels statistically comparable to those of untreated aged cells. Contrarily, when young secretome-derived EV exposure is coupled with the use of young 3D ECM-based bio-scaffolds, treated cells steady maintain a young phenotype. Indeed, they display a high number of PCNA positive cells and β-GAL and ROS activity comparable to those detected in young cells. This is paralleled by a steady increment of cell proliferation- (MKI67) and mitochondrial activity-related (TFAM, PDHA1, and COX4I1) gene expression levels, and a downregulation of P16, P21, P53 and ROMO1. These data confirm the results described above showing the young ECM-based scaffold ability to stabilize miR-200b/c-induced rejuvenation and support the hypothesis that a young microenvironment is able to synergistically act with soluble factors (Pennarossa et al., 2023). In addition, this is coherent with recent findings reporting that ECM has a crucial impact on cell differentiation, stem cell self-renewal and cell rejuvenation (Gattazzo et al., 2014; Zhou et al., 2017; Watt et al., 2013; Cai et al., 2022; Pennarossa et al., 2023).

# 5. Conclusion

The results described in this thesis clearly demonstrated that the decellularized ECM-based scaffolds may provide an optimal 3D microenvironment for ex vivo culture of ovarian cells, supporting the maintenance of their original expression pattern. Furthermore, these bio-matrixes are able to properly drive epigenetically erased cell differentiation, fate, and viability in vitro, encouraging repopulating cells to adopt a transcriptional shift in response to the scaffold environment. Significant changes, however, take place in ovarian ECM during aging progression. These include altered concentrations of the main structural molecules, such as collagen, elastin, laminins, and fibronectin, that lead to tissue architecture remodeling, increment of fibrosity, and reduced elasticity. Interestingly, our results demonstrate that it is possible to generate ECM-based scaffolds that mimic the senescent ovarian microstructure and offer an exciting opportunity to better characterize ovarian aging in vitro in a complex and physiologically relevant environment. This constitutes an alternative high predictive in vitro model for the research in the aging field, allowing for a reduction of the number of experimental animals used. At the same time, the bio-scaffold will in due time implement the production of an "aging ovary in a dish" model to further study the mechanisms driving aging and may lead to the identification of possible strategies to counteract tissue degeneration. In this context, we demonstrated that molecular mechanisms regulated by young cell secretome and by miR-200s are directly involved in erasing cellular senescence, however, an adequate microenvironment is required to stabilize the rejuvenating effects, suggesting the involvement of synergistic interactions among molecular effectors and bio-scaffold-derived mechanical cues. This

clearly highlighted the existence of multiple factors which cooperate to control a unique program, driving the cell clock.

Altogether, the strategy here proposed allow for the generation of a suitable 3D platform to investigate solutions for hormone and fertility restoration, toxicological and drug testing, as well as transplantation studies. In addition, the model obtained represent a useful tool to better characterize these complex regulations and to allow a fine dissection of the multiple and concurring biochemical and biomechanical stimuli driving the aging process.

# 6. References


Acharya, P., Chouhan, K., Weiskirchen, S., & Weiskirchen, R. (2021). Cellular Mechanisms of Liver Fibrosis. *Frontiers in Pharmacology*, *12*. https://doi.org/10.3389/fphar.2021.671640

Acosta, S., Quintanilla-Sierra, L., Lubinda Mbundi, Reboto, V., & José Carlos Rodríguez-Cabello. (2020). Elastin-Like Recombinamers: Deconstructing and Recapitulating the Functionality of Extracellular Matrix Proteins Using Recombinant Protein Polymers. *Advanced Functional Materials*, *30*(44). https://doi.org/10.1002/adfm.201909050

Ajjarapu, S. M., Tiwari, A., & Kumar, S. (2023). Applications and Utility of Three-Dimensional In Vitro Cell Culture for Therapeutics. *Future Pharmacology*, *3*(1), 213–228. https://doi.org/10.3390/futurepharmacol3010015

Alshaikh, A. B., Padma, A. M., Dehlin, M., Akouri, R., Song, M. J., Brännström, M., & Hellström, M. (2020). Decellularization and recellularization of the ovary for bioengineering applications; studies in the mouse. *Reproductive Biology and Endocrinology*, *18*(1). https://doi.org/10.1186/s12958-020-00630-y

Amack, J. D. (2021). Cellular dynamics of EMT: lessons from live in vivo imaging of embryonic development. *Cell Communication and Signaling*, *19*(1). https://doi.org/10.1186/s12964-021-00761-8

Amargant, F., Manuel, S. L., Tu, Q., Parkes, W. S., Rivas, F., Zhou, L. T., Duncan, F. E. (2020). Ovarian stiffness increases with age in the mammalian ovary and depends on collagen and hyaluronan matrices. *Aging Cell*, *19*(11). https://doi.org/10.1111/acel.13259

Amini, S., Salehi, H., Setayeshmehr, M., & Ghorbani, M. (2021). Natural and synthetic polymeric scaffolds used in peripheral nerve tissue engineering: Advantages and disadvantages. *Polymers for Advanced Technologies*. https://doi.org/10.1002/pat.5263

Anastasiadou, E., Messina, E., Sanavia, T., Mundo, L., Farinella, F., Lazzi, S., Marchese, C. (2021). MiR-200c-3p Contrasts PD-L1 Induction by Combinatorial Therapies and Slows Proliferation of Epithelial Ovarian Cancer through Downregulation of β-Catenin and c-Myc. *Cells*, *10*(3), 519. https://doi.org/10.3390/cells10030519

Andrée, B., Bela, K., Tibor Horváth, Lux, M., Ramm, R., Venturini, L., Hilfiker, A. (2014). Successful re-endothelialization of a perfusable biological vascularized matrix (BioVaM) for the generation of 3D artificial cardiac tissue. *Basic Research in Cardiology*, *109*(6). https://doi.org/10.1007/s00395-014-0441-x

Angelini, A., Trial, J., Ortiz-Urbina, J., & Cieslik, K. A. (2020). Mechanosensing dysregulation in the fibroblast: A hallmark of the aging heart. *Ageing Research Reviews*, *63*, 101150. https://doi.org/10.1016/j.arr.2020.101150

Arcuri, S., Pennarossa, G., Gandolfi, F., & Brevini, T. A. L. (2021). Generation of Trophoblast-Like Cells From Hypomethylated Porcine Adult Dermal Fibroblasts. *Frontiers in Veterinary Science*, *8*. https://doi.org/10.3389/fvets.2021.706106

Augustin-Voss, H. G., Voss, A. K., & Pauli, B. U. (1993). Senescence of aortic endothelial cells in culture: effects of basic fibroblast growth factor expression on cell phenotype, migration, and proliferation. *Journal of Cellular Physiology*, *157*(2), 279–288. https://doi.org/10.1002/jcp.1041570210

Aulino, P., Costa, A., Chiaravalloti, E., Perniconi, B., Adamo, S., Coletti, D., Teodori, L. (2015). Muscle Extracellular Matrix Scaffold Is a Multipotent Environment. *International Journal of Medical Sciences*, *12*(4), 336–340. https://doi.org/10.7150/ijms.10761

Aunan, J. R., Watson, M. M., Hagland, H. R., & Søreide, K. (2016). Molecular and biological hallmarks of ageing. *British Journal of Surgery*, *103*(2), e29–e46. https://doi.org/10.1002/bjs.10053

Bacakova, L., Zikmundova, M., Pajorova, J., Broz, A., Filova, E., Blanquer, A., Sinica, A. (2019, August 23). Nanofibrous Scaffolds for Skin Tissue Engineering and Wound Healing Based on Synthetic Polymers. Retrieved October 10, 2023, from www.intechopen.com website: https://www.intechopen.com/chapters/68760

Baiguera, S., Del Gaudio, C., Kuevda, E., Gonfiotti, A., Bianco, A., & Macchiarini, P. (2014). Dynamic decellularization and cross-linking of rat tracheal matrix. *Biomaterials*, *35*(24), 6344–6350. https://doi.org/10.1016/j.biomaterials.2014.04.070

Bajpai, A., Li, R., & Chen, W. (2020). The cellular mechanobiology of aging: from biology to mechanics. *Annals of the New York Academy of Sciences*, *1491*(1), 3–24. https://doi.org/10.1111/nyas.14529

Baker, B. M., & Chen, C. S. (2012). Deconstructing the third dimension – how 3D culture microenvironments alter cellular cues. *Journal of Cell Science*, *125*(13), 3015–3024. https://doi.org/10.1242/jcs.079509

Balzano, F., Cruciani, S., Basoli, V., Santaniello, S., Facchin, F., Ventura, C., & Maioli, M. (2018). MiR200 and miR302: Two Big Families Influencing Stem Cell Behavior. *Molecules*, *23*(2), 282. https://doi.org/10.3390/molecules23020282

Bandzerewicz, A., & Gadomska-Gajadhur, A. (2022). Into the Tissues: Extracellular Matrix and Its Artificial Substitutes: Cell Signalling Mechanisms. *Cells*, *11*(5), 914. https://doi.org/10.3390/cells11050914

Basu, A., & Tiwari, V. K. (2021). Epigenetic reprogramming of cell identity: lessons from development for regenerative medicine. *Clinical Epigenetics*, *13*(1). https://doi.org/10.1186/s13148-021-01131-4

Batchelder, C. A., Martinez, M. L., & Tarantal, A. F. (2015). Natural Scaffolds for Renal Differentiation of Human Embryonic Stem Cells for Kidney Tissue Engineering. *PLOS ONE*, *10*(12), e0143849. https://doi.org/10.1371/journal.pone.0143849

Batioglu-Karaaltin, A., Ovali, E., Karaaltin, M. V., Yener, M., Yılmaz, M., Eyüpoğlu, F., Cansiz, H. (2019). Decellularization of Trachea With Combined Techniques for Tissue-Engineered Trachea Transplantation. *Clinical and Experimental Otorhinolaryngology*, *12*(1), 86–94. https://doi.org/10.21053/ceo.2018.00486

Baumann, P., Wiegert, S., Greco, F., Ersch, J., & Cannizzaro, V. (2021). Strain-specific differences in lung tissue viscoelasticity of mechanically ventilated infant Sprague-Dawley and Wistar rats. *American Journal of Physiology. Lung Cellular and Molecular Physiology*, *320*(2), L220–L231. https://doi.org/10.1152/ajplung.00100.2020

Biernacka, A., & Frangogiannis, N. G. (2011). Aging and Cardiac Fibrosis. *Aging and Disease*, *2*(2), 158–173. Retrieved from https://pubmed.ncbi.nlm.nih.gov/21837283/

Birch, H. L. (2018). Extracellular Matrix and Ageing. *Sub-Cellular Biochemistry*, *90*, 169–190. https://doi.org/10.1007/978-981-13-2835-0_7

Biswas, S., & Rao, C. M. (2018). Epigenetic tools (The Writers, The Readers and The Erasers) and their implications in cancer therapy. *European Journal of Pharmacology*, *837*, 8–24. https://doi.org/10.1016/j.ejphar.2018.08.021

Bonnans, C., Chou, J., & Werb, Z. (2014). Remodelling the extracellular matrix in development and disease. *Nature Reviews Molecular Cell Biology*, *15*(12), 786–801. https://doi.org/10.1038/nrm3904

Booth, C., Soker, T., Baptista, P., Ross, C. L., Soker, S., Farooq, U., Orlando, G. (2012). Liver bioengineering: Current status and future perspectives. *World Journal of Gastroenterology : WJG*, *18*(47), 6926–6934. https://doi.org/10.3748/wjg.v18.i47.6926

Boulestreau, J., Maumus, M., Rozier, P., Jorgensen, C., & Noël, D. (2020). Mesenchymal Stem Cell Derived Extracellular Vesicles in Aging. *Frontiers in Cell and Developmental Biology*, *8*. https://doi.org/10.3389/fcell.2020.00107

Brevini, T. A. L., Pennarossa, G., Acocella, F., Brizzola, S., Zenobi, A., & Gandolfi, F. (2016). Epigenetic conversion of adult dog skin fibroblasts into insulin-secreting cells. *The Veterinary Journal*, *211*, 52–56. https://doi.org/10.1016/j.tvjl.2016.02.014

Brevini, T. A. L., Pennarossa, G., Maffei, S., & Gandolfi, F. (2015). Phenotype switching through epigenetic conversion. *Reproduction, Fertility, and Development*, *27*(5), 776–783. https://doi.org/10.1071/RD14246

Briley, S. M., Jasti, S., McCracken, J. M., Hornick, J. E., Fegley, B., Pritchard, M. T., & Duncan, F. E. (2016). Reproductive age-associated fibrosis in the stroma of the mammalian ovary. *Reproduction*, 245–260. https://doi.org/10.1530/rep-16-0129

Brunken, W., Varshney, S., & Hunter, D. (2015). Extracellular Matrix components regulate cellular polarity and tissue structure in the developing and mature Retina. *Journal of Ophthalmic and Vision Research*, *10*(3), 329. https://doi.org/10.4103/2008-322x.170354

Cacciamali, A., Villa, R., & Dotti, S. (2022). 3D Cell Cultures: Evolution of an Ancient Tool for New Applications. *Frontiers in Physiology*, *13*, 836480. https://doi.org/10.3389/fphys.2022.836480

Cai, Z., Gong, Z., Li, Z., Li, L., & Kong, W. (2021). Vascular Extracellular Matrix Remodeling and Hypertension. *Antioxidants & Redox Signaling*, *34*(10), 765–783. https://doi.org/10.1089/ars.2020.8110

Cao, S. S., & Kaufman, R. J. (2014). Endoplasmic Reticulum Stress and Oxidative Stress in Cell Fate Decision and Human Disease. *Antioxidants & Redox Signaling*, *21*(3), 396–413. https://doi.org/10.1089/ars.2014.5851

Casagrande, S., & Hau, M. (2019). Telomere attrition: metabolic regulation and signalling function? *Biology Letters*, *15*(3), 20180885. https://doi.org/10.1098/rsbl.2018.0885

Chakravarti, D., LaBella, K. A., & DePinho, R. A. (2021). Telomeres: history, health, and hallmarks of aging. *Cell*, *184*(2). https://doi.org/10.1016/j.cell.2020.12.028

Chandrakanthan, V., Yeola, A., Kwan, J. C., Oliver, R. A., Qiao, Q., Kang, Y. C., Hardy, P. (2016). PDGF-AB and 5-Azacytidine induce conversion of somatic cells into tissue-regenerative multipotent stem cells. *Proceedings of the National Academy of Sciences of the United States of America*, *113*(16), E2306-15. https://doi.org/10.1073/pnas.1518244113

Chen Wei Lan, Chen, M.-J., Pey Shynan Jan, Chen, S., & Hong Nerng Ho. (2013). Differentiation of Human Embryonic Stem Cells Into Functional Ovarian Granulosa-like Cells. *The Journal of Clinical Endocrinology and Metabolism*, *98*(9), 3713–3723. https://doi.org/10.1210/jc.2012-4302

Chen, C., Ding, S., & Wang, J. (2023). Digital health for aging populations. *Nature Medicine*, *29*(7), 1623–1630. https://doi.org/10.1038/s41591-023-02391-8

Chen, D., Le, T. H., Shahidipour, H., Read, S. A., & Ahlenstiel, G. (2019). The Role of Gut-Derived Microbial Antigens on Liver Fibrosis Initiation and Progression. *Cells*, *8*(11), 1324. https://doi.org/10.3390/cells8111324

Chen, S., Zhang, Q., Wu, X., Schultz, P. G., & Ding, S. (2003). Dedifferentiation of Lineage-Committed Cells by a Small Molecule. *Journal of the American Chemical Society*, *126*(2), 410–411. https://doi.org/10.1021/ja037390k

Chilosi, M., Carloni, A., Rossi, A., & Poletti, V. (2013). Premature lung aging and cellular senescence in the pathogenesis of idiopathic pulmonary fibrosis and COPD/emphysema. *Translational Research*, *162*(3), 156–173. https://doi.org/10.1016/j.trsl.2013.06.004

Chondronasiou, D., Gill, D., Mosteiro, L., Urdinguio, R. G., Berenguer-Llergo, A., Aguilera, M., … Serrano, M. (2022). Multi-omic rejuvenation of naturally aged tissues by a single cycle of transient reprogramming. *Aging Cell*, *21*(3). https://doi.org/10.1111/acel.13578

Comfort, N., Bloomquist, T. R., Shephard, A. P., Petty, C. R., Cunningham, A., Hauptman, M., … Baccarelli, A. (2021). Isolation and characterization of extracellular vesicles in saliva of children with asthma. *Extracellular Vesicles and Circulating Nucleic Acids*. https://doi.org/10.20517/evcna.2020.09

Courtot, A.-M., Magniez, A., Oudrhiri, N., Féraud, O., Bacci, J., Gobbo, E., Bennaceur-Griscelli, A. (2014). Morphological Analysis of Human Induced Pluripotent Stem Cells During Induced Differentiation and Reverse Programming. *BioResearch Open Access*, *3*(5), 206–216. https://doi.org/10.1089/biores.2014.0028

Dahl, S. L. M., Koh, J., Prabhakar, V., & Niklason, L. E. (2003). Decellularized Native and Engineered Arterial Scaffolds for Transplantation. *Cell Transplantation*, *12*(6), 659–666. https://doi.org/10.3727/000000003108747136

Dai, Q., Jiang, W., Huang, F., Song, F., Zhang, J., & Zhao, H. (2022). Recent Advances in Liver Engineering With Decellularized Scaffold. *Frontiers in Bioengineering and Biotechnology*, *10*. https://doi.org/10.3389/fbioe.2022.831477

De Coppi, P., Bartsch, G., Siddiqui, M. M., Xu, T., Santos, C. C., Perin, L., … Atala, A. (2007). Isolation of amniotic stem cell lines with potential for therapy. *Nature Biotechnology*, *25*(1), 100–106. https://doi.org/10.1038/nbt1274

de la Torre Gomez, C., Goreham, R. V., Bech Serra, J. J., Nann, T., & Kussmann, M. (2018). "Exosomics"—A Review of Biophysics, Biology and Biochemistry of Exosomes With a

Focus on Human Breast Milk. *Frontiers in Genetics*, *9*. https://doi.org/10.3389/fgene.2018.00092

de Lima Camillo, L. P., & Quinlan, R. B. A. (2021). A ride through the epigenetic landscape: aging reversal by reprogramming. *GeroScience*. https://doi.org/10.1007/s11357-021-00358-6

Debutify. (2022, September 19). The 9+1 Hallmarks of Aging and How to Reverse Them. Retrieved October 10, 2023, from Biohacker Center Store website: https://biohackercenter.com/blogs/biohacking-guides/91-hallmarks-aging-reverse-them

Diomede, F., Zini, N., Pizzicannella, J., Merciaro, I., Pizzicannella, G., D'Orazio, M., … Trubiani, O. (2018). 5-Aza Exposure Improves Reprogramming Process Through Embryoid Body Formation in Human Gingival Stem Cells. *Frontiers in Genetics*, *9*, 419. https://doi.org/10.3389/fgene.2018.00419

Dodig, S., Čepelak, I., & Pavić, I. (2019). Hallmarks of senescence and aging. *Biochemia Medica*, *29*(3), 483–497. https://doi.org/10.11613/bm.2019.030501

Dodson, R. B., Rozance, P. J., Fleenor, B. S., Petrash, C. C., Shoemaker, L. G., Hunter, K. S., & Ferguson, V. L. (2012). Increased arterial stiffness and extracellular matrix reorganization in intrauterine growth–restricted fetal sheep. *Pediatric Research*, *73*(2), 147–154. https://doi.org/10.1038/pr.2012.156

Dooling, L. J., Saini, K., Anlaş, A. A., & Discher, D. E. (2022). Tissue mechanics coevolves with fibrillar matrisomes in healthy and fibrotic tissues. *Matrix Biology*, *111*, 153–188. https://doi.org/10.1016/j.matbio.2022.06.006

Doyle, L., & Wang, M. (2019). Overview of Extracellular Vesicles, Their Origin, Composition, Purpose, and Methods for Exosome Isolation and Analysis. *Cells*, *8*(7), 727. https://doi.org/10.3390/cells8070727

Duck, F. A. (2013). *Physical Properties of Tissues*. Academic Press.

Durbeej, M. (2009). Laminins. *Cell and Tissue Research*, *339*(1), 259–268. https://doi.org/10.1007/s00441-009-0838-2

Dziechciaż, M., & Filip, R. (2014). Biological psychological and social determinants of old age: Bio-psycho-social aspects of human aging. *Annals of Agricultural and Environmental Medicine*, *21*(4), 835–838. https://doi.org/10.5604/12321966.1129943

Echeverria Molina, M. I., Malollari, K. G., & Komvopoulos, K. (2021). Design Challenges in Polymeric Scaffolds for Tissue Engineering. *Frontiers in Bioengineering and Biotechnology*, *9*. https://doi.org/10.3389/fbioe.2021.617141

Efroni, S., Duttagupta, R., Cheng, J., Dehghani, H., Hoeppner, D. J., Dash, C., Meshorer, E. (2008). Global Transcription in Pluripotent Embryonic Stem Cells. *Cell Stem Cell*, *2*(5), 437–447. https://doi.org/10.1016/j.stem.2008.03.021

Eleonore C.L. Bolle, Bartnikowski, N., Parvathi Haridas, Parker, T. J., Fraser, J. F., Gregory, S. D., & Dargaville, T. R. (2020). *Improving skin integration around long-term percutaneous devices using fibrous scaffolds in a reconstructed human skin equivalent model*. *108*(3), 738–749. https://doi.org/10.1002/jbm.b.34428

Ewald, C. (2019). The Matrisome during Aging and Longevity: A Systems-Level Approach toward Defining Matreotypes Promoting Healthy Aging. *Gerontology*, 1–9. https://doi.org/10.1159/000504295

Fafián-Labora, J. A., Rodríguez-Navarro, J. A., & O'Loghlen, A. (2020). Small Extracellular Vesicles Have GST Activity and Ameliorate Senescence-Related Tissue Damage. *Cell Metabolism*, *32*(1), 71-86.e5. https://doi.org/10.1016/j.cmet.2020.06.004

Fernández-Pérez, J., & Ahearne, M. (2019). The impact of decellularization methods on extracellular matrix derived hydrogels. *Scientific Reports*, *9*(1). https://doi.org/10.1038/s41598-019-49575-2

Fischer, M. A., Mahajan, A., Cabaj, M., Kimball, T. H., Morselli, M., Soehalim, E., Vondriska, T. M. (2022). DNA Methylation-Based Prediction of Post-operative Atrial Fibrillation. *Frontiers in Cardiovascular Medicine*, *9*. https://doi.org/10.3389/fcvm.2022.837725

Fleenor, B. S. (2012). Large elastic artery stiffness with aging: novel translational mechanisms and interventions. *Aging and Disease*, *4*(2), 76–83. Retrieved from https://www.ncbi.nlm.nih.gov/pmc/articles/PMC3659253/

Fraile, M., Eiro, N., Costa, L. A., Martín, A., & Vizoso, F. J. (2022). Aging and Mesenchymal Stem Cells: Basic Concepts, Challenges and Strategies. *Biology*, *11*(11), 1678. https://doi.org/10.3390/biology11111678

Frantz, C., Stewart, K. M., & Weaver, V. M. (2010). The extracellular matrix at a glance. *Journal of Cell Science*, *123*(24), 4195–4200. https://doi.org/10.1242/jcs.023820

Gailhouste, L., Liew, L. C., Hatada, I., Nakagama, H., & Ochiya, T. (2018). Epigenetic reprogramming using 5-azacytidine promotes an anti-cancer response in pancreatic adenocarcinoma cells. *Cell Death & Disease*, *9*(5). https://doi.org/10.1038/s41419-018-0487-z

Gandolfi, F., Arcuri, S., Pennarossa, G., & Brevini, T. A. L. (2019). New tools for cell reprogramming and conversion: Possible applications to livestock. *Animal Reproduction*, *16*(3), 475–484. https://doi.org/10.21451/1984-3143-ar2019-0043

Gardiner, C., Ferreira, Y. J., Dragovic, R. A., Redman, C. W. G., & Sargent, I. L. (2013). Extracellular vesicle sizing and enumeration by nanoparticle tracking analysis. *Journal of Extracellular Vesicles*, *2*(1), 19671. https://doi.org/10.3402/jev.v2i0.19671

Gardiner, C., Vizio, D. D., Sahoo, S., Théry, C., Witwer, K. W., Wauben, M., & Hill, A. F. (2016). Techniques used for the isolation and characterization of extracellular vesicles: results of a worldwide survey. *Journal of Extracellular Vesicles*, *5*(1), 32945. https://doi.org/10.3402/jev.v5.32945

Gattazzo, F., Urciuolo, A., & Bonaldo, P. (2014). Extracellular matrix: A dynamic microenvironment for stem cell niche. *Biochimica et Biophysica Acta (BBA) - General Subjects*, *1840*(8), 2506–2519. https://doi.org/10.1016/j.bbagen.2014.01.010

Gillette, R., Son, M. J., Ton, L., Gore, A. C., & Crews, D. (2018). Passing experiences on to future generations: endocrine disruptors and transgenerational inheritance of epimutations in brain and sperm. *Epigenetics*, *13*(10-11), 1106–1126. https://doi.org/10.1080/15592294.2018.1543506

Gilpin, A., & Yang, Y. (2017). Decellularization Strategies for Regenerative Medicine: From Processing Techniques to Applications. *BioMed Research International*, *2017*, 1–13. https://doi.org/10.1155/2017/9831534

Gimenez, A., Storrer, K., Kuranishi, L., Soares, M. R., Ferreira, R. G., & Pereira, C. A. C. (2018). Change in FVC and survival in chronic fibrotic hypersensitivity pneumonitis. *Thorax*, *73*(4), 391–392. https://doi.org/10.1136/thoraxjnl-2017-210035

Goh, S.-K., Bertera, S., Richardson, T., & Banerjee, I. (2023). Repopulation of decellularized organ scaffolds with human pluripotent stem cell-derived pancreatic progenitor cells. *Biomedical Materials (Bristol, England)*, *18*(2). https://doi.org/10.1088/1748-605X/acb7bf

Gollavilli, P. N., Parma, B., Siddiqui, A., Yang, H., Ramesh, V., Napoli, F., Ceppi, P. (2021). The role of miR-200b/c in balancing EMT and proliferation revealed by an activity reporter. *Oncogene*, *40*(12), 2309–2322. https://doi.org/10.1038/s41388-021-01708-6

Greenwell, J. C., Torres-Gonzalez, E., Ritzenthaler, J. D., & Roman, J. (2020). Interplay between aging, lung inflammation/remodeling, and fibronectin EDA in lung cancer progression. *Cancer Biology & Therapy*, *21*(12), 1109–1118. https://doi.org/10.1080/15384047.2020.1831372

Gruhn, W. H., Walfred W.C. Tang, Dietmann, S., João Pedro Alves-Lopes, Penfold, C. A., Wong, F. C. K., … M. Azim Surani. (2023). Epigenetic resetting in the human germ line entails histone modification remodeling. *Science Advances*, *9*(3). https://doi.org/10.1126/sciadv.ade1257

Guo, J., Huang, X., Dou, L., Yan, M., Shen, T., Tang, W., & Li, J. (2022). Aging and aging-related diseases: from molecular mechanisms to interventions and treatments. *Signal Transduction and Targeted Therapy*, *7*(1). https://doi.org/10.1038/s41392-022-01251-0

Hardt, M., Zatloukal, K., & Popper, H. (2023). Abstract 3614: 3D model to study migration and invasion of lung cancer. *Cancer Research*, *83*(7_Supplement), 3614–3614. https://doi.org/10.1158/1538-7445.am2023-3614

Harman, D. (1981). The aging process. *Proceedings of the National Academy of Sciences*, *78*(11), 7124–7128. https://doi.org/10.1073/pnas.78.11.7124

Harris, D. M., Hazan-Haley, I., Coombes, K., Bueso-Ramos, C., Liu, J., Liu, Z., Estrov, Z. (2011). Transformation of human mesenchymal cells and skin fibroblasts into hematopoietic cells. *PloS One*, *6*(6), e21250. https://doi.org/10.1371/journal.pone.0021250

Hassanpour, A., Talaei-Khozani, T., Kargar-Abarghouei, E., Razban, V., & Vojdani, Z. (2018). Decellularized human ovarian scaffold based on a sodium lauryl ester sulfate (SLES)-treated protocol, as a natural three-dimensional scaffold for construction of bioengineered ovaries. *Stem Cell Research & Therapy*, *9*. https://doi.org/10.1186/s13287-018-0971-5

He, Y., & Lu, F. (2016). Development of Synthetic and Natural Materials for Tissue Engineering Applications Using Adipose Stem Cells. *Stem Cells International*, *2016*, 1–12. https://doi.org/10.1155/2016/5786257

Hernandez-Segura, A., Nehme, J., & Demaria, M. (2018). Hallmarks of Cellular Senescence. *Trends in Cell Biology*, *28*(6), 436–453. https://doi.org/10.1016/j.tcb.2018.02.001

Hillebrandt, K. H., Everwien, H., Haep, N., Keshi, E., Pratschke, J., & Sauer, I. M. (2019). Strategies based on organ decellularization and recellularization. *Transplant International*. https://doi.org/10.1111/tri.13462

Hinderer, S., Layland, S. L., & Schenke-Layland, K. (2016). ECM and ECM-like materials — Biomaterials for applications in regenerative medicine and cancer therapy. *Advanced Drug Delivery Reviews*, *97*, 260–269. https://doi.org/10.1016/j.addr.2015.11.019

Hirshfeld-Cytron, J., Duncan, F. E., Xu, M., Jozefik, J. K., Anseth, K. S., & Woodruff, T. K. (2011). *Animal age, weight and estrus cycle stage impact the quality of in vitro grown follicles*. *26*(9), 2473–2485. https://doi.org/10.1093/humrep/der183

Hore, P. J., & Mouritsen, H. (2016). The Radical-Pair Mechanism of Magnetoreception. *Annual Review of Biophysics*, *45*(1), 299–344. https://doi.org/10.1146/annurev-biophys-032116-094545

Hu, C., Zhang, X., Hu, M., Teng, T., Yao, Y., Song, P., Tang, Q. (2022). Fibronectin type III domain-containing 5 improves aging-related cardiac dysfunction in mice. *Aging Cell*, *21*(3). https://doi.org/10.1111/acel.13556

Huang, H.-N., Chen, S.-Y., Hwang, S.-M., Yu, C.-C., Su, M.-W., Mai, W., Lu, J. (2014). miR-200c and GATA binding protein 4 regulate human embryonic stem cell renewal and differentiation. *Stem Cell Research*, *12*(2), 338–353. https://doi.org/10.1016/j.scr.2013.11.009

Ismagulov, G., Hamidi, S., & Sheng, G. (2021). Epithelial-Mesenchymal Transition Drives Three-Dimensional Morphogenesis in Mammalian Early Development. *Frontiers in Cell and Developmental Biology*, *9*. https://doi.org/10.3389/fcell.2021.639244

Jenkins, T. L., & Little, D. (2019). Synthetic scaffolds for musculoskeletal tissue engineering: cellular responses to fiber parameters. *Npj Regenerative Medicine*, *4*(1). https://doi.org/10.1038/s41536-019-0076-5

Jensen, C., & Teng, Y. (2020). Is It Time to Start Transitioning From 2D to 3D Cell Culture? *Frontiers in Molecular Biosciences*, *7*, 33. https://doi.org/10.3389/fmolb.2020.00033

Jo, Y., Hwang, S. H., & Jang, J. (2021). Employing Extracellular Matrix-Based Tissue Engineering Strategies for Age-Dependent Tissue Degenerations. *International Journal of Molecular Sciences*, *22*(17), 9367. https://doi.org/10.3390/ijms22179367

Kamatar, A., Gunay, G., & Acar, H. (2020). Natural and Synthetic Biomaterials for Engineering Multicellular Tumor Spheroids. *Polymers*, *12*(11), 2506. https://doi.org/10.3390/polym12112506

Kapałczyńska, M., Kolenda, T., Przybyła, W., Zajączkowska, M., Teresiak, A., Filas, V., Lamperska, K. (2016). 2D and 3D cell cultures – a comparison of different types of cancer cell cultures. *Archives of Medical Science*, *14*(4). https://doi.org/10.5114/aoms.2016.63743

Karamanos, N. K., Theocharis, A. D., Piperigkou, Z., Manou, D., Passi, A., Skandalis, S. S., … Onisto, M. (2021). A guide to the composition and functions of the extracellular matrix. *The FEBS Journal*, *288*(24). https://doi.org/10.1111/febs.15776

Karsdal, M. A., Manon-Jensen, T., Genovese, F., Kristensen, J. H., Nielsen, M. J., Sand, J. M. B., … Schuppan, D. (2015). Novel insights into the function and dynamics of extracellular matrix in liver fibrosis. *American Journal of Physiology-Gastrointestinal and Liver Physiology*, *308*(10), G807–G830. https://doi.org/10.1152/ajpgi.00447.2014

Keane, T. J., Swinehart, I. T., & Badylak, S. F. (2015). Methods of tissue decellularization used for preparation of biologic scaffolds and in vivo relevance. *Methods*, *84*, 25–34. https://doi.org/10.1016/j.ymeth.2015.03.005

Kesireddy, V., & Kasper, F. K. (2016). Approaches for building bioactive elements into synthetic scaffolds for bone tissue engineering. *Journal of Materials Chemistry B*, *4*(42), 6773–6786. https://doi.org/10.1039/C6TB00783J

Kim, J. W., Nam, S. A., Yi, J., Kim, J. Y., Lee, J. Y., Park, S., Kim, Y. K. (2022). Kidney Decellularized Extracellular Matrix Enhanced the Vascularization and Maturation of Human Kidney Organoids. *Advanced Science*, *9*(15), 2103526. https://doi.org/10.1002/advs.202103526

King, E., Richter, C., Daniels, K., Miller, A. F., Myer, G., & Strike, S. (2021). "Can Biomechanical Testing After ACLR Identify Athletes at Risk for Subsequent ACL Injury to the Contralateral Uninjured Limb?" and "Biomechanical but Not Strength or Performance Measures Differentiate Male Athletes Who Experience ACL Reinjury on Return to Level 1 Sports": Response. *The American Journal of Sports Medicine*, *49*(9), NP36–NP37. https://doi.org/10.1177/03635465211021400

Kohane, D. S., & Langer, R. (2008). Polymeric Biomaterials in Tissue Engineering. *Pediatric Research*, *63*(5), 487–491. https://doi.org/10.1203/01.pdr.0000305937.26105.e7

Kojima, H., Tanigawa, N., Komemushi, A., Kariya, S., & Sawada, S. (2004). Computed tomography perfusion of the liver: assessment of pure portal blood flow studied with CT perfusion during superior mesenteric arterial portography. *Acta Radiologica (Stockholm, Sweden: 1987)*, *45*(7), 709–715. https://doi.org/10.1080/02841850410001385

Krishani, M., Shin, W. Y., Suhaimi, H., & Sambudi, N. S. (2023). Development of Scaffolds from Bio-Based Natural Materials for Tissue Regeneration Applications: A Review. *Gels*, *9*(2), 100. https://doi.org/10.3390/gels9020100

Krizhanovsky, V., Yon, M., Dickins, R. A., Hearn, S., Simon, J., Miething, C., Lowe, S. W. (2008). Senescence of Activated Stellate Cells Limits Liver Fibrosis. *Cell*, *134*(4), 657–667. https://doi.org/10.1016/j.cell.2008.06.049

Kular, J. K., Basu, S., & Sharma, R. I. (2014). The extracellular matrix: Structure, composition, age-related differences, tools for analysis and applications for tissue engineering. *Journal of Tissue Engineering*, *5*, 204173141455711. https://doi.org/10.1177/2041731414557112

Kutten, J. C., McGovern, D., Hobson, C. M., Luffy, S. A., Nieponice, A., Tobita, K., Gilbert, T. W. (2015). Decellularized Tracheal Extracellular Matrix Supports Epithelial Migration, Differentiation, and Function. *Tissue Engineering Part A*, *21*(1-2), 75–84. https://doi.org/10.1089/ten.tea.2014.0089

Kwok, Z. H., Wang, C., & Jin, Y. (2021). Extracellular Vesicle Transportation and Uptake by Recipient Cells: A Critical Process to Regulate Human Diseases. *Processes*, *9*(2), 273. https://doi.org/10.3390/pr9020273

LaFoya, B., Munroe, J. A., Miyamoto, A., Michael Allen Detweiler, Crow, J. J., Tana Ranae Gazdik, & Albig, A. R. (2018). Beyond the Matrix: The Many Non-ECM Ligands for Integrins. *International Journal of Molecular Sciences*, *19*(2), 449–449. https://doi.org/10.3390/ijms19020449

Lecht, S., Stabler, C. T., Rylander, A. L., Chiaverelli, R., Schulman, E. S., Marcinkiewicz, C., & Lelkes, P. I. (2014). Enhanced reseeding of decellularized rodent lungs with mouse embryonic stem cells. *Biomaterials*, *35*(10), 3252–3262. https://doi.org/10.1016/j.biomaterials.2013.12.093

Lee, D. H., Oh, J.-H., & Chung, J. H. (2016). Glycosaminoglycan and proteoglycan in skin aging. *Journal of Dermatological Science*, *83*(3), 174–181. https://doi.org/10.1016/j.jdermsci.2016.05.016

Lee, J. S., Choi, Y. S., & Cho, S.-W. (2018). Decellularized Tissue Matrix for Stem Cell and Tissue Engineering. *Advances in Experimental Medicine and Biology*, *1064*, 161–180. https://doi.org/10.1007/978-981-13-0445-3_10

Lee, Y. J., Vega, S. L., Patel, P. J., Aamer, K. A., Moghe, P. V., & Cicerone, M. T. (2014). Quantitative, Label-Free Characterization of Stem Cell Differentiation at the Single-Cell Level by Broadband Coherent Anti-Stokes Raman Scattering Microscopy. *Tissue Engineering Part C: Methods*, *20*(7), 562–569. https://doi.org/10.1089/ten.tec.2013.0472

Leslie, S., Winney, B., Hellenthal, G., Davison, D., Boumertit, A., Day, T., Bodmer, W. (2015). The fine-scale genetic structure of the British population. *Nature*, *519*(7543), 309–314. https://doi.org/10.1038/nature14230

Levi, N., Papismadov, N., Solomonov, I., Sagi, I., & Krizhanovsky, V. (2020). The ECM path of senescence in aging: components and modifiers. *The FEBS Journal*, *287*(13), 2636–2646. https://doi.org/10.1111/febs.15282

Li, L., Wei, J.-R., Dong, J., Lin, Q.-G., Tang, H., Jia, Y.-X., Guan, X.-Y. (2021). Laminin γ2-mediating T cell exclusion attenuates response to anti-PD-1 therapy. *Science Advances*, *7*(6), eabc8346. https://doi.org/10.1126/sciadv.abc8346

Liang, G., & Zhang, Y. (2012). Embryonic stem cell and induced pluripotent stem cell: an epigenetic perspective. *Cell Research*, *23*(1), 49–69. https://doi.org/10.1038/cr.2012.175

Lliberos, C., Liew, S. H., Zareie, P., La Gruta, N. L., Mansell, A., & Hutt, K. (2021). Evaluation of inflammation and follicle depletion during ovarian ageing in mice. *Scientific Reports*, *11*(1), 278. https://doi.org/10.1038/s41598-020-79488-4

López-Otín, C., Blasco, M. A., Partridge, L., Serrano, M., & Kroemer, G. (2013). The Hallmarks of Aging. *Cell*, *153*(6), 1194–1217. https://doi.org/10.1016/j.cell.2013.05.039

Mahon, O. R., Browe, D. C., Diaz-Payno, P. J., Pitacco, P., Cunningham, K. T., Mills, K. H. G., Kelly, D. J. (2021). Extracellular matrix scaffolds derived from different musculoskeletal tissues drive distinct macrophage phenotypes and direct tissue-specific cellular differentiation. *Journal of Immunology and Regenerative Medicine*, *12*, 100041. https://doi.org/10.1016/j.regen.2021.100041

Mallis, P., Chachlaki, P., Katsimpoulas, M., Stavropoulos-Giokas, C., & Michalopoulos, E. (2018). Optimization of Decellularization Procedure in Rat Esophagus for Possible Development of a Tissue Engineered Construct. *Bioengineering*, *6*(1), 3. https://doi.org/10.3390/bioengineering6010003

Manzoni, E. F. M., Pennarossa, G., deEguileor, M., Tettamanti, G., Gandolfi, F., & Brevini, T. A. L. (2016). 5-azacytidine affects TET2 and histone transcription and reshapes morphology of human skin fibroblasts. *Scientific Reports*, *6*(1). https://doi.org/10.1038/srep37017

Matoba, S., & Zhang, Y. (2018). Somatic Cell Nuclear Transfer Reprogramming: Mechanisms and Applications. *Cell Stem Cell*, *23*(4), 471–485. https://doi.org/10.1016/j.stem.2018.06.018

Matthias Hebisch, Klostermeier, S., Wolf, K., Boccaccini, A. R., Wolf, S. E., Tanzi, R. E., & Doo Yeon Kim. (2023). *The Impact of the Cellular Environment and Aging on Modeling Alzheimer's Disease in 3D Cell Culture Models*. *10*(8). https://doi.org/10.1002/advs.202205037

Mattson, J. M., Turcotte, R., & Zhang, Y. (2016). Glycosaminoglycans contribute to extracellular matrix fiber recruitment and arterial wall mechanics. *Biomechanics and Modeling in Mechanobiology*, *16*(1), 213–225. https://doi.org/10.1007/s10237-016-0811-4

McCabe, M. C., Hill, R. C., Calderone, K., Cui, Y., Yan, Y., Quan, T., Hansen, K. C. (2020). Alterations in extracellular matrix composition during aging and photoaging of the skin. *Matrix Biology Plus*, 100041. https://doi.org/10.1016/j.mbplus.2020.100041

McCrary, M. W., Bousalis, D., Mobini, S., Song, Y. H., & Schmidt, C. E. (2020). Decellularized tissues as platforms for in vitro modeling of healthy and diseased tissues. *Acta Biomaterialia*, *111*, 1–19. https://doi.org/10.1016/j.actbio.2020.05.031

Merna, N., Robertson, C., La, A., & George, S. C. (2013). Optical Imaging Predicts Mechanical Properties During Decellularization of Cardiac Tissue. *Tissue Engineering Part C: Methods*, *19*(10), 802–809. https://doi.org/10.1089/ten.tec.2012.0720

Meschiari, C. A., Ero, O. K., Pan, H., Finkel, T., & Lindsey, M. L. (2017). The impact of aging on cardiac extracellular matrix. *GeroScience*, *39*(1), 7–18. https://doi.org/10.1007/s11357-017-9959-9

Mirakhori, F., Zeynali, B., Kiani, S., & Baharvand, H. (2015). Brief azacytidine step allows the conversion of suspension human fibroblasts into neural progenitor-like cells. *Cell Journal*, *17*(1), 153–158. https://doi.org/10.22074/cellj.2015.522

Mirakhori, F., Zeynali, B., Rassouli, H., Shahbazi, E., Hashemizadeh, S., Kiani, S., Baharvand, H. (2015). Induction of Neural Progenitor-Like Cells from Human Fibroblasts via a Genetic Material-Free Approach. *PLOS ONE*, *10*(8), e0135479. https://doi.org/10.1371/journal.pone.0135479

Mirsaidi, A., Genelin, K., Vetsch, J. R., Stanger, S., Theiss, F., Lindtner, R. A., … Richards, P. J. (2014). Therapeutic potential of adipose-derived stromal cells in age-related osteoporosis. *Biomaterials*, *35*(26), 7326–7335. https://doi.org/10.1016/j.biomaterials.2014.05.016

Mizutani, E., Torikai, K., Wakayama, S., Nagatomo, H., Ohinata, Y., Kishigami, S., & Wakayama, T. (2016). Generation of cloned mice and nuclear transfer embryonic stem cell lines from urine-derived cells. *Scientific Reports*, *6*(1). https://doi.org/10.1038/srep23808

Monguió-Tortajada, M., Gálvez-Montón, C., Bayes-Genis, A., Roura, S., & Borràs, F. E. (2019). Extracellular vesicle isolation methods: rising impact of size-exclusion chromatography. *Cellular and Molecular Life Sciences*, *76*(12), 2369–2382. https://doi.org/10.1007/s00018-019-03071-y

Morris, A. H., Stamer, D. K., & Kyriakides, T. R. (2017). The host response to naturally-derived extracellular matrix biomaterials. *Seminars in Immunology*, *29*, 72–91. https://doi.org/10.1016/j.smim.2017.01.002

Mossa, F., Walsh, S. W., Butler, S. T., Berry, D. P., Carter, F., Lonergan, P., … Evans, A. C. O. (2012). Low numbers of ovarian follicles ≥3 mm in diameter are associated with low fertility in dairy cows. *Journal of Dairy Science*, *95*(5), 2355–2361. https://doi.org/10.3168/jds.2011-4325

Musale, V., Wasserman, D. H., & Kang, L. (2023). Extracellular matrix remodelling in obesity and metabolic disorders. *Life Metabolism*, *2*(4), load021. https://doi.org/10.1093/lifemeta/load021

Nakayama, K. H., Batchelder, C. A., Lee, C. I., & Tarantal, A. F. (2010). Decellularized Rhesus Monkey Kidney as a Three-Dimensional Scaffold for Renal Tissue Engineering. *Tissue Engineering Part A*, *16*(7), 2207–2216. https://doi.org/10.1089/ten.tea.2009.0602

Napierala, H., Hillebrandt, K.-H. ., Haep, N., Tang, P., Tintemann, M., Gassner, J., … Struecker, B. (2017). Engineering an endocrine Neo-Pancreas by repopulation of a decellularized rat pancreas with islets of Langerhans. *Scientific Reports*, *7*, 41777. https://doi.org/10.1038/srep41777

Narciso, M., Ulldemolins, A., Júnior, C., Otero, J., Navajas, D., Farré, R., … Almendros, I. (2022). Novel Decellularization Method for Tissue Slices. *Frontiers in Bioengineering and Biotechnology*, *10*. https://doi.org/10.3389/fbioe.2022.832178

Natarajan, E., Omobono, J. D., Guo, Z., Hopkinson, S., Lazar, A. J. F., Brenn, T., … Rheinwald, J. G. (2006). A Keratinocyte Hypermotility/Growth-Arrest Response Involving Laminin 5 and p16INK4A Activated in Wound Healing and Senescence. *The American Journal of Pathology*, *168*(6), 1821–1837. https://doi.org/10.2353/ajpath.2006.051027

Neishabouri, A., Soltani Khaboushan, A., Daghigh, F., Kajbafzadeh, A.-M., & Majidi Zolbin, M. (2022). Decellularization in Tissue Engineering and Regenerative Medicine: Evaluation, Modification, and Application Methods. *Frontiers in Bioengineering and Biotechnology*, *10*. https://doi.org/10.3389/fbioe.2022.805299

Nikolova, M. P., & Chavali, M. S. (2019). Recent advances in biomaterials for 3D scaffolds: A review. *Bioactive Materials*, *4*, 271–292. https://doi.org/10.1016/j.bioactmat.2019.10.005

Nikolovski, J., & Mooney, D. J. (2000). Smooth muscle cell adhesion to tissue engineering scaffolds. *Biomaterials*, *21*(20), 2025–2032. https://doi.org/10.1016/s0142-9612(00)00079-x

Niwa, H. (2007). How is pluripotency determined and maintained? *Development*, *134*(4), 635–646. https://doi.org/10.1242/dev.02787

O'Brien, J., Hayder, H., Zayed, Y., & Peng, C. (2018). Overview of MicroRNA Biogenesis, Mechanisms of Actions, and Circulation. *Frontiers in Endocrinology*, *9*(402). https://doi.org/10.3389/fendo.2018.00402

O'Connor, B. B., Pope, B. D., Peters, M. M., Ris-Stalpers, C., & Parker, K. K. (2020). The role of extracellular matrix in normal and pathological pregnancy: Future applications of microphysiological systems in reproductive medicine. *Experimental Biology and Medicine*, *245*(13), 1163–1174. https://doi.org/10.1177/1535370220938741

O'Loghlen, A. (2022). The potential of aging rejuvenation. *Cell Cycle*, *21*(2), 111–116. https://doi.org/10.1080/15384101.2021.2013612

Ott, H. C., Clippinger, B., Conrad, C., Schuetz, C., Pomerantseva, I., Ikonomou, L., … Vacanti, J. P. (2010). Regeneration and orthotopic transplantation of a bioartificial lung. *Nature Medicine*, *16*(8), 927–933. https://doi.org/10.1038/nm.2193

Ott, H. C., Matthiesen, T. S., Goh, S.-K., Black, L. D., Kren, S. M., Netoff, T. I., & Taylor, D. A. (2008). Perfusion-decellularized matrix: using nature's platform to engineer a bioartificial heart. *Nature Medicine*, *14*(2), 213–221. https://doi.org/10.1038/nm1684

Ouni, E., Bouzin, C., Dolmans, M. M., Marbaix, E., Pyr dit Ruys, S., Vertommen, D., & Amorim, C. A. (2020). Spatiotemporal changes in mechanical matrisome components of the human ovary from prepuberty to menopause. *Human Reproduction*, *35*(6), 1391–1410. https://doi.org/10.1093/humrep/deaa100

Ouyang, M., Yu, J., Chen, Y., Deng, L., & Guo, C.-L. (2021). Cell-extracellular matrix interactions in the fluidic phase direct the topology and polarity of self-organized epithelial structures. *Cell Proliferation*, *54*(4). https://doi.org/10.1111/cpr.13014

Pampaloni, F., Reynaud, E. G., & Stelzer, E. H. K. (2007). The third dimension bridges the gap between cell culture and live tissue. *Nature Reviews. Molecular Cell Biology*, *8*(10), 839–845. https://doi.org/10.1038/nrm2236

Pankov, R. (2002). Fibronectin at a glance. *Journal of Cell Science*, *115*(20), 3861–3863. https://doi.org/10.1242/jcs.00059

Parisi, L., Toffoli, A., Ghezzi, B., Mozzoni, B., Lumetti, S., & Macaluso, G. M. (2020). A glance on the role of fibronectin in controlling cell response at biomaterial interface. *Japanese Dental Science Review*, *56*(1), 50–55. https://doi.org/10.1016/j.jdsr.2019.11.002

Park, K.-M., Hussein, K. H., Hong, S.-H., Ahn, C., Yang, S.-R., Park, S.-M., … Woo, H.-M. (2016). Decellularized Liver Extracellular Matrix as Promising Tools for Transplantable Bioengineered Liver Promotes Hepatic Lineage Commitments of Induced Pluripotent Stem Cells. *Tissue Engineering Part A*, *22*(5-6), 449–460. https://doi.org/10.1089/ten.tea.2015.0313

Pennarossa, G., Arcuri, S., De Iorio, T., Gandolfi, F., & Brevini, T. A. L. (2021). Current Advances in 3D Tissue and Organ Reconstruction. *International Journal of Molecular Sciences*, *22*(2), 830. https://doi.org/10.3390/ijms22020830

Pennarossa, G., Arcuri, S., De Iorio, T., Ledda, S., Gandolfi, F., & Brevini, T. A. L. (2023). Combination of epigenetic erasing and mechanical cues to generate human epiBlastoids from adult dermal fibroblasts. *Journal of Assisted Reproduction and Genetics*, *40*(5), 1015–1027. https://doi.org/10.1007/s10815-023-02773-4

Pennarossa, G., De Iorio, T., Arcuri, S., Gandolfi, F., & Brevini, T. A. L. (2023). Synergistic Effect of miR-200 and Young Extracellular Matrix-based Bio-scaffolds to Reduce Signs of Aging in Senescent Fibroblasts. *Stem Cell Reviews and Reports*, *19*(2), 417–429. https://doi.org/10.1007/s12015-022-10438-5

Pennarossa, G., De Iorio, T., Gandolfi, F., & Brevini, T. A. L. (2021). Ovarian Decellularized Bioscaffolds Provide an Optimal Microenvironment for Cell Growth and Differentiation In Vitro. *Cells*, *10*(8), 2126. https://doi.org/10.3390/cells10082126

Pennarossa, G., De Iorio, T., Gandolfi, F., & Brevini, T. A. L. (2022). Impact of Aging on the Ovarian Extracellular Matrix and Derived 3D Scaffolds. *Nanomaterials*, *12*(3), 345. https://doi.org/10.3390/nano12030345

Pennarossa, G., Ghiringhelli, M., Gandolfi, F., & Brevini, T. A. L. (2020). Whole-ovary decellularization generates an effective 3D bioscaffold for ovarian bioengineering. *Journal of Assisted Reproduction and Genetics*, *37*(6), 1329–1339. https://doi.org/10.1007/s10815-020-01784-9

Pennarossa, G., Maffei, S., Campagnol, M., Rahman, M. M., Brevini, T. A. L., & Gandolfi, F. (2014). Reprogramming of pig dermal fibroblast into insulin secreting cells by a brief exposure to 5-aza-cytidine. *Stem Cell Reviews and Reports*, *10*(1), 31–43. https://doi.org/10.1007/s12015-013-9477-9

Pennarossa, G., Maffei, S., Campagnol, M., Tarantini, L., Gandolfi, F., & Brevini, T. A. L. (2013). Brief demethylation step allows the conversion of adult human skin fibroblasts into insulin-secreting cells. *Proceedings of the National Academy of Sciences*, *110*(22), 8948–8953. https://doi.org/10.1073/pnas.1220637110

Perez-Puyana, V., Jiménez-Rosado, M., Romero, A., & Guerrero, A. (2020). Polymer-Based Scaffolds for Soft-Tissue Engineering. *Polymers*, *12*(7), 1566. https://doi.org/10.3390/polym12071566

Philips, C., Terrie, L., & Thorrez, L. (2022). Decellularized skeletal muscle: A versatile biomaterial in tissue engineering and regenerative medicine. *Biomaterials*, *283*, 121436. https://doi.org/10.1016/j.biomaterials.2022.121436

Phillip, J. M., Aifuwa, I., Walston, J., & Wirtz, D. (2015). The Mechanobiology of Aging. *Annual Review of Biomedical Engineering*, *17*(1), 113–141. https://doi.org/10.1146/annurev-bioeng-071114-040829

Pompili, S., Latella, G., Gaudio, E., Sferra, R., & Vetuschi, A. (2021). The Charming World of the Extracellular Matrix: A Dynamic and Protective Network of the Intestinal Wall. *Frontiers in Medicine*, *8*. https://doi.org/10.3389/fmed.2021.610189

Qi, H., Wang, Y., Fa, S., Yuan, C., & Yang, L. (2021). Extracellular Vesicles as Natural Delivery Carriers Regulate Oxidative Stress Under Pathological Conditions. *Frontiers in Bioengineering and Biotechnology*, *9*. https://doi.org/10.3389/fbioe.2021.752019

Raposo, G., & Stoorvogel, W. (2013). Extracellular vesicles: Exosomes, microvesicles, and friends. *The Journal of Cell Biology*, *200*(4), 373–383. https://doi.org/10.1083/jcb.201211138

Ravi, M., Paramesh, V., Kaviya, S. R., Anuradha, E., & Solomon, F. D. P. (2014). 3D Cell Culture Systems: Advantages and Applications. *Journal of Cellular Physiology*, *230*(1), 16–26. https://doi.org/10.1002/jcp.24683

Reddy, M. S. B., Ponnamma, D., Choudhary, R., & Sadasivuni, K. K. (2021). A Comparative Review of Natural and Synthetic Biopolymer Composite Scaffolds. *Polymers*, *13*(7), 1105. https://doi.org/10.3390/polym13071105

Richter, R. P., Baranova, N. S., Day, A. J., & Kwok, J. C. (2018). Glycosaminoglycans in extracellular matrix organisation: are concepts from soft matter physics key to understanding the formation of perineuronal nets? *Current Opinion in Structural Biology*, *50*, 65–74. https://doi.org/10.1016/j.sbi.2017.12.002

Rossiello, F., Jurk, D., Passos, J. F., & d'Adda di Fagagna, F. (2022). Telomere dysfunction in ageing and age-related diseases. *Nature Cell Biology*, *24*(2), 135–147. https://doi.org/10.1038/s41556-022-00842-x

Rozario, T., & DeSimone, D. W. (2010). The extracellular matrix in development and morphogenesis: A dynamic view. *Developmental Biology*, *341*(1), 126–140. https://doi.org/10.1016/j.ydbio.2009.10.026

Rui, Z., Jiang, J., Yu, Y., Wang, F., Gao, N., Zhou, Y., … Mei, J. (2021). Analysis of structural components of decellularized scaffolds in renal fibrosis. *Bioactive Materials*, *6*(7), 2187–2197. https://doi.org/10.1016/j.bioactmat.2020.12.028

Sacher, F., Feregrino, C., Tschopp, P., & Ewald, C. Y. (2021). Extracellular matrix gene expression signatures as cell type and cell state identifiers. *Matrix Biology Plus*, *10*, 100069. https://doi.org/10.1016/j.mbplus.2021.100069

Salbach-Hirsch, J., Rauner, M., Hofbauer, C., & Hofbauer, L. C. (2021). New insights into the role of glycosaminoglycans in the endosteal bone microenvironment. *Biological Chemistry*, *0*(0). https://doi.org/10.1515/hsz-2021-0174

Santoro, M., Shah, S. R., Walker, J. L., & Mikos, A. G. (2016). Poly(lactic acid) nanofibrous scaffolds for tissue engineering. *Advanced Drug Delivery Reviews*, *107*, 206–212. https://doi.org/10.1016/j.addr.2016.04.019

Sareh Rajabi-Zeleti, Hossein Baharvand, Mahnaz Azarnia, Fahimeh Khayyatan, Vahdat, S., Saman Nikeghbalian, … Nasser Aghdami. (2014). The behavior of cardiac progenitor cells on macroporous pericardium-derived scaffolds. *Biomaterials*, *35*(3), 970–982. https://doi.org/10.1016/j.biomaterials.2013.10.045

Sathananthan, H., Pera, M., & Trounson, A. (2002). The fine structure of human embryonic stem cells. *Reproductive Biomedicine Online*, *4*(1), 56–61. https://doi.org/10.1016/s1472-6483(10)61916-5

Scheffer, G. J. (2003). The number of antral follicles in normal women with proven fertility is the best reflection of reproductive age. *Human Reproduction*, *18*(4), 700–706. https://doi.org/10.1093/humrep/deg135

Schmauck-Medina, T., Molière, A., Lautrup, S., Zhang, J., Chlopicki, S., Madsen, H. B., … Rasmussen, L. J. (2022). New hallmarks of ageing: a 2022 Copenhagen ageing meeting summary. *Aging*, *14*(16), 6829–6839. https://doi.org/10.18632/aging.204248

Schnabl, B. (2003). Replicative senescence of activated human hepatic stellate cells is accompanied by a pronounced inflammatory but less fibrogenic phenotype. *Hepatology*, *37*(3), 653–664. https://doi.org/10.1053/jhep.2003.50097

Schwartz, M. A. (2010). Integrins and extracellular matrix in mechanotransduction. *Cold Spring Harbor Perspectives in Biology*, *2*(12), a005066. https://doi.org/10.1101/cshperspect.a005066

Seetapun, D., & Ross, J. J. (2017). Eliminating the organ transplant waiting list: The future with perfusion decellularized organs. *Surgery*, *161*(6), 1474–1478. https://doi.org/10.1016/j.surg.2016.09.041

Sefat, F., Mozafari, M., & Atala, A. (2019, January 1). 1 - Introduction to tissue engineering scaffolds (M. Mozafari, F. Sefat, & A. Atala, Eds.). Retrieved October 10, 2023, from ScienceDirect website: https://www.sciencedirect.com/science/article/abs/pii/B9780081025635000010

Selman, M., & Pardo, A. (2021). Fibroageing: An ageing pathological feature driven by dysregulated extracellular matrix-cell mechanobiology. *Ageing Research Reviews*, *70*, 101393. https://doi.org/10.1016/j.arr.2021.101393

Sherratt, M. J. (2009). Tissue elasticity and the ageing elastic fibre. *AGE*, *31*(4), 305–325. https://doi.org/10.1007/s11357-009-9103-6

Sherratt, M. J. (2013). Age-Related Tissue Stiffening: Cause and Effect. *Advances in Wound Care*, *2*(1), 11–17. https://doi.org/10.1089/wound.2011.0328

Sheta, M., Taha, E. A., Lu, Y., & Eguchi, T. (2023). Extracellular Vesicles: New Classification and Tumor Immunosuppression. *Biology*, *12*(1), 110. https://doi.org/10.3390/biology12010110

Simpson, D. J., Olova, N. N., & Chandra, T. (2021). Cellular reprogramming and epigenetic rejuvenation. *Clinical Epigenetics*, *13*(1). https://doi.org/10.1186/s13148-021-01158-7

Singh, A., Lee, D., Jeong, H., Yu, C., Li, J., Fang, C. H., … Bivalacqua, T. J. (2018). Tissue-Engineered Neo-Urinary Conduit from Decellularized Trachea. *Tissue Engineering Part A*, *24*(19-20), 1456–1467. https://doi.org/10.1089/ten.tea.2017.0436

Singh, P. B., & Newman, A. G. (2018). Age reprogramming and epigenetic rejuvenation. *Epigenetics & Chromatin*, *11*(1). https://doi.org/10.1186/s13072-018-0244-7

Sjöqvist, S., Jungebluth, P., Ling Lim, M., Haag, J. C., Gustafsson, Y., Lemon, G., … Ibarra, C. (2014). Experimental orthotopic transplantation of a tissue-engineered oesophagus in rats. *Nature Communications*, *5*(1). https://doi.org/10.1038/ncomms4562

Skolasinski, S., & Panoskaltsis-Mortari, A. (2017). Decellularization of Intact Lung Tissue Through Vasculature and Airways Using Negative and Positive Pressure. *Methods in Molecular Biology*, 307–315. https://doi.org/10.1007/7651_2017_32

Smith, M. L., Gourdon, D., Little, W. C., Kubow, K. E., Eguiluz, R. A., Luna-Morris, S., & Vogel, V. (2007). Force-Induced Unfolding of Fibronectin in the Extracellular Matrix of Living Cells. *PLoS Biology*, *5*(10), e268. https://doi.org/10.1371/journal.pbio.0050268

Song, J. J., Guyette, J. P., Gilpin, S. E., Gonzalez, G., Vacanti, J. P., & Ott, H. C. (2013). Regeneration and experimental orthotopic transplantation of a bioengineered kidney. *Nature Medicine*, *19*(5), 646–651. https://doi.org/10.1038/nm.3154

Srinivas, N., Rachakonda, S., & Kumar, R. (2020). Telomeres and Telomere Length: A General Overview. *Cancers*, *12*(3), 558. https://doi.org/10.3390/cancers12030558

Takahashi, K., & Yamanaka, S. (2006). Induction of Pluripotent Stem Cells from Mouse Embryonic and Adult Fibroblast Cultures by Defined Factors. *Cell*, *126*(4), 663–676. https://doi.org/10.1016/j.cell.2006.07.024

Tan, Y. H., Helms, H. R., & Nakayama, K. H. (2022). Decellularization Strategies for Regenerating Cardiac and Skeletal Muscle Tissues. *Frontiers in Bioengineering and Biotechnology*, *10*. https://doi.org/10.3389/fbioe.2022.831300

Taylor, D. A., Sampaio, L. C., Ferdous, Z., Gobin, A. S., & Taite, L. J. (2018). Decellularized matrices in regenerative medicine. *Acta Biomaterialia*, *74*, 74–89. https://doi.org/10.1016/j.actbio.2018.04.044

Tehrani, S. S., Zaboli, E., Sadeghi, F., Khafri, S., Karimian, A., Rafie, M., & Parsian, H. (2021). MicroRNA-26a-5p as a potential predictive factor for determining the effectiveness of trastuzumab therapy in HER-2 positive breast cancer patients. *BioMedicine*, *11*(2), 30–39. https://doi.org/10.37796/2211-8039.1150

Theocharis, A. D., Skandalis, S. S., Gialeli, C., & Karamanos, N. K. (2016). Extracellular Matrix Structure. *Advanced Drug Delivery Reviews*, *97*, 4–27. https://doi.org/10.1016/j.addr.2015.11.001

Tosato, M., Zamboni, V., Ferrini, A., & Cesari, M. (2007). The aging process and potential interventions to extend life expectancy. *Clinical Interventions in Aging*, *2*(3), 401–412. https://pubmed.ncbi.nlm.nih.gov/18044191/

United Nations Department of Economic and Social Affairs, Population Division. (2022). *World Population Prospects 2022 Summary of Results*. https://www.un.org/development/desa/pd/sites/www.un.org.development.desa.pd/files/

Uygun, B. E., Soto-Gutierrez, A., Yagi, H., Izamis, M.-L., Guzzardi, M. A., Shulman, C., Uygun, K. (2010). Organ reengineering through development of a transplantable recellularized liver graft using decellularized liver matrix. *Nature Medicine*, *16*(7), 814–820. https://doi.org/10.1038/nm.2170

Vaiserman, A., & Krasnienkov, D. (2021). Telomere Length as a Marker of Biological Age: State-of-the-Art, Open Issues, and Future Perspectives. *Frontiers in Genetics*, *11*. https://doi.org/10.3389/fgene.2020.630186

Veerman, R. E., Teeuwen, L., Czarnewski, P., Güclüler Akpinar, G., Sandberg, A., Cao, X., Eldh, M. (2021). Molecular evaluation of five different isolation methods for extracellular vesicles reveals different clinical applicability and subcellular origin. *Journal of Extracellular Vesicles*, *10*(9). https://doi.org/10.1002/jev2.12128

Veziroglu, E. M., & Mias, G. I. (2020). Characterizing Extracellular Vesicles and Their Diverse RNA Contents. *Frontiers in Genetics*, *11*. https://doi.org/10.3389/fgene.2020.00700

Villata, S., Canta, M., & Cauda, V. (2020). EVs and Bioengineering: From Cellular Products to Engineered Nanomachines. *International Journal of Molecular Sciences*, *21*(17), 6048. https://doi.org/10.3390/ijms21176048

Vogel, R., Coumans, F. A. W., Maltesen, R. G., Böing, A. N., Bonnington, K. E., Broekman, M. L., … de Vrij, J. (2016). A standardized method to determine the concentration of extracellular vesicles using tunable resistive pulse sensing. *Journal of Extracellular Vesicles*, *5*(1), 31242. https://doi.org/10.3402/jev.v5.31242

WADDINGTON, C. H. (1968). Towards a Theoretical Biology. *Nature*, *218*(5141), 525–527. https://doi.org/10.1038/218525a0

Wahlgren, J., Statello, L., Skogberg, G., Esbjörn Telemo, & Hadi Valadi. (2016). Delivery of Small Interfering RNAs to Cells via Exosomes. *Methods in Molecular Biology*, 105–125. https://doi.org/10.1007/978-1-4939-3112-5_10

Wang, G., Guo, X., Hong, W., Liu, Q., Tao, W., Lu, C., Liu, H. (2013). Critical regulation of miR-200/ZEB2 pathway in Oct4/Sox2-induced mesenchymal-to-epithelial transition and induced pluripotent stem cell generation. *Proceedings of the National Academy of Sciences of the United States of America*, *110*(8), 2858–2863. https://doi.org/10.1073/pnas.1212769110

Wang, S. T., Neo, B. H., & Betts, R. J. (2021). Glycosaminoglycans: Sweet as Sugar Targets for Topical Skin Anti-Aging. *Clinical, Cosmetic and Investigational Dermatology*, *Volume 14*, 1227–1246. https://doi.org/10.2147/ccid.s328671

Watt, F. M., & Fujiwara, H. (2011). Cell-Extracellular Matrix Interactions in Normal and Diseased Skin. *Cold Spring Harbor Perspectives in Biology*, *3*(4), a005124–a005124. https://doi.org/10.1101/cshperspect.a005124

Williams, D. F. (2019). Challenges With the Development of Biomaterials for Sustainable Tissue Engineering. *Frontiers in Bioengineering and Biotechnology*, *7*. https://doi.org/10.3389/fbioe.2019.00127

Wilmut, I., Beaujean, N., de Sousa, P. A., Dinnyes, A., King, T. J., Paterson, L. A., Young, L. E. (2002). Somatic cell nuclear transfer. *Nature*, *419*(6907), 583–587. https://doi.org/10.1038/nature01079

Woods, D. C., White, Y. A. R., Niikura, Y., Kiatpongsan, S., Lee, H.-J., & Tilly, J. L. (2013). Embryonic Stem Cell–Derived Granulosa Cells Participate in Ovarian Follicle Formation In Vitro and In Vivo. *Reproductive Sciences*, *20*(5), 524–535. https://doi.org/10.1177/1933719113483017

Wu, C., Zhang, D., Zhang, S., Sun, L., Liu, Y., & Dai, J. (2019). Optimizing treatment of DNA methyltransferase inhibitor RG108 on porcine fibroblasts for somatic cell nuclear transfer. *Reproduction in Domestic Animals*, *54*(12), 1604–1611. https://doi.org/10.1111/rda.13569

Wu, S., Sun, H., Zhang, Q., Jiang, Y., Fang, T., Cui, I., Hu, Y. (2015). MicroRNA-132 promotes estradiol synthesis in ovarian granulosa cells via translational repression of Nurr1. *Reproductive Biology and Endocrinology*, *13*(1). https://doi.org/10.1186/s12958-015-0095-z

Wynn, T. (2008). Cellular and molecular mechanisms of fibrosis. *The Journal of Pathology*, *214*(2), 199–210. https://doi.org/10.1002/path.2277

Wynn, T. A., & Ramalingam, T. R. (2012). Mechanisms of fibrosis: therapeutic translation for fibrotic disease. *Nature Medicine*, *18*(7), 1028–1040. https://doi.org/10.1038/nm.2807

Yan Efrata Sembiring, Rafaela Andira Ledyastatin, Atiya Nurrahmah, Ni Kadek Sulistyaningsih, Sinatra, R., Ito Puruhito, & Heri Suroto. (2022). Comparative Assessment of Various Concentration and Exposure Time of Sodium Dodecyl Sulfate as

Decellularization Agents for Small-Vessels Vascular Tissue Engineering. *Open Access Macedonian Journal of Medical Sciences*, *10*(B), 1–9. https://doi.org/10.3889/oamjms.2022.9396

Yang, B., Zhang, Y., Zhou, L., Sun, Z., Zheng, J., Chen, Y., & Dai, Y. (2010). Development of a Porcine Bladder Acellular Matrix with Well-Preserved Extracellular Bioactive Factors for Tissue Engineering. *Tissue Engineering Part C: Methods*, *16*(5), 1201–1211. https://doi.org/10.1089/ten.tec.2009.0311

Yoshida, M., Satoh, A., Lin, J. B., Mills, K. F., Sasaki, Y., Rensing, N., Imai, S.-I. (2019). Extracellular Vesicle-Contained eNAMPT Delays Aging and Extends Lifespan in Mice. *Cell Metabolism*, *30*(2), 329-342.e5. https://doi.org/10.1016/j.cmet.2019.05.015

Yue, B. (2014). Biology of the Extracellular Matrix. *Journal of Glaucoma*, *23*(8), S20–S23. https://doi.org/10.1097/ijg.0000000000000108

Zhang, M., Wang, Y., Matyunina, L. V., Akbar, A., & McDonald, J. F. (2020). The ability of miRNAs to induce mesenchymal-to-epithelial transition (MET) in cancer cells is highly dependent upon genetic background. *Cancer Letters*, *480*, 15–23. https://doi.org/10.1016/j.canlet.2020.03.023

Zhang, T., Lin, S., Shao, X., Zhang, Q., Xue, C., Zhang, S., Cai, X. (2017). Effect of matrix stiffness on osteoblast functionalization. *Cell Proliferation*, *50*(3), e12338. https://doi.org/10.1111/cpr.12338

Zhang, W., Liu, Y., & Zhang, H. (2021). Extracellular matrix: an important regulator of cell functions and skeletal muscle development. *Cell & Bioscience*, *11*(1). https://doi.org/10.1186/s13578-021-00579-4

Zhang, X., Chen, X., Hong, H., Hu, R., Liu, J., & Liu, C. (2022). Decellularized extracellular matrix scaffolds: Recent trends and emerging strategies in tissue engineering. *Bioactive Materials*, *10*, 15–31. https://doi.org/10.1016/j.bioactmat.2021.09.014

Zhou, Y., Horowitz, J. C., Naba, A., Ambalavanan, N., Atabai, K., Balestrini, J., White, E. S. (2018). Extracellular matrix in lung development, homeostasis and disease. *Matrix Biology*, *73*, 77–104. https://doi.org/10.1016/j.matbio.2018.03.005

Zhou, Y., & Hu, Z. (2016). Epigenetic DNA Demethylation Causes Inner Ear Stem Cell Differentiation into Hair Cell-Like Cells. *Frontiers in Cellular Neuroscience*, *10*. https://doi.org/10.3389/fncel.2016.00185

Zhu, Z., Wu, X., Li, Q., Zhang, J., Yu, S., Shen, Q., Chen, X. (2021). Histone demethylase complexes KDM3A and KDM3B cooperate with OCT4/SOX2 to define a pluripotency gene regulatory network. *FASEB Journal: Official Publication of the Federation of American Societies for Experimental Biology*, *35*(6), e21664. https://doi.org/10.1096/fj.202100230R

# 7. Supplementary works

This chapter is dedicated to the works I had the pleasure to collaborate during my PhD studies.

## 7.1. Current advances in 3D Tissue and Organ Reconstruction

Published in International Journal of Molecular Science on 15 January 2021.

DOI: 10.3390/ijms22020830.

*Review*

# Current Advances in 3D Tissue and Organ Reconstruction

**Georgia Pennarossa [1], Sharon Arcuri [1], Teresina De Iorio [1], Fulvio Gandolfi [2] and Tiziana A.L. Brevini [1,*]**

[1] Laboratory of Biomedical Embryology, Department of Health, Animal Science and Food Safety and Center for Stem Cell Research, Università degli Studi di Milano, via Celoria 10, 20133 Milan, Italy; georgia.pennarossa@unimi.it (G.P.); Sharon.arcuri@unimi.it (S.A.); teresina.deiorio@unimi.it (T.D.I.)

[2] Department of Agricultural and Environmental Sciences—Production, Landscape, Agroenergy and Center for Stem Cell Research, Università degli Studi di Milano, via Celoria 2, 20133 Milan, Italy; fulvio.gandolfi@unimi.it;

* Correspondence: tiziana.brevini@unimi.it; Tel.: +39-02-50317970

**Abstract:** Bi-dimensional culture systems have represented the most used method to study cell biology outside the body for over a century. Although they convey useful information, such systems may lose tissue-specific architecture, biomechanical effectors, and biochemical cues deriving from the native extracellular matrix, with significant alterations in several cellular functions and processes. Notably, the introduction of 3D platforms that are able to re-create in vitro the structures of the native tissue, have overcome some of these issues, since they better mimic the in vivo milieu and reduce the gap between the cell culture ambient and the tissue environment. 3D culture systems are currently used in a broad range of studies, from cancer and stem cell biology, to drug testing and discovery. Here, we describe the mechanisms used by cells to perceive and respond to biomechanical cues and the main signaling pathways involved. We provide an overall perspective of the most recent 3D technologies. Given the breadth of the subject, we concentrate on the use of hydrogels, bioreactors, 3D printing and bioprinting, nanofiber-based scaffolds, and preparation of a decellularized bio-matrix. In addition, we report the possibility to combine the use of 3D cultures with functionalized nanoparticles to obtain highly predictive in vitro models for use in the nanomedicine field.

**Keywords:** tissue engineering; 3D matrices; biomechanical cues; microenvironment remodeling; hydrogel; micro-bioreactor; 3D printing and bioprinting; nanofiber-based scaffolds; decellularization; nanomedicine

## 1. How to Overcome the Hurdles of 2D Cell Culture Systems

In vitro two-dimensional (2D) culture systems have represented, till recently, the most widely used strategy to study the mechanisms underlying cell biology, as well as diseases and drug action outside the body [1]. The first 2D approach was developed in 1907 by Harrison and colleagues to maintain nerve fibers in culture [2]. Subsequently, this method was applied for the study of different cell types, ranging from pluripotent and/or multipotent stem cells to terminally differentiated adult cells. The major advantages of 2D systems are associated with the simple and low-cost maintenance of cell cultures, the fast-downstream processing, and the easy performance of functional tests [3]. During the years, several steps forwards have been made to ameliorate and turn this technique into a more flexible and quicker platform. An example is represented by the modification and functionalization of the plastic surface onto which cells are seeded, using different materials and/or proteins, in order to resemble certain microenvironments [4]. Nevertheless, these improvements were not sufficient to mimic the natural structures of the original tissue and cells continued to be cultured in a monolayer bidirectional manner, providing sub-optimal conditions for their growth and specific functions. This negatively influences the fundamental cellular features and, usually, compromises the viability and reliability of the experiments, as well as the correct understanding of the whole organ activity [1,5]. Indeed, cells isolated from tissues and transferred onto flat and hard plastic substrates have been shown to

lose their specific phenotype, because of the absence of a tissue-specific architecture and of the naturally occurring biomechanical and biochemical cues that cannot be mimicked in 2D in vitro systems. In particular, one of the most compromising aspects is represented by the alterations and/or the complete loss of the cell-to-cell and cell-to-extracellular matrix interactions. This leads to significant changes in several cellular features and processes, including cell morphology, polarity, differentiation, proliferation, genetic pattern, responsiveness to stimuli and secretions, drug metabolism, and many other functions [6–10].

The recent biotechnological advances have partly overcome these hurdles, thanks to the use of three-dimensional (3D) culture systems, which more closely mimic the natural in vivo milieu. The 3D culture methods are currently used in a broad range of in vitro studies, including cancer and stem cell biology, and drug testing and discovery. The first pioneering attempt to produce a 3D culture model dates back to the 1970s, when Hamburg and Salmon used a solution of soft agar to embed and grow human single cells [11]. Since then, several cutting-edge techniques were developed, ranging from hydrogels to organoid models and synthetic or biological scaffolds. The common key aspect of these new approaches is represented by their ability to in vitro recreate the macro- and micro-architecture of tissues and organs, encouraging cells to re-organize in complex 3D structures that closely resemble the in vivo micro-topography. The resulting in vitro environment replicates the biochemical and biomechanical effectors, directly influencing both cell fate and behavior.

In this review, we describe the fundamental mechanosensing-related cues that enable cells to integrate and cooperate with the extracellular microenvironment. We provide an overview of the recent progress in cell culturing that implements the use of 3D models, including hydrogels, bioreactors, 3D printing and bioprinting, and preparation of decellularized bio-scaffolds.

## 2. Biomechanical Sensors and Effectors of the Microenvironment

The cell microenvironment is regulated by several factors, which include not only temperature, pH, oxygen, metabolites, growth factors or peptides, and hormones, but also macro- and micro-architecture-related cues as well as stretching and contracting stimuli. Externally applied forces are directly controlled by the stiffness of the substrate that the cells adhere to [12] and result in biomechanical signals that have a broad impact on cell behavior [13,14]. Cells are indeed able to sense the surrounding microenvironment and to interact with it, regulating their shape, their intracellular organization, growth, and differentiation, as well as their functionality. Interestingly enough, this ability is not limited to somatic cells and has emerged as an active property of oocytes and early embryos, which may actively sense biomechanical stimuli and convert them into intracellular signals, tuning their own behavior. In particular, in the context of the female gamete, the two main mechanosensing signaling pathways, namely Hippo and RhoGTPase, have been demonstrated to be involved in many fundamental oogenesis processes and to influence oocyte quality. Indeed, while the RhoGTPase signaling pathways are important actors in the coordination of actin filaments and microtubule formation, as well as polar body extrusion and spindle rotation during meiosis, the main actors of the Hippo pathway, YAP and TAZ, have an essential role during oogenesis, are highly transcribed in mouse and human oocytes, are maternally accumulated, and have been reported as strong candidates for zygotic genome activation (Pennarossa et al., submitted)

Altogether, the properties described above are defined with the term “mechano-transduction”, which indicates the cellular mechanisms by which mechanical inputs, such as stretching, tension or fluid flow, are converted into intracellular signals [15]. They are regulated by several membrane proteins that modify their folding in response to extracellular biomechanical stimuli [16]. Integrins have been recognized as the main molecular link between cells and the extracellular matrix (ECM). This protein family is characterized by the ability to sense, respond to, and bidirectionally interact with the cellular environment [17]. More in detail, integrin’s key function is to trigger the cytoplasmatic recruitment and activation of adaptors and signaling proteins, such as Protein Tyrosine Kinase 2 (PTK2B, also known as FAK), SRC Proto-Oncogene Non-Receptor Tyrosine Kinase (SRC), and Mitogen-Activated Protein Kinase 1 (MAPK1, known as ERK), which assemble into the focal adhesion complex [18]. Force-mediated

formation and/or reorganization of focal adhesion complexes, in turn, modify the Rho family small GTPase activities, leading to enhanced actin polymerization and the formation of stress fibers. This latter event can produce two different effects, described as short- or long-range transmission of force. The first directly affects the nuclear localization and function of the mechanosensitive transcription regulators, such as Myocardin Related Transcription Factor A (MRTFA, also known as MKL1) and Yes-associated protein (YAP)/WW domain-containing transcription regulator protein 1 (WWTR1 or TAZ) [19]. The long-range effect transmits the force from the surrounding environment into the cell nucleus, thanks to a physical actin-mediated connection between the ECM and the linker of the nucleoskeleton and cytoskeleton (LINC) complex (Figure 1) [20]. This results in several changes, including chromatin remodeling, exposure of specific sites to transcription factors, gene expression changes, and the modifications of nuclear pore conformation and size, finally promoting YAP/TAZ nuclear translocation.

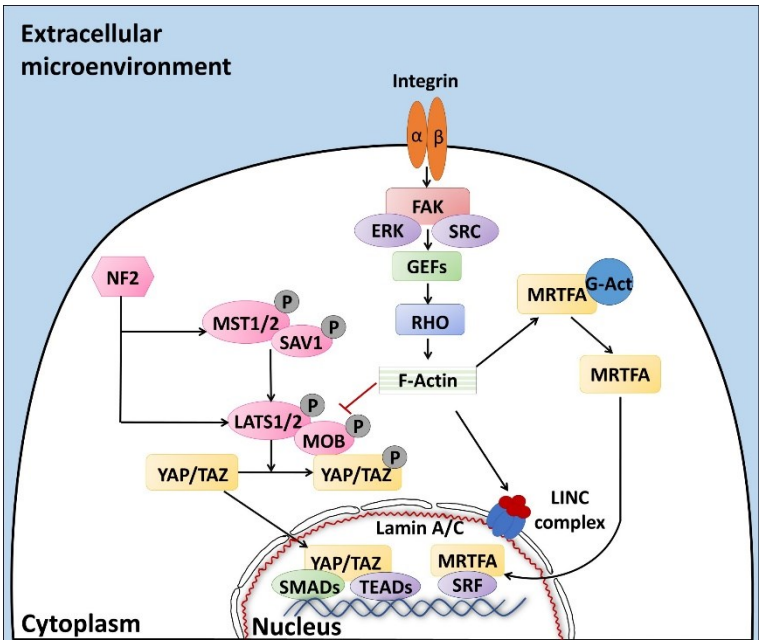


**Figure 1.** The sensors (integrins) and effectors (Rho and Hippo pathways) driving mechano-transduction processes, regulating YAP/TAZ localization and the subsequent cell behavior.

YAP/TAZ represent the main downstream effectors of the Hippo pathway cascade [21], which is involved in the cellular response to extracellular stimuli. Their compartmentalization is strictly correlated to mechanical signals, cellular stress, polarity, and adhesion cues [20], and influences gene expression, thus controlling cell fate. Recent studies also demonstrate the presence of upstream molecules, such as mammalian STE20-like protein kinase 1/2 (MST1/2), Salvador family WW domain containing protein 1 (SAV1), MOB kinase activator 1A/B (MOB1A/B), and large tumor suppressor 1/2 (LATS1/2), which regulate the Hippo pathway activity [22–24]. In particular, it has been shown that phosphorylation events are involved in the activation of the cascade, inducing cytoplasmatic retention of YAP and TAZ (Figure 1). In contrast, when the cascade is inactive, these two proteins translocate into the nucleus, interacting with different transcription factors (TFs). It is interesting to note that the YAP and TAZ subcellular localization is tightly controlled by substrate rigidity and topography [25–27], as well as by actin remodeling [28–30] and cell stretching [28]. This clearly demonstrates a specific role of these molecules as mechanotransducers and mechanosensors. In agreement with this, cells grown on a 3D soft matrix have been demonstrated to display YAP/TAZ localized to the cytoplasm, whereas cells plated on standard plastic supports (2D system) showed YAP/TAZ localized to the nucleus [26]. In addition, substrate stiffness is able to modulate the expression of the two molecules, which are upregulated in cells grown on hard hydrogels compared to soft substrates [31].

Furthermore, we recently demonstrated that YAP/TAZ localization is mirrored by a parallel compartmentalization of SMAD2/3. In particular, we observed that cells with cytoplasmic retention of YAP/TAZ exhibited a SMAD2/3 cytoplasmic distribution, while cells displaying the two molecules localized in the nucleus showed concomitant SMAD2/3 nuclear accumulation [23]. This latter event led to the formation of the YAP/TAZ–SMAD2/3 complex, which is known to bind to TEAD transcription factors, regulating cell fate and differentiation processes [32], both in bi-parental and mono-parental parthenogenetic cell lines [33–35].

It is indeed important to note that YAP/TAZ are transcriptional coactivators, unable to directly interact with DNA, but rather binding other TFs in order to elicit their functions [36]. Accumulating evidences point, in particular, to the TEAD protein family as the main actor, mediating YAP and TAZ nuclear activity and modulating the expression of different target genes involved in cell growth, proliferation, and organ development [23,37].

## 3. 3D Cell Culture Systems

The cellular microenvironment is a highly complex 3D natural structure, regulating in vivo cell functional activities through specific stimuli [38–41]. As a consequence, the organization and composition of the ECM, as well as the contribution of cell-to-cell and cell-to-ECM interactions, play a fundamental role in the control of cell behaviors and are strictly tied to the functions of tissues and whole organs.

The major aim of the recently introduced 3D cell culture systems is to model and in vitro re-create the tissue and organ in vivo milieu, mimicking the underlying biochemical and biomechanical signals [42,43]. A well-selected and -designed microenvironment can be therefore used in tissue and cell engineering to faithfully re-produce in vitro the conditions that promote all cell functions, including proliferation, migration, matrix production, and stem cell differentiation. The main 3D cell culture strategies that are available to this end are shortly described in the sections below.

### *3.1. Hydrogels*

The physiological relevance of Matrigel remained undisputed for many years. This material was considered the gold-standard support for 3D cell culture systems and, therefore, used in multiple applications, ranging from angiogenesis assays to organoid assembly and pluripotent embryonic stem cells expansion. However, due to its natural origin, Matrigel is inherently limited by its compositional complexity and lack of batch-to-batch reproducibility. Furthermore, the introduction of exogenous components by Matrigel interferes with mechanistic studies of cell behavior and limits its therapeutic applications [44]. Powerful alternatives were thus provided by the introduction of the chemically defined synthetic hydrogels that show minimal batch-to-batch variation, increased reproducibility, defined material properties, compositions, and controllable degradation properties [45,46]. Notably, Matrigel has recently found innovative applications, such as the reconstruction of 3D and hollow-shaped functional units of glandular tissues in a controlled microenvironment. This is achieved thanks to the development of a set of scaffolds (hemispheres, Matrigel beads, open and closed microtubes, or microcarriers) that serve as building blocks for a 3D toolbox aimed at producing such 3D constructs [47].

The term “hydrogel” was used for the first time in 1894 to describe a colloidal gel consisting of inorganic salt [48]. Hydrogels received considerable attention in the past 50 years and several materials displaying high swelling ability and good mechanical properties were developed for a various range of applications, including hygienic products, agriculture, drug delivery systems, sealing, coal dewatering, artificial snow, food additives, pharmaceuticals, biomedical applications, tissue engineering and regenerative medicines, diagnostics, wound dressing, separation of biomolecules or cells and barrier materials to regulate biological adhesions, and biosensors [49].

Hydrogels or hydrophilic gels are biomaterials consisting of a water-swollen network of physically or chemically crosslinked polymers [50]. They can be composed of chains of natural polymers (collagen, fibrin, or alginate), synthetic polymers (polyvinyl alcohol, polyacrylic acid, or polyethylene glycol), or hybrid materials, which combine elements of synthetic and natural

polymers (hyaluronic acid and polypeptides). Depending on the polymeric composition, as well as on the nature and density of the network joints, hydrogels can contain various amounts of water and, consequently, can display different degrees of flexibility. Indeed, the cross-linking processes used for their synthesis also influence the mechanical properties of the supports. In particular, hydrogels may be synthesized in a number of ways, including chemical cross-linking, thermal annealing, supramolecular self-assembly, ionic gelation, and electrostatic interactions [51]. Based on the variation in polymer concentrations and cross-linking methods, it is possible to tune the physical characteristics of the scaffolds, namely, their architecture, stiffness, pore size, diffusion of soluble factors, and ligand density [52].

The pivotal study that first demonstrated the use of hydrogels for producing cell culture supports is, however, more recent—dating back to 2006. In this manuscript, Engler et al. demonstrated that the substrate stiffness and elasticity directly influence cell fate as well as lineage specification [53]. Currently, a great number of hydrogels with different "stiffness" is commercially available. The term "stiffness" is used to indicate how a component bends under load, while still returning to its original shape once the load is removed. It is associated with the elastic deformation and directly depends on the modulus of elasticity, also known as Young's modulus of the material. In the field of biology and tissue engineering, ECM composition and elasticity regulate the Young's modulus of the extracellular microenvironment, which, in turn, plays a fundamental role in regulating cell behavior. These specific in vivo features are completely lost in 2D culture systems that use standard plastic supports, characterized by elevated stiffnesses. In contrast, hydrogels allow to better mimic native tissues and cellular environments, modulating the elasticity and stiffness. This aspect together with the hydrogel's enormous versatility, as well as their biocompatibility and viscoelastic properties, make them highly suitable for 3D culture support production. At present, the hydrogels are used in a wide variety of biological applications [54], including tissue engineering, micro-organ systems, drug delivery, cytotoxicity testing, and drug screening. Several tissue and cell types have been in vitro cultured using this technology, including cartilage [55,56], cornea [57,58], skin [59], tendon [60], vascular tissue [61], pancreatic endocrine cells [62], and pluripotent cells [63].

One potential drawback in hydrogel use for tissue engineering-related applications could be the employment of harmful crosslinkers and the lack of appropriate degradability. Several studies are currently in progress in order to carefully address these critical points and develop polymerization methods that allow for the production of safe and biocompatible hydrogels.

### *3.2. Micro-Bioreactors*

Keller et al. described the first in vitro culture method encouraging the formation of spheroid structures [64]. In this system, known as "hanging drop", cells are suspended in a droplet of medium and are allowed to self-aggregate under the influence of gravitational forces. It is interesting to note that reproducibility, production efficiency, and organoid size uniformity are common aspects in all 3D spheroid-based applications [65]. Nevertheless, the hanging-drop technique consists of a stationary system, primarily based on diffusion-limited conditions, which usually results in the formation of loose-aggregated clusters. Indeed, cell suspension deposition onto the underside of the lid of a tissue culture dish leads to the creation of a microgravity environment that concentrates cells at the free liquid–air interface, inducing the generation of low-aggregated multicellular spheres. Based on this, during the last decades, several studies were focused on the development of novel and more efficient in vitro culture models that maximize cell-to-cell interactions, promote self-assembly, and encourage the formation of organoids.

To date, very promising results were generated encapsulating cells in Matrigel microbeads, acting as a single-cell culture compartment and serving as microcarriers for flow-based high-throughput analysis, opening novel possibilities for performing high throughput screens on 3D culture structures in biological and pharmaceutical research [66]. In parallel, other studies demonstrated the successful use of 3D scaffold-free models, consisting of a small liquid droplet coated with a hydrophobic powder that eliminates the direct contact between the interior liquid and the external environment. The idea of encapsulating cells resuspended in a liquid with hydrophobic powder was derived from gall-dwelling aphids [67], where the honeydew waste

secreted from the aphid is covered with a powdery wax before being rolled away, preventing it from drowning the insects. The first microbioreactor, also known as "liquid marble", was reported by Aussillous et al., who covered a water droplet with hydrophobic microparticles [68]. Subsequently, several other studies demonstrated the significant advantages offered by the use of microreactors, compared to other culture approaches. First of all, these systems provide a non-adherent liquid surface that induces rapid cell aggregation and the generation of compact spheroids (Figure 2). Furthermore, the concave bottom, the spherical shape, and the internal liquid flow, distinctive of the liquid marbles, allow cells to settle onto the bottom of the micro-bioreactor, forming organoids uniform in size and shape [65]. Liquid marbles also display a remarkably high surface/volume ratio, which enhances the mass and heat transfer, increasing the reaction kinetics and improving the yield, and an optimal gas exchange that can occur through the entire surface. Lastly, the use of micro-bioreactors allows for a reduction in reagents and volumes, a more precise control over reaction parameters, and a safer handling of hazardous or exothermic reactions [69–72]. Thanks to all these unique properties, together with the easy manipulation and the high reproducibility and efficiency, liquid marbles have found numerous applications in the field of microfluidics, storage, transportation, and mechanical computation [73–76], as well as in the chemical and biological areas [77]. Recently, several studies have pointed to micro-bioreactors as ideal platforms, essential for biomedical applications and culture of microorganisms or cells of different types, spanning from oocyte [78], cardiac [79], pancreatic [80], toroid [81], and olfactory ensheathing [82] to high plasticity cells [32]. In particular, we demonstrated that cell encapsulation in micro-bioreactors induces distinctive 3D cell rearrangements and specific cell-to-cell interactions [32]. In parallel, in our experience, the use of micro-bioreactors significantly enhance the acquisition and maintenance of a high plasticity state, providing a useful platform in stem cell organoid technology for long-term culture of different cell types, ranging from epigenetically erased cells to ESCs and iPSCs, as well as MSCs [65]. Interestingly, parallel studies also demonstrated that encapsulation systems can be successfully used to store and cryopreserve organoids without altering cell growth and differentiation ability, as well as to perform post-treatments, such as direct transfection, and post-genetic screen and organoid analysis [83].

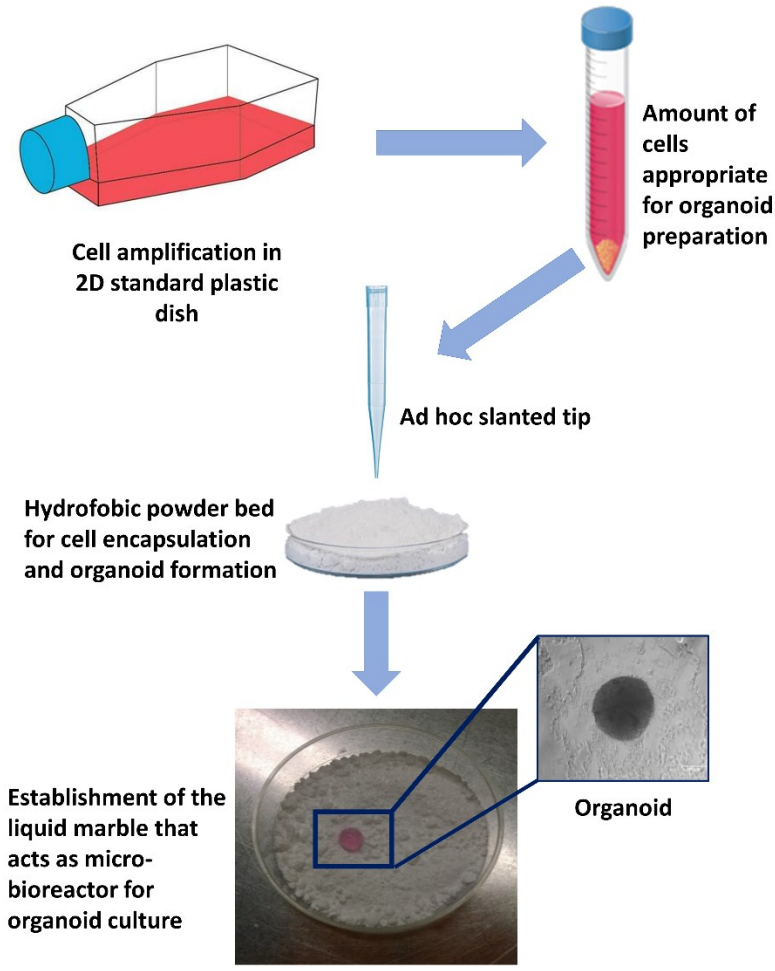


**Figure 2.** Schematic representation of the protocol used to produce micro-bioreactors and obtain spheroid organoids. 2D cultured cells are detached for the dish and centrifuged. Droplets of medium containing cells are dispensed onto the hydrophobic powder bed. The powder covers the drop, leading to the creation of the liquid marble that allows cell aggregation and organoid formation.

*3.3. 3D Printing Scaffolds*

3D printing is an additive manufacturing technique for fabricating a wide range of objects with complex geometries. The first 3D printer was created in 1986 by Charles W. Hull, who indicated with the term "stereolithography" the method and the machinery used for producing solid structures by a gradual accumulation of thin layers of material, one on top of the other [84]. Subsequently, the term "3D printing" was coined and used to describe a work done in 1993, in which a standard inkjet printer was modified to a custom processing apparatus [85].

This technique was immediately considered of particular interest due to its great potential in the production of reliable and reproducible scaffolds, suitable for tissue engineering application.

The fabrication of 3D supports is based on a consecutive deposition of material layer by layer, or even pixel by pixel. The shape of the scaffold is firstly modeled using computer-aided design (CAD) software, such as UG, CATIA, Tinkercad, or ProE, in order to produce a file containing all the information required to control the moving track of the printing device (Figure 3). The most adequate 3D printing method need then to be selected among the different technologies currently available. These are categorized into three different groups, namely, powder-, ink-, and polymerization-based. The most common approach involves the use of a continuous filament of thermoplastic polymers that are heated at the nozzle to reach a semi-liquid state and, then, extruded on the platform or on top of previously printed layers (fused deposition modelling).

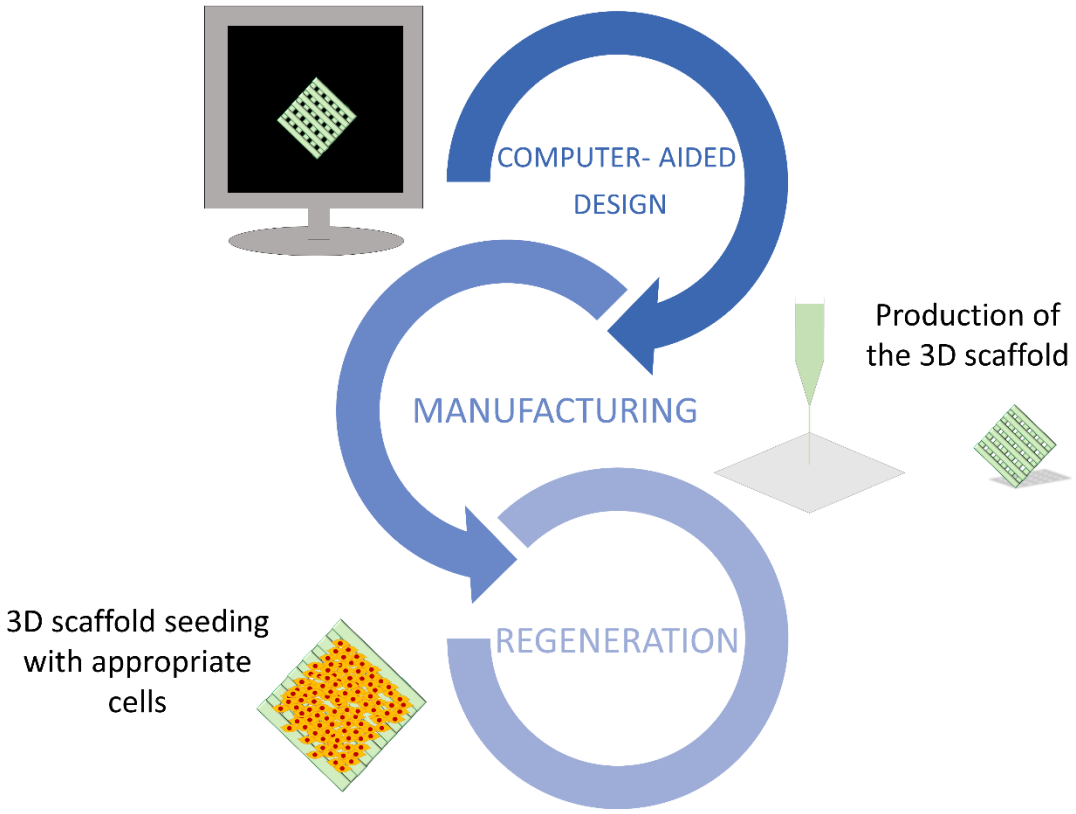


**Figure 3.** The main fundamental steps needed to construct an artificial organ in vitro. The 3D scaffold shape is modeled using computer-aided design (CAD) software (design). The support is 3D printed after an accurate selection of the most adequate method (manufacturing). Lastly, it is repopulated with the specific cell type/types (regeneration).

Although the post-manufacturing processes, such as heat treatments and hot isostatic pressing, can tailor the general characteristics of the scaffolds, including microstructure and surface roughness [86], the material selection remains a fundamental step. Indeed, the physical properties, cytotoxicity, bioactivity, and biodegradability significantly influence the mechanical features and the performance of the scaffolds. To date, several materials and biomaterials have been developed and proposed for tissue engineering applications. Among them, the most common used are the biodegradable natural and synthetic polymers, such as poly lactic acid, polycaprolactone, polyglycolic acid, or their copolymers [87–89]. In contrast, although non-degradable ceramics, such as alumina and zirconia, represent excellent candidates for joint replacement, they cannot be successfully adopted in other tissue engineering areas, because of their biological inertness [90]. This problem can be solved by using hydroxyapatite and other bioactive glasses composed by silicon dioxide and calcium oxide, which have shown to possess both high mechanical and bioactivity properties [91]. In contrast, metals are the least used in tissue engineering scaffolding due to their low biocompatibility, with the exception of titanium and its alloys, which have high bioactivity and biocompatibility [92].

During the last years, particular emphasis was also given to 3D bioprinting, which applies a layer-by-layer concept, but, unlike standard 3D printing, deposits cell-laden filaments or cell-containing droplets into specific substrates, in order to generate 3D biological structures [93,94]. Currently, there are different bioprinting strategies are available, namely, inkjet-based bioprinting, laser-assisted (LAB) bioprinting, pressure-assisted (extrusion) based bioprinting, acoustic bioprinting, stereolithography (SLA)-based bioprinting, and magnetic bioprinting [95,96]. These techniques can be used alone or in combination, depending on the tissue type to be reconstructed. Many factors affect printing fidelity and influence the overall porosity, mechanical strength, and layer height of the scaffold, including applied pressure, printing speed, and printing distance [97].

Another working parameter to be critically considered is represented by the solution of the biomaterial loaded with the desired cell types. This is usually referred to as "bioink" and its appropriate selection represents a crucial aspect for developing functional tissue or organ constructs. To date, several natural and synthetic polymers have been used in bioprinting techniques, including alginate, collagen, silk, dextran, gelatin, fibrin, agarose-chitosan, agarose, gellan gum, hyaluronic acid, decellularized matrix, matrigel, hydroxyapatite, polyethylene glycol, methacrylated hyaluronic acid, polyvinylpyrrolidone, poly-epta-caprolactone, pluronic, polyglycidol-hyaluronic acid, and polyhydroxybutyrate. The selection of the appropriate polymer is carried out based on the specific cell/tissue to be used.

A fascinating application of the 3D printing technology was also used for the creation of innovative models for medical purposes. In particular, anatomically accurate internal organ images, obtained with X-rays, computed tomography, dual-energy imaging, cone beam CT, or digital tomosynthesis, can be printed in order to produce modular anthropomorphic mannequins [98]. This allow for replicating and studying a wide range of pathologies [99–103], as well as for reducing the ethical concerns [101,103,104] relative to the use of cadaveric and animal models for education, surgical planning, and training purposes.

Currently, the development and optimization of novel materials, combined with reduced manufacturing costs and advanced printers, enabled the use of 3D printing in many research laboratories as well as in industrial settings [105–107]. Nevertheless, although 3D printing techniques allowed to in vitro re-create several tissues, such as bone, cartilage, skin, nerve, and complex organs, like teeth, nose, ears, heart, and liver, there are few studies utilizing 3D-printed scaffolds in preclinical models and trials. This is mainly related to technical drawbacks that limit the transfer from bench to bedside of 3D printing techniques, possibly caused by poor cell survival and differentiation, insufficient vascularization rate, and altered metabolite diffusion. In order to solve these issues, several translational studies are currently in progress to overcome the problems mentioned above and eventually ensure a smooth transfer of knowledge acquired at the laboratory benches to the patient bed sites.

### *3.4. Nanofiber-Based Electrospun Scaffolds*

The recent development of nanofibers has attracted attention and led to significant improvement in the production of scaffolds that can replicate the architecture of natural tissues at the nanoscale [108]. It is well known that natural ECM consists of several interwoven protein fibers, with variable diameters ranging from 10 to 100 nm [109], which modulate cell adhesion as well as their growth and behavior [110].

To date, different techniques have been developed to fabricate nanofibrous scaffolds, including phase separation [111], self-assembly [111], electrospinning [112], liquid-assisted collection [113], and template-assisted collection [114]. Among all these approaches, electrospinning is considered one the most promising process, thanks to its ability to generate fibers, which are similar to those of native ECM, obtained with the use a wide range of materials [108]. A great advantage is also represented by the observation that electrospun nanofibers display a large surface area, as well as their porous structure that significantly favor cell adhesion, proliferation, migration, and differentiation [108]. A variety of natural polymers, such as collagen, gelatin, elastin, and silk, as well as synthetic materials, such as polylactic acid, polyglycolic acid, polycaprolactone, and polylactic-co-glycolic acid, have been used as biomimetic substrates. However, it must be noted that the use of synthetic or natural polymers alone have shown important limitations [115]. Indeed, synthetic polymers have great flexibility in synthesis and modification, while they lack cell affinity due to the low hydrophilicity and the absence of surface cell recognition sites [110]. On the other hand, natural polymers provide good biocompatibility, but display poor processing ability and mechanical properties [116]. It is therefore desirable to produce scaffolds using composite nanofibers that possess not only suitable structural properties, but also bioactive surfaces [117]. In addition, when required, nanofibers can be further functionalized via incorporation of bioactive molecules, including enzymes, DNA, and growth factors [118].

Nanofibers can be electrospun in various patterns, depending on the biomedical application required. It is therefore fundamental to know the structural and biological properties of tissue in order to choose the materials and the fiber orientation that best fit the 3D reconstruction. Indeed, electrospun nanofibrous scaffolds can have different alignments, such as axial, yarn, and radial, providing an increased ability in shaping cell morphology, guiding cell migration, and encouraging cell differentiation, compared to other types of scaffolds [119,120]. Currently, several strategies have been developed for controlling nanofiber alignment. Overall, these methods can be classified into three major categories, namely, mechanical, electrostatic, and magnetic, depending on the type of forces involved [121–124].

This approach has been used for in vitro reconstruction of different structures, including vascular [125–128], neural [129–132], bone [133–137], cartilage [138–141], and tendon/ligament [142–146] tissues. Nevertheless, despite the recent advances in creating biomimetic nanofibrous scaffolds for tissue engineering applications, several issues still remain unsolved. One of the most challenging aspect is related to the complexity of creating 3D porous scaffolds, combined with cells and growth factors, to optimize the engrafting and viability of the cells. It is also crucial to develop novel strategies for producing fibers with a diameter similar to that of native tissue (usually less than 100 nm, preferably in the range of 10–50 nm). These fibers must display high porosity, which is necessary for cell infiltration and migration [118]. Several studies are currently in progress to address these problems. Among them, the electro-spinning/netting technique appeared to be very promising and seems a versatile method for the generation of spider-web-like nano-nets with an ultrafine fiber diameter (less than 50 nm), maintaining a high porosity [110]. Last but not least, it is important to highlight that the majority of the published studies report results generated in vitro. It is now mandatory to confirm the potential of this technique in vivo, further optimizing nanofiber scaffold composition and structure and, as a consequence, translating electrospun nanofiber production from the laboratory dimension to the industrial scale.

### *3.5. Decellularized Scaffolds*

A promising alternative is represented by the creation of natural bio-scaffolds through a recently developed method that involves the complete decellularization of an organ. The process is based on the removal of the cellular components from the tissues to obtain an acellular extracellular matrix (ECM), also known as a "decellularized scaffold". This approach involves the use of different strategies that allow the removal of native cells and genetic materials, while preserving ECM with its structural, biochemical, and biomechanical properties. Decellularization can be performed through chemical, enzymatic, physical, or combinative techniques. The chemical approach can involve the use of surfactants, acids (i.e., peracetic acid), or bases (i.e., sodium hydroxide), which are able to solubilize the cell membrane and nuclear material. Among the several surfactants adopted for disarranging the phospholipid membranes, sodium dodecyl sulfate (SDS) represents the most effective decellularizing agent, successfully used for several tissue and organs, including forearm [147], cornea [148], myocardium [149], heart valve [150], small intestine [151], kidney [152], vein [153], lungs [154,155], ovary [156], and heart [157]. However, it has been demonstrated that this compound can induce damages to the structural and signaling proteins, such as collagen [150], GAGs, and growth factors [158], preventing the full retention of ECM biomechanical and biochemical properties. It is therefore imperative to choose and develop specific protocols that limit the concentration and the exposure time for this agent. In parallel, different studies also indicated that Triton X-100 and sodium deoxycholate (SD) could represent promising substitutes for SDS, thanks to their low aggressiveness that allow for an efficient cell removal, while preserving the ECM [151,154,158,159].

Enzymatic approaches, including DNase I, RNase, or trypsin/ethylenediaminetetraacetic acid (EDTA), can be used to remove the nucleic acid residuals after cell rupture or to target the peptides that anchor cells to the ECM. These enzymes are usually inefficient when applied alone and need to be used in combination, in order to supplement the chemicals' activities. Furthermore, a protracted exposure to enzymes may result in the alteration of collagen, laminin, fibronectin, elastin, and GAG, damaging the ECM microstructure.

Lastly, the physical and mechanical methods, such as freeze–thaw cycles (freezing temperatures around −80 °C and biological temperatures around 37 °C), high hydrostatic pressure (higher than 600 MPa), supercritical carbon dioxide ($CO_2$, higher than the critical temperature of 31.1 °C and the critical pressure of 7.40 MPa), and nonthermal permanent electroporation, can also be used in decellularization protocols. These approaches remove tissue constituent cells and genetic materials, while maintaining the ECM architecture and composition, combining cell lysis and cell-matrix adhesive protein disruption.

It is important to highlight that all the approaches listed above show advantages and limitations. For example, the mechanical methods are usually less damaging to the tissue structure, but they fail to eliminate genetic materials. On the other hand, surfactants at low concentrations or enzymes used alone may not completely remove all cellular debris. As a consequence, several protocols present in the literature combine two or more types of treatment, in order to complement one another, with the final goal of retaining the ECM's desired characteristics and yield an optimal decellularized scaffold. In our experience, the use of a four-step protocol, involving a freeze–thaw cycle, followed by sequential incubations with SDS, Triton X-100, and deoxycholate, allow to obtain whole-ovary bio-scaffolds that successfully preserve the shape, architecture, and ECM of the original organ [156]. We also demonstrate that the obtained ECM-based scaffold recreates in vitro the complex in vivo ovarian milieu, facilitating the necessary interactions between cells and their surroundings and ensuring a correct cell growth, differentiation, and function [160].

While there are no official guidelines for an adequate decellularization, standard metrics are beginning to emerge. It has been recently proposed that at least four parameters need to be met in order to assess the achievement of a proper decellularization process:

1. cell removal: no visible nuclear material by histological H&E and 4′,6-diamidino-2-phenylindole (DAPI) staining;
2. elimination of genetic material: less than 50 ng double-stranded DNA (dsDNA) per mg ECM dry weight and less than 200 bp DNA fragment length;
3. preservation of structural protein (i.e., collagen, fibronectin, and laminin), glycosaminoglycans (GAGs) and growth factor content;
4. retention of mechanical properties, including elastic modulus and tensile strength.

The tissue decellularization technique can be applied to any organ. To date, different protocols have been developed for a variety of tissues, as reported in Table 1. However, no conclusive evidence is available and further improvements are mandatory to optimize methods for obtaining acellular ECMs that fully preserve the structural, biochemical, and biomechanical properties of the native tissue. Furthermore, the resulting scaffolds need to be reproducible, sterile, and successfully undergo long-term storage for future procedures. These advances, together with the development of scaled-up methods, are crucial to produce bio-scaffolds that can be of use in tissue engineering and, more in general, in regenerative medicine applications.

**Table 1.** Overview of the protocols developed for the decellularization of organ fragments and whole organs.

| Organ Fragments | Protocol | Reference |
|---|---|---|
| Porcine testis | −80 °C, 0.01% SDS, 1% Triton X-100 | [161] |
| Goat lung | 0.25%Trypsin-EDTA, 0.1% SDS, 20 μg/mL RNase A and 0.2 mg/mL DNase I | [162] |
| Human lung | 8 mM CHAPS [1] | [155] |
| Porcine myocardium | 0.1% SDS, 0.01% Trypsin, 1 mM PMSF [2], 20 μg/mL RNase A and 0.2 mg/mL DNase I | [163] |
| Porcine liver | 0.01% SDS, 1% Triton X-100 | [164] |
| Porcine kidney | 1% Triton X-100 | [165] |
| **Whole Organ** | **Protocol** | **Reference** |
| Bovine ovaries | 0,1% SDS | [166] |
| Porcine ovaries | −80 °C, 0.5% SDS, 1% Triton X-100, 2% SD | [156] |
| Ovine testis | 1% SDS | [167] |
| Human trachea | 4% SD, 2000 kU DNase I in 1 mM NaCl | [168] |
| Porcine trachea | 4% SD, 2 kU/mL DNase I in 1 M NaCl | [169] |
| Porcine lung | −80 °C, 2% SDS, 1% SDS | [170] |
| Human lung | 1% Triton X-100, 0.5% SDS | [154] |
| Porcine heart | 0.2% Trypsin/0.05% EDTA/0.05% $NaN_3$, 3% Triton X-100/0.05% EDTA/0.05% $NaN_3$, 4% SD | [171] |
| Rabbit liver | dd$H_2O$, 1% Triton X/0.1% $NH_4OH$ | [172] |
| Porcine liver | 1% SDS, 1% Triton X-100, 1% SD | [173] |
| Porcine cornea | 0.5% SDS | [148] |
| Goat kidney | 50 U/mL heparin, 0.1% SDS, 0.5% SDS, 1% SDS, 0.1% Triton X-100, 5 mM $CaCl_2$ and $MgSO_4$, 0.2 mg/mL DNase I | [174] |

[1] CHAPS = 3-((3-Cholamidopropyl)-dimethylammonio)-1-propanesulfonate. [2] PMSF = phenylmethylsulfonylfluoride.

## 4. Tissue and Organ Regeneration Approaches

The first reports describing in vitro skin reconstruction date back to over 30 years ago [175–178], while the first bio-artificial bone tissue was developed in the 1990s by Ishaug et al. [179] and Baksh et al. [180]. Following these pioneering studies, extraordinary progress has been made in tissue engineering, not only for the optimization of scaffold production processes, but also for the regeneration and recellularization methods [181,182]. Indeed, cell repopulation plays a key role in getting fully functional bio-artificial organs. Needless to say, this procedure needs to be improved and optimized, and above all, adapted to the specific biophysical and biomechanical proprieties of the scaffold used as well as to the complexity of the tissue or organ of interest.

Indeed, each organ varies in its unique structural components, namely, its cell types, matrix, architecture, as well as in its biophysical and biochemical environment, such as pressure, flow, oxygen tension, cytokines, and growth factors. As a consequence, the repopulation step requires the use of appropriate specific cell types, while commanding an optimized seeding method and a physiologically relevant culture approach (Figure 4). Skin cell sheet or blood vessel in vitro re-creation, for example, requires a single cell type, whereas whole organ reconstruction necessitates the seeding of multiple cell types to reestablish all the functional structures, including parenchyma, vasculature, and supporting components.

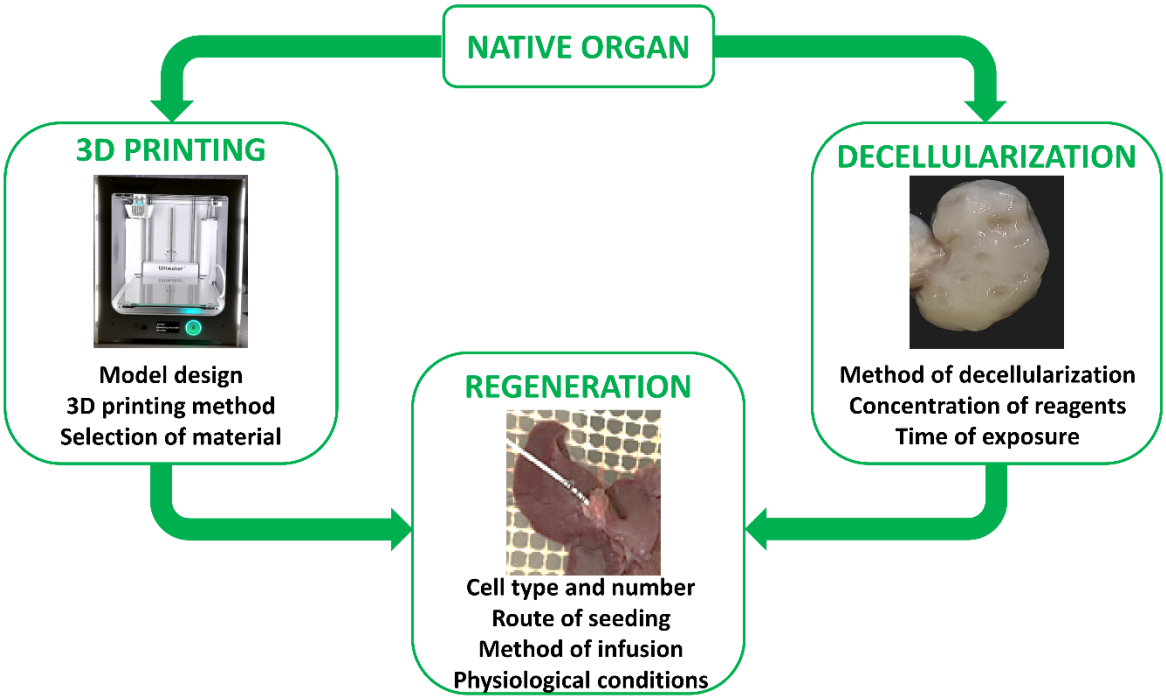


**Figure 4.** The two main ways and essential key aspects to successfully recreate in vitro a fully functional bio-artificial organ.

To date, distinct cell sources, such as embryonic stem cells, mesenchymal stem cells, fetal and adult tissue cells, and induced pluripotent cells, have been used to repopulate both artificial scaffolds as well as biological ones. The first tissue-engineered airway was transplanted into a patient in 2008. In this work, the authors repopulated a trachea scaffold with epithelial cells and mesenchymal stem-cell-derived chondrocytes. The results obtained demonstrated that it was possible to in vitro re-create a tissue-engineered trachea with mechanical properties that allow normal functioning, providing successful treatment for patients [168]. Following this, many studies using a single type of tissue-specific stem cells [160,172,183–187] or induced pluripotent cells [188–191] were carried out, and others are currently ongoing, in order to identify the best 3D supports able to boost cell differentiation and successfully produce in vitro functional tissues and organs for future possible transplantation. In parallel, both synthetic and biological scaffolds were repopulated with terminally differentiated cells, including fibroblasts [156], mature hepatocytes [192–194], and pancreatic endocrine [195–197], cardiac [198], and ovarian cells [199].

Nevertheless, it is still difficult to identify and standardize common protocols indicating routes of delivery, methods of infusion, and the correct cell number to be applied for the generation of functional organs. The main limitations are currently related to the complexity and the specialization of tissues, and, in some instances, to the elevated experimental costs. Indeed, although, different studies have already described distinct approaches obtaining encouraging results, none of them have proved their absolute potential to replace a damaged organ or tissue and several issues need to be solved.

In the kidney, a variety of successful strategies were developed [200]. However, the current techniques still show important limitations that impede the obtainment of a complete and functional whole-organ. In particular, while a piecemeal of renal components were reconstructed in vitro, the nephron structure has not yet been recreated [201].

In contrast, the liver represents a simpler, more feasible model, thanks to its regular structure and clear cellular organization. The current technical approaches in liver tissue engineering are based on the use of different methods, such as cell encapsulation, 3D printing, 3D bioprinting, and decellularized organs, which display the appropriate topography and biomechanical properties that facilitate hepatocyte colonization, migration, differentiation, proliferation, and cell polarity [202–204]. It is, however, important to highlight that, to date, 3D liver tissue organization and function has been mostly demonstrated in animal models and further studies and evidence are necessary in order to confirm the generation of a functional liver for human transplantation.

Many strategies were also developed for 3D heart recreation. Nevertheless, they led to the production of functionally immature contractile cardiac constructs [205–207]. Furthermore, although cardiomyocytes represent the key cell type of this tissue, the engrafting of stromal and endothelial populations, for the recreation of vascular system, remains the most immediate need for obtaining functional organs [201].

Lastly, the lung represents an extraordinary challenge to engineer almost from scratch. The studies carried out up to now demonstrated the recreation of some microscopic aspects of alveolar organization, without any gas exchange [208–210]. This organ, in fact, displays a unique and complicated architecture and is composed of more than 40 different highly specialized cell types. Furthermore, the peculiar structure of each capillary vessel, surrounded on both sides by a one cell-thick epithelium, which is needed to ensure carbon dioxide–oxygen exchange, represents the greatest obstacle for successful lung tissue engineering [208].

## 5. Combining 3D Cell Culture Systems with Nanoparticles for the Creation of Predictive Models

During the last two decades, research in the nanotechnology field has undergone a fast development. Following the first work by Brus [211], inorganic nanoparticles (NPs) have been largely investigated for diverse applications in biology and medicine, ranging from NP-based therapies [212] to biosensors [213]. NPs can display different shapes, such as spherical [214,215], rod-shaped [216,217], wire [218], plane [219,220], star [221], cage [222], and multipod [223,224], and are generally described as particulate material characterized by dimensions ranging from 1 to 100 nm [225,226]. They possess several peculiar properties, namely, a high surface-to-volume ratio, elevated chemical reactivity and dispersibility, significant surface energy, and unique mechanical, thermal, electrical, magnetic, and optical behaviors [227]. All these features make NPs highly promising for nanomedicine applications. Indeed, the delivery of small and macro molecules using nanoparticulate vehicles offers a number of advantages compared to the administration alone [228], solving the main issues related to poor bioavailability, impaired target specificity, and systemic and organ toxicity [229–231].

The earlier examples of nanomedicine involved the use of lipid- and polymer-based nanocarriers for drug encapsulation and delivery [232–234]. Subsequently, innovative techniques involving the use of NPs were developed for biosensing [235], stem-cell modulation [236], and tissue engineering [237].

The evaluation of NP delivery is currently being carried out in 3D culture systems because of the 2D culture approach's failure to account for the extracellular microenvironment that is present in vivo [238]. This also allows for studying how the interactions with ECM components can affect fate and stability of the NPs. In addition, this approach makes it possible to understand how the mechanical forces, such as tension, compression, and interstitial fluid flow, can alter the bioavailability of the delivery vehicle, by redirecting the NPs in the direction of flow and potentially away from the target sites. Furthermore, it is important to remember that cell culture conditions also affect the cell phenotype and thereby influence the cellular response to the delivered drugs. In particular, multicellular drug resistance, possibly caused by the occurrence of hypoxic tissue regions, is able to alter cell proliferation, and poor availability of delivered drugs in

deeper tissue layers [239] can be only mimicked in 3D culture conditions. For these reasons, researchers are combining the use of 3D culture systems with nanomedicine, with the final goal to design better predictive in vitro models (Figure 5). Reproducible in vitro 3D tissue culture systems that more closely mimic in vivo tissues, in terms of functionality, morphological, and mechanical architecture, could be applied during the development and evaluation of delivery vehicles, to offer a more predictive platform for assessing in vivo delivery efficiencies. Such systems can serve to bridge the considerable gap between traditional 2D monolayer experiments, animal studies, and clinical trials, since NP formulations can be more effectively optimized in 3D in vitro models.

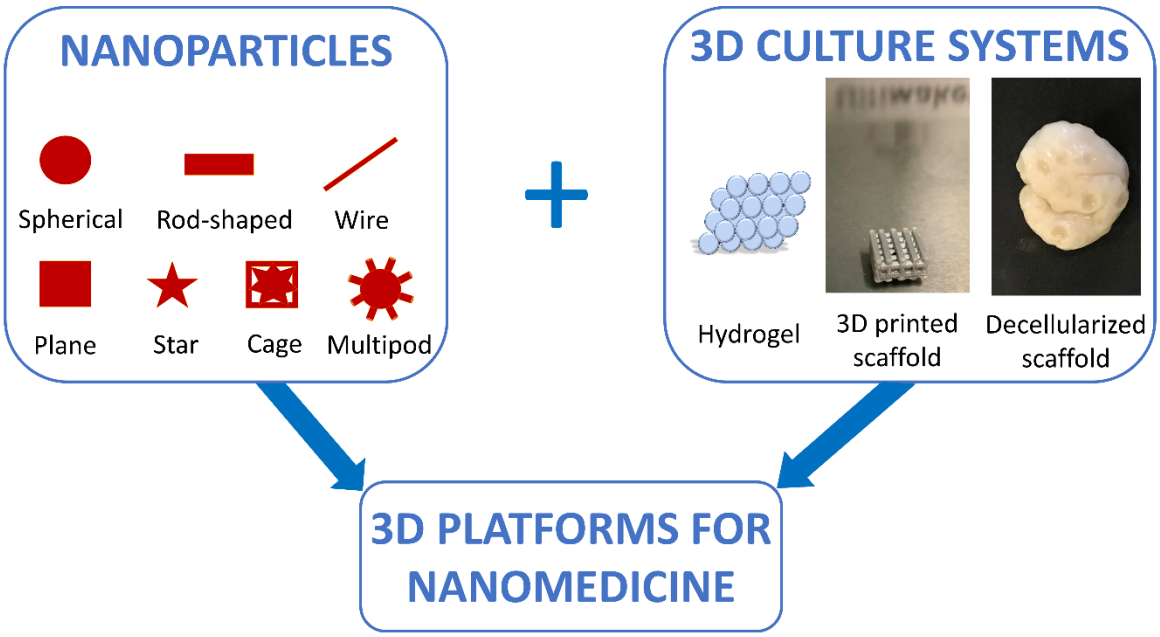


**Figure 5.** Nanomedicine approaches are improved through a combined use of NP-based techniques and 3D culture systems.

NPs were, for example, combined with the use of micro-bioreactors to investigate their accumulation and penetration in spheroid organoids and in solid tumors [240,241]. Using this 3D model, different studies demonstrated that smaller particles can penetrate deeper into 3D multicellular structures [242]. This led researchers to develop novel size-switching NPs, contributing to the advance of nanotheranostics [243]. Indeed, NPs are being investigated for use in photothermal therapy as theranostic agents. Currently, ongoing preclinical in vitro studies involve the use of 3D culture systems to analyze the efficacy of NP-based therapy [238].

It is also interesting to note that, although scaffold-free 3D models are suitable for studying the penetration of NPs in multicellular organoids, this method lacks the complexity of an organ with its parenchyma and stromal-supporting components, which the NPs have to pass through in an in vivo setting. To overcome this problem and verify the influence of the ECM on NP internalization, it is possible to use the so called "scaffold-embedded models", namely hydrogel (as described above), to display an architecture and mechanical properties that closely resemble a natural ECM.

Presently, one of the most interesting approaches is represented by the use of bioengineered 3D models to produce in vitro platforms that replicate host–pathogen early interactions and offer a powerful insight into the possible strategies to prevent virus entry into the cell. In this context, we recently described a model to investigate early infection events in the upper airway [244]. More in detail, we created a synthetic hydrogel-based 3D culture system that mimics in vitro the complex architectures and mechanical cues distinctive of the upper airway epithelia. We then exposed the in vitro-generated 3D nasal and tracheal epithelia to virus-mimicking gold NPs (AuNPs),

displaying the typical shape and size distinctive of SARS-CoV-2 and of the majority of Coronaviridae presently known. This infection platform, beside its predictive power and flexibility, is aimed also at ensuring safety. In our understanding, this represents a crucial aspect, since dealing with a virus that is highly contagious, virulent, and even deadly, inevitably reduces the manpower and the number of laboratories that have high protection facilities, significantly affecting in a way the intellectual and scientific resources to fight this as well as other future pandemics [245].

Although a completely different prospect, an innovative nanomedicine approach can be found in the use of thrombospondins (TSPs) to remodel the cell microenvironment. TSP is an ECM protein family, with the ability to modulate multiple physiological and pathological events in healthy tissues as well as in tumors, including cell growth and spreading, angiogenesis, inflammation, and immunity. In addition, it has been recently demonstrated that TSPs play a fundamental role in tissue remodeling, influencing the extracellular microenvironment properties and composition and regulating the interactions between the ECM structural proteins and cells [246]. Based on this, the use of TSPs in nanomedicine can be useful to modify the tumor microenvironment and regulate the progression of cancer growth, which is strictly related to the vascular and ECM remodeling as well as the inflammatory response [247,248]. It must be noted, however, that the complex nature of TSP interactions and functions, including their different cell and tissue specific effects, have led to confusing results and controversial conclusions and it is still debated where these proteins might become desirable targets for an integrative anti-cancer approach.

## 6. Conclusions and Perspectives

The research of the last years have clearly demonstrated that traditional in vitro 2D culture systems do not faithfully imitate the physiological and biochemical features of cells in their original tissue. Indeed, growing evidence shows significant differences between the microenvironment and the effectors provided by bi-dimensional in vitro cell culture models and those of in vivo tissues. This may greatly alter cell response and behavior, in turn heavily affecting the translation of results from bench to bedside, and inevitably leading to the use of large numbers of experimental animal testing, in order to gain reproducible and reliable data.

All these aspects eventually have an impact on the applications of the results, greatly affecting the final outcome of the research. A good example is provided by the high attrition rate that the pharmaceutical industry has been struggling with over the past years when trying to introduce a new prescription medicine into the market [249], only gaining marketing approval after astronomic costs, largely due to unsatisfactory, misleading testing models during the early pre-clinical phase [250,251].

Altogether, this clearly points to the need for continuous improvement of our in vitro models, in an attempt to ensure their physiological meaning and predictive capability. The powerful experimental strategies discussed in the present manuscript all have the common aim to exploit combinations of mechanosensing-related effectors and chemical cues. This can be generated by modulating substrate stiffness, printing functional scaffolds, or preparing a decellularized biological matrix. Regardless of the approach selected, the result will allow for a fine-tuning of the in vitro micro- and macro-environment that produces organized arrangements of cells and encourages the derivation of a well-defined, physiologically organized tissue structure, improving/leading to the acquisition of a specific cell phenotype.

Selecting the most appropriate culture system that best mimic the in vivo situation would lead to the generation of refined models that more closely mimic the physiological environment, enhancing the predictive power of the culture system. This, in turn, would allow for a reduction in the number of animals used to translate the results in vivo, emphasizing the concept of non-invasive investigations and animal welfare and protection.

**Author Contributions:** Conceptualization, T.A.L.B. and F.G.; investigation, G.P., S.A. and T.D.I.; writing—original draft preparation, G.P. and T.A.L.B.; writing—review and editing, T.A.L.B. and F.G.; project administration, T.A.L.B. and F.G.; funding acquisition, T.A.L.B. All authors have read and agreed to the published version of the manuscript.

**Funding:** This research was funded by Carraresi Foundation and MiND FoodS Hub (ID: 1176436).

**Acknowledgments:** Authors are members of the COST Action CA16119 In vitro 3-D total cell guidance and fitness (CellFit) and of the Inter-COST Actions Task-Force on Covid-19.

**Conflicts of Interest:** The authors declare no conflict of interest.

## Abbreviations

| | |
|---|---|
| 2D | Two-dimensional |
| 3D | Three-dimensional |
| ECM | Extracellular matrix |
| FAK | Protein Tyrosine Kinase 2 |
| SRC | SRC Proto-Oncogene Non-Receptor Tyrosine Kinase |
| ERK | Mitogen-Activated Protein Kinase 1 |
| MRTFA | Myocardin Related Transcription Factor A |
| YAP | Yes-associated protein |
| TAZ | WW domain-containing transcription regulator protein 1 |
| LINC | Linker of nucleoskeleton and cytoskeleton |
| MST1/2 | STE20-like protein kinase ½ |
| SAV1 | Salvador family WW domain containing protein 1 |
| MOB1A/B | MOB kinase activator 1A/B |
| LATS1/2 | Large tumor suppressor 1/2 |
| TFs | Transcription factors |
| SMAD2/3 | SMAD Family Member 2/3 |
| TEAD | TEA Domain Transcription Factor |
| ESCs | Embryonic stem cells |
| iPSCs | Induced Pluripotent Stem Cells |
| MSCs | Mesenchymal Stem Cells |
| CAD | Computer-aided design |
| SDS | Sodium dodecyl sulfate |
| GAGs | Glycosaminoglycans |
| SD | Sodium deoxycholate |
| EDTA | Ethylenediaminetetraacetic acid |
| H&E | Hematoxylin and Eosin |
| DAPI | 4′,6-diamidino-2-phenylindole |
| CHAPS | 3-((3-Cholamidopropyl)-dimethylammonio)-1-propanesulfonate |
| PMSF | Phenylmethylsulfonylfluoride |
| NPs | Nanoparticles |
| AuNPs | Gold nanoparticles |

## References

1. Kapałczyńska, M.; Kolenda, T.; Przybyła, W.; Zajączkowska, M.; Teresiak, A.; Filas, V.; Ibbs, M.; Bliźniak, R.; Łuczewski, Ł.; Lamperska, K. 2D and 3D cell cultures—A comparison of different types of cancer cell cultures. *Arch. Med. Sci.* **2018**, *14*, 910–919, doi:10.5114/aoms.2016.63743.
2. Harrison, R.G.; Greenman, M.J.; Mall, F.P.; Jackson, C.M. Observations of the living developing nerve fiber. *Anat. Rec.* **1907**, *1*, 116–128, doi:10.1002/ar.1090010503.
3. Kolenda, T.; Kapałczyńska, M.; Przybyła, W.; Zajączkowska, M.; Teresiak, A.; Filas, V.; Ibbs, M.; Bliźniak, R.; Łuczewski, Ł.; Lamperska, K. State of the art paper 2D and 3D cell cultures-a comparison of different types of cancer cell cultures. **2016**, doi:10.5114/aoms.2016.63743.
4. Langhans, S.A. Three-dimensional in vitro cell culture models in drug discovery and drug repositioning. *Front. Pharmacol.* **2018**, *9*, 6.
5. Duval, K.; Grover, H.; Han, L.H.; Mou, Y.; Pegoraro, A.F.; Fredberg, J.; Chen, Z. Modeling physiological events in 2D vs. 3D cell culture. *Physiology* **2017**, *32*, 266–277.
6. Baker, B.M.; Chen, C.S. Deconstructing the third dimension—How 3D culture microenvironments alter cellular cues. *J. Cell Sci.* **2012**, *125*, 3015–3024, doi:10.1242/jcs.079509.

7. Bissell, M.J.; Rizki, A.; Mian, I.S. Tissue architecture: The ultimate regulator of breast epithelial function. *Curr. Opin. Cell Biol.* **2003**, *15*, 753–62, doi:10.1016/j.ceb.2003.10.016.
8. Hickman, J.A.; Graeser, R.; de Hoogt, R.; Vidic, S.; Brito, C.; Gutekunst, M.; van der Kuip, H. IMI PREDECT consortium Three-dimensional models of cancer for pharmacology and cancer cell biology: Capturing tumor complexity in vitro/ex vivo. *Biotechnol. J.* **2014**, *9*, 1115–1128, doi:10.1002/biot.201300492.
9. Kleinman, H.K.; Philp, D.; Hoffman, M.P. Role of the extracellular matrix in morphogenesis. *Curr. Opin. Biotechnol.* **2003**, *14*, 526–532, doi:10.1016/J.COPBIO.2003.08.002.
10. Pampaloni, F.; Reynaud, E.G.; Stelzer, E.H.K. The third dimension bridges the gap between cell culture and live tissue. *Nat. Rev. Mol. Cell Biol.* **2007**, *8*, 839–845, doi:10.1038/nrm2236.
11. Hamburger, A.; Salmon, S. Primary bioassay of human tumor stem cells. *Science (80-)* **1977**, *197*, 461–463, doi:10.1126/science.560061.
12. Discher, D.E.; Janmey, P.; Wang, Y.L. Tissue cells feel and respond to the stiffness of their substrate. *Science (80-)* **2005**, *310*, 1139–1143.
13. Chicurel, M.E.; Singer, R.H.; Meyer, C.J.; Ingber, D.E. Integrin binding and mechanical tension induce movement of mRNA and ribosomes to focal adhesions. *Nature* **1998**, *392*, 730–733, doi:10.1038/33719.
14. Wozniak, M.A.; Modzelewska, K.; Kwong, L.; Keely, P.J. Focal adhesion regulation of cell behavior. *Biochim. Biophys. Acta Mol. Cell Res.* **2004**, *1692*, 103–119, doi:10.1016/j.bbamcr.2004.04.007.
15. Pruitt, B.L.; Dunn, A.R.; Weis, W.I.; Nelson, W.J. Mechano-Transduction: From Molecules to Tissues. *PLoS Biol.* **2014**, *12*, doi:10.1371/journal.pbio.1001996.
16. Shen, Z.; Niethammer, P. A cellular sense of space and pressure. *Science* **2020**, *370*, 295–296, doi:10.1126/science.abe3881.
17. Kechagia, J.Z.; Ivaska, J.; Roca-Cusachs, P. Integrins as biomechanical sensors of the microenvironment. *Nat. Rev. Mol. Cell Biol.* **2019**, *20*, 457–473.
18. Huveneers, S.; Danen, E.H.J. Adhesion signaling—Crosstalk between integrins, Src and Rho. *J. Cell Sci.* **2009**, *122*, 1059–1069.
19. Trembley, M.A.; Quijada, P.; Agullo-Pascual, E.; Tylock, K.M.; Colpan, M.; Dirkx, R.A.; Myers, J.R.; Mickelsen, D.M.; De Mesy Bentley, K.; Rothenberg, E.; et al. Mechanosensitive gene regulation by myocardin-related transcription factors is required for cardiomyocyte integrity in load-induced ventricular hypertrophy. *Circulation* **2018**, *138*, 1864–1878, doi:10.1161/CIRCULATIONAHA.117.031788.
20. Martino, F.; Perestrelo, A.R.; Vinarský, V.; Pagliari, S.; Forte, G. Cellular Mechanotransduction: From Tension to Function. *Front. Physiol.* **2018**, *9*, 824, doi:10.3389/fphys.2018.00824.
21. Varelas, X. The Hippo pathway effectors TAZ and YAP in development, homeostasis and disease. *Development* **2014**, *141*, 1614–1626, doi:10.1242/dev.102376.
22. Hansen, C.G.; Moroishi, T.; Guan, K.-L. YAP and TAZ: A nexus for Hippo signaling and beyond. *Trends Cell Biol.* **2015**, *25*, 499–513, doi:10.1016/J.TCB.2015.05.002.
23. Pennarossa, G.; Paffoni, A.; Ragni, G.; Gandolfi, F.; Brevini, T.A.L. Rho Signaling-Directed YAP/TAZ Regulation Encourages 3D Spheroid Colony Formation and Boosts Plasticity of Parthenogenetic Stem Cells. *Adv. Exp. Med. Biol.* **2020**, *1237*, 49–60, doi:10.1007/5584_2019_423.
24. Brevini, T.A.L.; Pennarossa, G.; Gandolfi, F. A 3D approach to reproduction. *Theriogenology* **2020**, doi:10.1016/j.theriogenology.2020.01.020.
25. Halder, G.; Dupont, S.; Piccolo, S. Transduction of mechanical and cytoskeletal cues by YAP and TAZ. *Nat. Rev. Mol. Cell Biol.* **2012**, *13*, 591–600, doi:10.1038/nrm3416.
26. Dupont, S.; Morsut, L.; Aragona, M.; Enzo, E.; Giulitti, S.; Cordenonsi, M.; Zanconato, F.; Le Digabel, J.; Forcato, M.; Bicciato, S.; et al. Role of YAP/TAZ in mechanotransduction. *Nature* **2011**, *474*, 179–183, doi:10.1038/nature10137.
27. Schroeder, M.C.; Halder, G. Regulation of the Hippo pathway by cell architecture and mechanical signals. *Semin. Cell Dev. Biol.* **2012**, *23*, 803–811.
28. Aragona, M.; Panciera, T.; Manfrin, A.; Giulitti, S.; Michielin, F.; Elvassore, N.; Dupont, S.; Piccolo, S. A mechanical checkpoint controls multicellular growth through YAP/TAZ regulation by actin-processing factors. *Cell* **2013**, *154*, 1047–1059, doi:10.1016/j.cell.2013.07.042.
29. Fernández, B.G.; Gaspar, P.; Brás-Pereira, C.; Jezowska, B.; Rebelo, S.R.; Janody, F. Actin-capping Protein and the Hippo pathway regulate F-actin and tissue growth in Drosophila. *Development* **2011**, *138*, 2337–2346, doi:10.1242/dev.063545.
30. Calvo, F.; Ege, N.; Grande-Garcia, A.; Hooper, S.; Jenkins, R.P.; Chaudhry, S.I.; Harrington, K.; Williamson, P.; Moeendarbary, E.; Charras, G.; et al. Mechanotransduction and YAP-dependent matrix remodelling is required for the generation and maintenance of cancer-associated fibroblasts. *Nat. Cell Biol.* **2013**, *15*, 637–646, doi:10.1038/ncb2756.
31. Thomasy, S.M.; Morgan, J.T.; Wood, J.A.; Murphy, C.J.; Russell, P. Substratum stiffness and latrunculin B modulate the gene expression of the mechanotransducers YAP and TAZ in human trabecular meshwork cells. *Exp. Eye Res.* **2013**, *113*, 66–73, doi:10.1016/j.exer.2013.05.014.
32. Pennarossa, G.; Manzoni, E.F.M.E.F.M.; Ledda, S.; de Eguileor, M.; Gandolfi, F.; Brevini, T.A. Use of a PTFE Micro-Bioreactor to Promote 3D Cell Rearrangement and Maintain High Plasticity in Epigenetically Erased Fibroblasts. *Stem Cell Rev. Reports* **2019**, *15*, 82–92, doi:10.1007/s12015-018-9862-5.
33. Brevini, T.A.L.; Pennarossa, G.; Maffei, S.; Gandolfi, F. Pluripotency network in porcine embryos and derived cell lines. *Reprod. Domest. Anim.* **2012**, *47*, doi:10.1111/j.1439-0531.2012.02060.x.
34. Brevini, T.A.L.; Pennarossa, G.; Antonini, S.; Gandolfi, F. Parthenogenesis as an approach to pluripotency: Advantages and limitations involved. *Stem Cell Rev.* **2008**, *4*, doi:10.1007/s12015-008-9027-z.

35. Brevini, T.A.L.; Pennarossa, G.; Gandolfi, F. No shortcuts to pig embryonic stem cells. *Theriogenology* **2010**, *74*, doi:10.1016/j.theriogenology.2010.04.020.
36. Pan, D. The Hippo Signaling Pathway in Development and Cancer. *Dev. Cell* **2010**, *19*, 491–505, doi:10.1016/j.devcel.2010.09.011.
37. Holden, J.K.; Cunningham, C.N. Targeting the Hippo Pathway and Cancer through the TEAD Family of Transcription Factors. *Cancers* **2018**, *10*, doi:10.3390/cancers10030081.
38. Burdick, J.A.; Vunjak-Novakovic, G. Engineered microenvironments for controlled stem cell differentiation. *Tissue Eng. Part A* **2009**, *15*, 205–219.
39. Scadden, D.T. The stem-cell niche as an entity of action. *Nature* **2006**, *441*, 1075–1079.
40. Underhill, G.H.; Bhatia, S.N. High-throughput analysis of signals regulating stem cell fate and function. *Curr. Opin. Chem. Biol.* **2007**, *11*, 357–366.
41. Vining, K.H.; Mooney, D.J. Mechanical forces direct stem cell behaviour in development and regeneration. *Nat. Rev. Mol. Cell Biol.* **2017**, *18*, 728, doi:10.1038/NRM.2017.108.
42. Huh, D.; Hamilton, G.A.; Ingber, D.E. From 3D cell culture to organs-on-chips. *Trends Cell Biol.* **2011**, *21*, 745–754.
43. Gu, L.; Mooney, D.J. Biomaterials and emerging anticancer therapeutics: Engineering the microenvironment. *Nat. Rev. Cancer* **2016**, *16*, 56–66.
44. Nguyen, E.H.; Daly, W.T.; Le, N.N.T.; Farnoodian, M.; Belair, D.G.; Schwartz, M.P.; Lebakken, C.S.; Ananiev, G.E.; Saghiri, M.A.; Knudsen, T.B.; et al. Versatile synthetic alternatives to Matrigel for vascular toxicity screening and stem cell expansion. *Nat. Biomed. Eng.* **2017**, *1*, doi:10.1038/s41551-017-0096.
45. Villa-Diaz, L.G.; Ross, A.M.; Lahann, J.; Krebsbach, P.H. Concise review: The evolution of human pluripotent stem cell culture: From feeder cells to synthetic coatings. *Stem Cells* **2013**, *31*, 1–7, doi:10.1002/stem.1260.
46. Xu, C.; Inokuma, M.S.; Denham, J.; Golds, K.; Kundu, P.; Gold, J.D.; Carpenter, M.K. Feeder-free growth of undifferentiated human embryonic stem cells. *Nat. Biotechnol.* **2001**, *19*, 971–974, doi:10.1038/nbt1001-971.
47. Picollet-D'hahan, N.; Dolega, M.E.; Liguori, L.; Marquette, C.; Le Gac, S.; Gidrol, X.; Martin, D.K. A 3D Toolbox to Enhance Physiological Relevance of Human Tissue Models. *Trends Biotechnol.* **2016**, *34*, 757–769.
48. Bemmelen, J.M. Der Hydrogel und das kristallinische Hydrat des Kupferoxydes. *Zeitschrift für Chemie und Ind. der Kolloide* **1907**, *1*, 213–214, doi:10.1007/BF01830147.
49. Ahmed, E.M. Hydrogel: Preparation, characterization, and applications: A review. *J. Adv. Res.* **2015**, *6*, 105–121.
50. Ahmed, E.M.; Aggor, F.S.; Awad, A.M.; El-Aref, A.T. An innovative method for preparation of nanometal hydroxide superabsorbent hydrogel. *Carbohydr. Polym.* **2013**, *91*, 693–698, doi:10.1016/j.carbpol.2012.08.056.
51. Hu, W.; Wang, Z.; Xiao, Y.; Zhang, S.; Wang, J. Advances in crosslinking strategies of biomedical hydrogels. *Biomater. Sci.* **2019**, *7*, 843–855.
52. Campiglio, C.E.; Contessi Negrini, N.; Farè, S.; Draghi, L. Cross-Linking Strategies for Electrospun Gelatin Scaffolds. *Materials* **2019**, *12*, 2476, doi:10.3390/ma12152476.
53. Engler, A.J.; Sen, S.; Sweeney, H.L.; Discher, D.E. Matrix elasticity directs stem cell lineage specification. *Cell* **2006**, *126*, 677–689, doi:10.1016/j.cell.2006.06.044.
54. Oyen, M.L. Mechanical characterisation of hydrogel materials. *Int. Mater. Rev.* **2014**, *59*, 44–59, doi:10.1179/1743280413Y.0000000022.
55. Kisiday, J.; Jin, M.; Kurz, B.; Hung, H.; Semino, C.; Zhang, S.; Grodzinsky, A.J. Self-assembling peptide hydrogel fosters chondrocyte extracellular matrix production and cell division: Implications for cartilage tissue repair. *Proc. Natl. Acad. Sci. USA* **2002**, *99*, 9996–10001, doi:10.1073/pnas.142309999.
56. Yamaoka, H.; Asato, H.; Ogasawara, T.; Nishizawa, S.; Takahashi, T.; Nakatsuka, T.; Koshima, I.; Nakamura, K.; Kawaguchi, H.; Chung, U. Il; et al. Cartilage tissue engineering using human auricular chondrocytes embedded in different hydrogel materials. *J. Biomed. Mater. Res. Part A* **2006**, *78*, 1–11, doi:10.1002/jbm.a.30655.
57. Li, F.; Carlsson, D.; Lohmann, C.; Suuronen, E.; Vascotto, S.; Kobuch, K.; Sheardown, H.; Munger, R.; Nakamura, M.; Griffith, M. Cellular and nerve regeneration within a biosynthetic extracellular matrix for corneal transplantation. *Proc. Natl. Acad. Sci. USA* **2003**, *100*, 15346–15351, doi:10.1073/pnas.2536767100.
58. Hu, X.; Lui, W.; Cui, L.; Wang, M.; Cao, Y. Tissue engineering of nearly transparent corneal stroma. *Tissue Eng*. **2005**, *11*, 1710–1717.
59. Black, A.F.; Bouez, C.; Perrier, E.; Schlotmann, K.; Chapuis, F.; Damour, O. Optimization and characterization of an engineered human skin equivalent. *Tissue Eng.* **2005**, *11*, 723–733, doi:10.1089/ten.2005.11.723.
60. Fuchs, J.R.; Kaviani, A.; Oh, J.T.; LaVan, D.; Udagawa, T.; Jennings, R.W.; Wilson, J.M.; Fauza, D.O. Diaphragmatic reconstruction with autologous tendon engineered from mesenchymal amniocytes. *J. Pediatr. Surg.* **2004**, *39*, 834–838, doi:10.1016/j.jpedsurg.2004.02.014.
61. Nerem, R.M.; Seliktar, D. Vascular Tissue Engineering. *Annu. Rev. Biomed. Eng.* **2001**, *3*, 225–243, doi:10.1146/annurev.bioeng.3.1.225.
62. Pennarossa, G.; Santoro, R.; Manzoni, E.F.M.; Pesce, M.; Gandolfi, F.; Brevini, T.A.L. Epigenetic Erasing and Pancreatic Differentiation of Dermal Fibroblasts into Insulin-Producing Cells are Boosted by the Use of Low-Stiffness Substrate. *Stem Cell Rev. Rep.* **2018**, *14*, 398–411, doi:10.1007/s12015-017-9799-0.
63. Manzoni, E.F.M.; Pennarossa, G.; Deeguileor, M.; Tettamanti, G.; Gandolfi, F.; Brevini, T.A.L. 5-azacytidine affects TET2 and histone transcription and reshapes morphology of human skin fibroblasts. *Sci. Rep.* **2016**, *6*, doi:10.1038/srep37017.
64. Keller, G.M. In vitro differentiation of embryonic stem cells. *Curr. Opin. Cell Biol.* **1995**, *7*, 862–869, doi:10.1016/0955-0674(95)80071-9.
65. Pennarossa, G.; Ledda, S.; Arcuri, S.; Gandolfi, F.; Brevini, T.A.L. A Two-Step Strategy that Combines Epigenetic Modification and Biomechanical Cues to Generate Mammalian Pluripotent Cells. *J. Vis. Exp.* **2020**, doi:10.3791/61655.

66. Dolega, M.E.; Abeille, F.; Picollet-D'hahan, N.; Gidrol, X. Controlled 3D culture in Matrigel microbeads to analyze clonal acinar development. *Biomaterials* **2015**, *52*, 347–357, doi:10.1016/j.biomaterials.2015.02.042.
67. Nguyen, N.K.; Ooi, C.H.; Singha, P.; Jin, J.; Sreejith, K.R.; Phan, H.P.; Nguyen, N.T. Liquid marbles as miniature reactors for chemical and biological applications. *Processes* **2020**, *8*, 793.
68. Aussillous, P.; Quéré, D. Liquid marbles. *Nature* **2001**, *411*, 924–927, doi:10.1038/35082026.
69. Tanimu, A.; Jaenicke, S.; Alhooshani, K. Heterogeneous catalysis in continuous flow microreactors: A review of methods and applications. *Chem. Eng. J.* **2017**, *327*, 792–821.
70. Watts, P.; Haswell, S.J. The application of micro reactors for organic synthesis. *Chem. Soc. Rev.* **2005**, *34*, 235–246, doi:10.1039/b313866f.
71. Yoshida, J.; Nagaki, A.; Yamada, T. Flash Chemistry: Fast Chemical Synthesis by Using Microreactors. *Chem. A Eur. J.* **2008**, *14*, 7450–7459, doi:10.1002/chem.200800582.
72. Jiao, Z.; Huang, X.; Nguyen, N.T.; Abgrall, P. Thermocapillary actuation of droplet in a planar microchannel. *Microfluid. Nanofluidics* **2008**, *5*, 205–214, doi:10.1007/s10404-007-0235-7.
73. Draper, T.C.; Fullarton, C.; Phillips, N.; de Lacy Costello, B.P.J.; Adamatzky, A. Mechanical sequential counting with liquid marbles. In *Proceedings of the Lecture Notes in Computer Science (Including Subseries Lecture Notes in Artificial Intelligence and Lecture Notes in Bioinformatics)*; Springer: 2018; Volume 10867 LNCS, pp. 59–71.
74. Nguyen, N.-T.; Hejazian, M.; Ooi, C.; Kashaninejad, N. Recent Advances and Future Perspectives on Microfluidic Liquid Handling. *Micromachines* **2017**, *8*, 186, doi:10.3390/mi8060186.
75. Draper, T.C.; Fullarton, C.; Phillips, N.; Costello, B.P.J.D.L.; Adamatzky, A. Liquid Marble Interaction Gate for Collision-Based Computing. *Mater. Today* **2017**, *20*, 561–568, doi:10.1016/j.mattod.2017.09.004.
76. McHale, G.; Newton, M.I. Liquid marbles: Principles and applications. *Soft Matter* **2011**, *7*, 5473–5481, doi:10.1039/c1sm05066d.
77. Vadivelu, R.K.; Kamble, H.; Munaz, A.; Nguyen, N.T. Liquid marbles as bioreactors for the study of three-dimensional cell interactions. *Biomed. Microdevices* **2017**, *19*, doi:10.1007/s10544-017-0171-6.
78. Ledda, S.; Idda, A.; Kelly, J.; Ariu, F.; Bogliolo, L.; Bebbere, D. A novel technique for in vitro maturation of sheep oocytes in a liquid marble microbioreactor. *J. Assist. Reprod. Genet.* **2016**, *33*, 513–8, doi:10.1007/s10815-016-0666-8.
79. Sarvi, F.; Arbatan, T.; Chan, P.P.Y.; Shen, W.A. A novel technique for the formation of embryoid bodies inside liquid marbles. *RSC Adv.* **2013**, *3*, 14501–14508, doi:10.1039/C3RA40364E.
80. Brevini, T.A.L.L.; Manzoni, E.F.M.M.; Ledda, S.; Gandolfi, F. Use of a Super-hydrophobic Microbioreactor to Generate and Boost Pancreatic Mini-organoids. In *Methods in Molecular Biology (Clifton, N.J.)*; 2017; Volume 1576, pp. 291–299.
81. Vadivelu, R.K.; Kamble, H.; Munaz, A.; Nguyen, N.-T. Liquid Marble as Bioreactor for Engineering Three-Dimensional Toroid Tissues. *Sci. Rep.* **2017**, *7*, 12388, doi:10.1038/s41598-017-12636-5.
82. Vadivelu, R.K.; Ooi, C.H.; Yao, R.-Q.; Tello Velasquez, J.; Pastrana, E.; Diaz-Nido, J.; Lim, F.; Ekberg, J.A.K.; Nguyen, N.-T.; St John, J.A. Generation of three-dimensional multiple spheroid model of olfactory ensheathing cells using floating liquid marbles. *Sci. Rep.* **2015**, *5*, 15083, doi:10.1038/srep15083.
83. Laperrousaz, B.; Porte, S.; Gerbaud, S.; Härmä, V.; Kermarrec, F.; Hourtane, V.; Bottausci, F.; Gidrol, X.; Picollet-D'Hahan, N. Direct transfection of clonal organoids in Matrigel microbeads: A promising approach toward organoid-based genetic screens. *Nucleic Acids Res.* **2018**, *46*, doi:10.1093/nar/gky030.
84. Hull, C.W.; Arcadia, C. *United States Patent (19) Hull (54) (75) (73) 21) 22 (51) 52) (58) (56) Apparatus for Production of Three-Dmensonal Objects by Stereo Thography*; 1984.
85. Do, A.V.; Khorsand, B.; Geary, S.M.; Salem, A.K. 3D Printing of Scaffolds for Tissue Regeneration Applications. *Adv. Healthc. Mater.* **2015**, *4*, 1742–1762.
86. Lowther, M.; Louth, S.; Davey, A.; Hussain, A.; Ginestra, P.; Carter, L.; Eisenstein, N.; Grover, L.; Cox, S. Clinical, industrial, and research perspectives on powder bed fusion additively manufactured metal implants. *Addit. Manuf.* **2019**, *28*, 565–584.
87. Cools, P.; Declercq, H.; Ghobeira, R.; Morent, R.; De Geyter, N. Acrylic acid plasma coatings for enhanced cell migration in PCL 3D additive manufactured scaffolds. *Surf. Coatings Technol.* **2018**, *350*, 925–935, doi:10.1016/j.surfcoat.2018.03.067.
88. Ferreira, R.T.L.; Amatte, I.C.; Dutra, T.A.; Bürger, D. Experimental characterization and micrography of 3D printed PLA and PLA reinforced with short carbon fibers. *Compos. Part B Eng.* **2017**, *124*, 88–100, doi:10.1016/j.compositesb.2017.05.013.
89. Adhikari, A.R.; Geranpayeh, T.; Chu, W.K.; Otteson, D.C. Improved cellular response of ion modified poly(lactic acid-co-glycolic acid) substrates for mouse fibroblast cells. *Mater. Sci. Eng. C* **2016**, *60*, 151–155, doi:10.1016/j.msec.2015.11.020.
90. Miguez-Pacheco, V.; Hench, L.L.; Boccaccini, A.R. Bioactive glasses beyond bone and teeth: Emerging applications in contact with soft tissues. *Acta Biomater.* **2015**, *13*, 1–15.
91. Liu, J.; Yan, C. 3D Printing of Scaffolds for Tissue Engineering. In *3D Printing*; InTech: 2018.
92. Pei, X.; Zhang, B.; Fan, Y.; Zhu, X.; Sun, Y.; Wang, Q.; Zhang, X.; Zhou, C. Bionic mechanical design of titanium bone tissue implants and 3D printing manufacture. *Mater. Lett.* **2017**, *208*, 133–137, doi:10.1016/j.matlet.2017.04.128.
93. Cui, H.; Nowicki, M.; Fisher, J.P.; Zhang, L.G. 3D Bioprinting for Organ Regeneration. *Adv. Healthc. Mater.* **2017**, *6*, 1601118.
94. Felgueiras, J.; Ribeiro, R.; Brevini, T.A.L.; Costa, P.F. State-of-the-art in reproductive bench science: Hurdles and new technological solutions. *Theriogenology* **2020**, *150*, 34–40, doi:10.1016/j.theriogenology.2020.01.067.
95. Li, J.; Chen, M.; Fan, X.; Zhou, H. Recent advances in bioprinting techniques: Approaches, applications and future prospects. *J. Transl. Med.* **2016**, *14*, doi:10.1186/s12967-016-1028-0.

96. Leberfinger, A.N.; Ravnic, D.J.; Dhawan, A.; Ozbolat, I.T. Concise Review: Bioprinting of Stem Cells for Transplantable Tissue Fabrication. *Stem Cells Transl. Med.* **2017**, *6*, 1940–1948.
97. Matai, I.; Kaur, G.; Seyedsalehi, A.; McClinton, A.; Laurencin, C.T. Progress in 3D bioprinting technology for tissue/organ regenerative engineering. *Biomaterials* **2020**, *226*, 119536.
98. Anwari, V.; Lai, A.; Ursani, A.; Rego, K.; Karasfi, B.; Sajja, S.; Paul, N. 3D printed CT-based abdominal structure mannequin for enabling research. *3D Print. Med.* **2020**, *6*, 1–12, doi:10.1186/s41205-020-0056-9.
99. Chung, M.; Radacsi, N.; Robert, C.; McCarthy, E.D.; Callanan, A.; Conlisk, N.; Hoskins, P.R.; Koutsos, V. On the optimization of low-cost FDM 3D printers for accurate replication of patient-specific abdominal aortic aneurysm geometry. *3D Print. Med.* **2018**, *4*, 2, doi:10.1186/s41205-017-0023-2.
100. Jacobs, S.; Grunert, R.; Mohr, F.W.; Falk, V. Work in progress report—Experimental. 3D-Imaging of cardiac structures using 3D heart models for planning in heart surgery: A preliminary study. *Interact. Cardiovasc. Thorac. Surg.* **2008**, *7*, 6–9, doi:10.1510/icvts.2007.156588.
101. Marro, A.; Bandukwala, T.; Mak, W. Three-Dimensional Printing and Medical Imaging: A Review of the Methods and Applications. *Curr. Probl. Diagn. Radiol.* **2016**, *45*, 2–9.
102. Mitsouras, D.; Liacouras, P.; Imanzadeh, A.; Giannopoulos, A.A.; Cai, T.; Kumamaru, K.K.; George, E.; Wake, N.; Caterson, E.J.; Pomahac, B.; et al. Medical 3D printing for the radiologist. *Radiographics* **2015**, *35*, 1965–1988, doi:10.1148/rg.2015140320.
103. Grillo, F.W.; Souza, V.H.; Matsuda, R.H.; Rondinoni, C.; Pavan, T.Z.; Baffa, O.; Machado, H.R.; Carneiro, A.A.O. Patient-specific neurosurgical phantom: Assessment of visual quality, accuracy, and scaling effects. *3D Print. Med.* **2018**, *4*, 3, doi:10.1186/s41205-018-0025-8.
104. Mcmenamin, P.G.; Quayle, M.R.; Mchenry, C.R.; Adams, J.W. The production of anatomical teaching resources using three-dimensional (3D) printing technology. *Anat. Sci. Educ.* **2014**, *7*, 479–486, doi:10.1002/ase.1475.
105. Yan, Q.; Dong, H.; Su, J.; Han, J.; Song, B.; Wei, Q.; Shi, Y. A Review of 3D Printing Technology for Medical Applications. *Engineering* **2018**, *4*, 729–742.
106. Shahrubudin, N.; Lee, T.C.; Ramlan, R. An overview on 3D printing technology: Technological, materials, and applications. In *Proceedings of the Procedia Manufacturing*; Elsevier B.V.: 2019; Volume 35, pp. 1286–1296.
107. Ngo, T.D.; Kashani, A.; Imbalzano, G.; Nguyen, K.T.Q.; Hui, D. Additive manufacturing (3D printing): A review of materials, methods, applications and challenges. *Compos. Part B Eng.* **2018**, *143*, 172–196.
108. Nemati, S.; Kim, S. jeong; Shin, Y.M.; Shin, H. Current progress in application of polymeric nanofibers to tissue engineering. *Nano Converg.* **2019**, *6*, 1–16.
109. Wang, J.; Cai, B.G.; Liu, J.; Shangguan, W. Electromagnetic compatibility design of multi-sensor based train integrated positioning system. In Proceedings of the 2010 12th International Conference on Electromagnetics in Advanced Applications, ICEAA'10, Sydney, Australia, 20–24 September 2010; pp. 753–756.
110. Wang, X.; Ding, B.; Li, B. Biomimetic electrospun nanofibrous structures for tissue engineering. *Mater. Today* **2013**, *16*, 229–241.
111. Eatemadi, A.; Daraee, H.; Zarghami, N.; Melat Yar, H.; Akbarzadeh, A. Nanofiber: Synthesis and biomedical applications. *Artif. Cells Nanomed. Biotechnol.* **2016**, *44*, 111–121, doi:10.3109/21691401.2014.922568.
112. Soliman, S.; Pagliari, S.; Rinaldi, A.; Forte, G.; Fiaccavento, R.; Pagliari, F.; Franzese, O.; Minieri, M.; Di Nardo, P.; Licoccia, S.; et al. Multiscale three-dimensional scaffolds for soft tissue engineering via multimodal electrospinning. *Acta Biomater.* **2010**, *6*, 1227–1237, doi:10.1016/j.actbio.2009.10.051.
113. Wu, J.; Huang, C.; Liu, W.; Yin, A.; Chen, W.; He, C.; Wang, H.; Liu, S.; Fan, C.; Bowlin, G.L.; et al. Cell infiltration and vascularization in porous nanoyarn scaffolds prepared by dynamic liquid electrospinning. *J. Biomed. Nanotechnol.* **2014**, *10*, 603–614, doi:10.1166/jbn.2014.1733.
114. Badrossamay, M.R.; McIlwee, H.A.; Goss, J.A.; Parker, K.K. Nanofiber assembly by rotary jet-spinning. *Nano Lett.* **2010**, *10*, 2257–2261, doi:10.1021/nl101355x.
115. Min, L.; Pan, H.; Chen, S.; Wang, C.; Wang, N.; Zhang, J.; Cao, Y.; Chen, X.; Hou, X. Recent progress in bio-inspired electrospun materials. *Compos. Commun.* **2019**, *11*, 12–20.
116. Agarwal, S.; Wendorff, J.H.; Greiner, A. Progress in the field of electrospinning for tissue engineering applications. *Adv. Mater.* **2009**, *21*, 3343–3351, doi:10.1002/adma.200803092.
117. Ulery, B.D.; Nair, L.S.; Laurencin, C.T. Biomedical applications of biodegradable polymers. *J. Polym. Sci. Part B Polym. Phys.* **2011**, *49*, 832–864.
118. Liu, W.; Thomopoulos, S.; Xia, Y. Electrospun nanofibers for regenerative medicine. *Adv. Healthc. Mater.* **2012**, *1*, 10–25, doi:10.1002/adhm.201100021.
119. Huang, C.; Fu, X.; Liu, J.; Qi, Y.; Li, S.; Wang, H. The involvement of integrin β1 signaling in the migration and myofibroblastic differentiation of skin fibroblasts on anisotropic collagen-containing nanofibers. *Biomaterials* **2012**, *33*, 1791–1800, doi:10.1016/j.biomaterials.2011.11.025.
120. Xie, J.; MacEwan, M.R.; Ray, W.Z.; Liu, W.; Siewe, D.Y.; Xia, Y. Radially aligned, electrospun nanofibers as dural substitutes for wound closure and tissue regeneration applications. *ACS Nano* **2010**, *4*, 5027–5036, doi:10.1021/nn101554u.
121. Li, D.; Wang, Y.; Xia, Y. Electrospinning Nanofibers as Uniaxially Aligned Arrays and Layer-by-Layer Stacked Films. *Adv. Mater.* **2004**, *16*, 361–366, doi:10.1002/adma.200306226.
122. Yang, D.; Lu, B.; Zhao, Y.; Jiang, X. Fabrication of aligned fibrous arrays by magnetic electrospinning. *Adv. Mater.* **2007**, *19*, 3702–3706, doi:10.1002/adma.200700171.
123. Matthews, J.A.; Wnek, G.E.; Simpson, D.G.; Bowlin, G.L. Electrospinning of collagen nanofibers. *Biomacromolecules* **2002**, *3*, 232–238, doi:10.1021/bm015533u.

124. Teo, W.E.; Ramakrishna, S. A review on electrospinning design and nanofibre assemblies. *Nanotechnology* **2006**, *17*, doi:10.1088/0957-4484/17/14/R01.
125. Tan, Z.; Gao, X.; Liu, T.; Yang, Y.; Zhong, J.; Tong, C.; Tan, Y. Electrospun vein grafts with high cell infiltration for vascular tissue engineering. *Mater. Sci. Eng. C* **2017**, *81*, 407–415, doi:10.1016/j.msec.2017.08.034.
126. Wu, T.; Zhang, J.; Wang, Y.; Li, D.; Sun, B.; El-Hamshary, H.; Yin, M.; Mo, X. Fabrication and preliminary study of a biomimetic tri-layer tubular graft based on fibers and fiber yarns for vascular tissue engineering. *Mater. Sci. Eng. C* **2018**, *82*, 121–129, doi:10.1016/j.msec.2017.08.072.
127. Li, Y.; Wang, Y.; Ye, J.; Yuan, J.; Xiao, Y. Fabrication of poly(ϵ-caprolactone)/keratin nanofibrous mats as a potential scaffold for vascular tissue engineering. *Mater. Sci. Eng. C* **2016**, *68*, 177–183, doi:10.1016/j.msec.2016.05.117.
128. Zhu, T.; Yu, K.; Bhutto, M.A.; Guo, X.; Shen, W.; Wang, J.; Chen, W.; El-Hamshary, H.; Al-Deyab, S.S.; Mo, X. Synthesis of RGD-peptide modified poly(ester-urethane) urea electrospun nanofibers as a potential application for vascular tissue engineering. *Chem. Eng. J.* **2017**, *315*, 177–190, doi:10.1016/j.cej.2016.12.134.
129. Malkoc, V.; Chang, L. Applications of electrospun nanofibers in neural tissue engineering. *Eur. J. Biomed. Res.* **2015**, *1*, 25, doi:10.18088/ejbmr.1.3.2015.pp25-29.
130. Hu, J.; Tian, L.; Prabhakaran, M.; Ding, X.; Ramakrishna, S. Fabrication of Nerve Growth Factor Encapsulated Aligned Poly(ε-Caprolactone) Nanofibers and Their Assessment as a Potential Neural Tissue Engineering Scaffold. *Polymers* **2016**, *8*, 54, doi:10.3390/polym8020054.
131. Golafshan, N.; Kharaziha, M.; Fathi, M. Tough and conductive hybrid graphene-PVA: Alginate fibrous scaffolds for engineering neural construct. *Carbon N. Y.* **2017**, *111*, 752–763, doi:10.1016/j.carbon.2016.10.042.
132. Yan, L.; Zhao, B.; Liu, X.; Li, X.; Zeng, C.; Shi, H.; Xu, X.; Lin, T.; Dai, L.; Liu, Y. Aligned Nanofibers from Polypyrrole/Graphene as Electrodes for Regeneration of Optic Nerve via Electrical Stimulation. *ACS Appl. Mater. Interfaces* **2016**, *8*, 6834–6840, doi:10.1021/acsami.5b12843.
133. Xie, J.; Peng, C.; Zhao, Q.; Wang, X.; Yuan, H.; Yang, L.; Li, K.; Lou, X.; Zhang, Y. Osteogenic differentiation and bone regeneration of iPSC-MSCs supported by a biomimetic nanofibrous scaffold. *Acta Biomater.* **2016**, *29*, 365–379, doi:10.1016/j.actbio.2015.10.007.
134. Bhattacharjee, P.; Naskar, D.; Maiti, T.K.; Bhattacharya, D.; Kundu, S.C. Non-mulberry silk fibroin grafted poly (Ie-caprolactone)/nano hydroxyapatite nanofibrous scaffold for dual growth factor delivery to promote bone regeneration. *J. Colloid Interface Sci.* **2016**, *472*, 16–33, doi:10.1016/j.jcis.2016.03.020.
135. Zhu, Y.; Li, D.; Zhang, K.; Jiang, L.; Shi, C.; Fangteng, J.; Zheng, C.; Yang, B.; Sun, H. Novel synthesized nanofibrous scaffold efficiently delivered hBMP-2 encoded in adenoviral vector to promote bone regeneration. *J. Biomed. Nanotechnol.* **2017**, *13*, 437–446, doi:10.1166/jbn.2017.2361.
136. Dhand, C.; Ong, S.T.; Dwivedi, N.; Diaz, S.M.; Venugopal, J.R.; Navaneethan, B.; Fazil, M.H.U.T.; Liu, S.; Seitz, V.; Wintermantel, E.; et al. Bio-inspired in situ crosslinking and mineralization of electrospun collagen scaffolds for bone tissue engineering. *Biomaterials* **2016**, *104*, 323–338, doi:10.1016/j.biomaterials.2016.07.007.
137. Miszuk, J.M.; Xu, T.; Yao, Q.; Fang, F.; Childs, J.D.; Hong, Z.; Tao, J.; Fong, H.; Sun, H. Functionalization of PCL-3D electrospun nanofibrous scaffolds for improved BMP2-induced bone formation. *Appl. Mater. Today* **2018**, *10*, 194–202, doi:10.1016/j.apmt.2017.12.004.
138. Li, W.J.; Danielson, K.G.; Alexander, P.G.; Tuan, R.S. Biological response of chondrocytes cultured in three-dimensional nanofibrous poly(ε-caprolactone) scaffolds. *J. Biomed. Mater. Res. Part A* **2003**, *67*, 1105–1114, doi:10.1002/jbm.a.10101.
139. Baker, B.M.; Nathan, A.S.; Gee, A.O.; Mauck, R.L. The influence of an aligned nanofibrous topography on human mesenchymal stem cell fibrochondrogenesis. *Biomaterials* **2010**, *31*, 6190–6200, doi:10.1016/j.biomaterials.2010.04.036.
140. Wimpenny, I.; Ashammakhi, N.; Yang, Y. Chondrogenic potential of electrospun nanofibres for cartilage tissue engineering. *J. Tissue Eng. Regen. Med.* **2012**, *6*, 536–549, doi:10.1002/term.459.
141. Chen, W.; Xu, Y.; Liu, Y.; Wang, Z.; Li, Y.; Jiang, G.; Mo, X.; Zhou, G. Three-dimensional printed electrospun fiber-based scaffold for cartilage regeneration. *Mater. Des.* **2019**, *179*, 107886, doi:10.1016/j.matdes.2019.107886.
142. Deepthi, S.; Nivedhitha Sundaram, M.; Deepti Kadavan, J.; Jayakumar, R. Layered chitosan-collagen hydrogel/aligned PLLA nanofiber construct for flexor tendon regeneration. *Carbohydr. Polym.* **2016**, *153*, 492–500, doi:10.1016/j.carbpol.2016.07.124.
143. Laranjeira, M.; Domingues, R.M.A.; Costa-Almeida, R.; Reis, R.L.; Gomes, M.E. 3D Mimicry of Native-Tissue-Fiber Architecture Guides Tendon-Derived Cells and Adipose Stem Cells into Artificial Tendon Constructs. *Small* **2017**, *13*, 1700689, doi:10.1002/smll.201700689.
144. Jiang, W.; Li, L.; Zhang, D.; Huang, S.; Jing, Z.; Wu, Y.; Zhao, Z.; Zhao, L.; Zhou, S. Incorporation of aligned PCL-PEG nanofibers into porous chitosan scaffolds improved the orientation of collagen fibers in regenerated periodontium. *Acta Biomater.* **2015**, *25*, 240–252, doi:10.1016/j.actbio.2015.07.023.
145. Madhurakkat Perikamana, S.K.; Lee, J.; Ahmad, T.; Kim, E.M.; Byun, H.; Lee, S.; Shin, H. Harnessing biochemical and structural cues for tenogenic differentiation of adipose derived stem cells (ADSCs) and development of an in vitro tissue interface mimicking tendon-bone insertion graft. *Biomaterials* **2018**, *165*, 79–93, doi:10.1016/j.biomaterials.2018.02.046.
146. Orr, S.B.; Chainani, A.; Hippensteel, K.J.; Kishan, A.; Gilchrist, C.; Garrigues, N.W.; Ruch, D.S.; Guilak, F.; Little, D. Aligned multilayered electrospun scaffolds for rotator cuff tendon tissue engineering. *Acta Biomater.* **2015**, *24*, 117–126, doi:10.1016/j.actbio.2015.06.010.
147. Jank, B.J.; Xiong, L.; Moser, P.T.; Guyette, J.P.; Ren, X.; Cetrulo, C.L.; Leonard, D.A.; Fernandez, L.; Fagan, S.P.; Ott, H.C. Engineered composite tissue as a bioartificial limb graft. *Biomaterials* **2015**, *61*, 246–256, doi:10.1016/j.biomaterials.2015.04.051.

148. Pang, K.; Du, L.; Wu, X. A rabbit anterior cornea replacement derived from acellular porcine cornea matrix, epithelial cells and keratocytes. *Biomaterials* **2010**, *31*, 7257–7265, doi:10.1016/j.biomaterials.2010.05.066.
149. Wang, B.; Borazjani, A.; Tahai, M.; De Jongh Curry, A.L.; Simionescu, D.T.; Guan, J.; To, F.; Elder, S.H.; Liao, J. Fabrication of cardiac patch with decellularized porcine myocardial scaffold and bone marrow mononuclear cells. *J. Biomed. Mater. Res. Part A* **2010**, *94*, 1100–1110, doi:10.1002/jbm.a.32781.
150. Zhou, J.; Fritze, O.; Schleicher, M.; Wendel, H.-P.; Schenke-Layland, K.; Harasztosi, C.; Hu, S.; Stock, U.A. Impact of heart valve decellularization on 3-D ultrastructure, immunogenicity and thrombogenicity. *Biomaterials* **2010**, *31*, 2549–2554, doi:10.1016/J.BIOMATERIALS.2009.11.088.
151. Syed, O.; Walters, N.J.; Day, R.M.; Kim, H.W.; Knowles, J.C. Evaluation of decellularization protocols for production of tubular small intestine submucosa scaffolds for use in oesophageal tissue engineering. *Acta Biomater.* **2014**, *10*, 5043–5054, doi:10.1016/j.actbio.2014.08.024.
152. Sullivan, D.C.; Mirmalek-Sani, S.H.; Deegan, D.B.; Baptista, P.M.; Aboushwareb, T.; Atala, A.; Yoo, J.J. Decellularization methods of porcine kidneys for whole organ engineering using a high-throughput system. *Biomaterials* **2012**, *33*, 7756–7764, doi:10.1016/j.biomaterials.2012.07.023.
153. Schaner, P.J.; Martin, N.D.; Tulenko, T.N.; Shapiro, I.M.; Tarola, N.A.; Leichter, R.F.; Carabasi, R.A.; DiMuzio, P.J. Decellularized vein as a potential scaffold for vascular tissue engineering. *J. Vasc. Surg.* **2004**, *40*, 146–153, doi:10.1016/j.jvs.2004.03.033.
154. Gilpin, S.E.; Guyette, J.P.; Gonzalez, G.; Ren, X.; Asara, J.M.; Mathisen, D.J.; Vacanti, J.P.; Ott, H.C. Perfusion decellularization of human and porcine lungs: Bringing the matrix to clinical scale. *J. Hear. Lung Transplant.* **2014**, *33*, 298–308, doi:10.1016/j.healun.2013.10.030.
155. O'Neill, J.D.; Anfang, R.; Anandappa, A.; Costa, J.; Javidfar, J.; Wobma, H.M.; Singh, G.; Freytes, D.O.; Bacchetta, M.D.; Sonett, J.R.; et al. Decellularization of Human and Porcine Lung Tissues for Pulmonary Tissue Engineering. *Ann. Thorac. Surg.* **2013**, *96*, 1046–1056, doi:10.1016/j.athoracsur.2013.04.022.
156. Pennarossa, G.; Ghiringhelli, M.; Gandolfi, F.; Brevini, T.A.L. Whole-ovary decellularization generates an effective 3D bioscaffold for ovarian bioengineering. *J. Assist. Reprod. Genet.* **2020**, 1–11, doi:10.1007/s10815-020-01784-9.
157. Guyette, J.P.; Charest, J.M.; Mills, R.W.; Jank, B.J.; Moser, P.T.; Gilpin, S.E.; Gershlak, J.R.; Okamoto, T.; Gonzalez, G.; Milan, D.J.; et al. Bioengineering Human Myocardium on Native Extracellular Matrix. *Circ. Res.* **2016**, *118*, 56–72, doi:10.1161/CIRCRESAHA.115.306874.
158. Uygun, B.E.; Soto-Gutierrez, A.; Yagi, H.; Izamis, M.-L.; Guzzardi, M.A.; Shulman, C.; Milwid, J.; Kobayashi, N.; Tilles, A.; Berthiaume, F.; et al. Organ reengineering through development of a transplantable recellularized liver graft using decellularized liver matrix. *Nat. Med.* **2010**, *16*, 814–820, doi:10.1038/nm.2170.
159. Ott, H.C.; Matthiesen, T.S.; Goh, S.K.; Black, L.D.; Kren, S.M.; Netoff, T.I.; Taylor, D.A. Perfusion-decellularized matrix: Using nature's platform to engineer a bioartificial heart. *Nat. Med.* **2008**, *14*, 213–221, doi:10.1038/nm1684.
160. Pennarossa, G.; Ghiringhelli, M.; Gandolfi, F.; Brevini, T.A.L. Creation of a bioengineered ovary: Isolation of female germline stem cells for the repopulation of a decellularized ovarian bio-scaffold. *Methods Mol. Biol.*
161. Vermeulen, M.; del Vento, F.; de Michele, F.; Poels, J.; Wyns, C. Development of a cytocompatible scaffold from pig immature testicular tissue allowing human Sertoli cell attachment, proliferation and functionality. *Int. J. Mol. Sci.* **2018**, *19*, doi:10.3390/ijms19010227.
162. Gupta, S.K.; Dinda, A.K.; Potdar, P.D.; Mishra, N.C. Modification of decellularized goat-lung scaffold with chitosan/ nanohydroxyapatite composite for bone tissue engineering applications. *Biomed Res. Int.* **2013**, *2013*, doi:10.1155/2013/651945.
163. Wang, B.; Tedder, M.E.; Perez, C.E.; Wang, G.; De Jongh Curry, A.L.; To, F.; Elder, S.H.; Williams, L.N.; Simionescu, D.T.; Liao, J. Structural and biomechanical characterizations of porcine myocardial extracellular matrix. *J. Mater. Sci. Mater. Med.* **2012**, *23*, 1835–1847, doi:10.1007/s10856-012-4660-0.
164. Shimoda, H.; Yagi, H.; Higashi, H.; Tajima, K.; Kuroda, K.; Abe, Y.; Kitago, M.; Shinoda, M.; Kitagawa, Y. Decellularized liver scaffolds promote liver regeneration after partial hepatectomy. *Sci. Rep.* **2019**, *9*, 1–11, doi:10.1038/s41598-019-48948-x.
165. Choi, S.H.; Chun, S.Y.; Chae, S.Y.; Kim, J.R.; Oh, S.H.; Chung, S.K.; Lee, J.H.; Song, P.H.; Choi, G.S.; Kim, T.H.; et al. Development of a porcine renal extracellular matrix scaffold as a platform for kidney regeneration. *J. Biomed. Mater. Res. Part A* **2015**, *103*, 1391–1403, doi:10.1002/jbm.a.35274.
166. Laronda, M.M.; Jakus, A.E.; Whelan, K.A.; Wertheim, J.A.; Shah, R.N.; Woodruff, T.K. Initiation of puberty in mice following decellularized ovary transplant. *Biomaterials* **2015**, *50*, 20–9, doi:10.1016/j.biomaterials.2015.01.051.
167. Akbarzadeh, A.; Kianmanesh, M.; Fendereski, K.; Ebadi, M.; Daryabari, S.S.; Masoomi, A.; Ghazisaeedi, F.; Seyyed Hossein Beigi, R.; Sheikh, R.; Kajbafzadeh, A.M. Decellularised whole ovine testis as a potential bio-scaffold for tissue engineering. *Reprod. Fertil. Dev.* **2019**, *31*, 1665–1673, doi:10.1071/RD19070.
168. Macchiarini, P.; Jungebluth, P.; Go, T.; Asnaghi, M.A.; Rees, L.E.; Cogan, T.A.; Dodson, A.; Martorell, J.; Bellini, S.; Parnigotto, P.P.; et al. Clinical transplantation of a tissue-engineered airway. *Lancet* **2008**, *372*, 2023–2030, doi:10.1016/S0140-6736(08)61598-6.
169. Partington, L.; Mordan, N.J.; Mason, C.; Knowles, J.C.; Kim, H.W.; Lowdell, M.W.; Birchall, M.A.; Wall, I.B. Biochemical changes caused by decellularization may compromise mechanical integrity of tracheal scaffolds. *Acta Biomater.* **2013**, *9*, 5251–5261, doi:10.1016/j.actbio.2012.10.004.
170. Nichols, J.E.; Niles, J.; Riddle, M.; Vargas, G.; Schilagard, T.; Ma, L.; Edward, K.; La Francesca, S.; Sakamoto, J.; Vega, S.; et al. Production and assessment of decellularized pig and human lung scaffolds. *Tissue Eng. Part A* **2013**, *19*, 2045–2062, doi:10.1089/ten.tea.2012.0250.
171. Remlinger, N.T.; Wearden, P.D.; Gilbert, T.W. Procedure for decellularization of porcine heart by retrograde coronary perfusion. *J. Vis. Exp.* **2012**, 2–9, doi:10.3791/50059.

172. Ghiringhelli, M.; Zenobi, A.; Brizzola, S.; Gandolfi, F.; Bontempo, V.; Rossi, S.; Brevini, T.A.L.; Acocella, F. Simple and quick method to obtain a decellularized, functional liver bioscaffold. *Methods Mol. Biol.* **2018**, *1577*, 283–292, doi:10.1007/7651_2017_97.
173. Wu, Q.; Bao, J.; Zhou, Y.J.; Wang, Y.J.; Du, Z.G.; Shi, Y.J.; Li, L.; Bu, H. Optimizing perfusion-decellularization methods of porcine livers for clinical-scale whole-organ bioengineering. *Biomed Res. Int.* **2015**, *2015*, doi:10.1155/2015/785474.
174. Vishwakarma, S.K.; Bhavani, P.G.; Bardia, A.; Abkari, A.; Murthy, G.S.N.; Venkateshwarulu, J.; Khan, A.A. Preparation of natural three-dimensional goat kidney scaffold for the development of bioartificial organ. *Indian J. Nephrol.* **2014**, *24*, 372–375, doi:10.4103/0971-4065.133008.
175. Burke, J.F.; Yannas, O.V.; Quinby, W.C.; Bondoc, C.C.; Jung, W.K. Successful use of a physiologically acceptable artificial skin in the treatment of extensive burn injury. *Ann. Surg.* **1981**, *194*, 413–427, doi:10.1097/00000658-198110000-00005.
176. Spira, M.; Fissette, J.; Hall, C.W.; Hardy, S.B.; Gerow, F.J. Evaluation of synthetic fabrics as artificial skin grafts to experimental burn wounds. *J. Biomed. Mater. Res.* **1969**, *3*, 213–234, doi:10.1002/jbm.820030203.
177. Hall, C.W.; Liotta, D.; De Bakey, M.E. Artificial skin. *Trans. Am. Soc. Artif. Intern. Organs* **1966**, *12*, 340–343.
178. O'Connor, N.E.; Mulliken, J.B.; Banks-Schlegel, S.; Kehinde, O.; Green, H. Grafting of Burns with Cultured Epithelium Prepared from Autologous Epidermal Cells. *Lancet* **1981**, *317*, 75–78, doi:10.1016/S0140-6736(81)90006-4.
179. Ishaug, S.L.; Crane, G.M.; Miller, M.J.; Yasko, A.W.; Yaszemski, M.J.; Mikos, A.G. Bone formation by three-dimensional stromal osteoblast culture in biodegradable polymer scaffolds. *J. Biomed. Mater. Res.* **1997**, *36*, 17–28, doi:10.1002/(SICI)1097-4636(199707)36:1<17::AID-JBM3>3.0.CO;2-O.
180. Baksh, D.; Davies, J.E.; Kim, S. Three-dimensional matrices of calcium polyphosphates support bone growth in vitro and in vivo. *J. Mater. Sci. Mater. Med.* **1998**, *9*, 743–748, doi:10.1023/A:1008959103864.
181. Khan, A.A.; Vishwakarma, S.K.; Bardia, A.; Venkateshwarulu, J. Repopulation of decellularized whole organ scaffold using stem cells: An emerging technology for the development of neo-organ. *J. Artif. Organs* **2014**, *17*, 291–300, doi:10.1007/s10047-014-0780-2.
182. Article, R.; Scarritt, M.E.; Pashos, N.C.; Bunnell, B.A.; Bussolati, B. BIOENGINEERING AND BIOTECHNOLOGY A review of cellularization strategies for tissue engineering of whole organs. **2015**, doi:10.3389/fbioe.2015.00043.
183. Shackleton, M.; Vaillant, F.; Simpson, K.J.; Stingl, J.; Smyth, G.K.; Asselin-Labat, M.L.; Wu, L.; Lindeman, G.J.; Visvader, J.E. Generation of a functional mammary gland from a single stem cell. *Nature* **2006**, *439*, 84–88, doi:10.1038/nature04372.
184. Stingl, J.; Eirew, P.; Ricketson, I.; Shackleton, M.; Vaillant, F.; Choi, D.; Li, H.I.; Eaves, C.J. Purification and unique properties of mammary epithelial stem cells. *Nature* **2006**, *439*, 993–997, doi:10.1038/nature04496.
185. Schlieve, C.R.; Grikscheit, T.C. A Purpose in Liquidity: Perfusing 3D Open Scaffolds Improves "Mini-gut" Morphogenesis and Longevity. *Cell Stem Cell* **2020**, *27*, 699–701, doi:10.1016/j.stem.2020.10.010.
186. Han, Y.; Baltriukienė, D.; Kozlova, E.N. Effect of scaffold properties on adhesion and maintenance of boundary cap neural crest stem cells in vitro. *J. Biomed. Mater. Res. Part A* **2020**, *108*, 1274–1280, doi:10.1002/jbm.a.36900.
187. Croce, S.; Peloso, A.; Zoro, T.; Avanzini, M.A.; Cobianchi, L. A hepatic scaffold from decellularized liver tissue: Food for thought. *Biomolecules* **2019**, *9*, 813.
188. Santarella, F.; Sridharan, R.; Marinkovic, M.; Do Amaral, R.J.F.C.; Cavanagh, B.; Smith, A.; Kashpur, O.; Gerami-Naini, B.; Garlick, J.A.; O'Brien, F.J.; et al. Scaffolds Functionalized with Matrix from Induced Pluripotent Stem Cell Fibroblasts for Diabetic Wound Healing. *Adv. Healthc. Mater.* **2020**, *9*, 2000307, doi:10.1002/adhm.202000307.
189. Murphy, A.R.; Haynes, J.M.; Laslett, A.L.; Cameron, N.R.; O'Brien, C.M. Three-dimensional differentiation of human pluripotent stem cell-derived neural precursor cells using tailored porous polymer scaffolds. *Acta Biomater.* **2020**, *101*, 102–116, doi:10.1016/j.actbio.2019.10.017.
190. Ding, M.; Andersson, H.; Martinsson, S.; Sabirsh, A.; Jonebring, A.; Wang, Q.D.; Plowright, A.T.; Drowley, L. Aligned nanofiber scaffolds improve functionality of cardiomyocytes differentiated from human induced pluripotent stem cell-derived cardiac progenitor cells. *Sci. Rep.* **2020**, *10*, doi:10.1038/s41598-020-70547-4.
191. Croce, S.; Peloso, A.; Zoro, T.; Avanzini, M.A.; Cobianchi, L. A hepatic scaffold from decellularized liver tissue: Food for thought. *Biomolecules* **2019**, *9*, 813.
192. Nyberg, S.L.; Remmel, R.P.; Mann, H.J.; Peshwa, M.V.; Hu, W.S.; Cerra, F.B. Primary hepatocytes outperform Hep G2 cells as the source of biotransformation functions in a bioartificial liver. *Ann. Surg.* **1994**, *220*, 59–67.
193. Nagaki, M.; Miki, K.; Kim, Y. Il; Ishiyama, H.; Hirahara, I.; Takahashi, H.; Sugiyama, A.; Muto, Y.; Moriwaki, H. Development and characterization of a hybrid bioartificial liver using primary hepatocytes entrapped in a basement membrane matrix. *Dig. Dis. Sci.* **2001**, *46*, 1046–1056, doi:10.1023/A:1010714112675.
194. Hosseini, V.; Maroufi, N.F.; Saghati, S.; Asadi, N.; Darabi, M.; Ahmad, S.N.S.; Hosseinkhani, H.; Rahbarghazi, R. Current progress in hepatic tissue regeneration by tissue engineering. *J. Transl. Med.* **2019**, *17*, 383.
195. De Carlo, E.; Baiguera, S.; Conconi, M.T.; Vigolo, S.; Grandi, C.; Lora, S.; Martini, C.; Maffei, P.; Tamagno, G.; Vettor, R.; et al. Pancreatic acellular matrix supports islet survival and function in a synthetic tubular device: In vitro and in vivo studies. *Int. J. Mol. Med.* **2010**, *25*, 195–202, doi:10.3892/ijmm_00000330.
196. Conrad, C.; Schuetz, C.; Clippinger, B.; Vacanti, J.P.; Markmann, J.F.; Ott, H.C. Bio-engineered endocrine pancreas based on decellularized pancreatic matrix and mesenchymal stem cell/islet cell coculture. *J. Am. Coll. Surg.* **2010**, *211*, S62, doi:10.1016/j.jamcollsurg.2010.06.161.
197. Peloso, A.; Citro, A.; Oldani, G.; Brambilla, S.; Piemonti, L.; Cobianchi, L. Bioengineering the Pancreas: Cell-on-Scaffold Technology. In *Scaffolds in Tissue Engineering—Materials, Technologies and Clinical Applications*; InTech: 2017.
198. Silva, A.C.; Rodrigues, S.C.; Caldeira, J.; Nunes, A.M.; Sampaio-Pinto, V.; Resende, T.P.; Oliveira, M.J.; Barbosa, M.A.; Thorsteinsdóttir, S.; Nascimento, D.S.; et al. Three-dimensional scaffolds of fetal decellularized hearts exhibit enhanced

potential to support cardiac cells in comparison to the adult. *Biomaterials* **2016**, *104*, 52–64, doi:10.1016/j.biomaterials.2016.06.062.
199. Laronda, M.M. Engineering a bioprosthetic ovary for fertility and hormone restoration. *Theriogenology* **2020**, doi:10.1016/j.theriogenology.2020.01.021.
200. Wragg, N.M.; Burke, L.; Wilson, S.L. A critical review of current progress in 3D kidney biomanufacturing: Advances, challenges, and recommendations. *Ren. Replace. Ther.* **2019**, *5*, 1–16.
201. Mandrycky, C.; Phong, K.; Zheng, Y. Tissue engineering toward organ-specific regeneration and disease modeling. *MRS Commun.* **2017**, *7*, 332–347, doi:10.1557/mrc.2017.58.
202. Mirdamadi, E.S.; Kalhori, D.; Zakeri, N.; Azarpira, N.; Solati-Hashjin, M. Liver tissue engineering as an emerging alternative for liver disease treatment. *Tissue Eng. Part B Rev.* **2020**, *26*, 145–163.
203. Vo, T.N.; Chen, A.X.; Smith, Q.B.; Chhabra, A.; Bhatia, S.N. Integrated Technologies for Liver Tissue Engineering. In *The Liver*; Wiley: Hoboken, NJ, USA, 2020; pp. 1028–1035.
204. Heydari, Z.; Najimi, M.; Mirzaei, H.; Shpichka, A.; Ruoss, M.; Farzaneh, Z.; Montazeri, L.; Piryaei, A.; Timashev, P.; Gramignoli, R.; et al. Tissue Engineering in Liver Regenerative Medicine: Insights into Novel Translational Technologies. *Cells* **2020**, *9*, 304, doi:10.3390/cells9020304.
205. West, J.L. Biomaterials for Cardiovascular Tissue Engineering. In *Biomaterials Science*; Elsevier: Amsterdam, The Netherlands, 2020; pp. 1389–1397.
206. Jang, Y.; Park, Y.; Kim, J. Engineering Biomaterials to Guide Heart Cells for Matured Cardiac Tissue. *Coatings* **2020**, *10*, 925, doi:10.3390/coatings10100925.
207. Bolonduro, O.A.; Duffy, B.M.; Rao, A.A.; Black, L.D.; Timko, B.P. From biomimicry to bioelectronics: Smart materials for cardiac tissue engineering. *Nano Res.* **2020**, *13*, 1253–1267.
208. Tebyanian, H.; Karami, A.; Nourani, M.R.; Motavallian, E.; Barkhordari, A.; Yazdanian, M.; Seifalian, A. Lung tissue engineering: An update. *J. Cell. Physiol.* **2019**, *234*, 19256–19270, doi:10.1002/jcp.28558.
209. Calle, E.A.; Ghaedi, M.; Sundaram, S.; Sivarapatna, A.; Tseng, M.K.; Niklason, L.E. Strategies for whole lung tissue engineering. *IEEE Trans. Biomed. Eng.* **2014**, *61*, 1482–1496, doi:10.1109/TBME.2014.2314261.
210. Petersen, T.H.; Calle, E.A.; Zhao, L.; Lee, E.J.; Gui, L.; Raredon, M.S.B.; Gavrilov, K.; Yi, T.; Zhuang, Z.W.; Breuer, C.; et al. Tissue-engineered lungs for in vivo implantation. *Science (80-)* **2010**, *329*, 538–541, doi:10.1126/science.1189345.
211. Brus, L.E. Electron-electron and electron-hole interactions in small semiconductor crystallites: The size dependence of the lowest excited electronic state. *J. Chem. Phys.* **1984**, *80*, 4403–4409, doi:10.1063/1.447218.
212. Dreaden, E.C.; Mac key, M.A.; Huang, X.; Kang, B.; El-Sayed, M.A. Beating cancer in multiple ways using nanogold. *Chem. Soc. Rev.* **2011**, *40*, 3391–3404, doi:10.1039/c0cs00180e.
213. Bhatia, S.; Bhatia, S. Nanoparticles Types, Classification, Characterization, Fabrication Methods and Drug Delivery Applications. In *Natural Polymer Drug Delivery Systems*; Springer International Publishing: 2016; pp. 33–93.
214. Perrault, S.D.; Chan, W.C.W. Synthesis and surface modification of highly monodispersed, spherical gold nanoparticles of 50-200 nm. *J. Am. Chem. Soc.* **2009**, *131*, 17042–17043, doi:10.1021/ja907069u.
215. Gao, X.; Cui, Y.; Levenson, R.M.; Chung, L.W.K.; Nie, S. In vivo cancer targeting and imaging with semiconductor quantum dots. *Nat. Biotechnol.* **2004**, *22*, 969–976, doi:10.1038/nbt994.
216. Nikoobakht, B.; El-Sayed, M.A. Preparation and growth mechanism of gold nanorods (NRs) using seed-mediated growth method. *Chem. Mater.* **2003**, *15*, 1957–1962, doi:10.1021/cm020732l.
217. Kan, S.; Mokari, T.; Rothenberg, E.; Banin, U. Synthesis and size-dependent properties of zinc-blende semiconductor quantum rods. *Nat. Mater.* **2003**, *2*, 155–158.
218. Cui, Y.; Wei, Q.; Park, H.; Lieber, C.M. Nanowire nanosensors for highly sensitive and selective detection of biological and chemical species. *Science (80-)* **2001**, *293*, 1289–1292, doi:10.1126/science.1062711.
219. Coleman, J.N.; Lotya, M.; O'Neill, A.; Bergin, S.D.; King, P.J.; Khan, U.; Young, K.; Gaucher, A.; De, S.; Smith, R.J.; et al. Two-dimensional nanosheets produced by liquid exfoliation of layered materials. *Science (80-)* **2011**, *331*, 568–571, doi:10.1126/science.1194975.
220. Shi, F.; Wang, J.; Zhai, X.; Zhao, D.; Qin, W. Facile synthesis of β-NaLuF4:Yb/Tm hexagonal nanoplates with intense ultraviolet upconversion luminescence. *CrystEngComm* **2011**, *13*, 3782–3787, doi:10.1039/c1ce05092c.
221. Hao, F.; Nehl, C.L.; Hafner, J.H.; Nordlander, P. Plasmon resonances of a gold nanostar. *Nano Lett.* **2007**, *7*, 729–732, doi:10.1021/nl062969c.
222. Chen, J.; Saeki, F.; Wiley, B.J.; Cang, H.; Cobb, M.J.; Li, Z.Y.; Au, L.; Zhang, H.; Kimmey, M.B.; Li, X.; et al. Gold nanocages: Bioconjugation and their potential use as optical imaging contrast agents. *Nano Lett.* **2005**, *5*, 473–477, doi:10.1021/nl047950t.
223. Yong, K.-T.; Sahoo, Y.; Swihart, M.T.; Prasad, P.N. Growth of CdSe Quantum Rods and Multipods Seeded by Noble-Metal Nanoparticles. *Adv. Mater.* **2006**, *18*, 1978–1982, doi:10.1002/adma.200600368.
224. Teng, X.; Yang, H. Synthesis of platinum multipeds: An induced anisotropic growth. *Nano Lett.* **2005**, *5*, 885–891, doi:10.1021/nl0503072.
225. Prasad, P.N. *Introduction to Biophotonics*; John Wiley & Sons, Inc.: Hoboken, NJ, USA, 2003; ISBN 0471287709.
226. Prasad, P.N. *Nanophotonics*; John Wiley & Sons, Inc.: Hoboken, NJ, USA, 2004; ISBN 0471649880.
227. Chen, G.; Roy, I.; Yang, C.; Prasad, P.N. Nanochemistry and Nanomedicine for Nanoparticle-based Diagnostics and Therapy. *Chem. Rev.* **2016**, *116*, 2826–2885.
228. Goodman, T.T.; Chee, P.N.; Suzie, H.P. 3-D tissue culture systems for the evaluation and optimization of nanoparticle-based drug carriers. *Bioconjug. Chem.* **2008**, *19*, 1951–1959.
229. Riehemann, K.; Schneider, S.W.; Luger, T.A.; Godin, B.; Ferrari, M.; Fuchs, H. Nanomedicine—Challenge and perspectives. *Angew. Chemie Int. Ed.* **2009**, *48*, 872–897.
230. Allen, T.M.; Cullis, P.R. Drug Delivery Systems: Entering the Mainstream. *Science (80-)* **2004**, *303*, 1818–1822.

231. Boisselier, E.; Astruc, D. Gold nanoparticles in nanomedicine: Preparations, imaging, diagnostics, therapies and toxicity. *Chem. Soc. Rev.* **2009**, *38*, 1759–1782, doi:10.1039/b806051g.
232. Cormode, D.P.; Jarzyna, P.A.; Mulder, W.J.M.; Fayad, Z.A. Modified natural nanoparticles as contrast agents for medical imaging. *Adv. Drug Deliv. Rev.* **2010**, *62*, 329–338.
233. Müller, R.H.; Mäder, K.; Gohla, S. Solid lipid nanoparticles (SLN) for controlled drug delivery—A review of the state of the art. *Eur. J. Pharm. Biopharm.* **2000**, *50*, 161–177.
234. Nicolas, J.; Mura, S.; Brambilla, D.; Mackiewicz, N.; Couvreur, P. Design, functionalization strategies and biomedical applications of targeted biodegradable/biocompatible polymer-based nanocarriers for drug delivery. *Chem. Soc. Rev.* **2013**, *42*, 1147–1235, doi:10.1039/c2cs35265f.
235. Anker, J.N.; Hall, W.P.; Lyandres, O.; Shah, N.C.; Zhao, J.; Van Duyne, R.P. Biosensing with plasmonic nanosensors. *Nat. Mater.* **2008**, *7*, 442–453.
236. Lewin, M.; Carlesso, N.; Tung, C.H.; Tang, X.W.; Cory, D.; Scadden, D.T.; Weissleder, R. Tat peptide-derivatized magnetic nanoparticles allow in vivo tracking and recovery of progenitor cells. *Nat. Biotechnol.* **2000**, *18*, 410–414, doi:10.1038/74464.
237. Goldberg, M.; Langer, R.; Jia, X. Nanostructured materials for applications in drug delivery and tissue engineering. *J. Biomater. Sci. Polym. Ed.* **2007**, *18*, 241–268.
238. Darrigues, E.; Nima, Z.A.; Griffin, R.J.; Anderson, J.M.; Biris, A.S.; Rodriguez, A. 3D cultures for modeling nanomaterial-based photothermal therapy. *Nanoscale Horizons* **2020**, *5*, 400–430.
239. Dykman, L.; Khlebtsov, N. Gold nanoparticles in biomedical applications: Recent advances and perspectives. *Chem. Soc. Rev.* **2012**, *41*, 2256–2282, doi:10.1039/c1cs15166e.
240. Lazzari, G.; Couvreur, P.; Mura, S. Multicellular tumor spheroids: A relevant 3D model for the: In vitro preclinical investigation of polymer nanomedicines. *Polym. Chem.* **2017**, *8*, 4947–4969.
241. Lu, H.; Stenzel, M.H. Multicellular Tumor Spheroids (MCTS) as a 3D In Vitro Evaluation Tool of Nanoparticles. *Small* **2018**, *14*, 1702858, doi:10.1002/smll.201702858.
242. Van Zundert, I.; Fortuni, B.; Rocha, S. From 2d to 3d cancer cell models—The enigmas of drug delivery research. *Nanomaterials* **2020**, *10*, 1–30.
243. Mapanao, A.K.; Voliani, V. Three-dimensional tumor models: Promoting breakthroughs in nanotheranostics translational research. *Appl. Mater. Today* **2020**, *19*, 100552, doi:10.1016/j.apmt.2019.100552.
244. Pennarossa, G.; Fazeli, A.; Ledda, S.; Gandolfi, F.; Brevini, T.A.L. Use of virus-mimicking nanoparticles to investigate early infection events in upper airway 3D models. *Methods Mol. Biol. (Clifton, N.J.) Mol Biol*.
245. Vasconcelos, H.; Alcaro, S.; Arechavala-Gomeza, V.; Baumbach, J.; Borges, F.; Brevini, T.A.L.; De Las Rivas, J.; Devaux, Y.; Hozak, P.; Keinänen-Toivola, M.; et al. Joining european scientific forces now to face pandemics. *Trends Microbiol.* **2020**.
246. Tan, K.; Lawler, J. The interaction of Thrombospondins with extracellular matrix proteins. *J. Cell Commun. Signal.* **2009**, *3*, 177–187.
247. Stenina-Adognravi, O. Invoking the power of thrombospondins: Regulation of thrombospondins expression. *Matrix Biol.* **2014**, *37*, 69–82.
248. Stenina-Adognravi, O.; Muppala, S.; Gajeton, J. Thrombospondins and remodeling of the tumor microenvironment. *Vessel Plus* **2018**, *2*, 30, doi:10.20517/2574-1209.2018.40.
249. Jonsson, M.K.B.; Veen, T.A.B.V.; Synnergren, J.; Becker, B. Towards Creating the Perfect in Vitro Cell Model. *Stem Cells Int.* **2016**, *2016*.
250. Tufts CSDD Cost Study—Tufts CSDD. Available online: https://csdd.tufts.edu/tufts-csdd-cost-study (accessed on 11 August 2020).
251. DiMasi, J.A.; Grabowski, H.G.; Hansen, R.W. Innovation in the pharmaceutical industry: New estimates of R&D costs. *J. Health Econ.* **2016**, *47*, 20–33, doi:10.1016/j.jhealeco.2016.01.012.

## 7.2. Combination of epigenetic erasing and mechanical cues to generate human epiBlastoids from adult dermal fibroblasts

Published in Journal of Assisted Reproduction and Genetics on 18 March 2023.

DOI: 10.1007/s10815-023-02773-4.

*Article*

# Combination of epigenetic erasing and mechanical cues to generate human epiBlastoids from adult dermal fibroblasts

**Georgia Pennarossa [1], Sharon Arcuri [1], Teresina De Iorio [1], Sergio Ledda [2], Fulvio Gandolfi [3] and Tiziana A.L. Brevini [1,*]**

[1] Department of Veterinary Medicine and Animal Science, Center for Stem Cell Research, Laboratory of Biomedical Embryology and Tissue Engineering, Università Degli Studi Di Milano, 26900 Lodi, Italy.
[2] Department of Veterinary Medicine, University of Sassari, 07100 Sassari, Italy;
[3] Department of Agricultural and Environmental Sciences—Production, Landscape, Agroenergy and Center for Stem Cell Research, Università degli Studi di Milano, via Celoria 2, 20133 Milan, Italy;
* Correspondence: tiziana.brevini@unimi.it; Tel.: +39-02-50317970

**Abstract**

*Purpose*

To develop a new protocol that combines the use of epigenetic cues and mechanical stimuli to assemble 3D spherical structures, arbitrarily defined "epiBlastoids", whose phenotype is remarkably similar to natural embryos.

*Methods*

A 3-step approach is used to generate epiBlastoids. In the first step, adult dermal fibroblasts are converted into trophoblast (TR)-like cells, combining the use of 5-azacytidine, to erase the original cell phenotype, with an ad hoc induction protocol, to drive erased cells into the TR lineage. In the second step, epigenetic erasing is applied once again, in combination with mechanosensing-related cues, to generate ICM-like organoids. Specifically, erased cells are encapsulated in micro-bioreactors to promote 3D cell rearrangement and boost pluripotency. In the third step, chemically induced TR-like cells are co-cultured with ICM-like spheroids in the same micro-bioreactors. Subsequently, the newly generated embryoids are transferred to microwells, to encourage further differentiation and favor epiBlastoid formation.

*Results*

Adult dermal fibroblasts are successfully readdressed towards TR. In parallel, cells subjected to epigenetic erasing and encapsulated into micro-bioreactors rearrange in 3D ICM-like structures.

When TR-like cells and ICM-like spheroids are co-culture in micro-bioreactors and microwells, they formed single structures with uniform round shape reminiscent in vivo embryos. In addition, $CDX2^+$ cells localized in the out layer of the spheroids, while the $OCT4^+$ cells in the inner of the structures. Consistently, $TROP2^+$ cells display YAP nuclear accumulation and actively transcribed for mature TR markers, while $TROP2^-$ cells showed YAP cytoplasmic compartmentalization and expressed pluripotency-related genes.

*Conclusion*

We describe the generation of 3D spherical structures, phenotypically similar to natural embryos, that may constitute a suitable in vitro model to study early embryogenesis as well as embryo disorders.

**Keywords:** 3D culture system, epiBlastoids, epigenetic erasing, ICM-like cells, mechanosensing-related cues, trophoblast-like cells.

## Introduction

Early mammalian embryogenesis encompasses several events that lead to the formation of the blastocyst that comprises two distinct structures: the trophectoderm (TE) and inner cell mass (ICM) [1]. The TE consists of trophoblast (TR) cells and contributes to the formation of the placenta that nourishes and supports the fetus during intrauterine life [2–4]. The ICM contains pluripotent cells that able to differentiate in the three definitive germ layers, giving rise to all tissues of the embryo proper [5].

All these events are driven by molecular mechanisms and mechanical cues that have long aroused great interest. However, due to the in vivo microenvironment inaccessibility, the material paucity and the ethical and legal issues, the study of the peri-implantation period in human remains a daunting task [6].

During the last few years, several efforts have been directed towards the creation of in vitro models that recapitulate embryogenesis in vivo. In this context, a number of different methods have been applied to various murine and human cell types to successfully generate blastocyst-like structures (termed blastoids) [7–13].

Here, we describe a new 3-step approach that allows the generation of 3D spherical structures, remarkably similar to natural embryos, starting from terminally differentiated somatic cells and combining the use of epigenetic cues with mechanical stimuli. In the first step, we convert adult dermal fibroblasts into TR-like cells, using 5-azacytidine (5-aza-CR) to erase the original cell phenotype, and apply an ad hoc induction protocol to drive cells into the TR lineage [14, 15]. In the second step, we combine epigenetic and mechanosensing-related stimuli to generate ICM-like spheroids. Specifically, we apply the same epigenetic erasing protocol and encapsulate cells into polytetrafluoroethylene (PTFE) micro-bioreactors to promote 3D cell rearrangement and boost pluripotency [16, 17]. In the third step, we co-culture chemically induced TR-like cells with ICM-like spheroids in the same micro-bioreactor and, subsequently, into microwells, to further encourage differentiation and favor the formation of 3D spherical structures that resemble in vivo blastocysts and that we arbitrarily defined "epiBlastoids".

The results obtained indicate that the approach here described allows for the generation of a human blastocyst-like model that is able to mimic the physiological organization of early embryos in vivo and may find useful application in the assisted reproduction field.

**Materials and methods**

All reagents were purchased from Thermo Fisher Scientific unless otherwise indicated.

*Ethical statement*

Human cell isolation from healthy adult individuals was approved by the Ethical Committee of the Ospedale Maggiore Policlinico, Milano (CE 479_20071.6). All experiments performed were in accordance with the approved guidelines.

*Isolation and culture of human dermal fibroblasts*

Human fibroblasts were isolated from fresh skin biopsies of 6 healthy individuals (3 women and 3 men). Tissue fragments of approximately 2 $mm^3$ were transferred onto petri dishes (Sarstedt) previously coated with 0.1% porcine gelatin (Sigma-Aldrich) and cultured in Dulbecco's modified Eagle's medium (DMEM) supplemented with 20% Fetal Bovine Serum (FBS), 2 mM glutamine (Sigma-Aldrich) and antibiotics (Sigma-Aldrich). After 6 days of culture, fibroblasts grown out of the original skin explants and fragments were carefully removed. Cells were subsequently cultured in fibroblast culture medium (FCM) composed of Dulbecco's modified Eagle's medium (DMEM), 10% Fetal Bovine Serum (FBS), 2 mM glutamine (Sigma-Aldrich), and antibiotics (Sigma-Aldrich), and maintained in 5% $CO_2$ at 37°C. Passages were carried out twice a week at 1:3 ratio. From each individual (n = 6) were obtained one primary cell line that was used at least in triplicate in 3 independent experiments.

*Generation of TR-like cells by exposing fibroblasts to 5-aza-CR and trophoblast induction*

Cells at passages between 6 and 8 after isolation were plated in 0.1% gelatin (Sigma-Aldrich) pre-coated 4-well multidishes (Nunc) at concentration of 7.8 x $10^4$ cells/$cm^2$. Based on our previous studies [15, 18–26], 24 hours after seeding, fibroblasts were treated with 1 μM of 5-aza-CR (Sigma-Aldrich) for 18 hours at 37°C. At the end of 5-aza-CR treatment, cells were incubated in Embryonic Stem Cell (ESC) medium consisting of DMEM-low glucose:HAM'S F10 (1:1) supplemented with 5% FBS, 10% K.O. serum, 2 mM glutamine (Sigma-Aldrich), 0.1 mM β-mercaptoethanol (Sigma-Aldrich), nucleoside mix, 1% non-essential amino acids, 1000 IU/ml ES-growth factor (LIF, Chemicon), and 5 ng/ml b-FGF (R&D System) [27–29] for 3 hours at 37°C in 5% $CO_2$. TR differentiation was then induced using mouse embryonic fibroblast (MEF) conditioned medium, obtained by culturing 20.000 (cells/$cm^2$) inactivated MEF in ESC medium without b-FGF for 24 hours, supplemented with 10 ng/ml Bone Morphogenetic protein 4 (BMP4, Sigma-Aldrich), 1 μM activin/nodal signalling inhibitor (A83-01, Sigma-Aldrich) and 0.1 μM basic fibroblast growth factor (FGF2) signalling inhibitor (PD173074, Sigma-Aldrich) [30–32] at

37°C in low $O_2$ condition (5% $O_2$, 5% $CO_2$ and 90% $N_2$ atmosphere) for 11 days. Culture medium was refreshed every other day. TR differentiation was daily monitored using a Nikon Eclipse TE200 microscope (Nikon).

*Creation of ICM-like spheroids by fibroblast exposure to 5-aza-CR and encapsulation in PTFE micro-bioreactors*

Fibroblasts at passages between 6 and 8 after isolation were exposed to 1 μM 5-aza-CR (Sigma-Aldrich) and encapsulated in polytetrafluoroethylene (PTFE, Sigma-Aldrich) micro-bioreactors for 18 hours, in order to generate ICM-like spheroids [16, 17]. A PTFE powder bed with particle size of 1 μm (Sigma-Aldrich 430935) was created inside a petri dish (Sarstedt) and 1 x $10^4$ cells/30 μl of 1 μM 5-aza-CR in FCM was dispensed on it. The dish was gently rotated in a circular motion to generate the micro-bioreactor that were then transferred in a new petri dish and incubated at 37 °C in 5% $CO_2$, using a humidified chamber to avoid dehydration.

*Production of epiBlastoids by assembling TR-like cells and ICM-like spheroids*

At the end of 5-aza-CR exposure, PTFE micro-bioreactors were broken by puncturing them with a needle and ICM-like spheroids were recovered using a 200 μl pipette tip cut at the edge. Each single spheroid was resuspended in 30 μl droplets of ESC medium and dispensed onto fresh PTFE powder bed. The new generated micro-bioreactors were cultured for 3 hours at 37 °C in 5% $CO_2$. At the end of incubation period, ICM-like spheroids were collected and transferred in a 10 μL drop of G1-PLUS medium (Vitrolife). In parallel, TR-like cells differentiated for 11 days were detached from culture supports, centrifuged at 150 g for 5 min and resuspended in G1-PLUS medium (Vitrolife) to obtain 3 x $10^4$ cells/30 μL. A 40 μL drop containing 3 x $10^4$ TR-like cells (30 μL) and one single ICM-like spheroid (10 μL) was dispensed onto PTFE powder bed. The obtained micro-bioreactor was cultured for 48 hours at 37 °C in 5% $CO_2$. Subsequently, spheroid structures were collected, placed into non-adherent microwells (AggreWell™, Stemcell technologies) and grown in G2-PLUS medium (Vitrolife). After 24 hours of culture, $10^5$ PODS

Activin A (Cell guidance systems) were added into 150 µl G2-PLUS medium (Vitrolife) and epiBlastoids were cultured for 4 days at 37 °C in 5% $CO_2$.

*Morphometric evaluation*

EpiBlastoids were observed under an Eclipse TE200 microscope (Nikon), equipped with a digital camera (Nikon). Pictures were acquired with NIS-Elements Software (Version 4.6; Nikon). Spheroid diameters were measured using ImageJ software (ImageJ software version 1.53j).

*EpiBlastoid cell separation*

EpiBlastoids were dissociated to single cell suspension by a double enzymatic digestion with collagenase IV (300U/ml, Sigma) for 30 minutes and trypsin-EDTA solution (Sigma) for 20 minutes, followed by mechanical dissociation by pipetting. Cell suspension was filtered with a 30 µm nylon mesh (Pre-Separation Filters, 30 µm, # 130-041-407, Miltenyi Biotec) and centrifuged at 300 x g for 5 minutes. Supernatants were removed and trophoblast cell surface antigen 2 (TROP2) positive cells were isolated using Magnetic-Activated Cell Sorting (MACS, Miltenyi Biotec) protocol, following the manufacture's instruction. ICM cells were isolated by applying the same protocol and collecting the flow-through. The two cell populations obtained were subjected to gene expression and immunostaining analysis.

*Gene expression analysis*

TaqManGene Expression Cells-to-CT kit was used to extract RNA, following the manufacturer's instruction, and DNase I was added in lysis solution at 1:100 concentration. Quantitative Real-Time PCR was performed with CFX96 Real-Time PCR detection system (Bio-Rad Laboratories) using the predesigned gene-specific primers and probe sets from TaqManGene Expression Assays listed in Table 1. GAPDH and ACTB were used as internal reference genes. Target gene quantification was carried out with CFX Manager software (Bio-Rad Laboratories).

**Table 1. List of primers used for quantitative PCR.**

| GENE | DESCRIPTION | CAT.N. |
|---|---|---|

| | | |
|---|---|---|
| ACTB | Actin, beta | Hs01060665_g1 |
| CDX2 | Caudal type homeobox 2 | Hs01078080_m1 |
| CGA | Glycoprotein hormones, alpha polypeptide | Hs00985275_g1 |
| CGB | Chorionic gonadotropin beta | Hs03407524_uH |
| CYP11A1 | Cytochrome P450 family 11 subfamily A member 1 | Hs00167984_m1 |
| GAPDH | Glyceraldehyde-3-phosphate dehydrogenase | Hs02786624_g1 |
| GCM1 | Glial cells missing homolog 1 | Hs00172692_m1 |
| HSD17B1 | Hydroxysteroid 17-beta dehydrogenase 1 | Hs00166219_g1 |
| NANOG | Nanog Homeobox | Hs02387400_g1 |
| OCT4 | POU Class 5 Homeobox 1 | Hs04260367_gH |
| PGF | Placental growth factor | Hs00182176_m1 |
| REX1 | ZFP42 Zinc Finger Protein | Hs01938187_s1 |
| SOX2 | SRY-Box Transcription Factor 2 | Hs04234836_s1 |
| THY1 | Thy-1 cell surface antigen | Hs06633377_s1 |
| VIM | Vimentin | Hs00958111_m1 |

*Western Blot Analysis*

Constitutive proteins were extracted from cell lysates using the ReadyPrep Protein Extraction Kit (Bio-Rad). Cell nuclear extracts were isolated using the NXtract CelLytic NuCLEAR Extraction Kit (Sigma-Aldrich). Protein concentration was measured by Coomassie Blue-G Dye-binding method. 100 μg of proteins were resuspended in sample buffer (1:1) consisting of 4% SDS (Sigma-Aldrich), 10% 2-mercaptoethanol (Sigma-Aldrich), 20% glycerol (Sigma-Aldrich), 0.004% bromophenol blue (Sigma-Aldrich), and 0.125 M Tris–HCl (Sigma-Aldrich) at pH 6.8. Equal amounts of proteins were loaded, electrophoresed on SDS-polyacrylamide gels, transferred onto 0.45 μm pore size nitrocellulose membranes (Hybond-C Extra, GE Healthcare Life Sciences) and probed with primary antibodies listed in Table 2. Protein bands were visualized by the WesternBreeze chemiluminescent kit and densitometric analysis was performed using the ImageJ software (ImageJ software version 1.53j).

**Table 2. List of primary antibodies used for western blot (WB) and immunostaining (ICC).**

| ANTIBODY | HOST SPECIES | COMPANY | CAT. N. | WORKING DILUTION WB | WORKING DILUTION ICC |
|---|---|---|---|---|---|
| CDX2 | Mouse | Santa Cruz Biotechnology | sc-166830 | -- | 1:50 |
| GAPDH | Mouse | Abcam | ab8245 | 1:1000 | -- |
| OCT4 | Rabbit | Chemicon | ab3209 | -- | 1:50 |
| YAP | Rabbit | Cell signaling | 14074 | 1:1000 | 1:100 |

*Immunostaining*

EpiBlastoids were fixed in 4% paraformaldehyde in PBS for 20 minutes at room temperature, washed three times in PBS, permeabilized with 0.5% Triton X-100 (Sigma) in PBS for 30 minutes and treated with a blocking solution containing 10% goat serum (Sigma) in PBS for 30 minutes. Primary antibodies for CDX2, OCT4 and PAR3 were incubated overnight at +4°C (see Table 2). The day after, samples were washed three times in PBS and incubated with the appropriate secondary antibodies (Alexa Fluor) for 45 minutes at room temperature using a 1:250 dilution. Nuclei were stained with 4′,6-diamidino-2-phenylindole (DAPI). At the end of the immunostaining procedure, epiBlastoids were transferred and mounted to glass slides and analyzed under an Eclipse E600 microscope (Nikon) equipped with a digital camera (Nikon). Pictures were acquired with NIS-Elements Software (Version 4.6; Nikon).

For YAP localization, $TROP2^+$ and $TROP2^-$ cells were isolated (see paragraph below) and attached to slides using the cytocentrifuge Cytospin 4 (Thermo Shandon). Cells were then fixed in 4% paraformaldehyde in PBS (Sigma), washed three times in PBS, permeabilized and blocked with a solution containing 0.3% Triton X-100 (Sigma) and 5% serum in PBS for 1 hour. Primary antibody was incubated overnight at + 4 °C (see table 2 for working dilutions). Cells were incubated with suitable secondary antibody (Alexa Fluor) for 45 min. Nuclei were stained with 4′,6-diamidino-2- phenylindole (DAPI, Sigma). Samples were observed under a Nikon Eclipse

TE200 (Nikon) equipped with a digital camera (Nikon). Pictures were acquired with NIS-Elements Software (Version 4.6; Nikon).

*Statistical analysis*

Statistical analysis was performed using the Student t-test (SPSS 19.1; IBM). Data were presented as mean ± standard deviation (SD). Differences of $p \leq 0.05$ were considered significant and were indicated with different superscripts.

**Results**

*Generation of TR-like cells by exposing fibroblasts to 5-aza-CR and trophoblast induction*

Fibroblasts obtained from skin biopsies grew out of the original explants within 6 days of culture forming a monolayer with cells displaying the standard elongated morphology (Fig. 1A, T0). After 5-aza-CR exposure, cell phenotype changed, and treated fibroblasts acquired an oval or round shape and became smaller with larger nuclei and granular and vacuolated cytoplasm (Fig. 1A, Post 5-aza-CR). These changes were accompanied by in the onset of the pluripotency-related genes OCT4, NANOG, REX1, and SOX2, which were undetectable in untreated fibroblasts (Fig. 1B). In agreement with these observations, epigenetically erased cells significantly downregulated the typical fibroblast markers VIM and THY (Fig. 1B). At the end of 11-day TR induction, cells acquired a mature TR morphology, with cells exhibiting round or ellipsoid shape, round nuclei, and well-defined borders (Fig. 1A, Trophoblast-like cells). Consistent with these morphological changes, TR-like cells actively transcribed for mature TR related genes, namely GCM1, CGA, CGB, HSD17B1, CYP11A1 and PGF, which were originally absent in untreated fibroblasts (Fig. 1B).

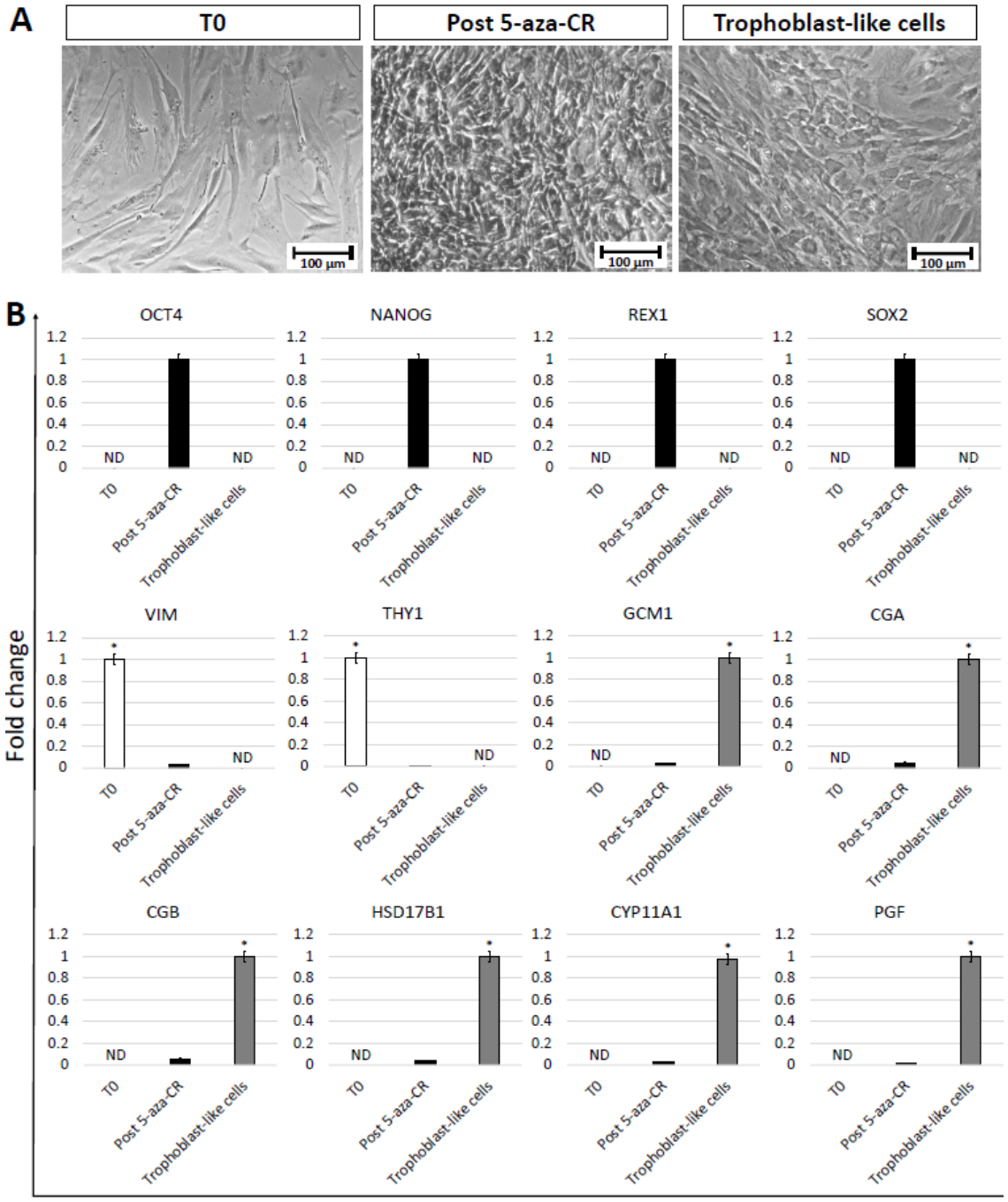


**Figure 1.** *Generation of TR-like cells by exposing fibroblasts to 5-aza-CR and trophoblast induction.* Fibroblasts exposed to 5-aza-CR lost their typical elongated shape (T0) and became smaller with larger nuclei and granular cytoplasm (Post 5-aza-CR) (A). At day 11 of trophoblast induction, cells acquired a tight adherent epithelial morphology, exhibiting round or ellipsoid shape, with round nuclei and well-defined borders (Trophoblast-like cells). Scale bars: 100 µm (A). Transcription levels for pluripotent (OCT4, NANOG, REX1, SOX2), fibroblast (VIM, THY1), and TR (GCM1, CGA, CGB, HSD17B1, CYP11A1, and PGF) genes in untreated fibroblasts (T0, white bars), in fibroblasts exposed to 5-aza-CR

(Post 5-aza-CR, black bars) and at day 11 of trophoblast induction (Trophoblast-like cells, grey bars). Gene expression values are reported with the highest expression set to 1 and all others relative to this. *Superscripts denote significant differences ($P < 0.05$) (B).

*Creation of ICM-like spheroids by fibroblast exposure to 5-aza-CR and encapsulation in PTFE micro-bioreactors*

After 5-aza-CR exposure and encapsulation in PTFE, fibroblasts became rounded, with large and granulated nuclei, lost their monolayer distribution and rearranged in 3 dimensional (3D) spherical structures that clearly resemble the ICM cell organization (Fig. 2A, Post 5-aza-CR + PTFE). Consistently with this, the obtained ICM-like spheroids actively transcribed for the main pluripotency-related genes OCT4, NANOG, REX1 and SOX2, originally absent in untreated cells (T0), while significantly decreased the expression of the fibroblast-specific markers VIM and THY1 (Fig. 2B).

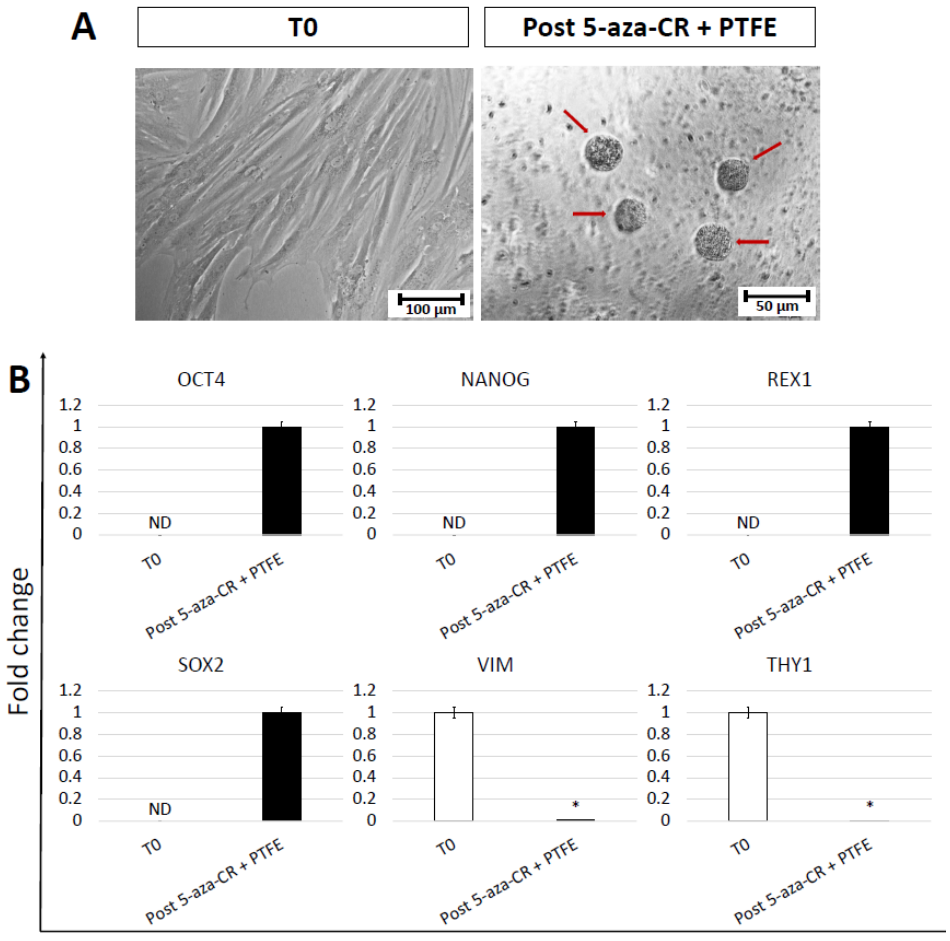

**Figure 2.** *Creation of ICM-like spheroids by fibroblast exposure to 5-aza-CR and encapsulation in PTFE micro-bioreactors.* Fibroblasts (T0) encapsulated in PTFE and treated with 5-aza-CR form 3D spherical structures (Post 5-aza-CR+PTFE). Scale bars, 100 μm (left panel) and 50 μm (right panel) (A). Transcription levels for pluripotent- (OCT4, NANOG, REX1, SOX2) and fibroblast- (VIM, THY1) related genes in untreated fibroblasts (T0, white bars) and in fibroblasts exposed to 5-aza-CR (Post 5-aza-CR+PTFE, black bars). Gene expression values are reported with the highest expression set to 1 and all others relative to this. *Superscripts denote significant differences ($P < 0.05$) (B).

*Production of epiBlastoids by assembling TR-like cells and ICM-like spheroids*

After 2 days of co-culture in PTFE micro-bioreactors, chemically induced TR-like cells and ICM-like spheroids self-assembled in 3D single structures that were transferred and maintained in microwells for an additional 5 days (Fig. 3A). At the end of this culture period, the obtained epiBlastoids displayed uniform round shape with diameters raging from 100 μm to 200 μm. More in detail, morphometric analysis showed that 78.67% of spheroids exhibited a diameter of 150-200 μm, while 21.33% of 100-150 μm (Fig. 3B).

Immunostaining studies demonstrated $CDX2^+$ cells localized in out layer of the epiBlastoids, while OCT4 was expressed by cells of the inner compartment (Fig 3C). In addition, $TROP2^+$ cells display nuclear accumulation of YAP, while $TROP2^-$ cells showed a cytoplasmic compartmentalization of the molecule (Fig. 3D).

These morphological observations were also supported by molecular analyses indicating that $TROP2^+$ cells expressed the TR markers GCM1, CGA, CGB, HSD17B1, CYP11A1 and PGF, while $TROP2^-$ cells transcribed for the pluripotency-related genes OCT4, NANOG, REX1 and SOX2 (Fig. 3E).

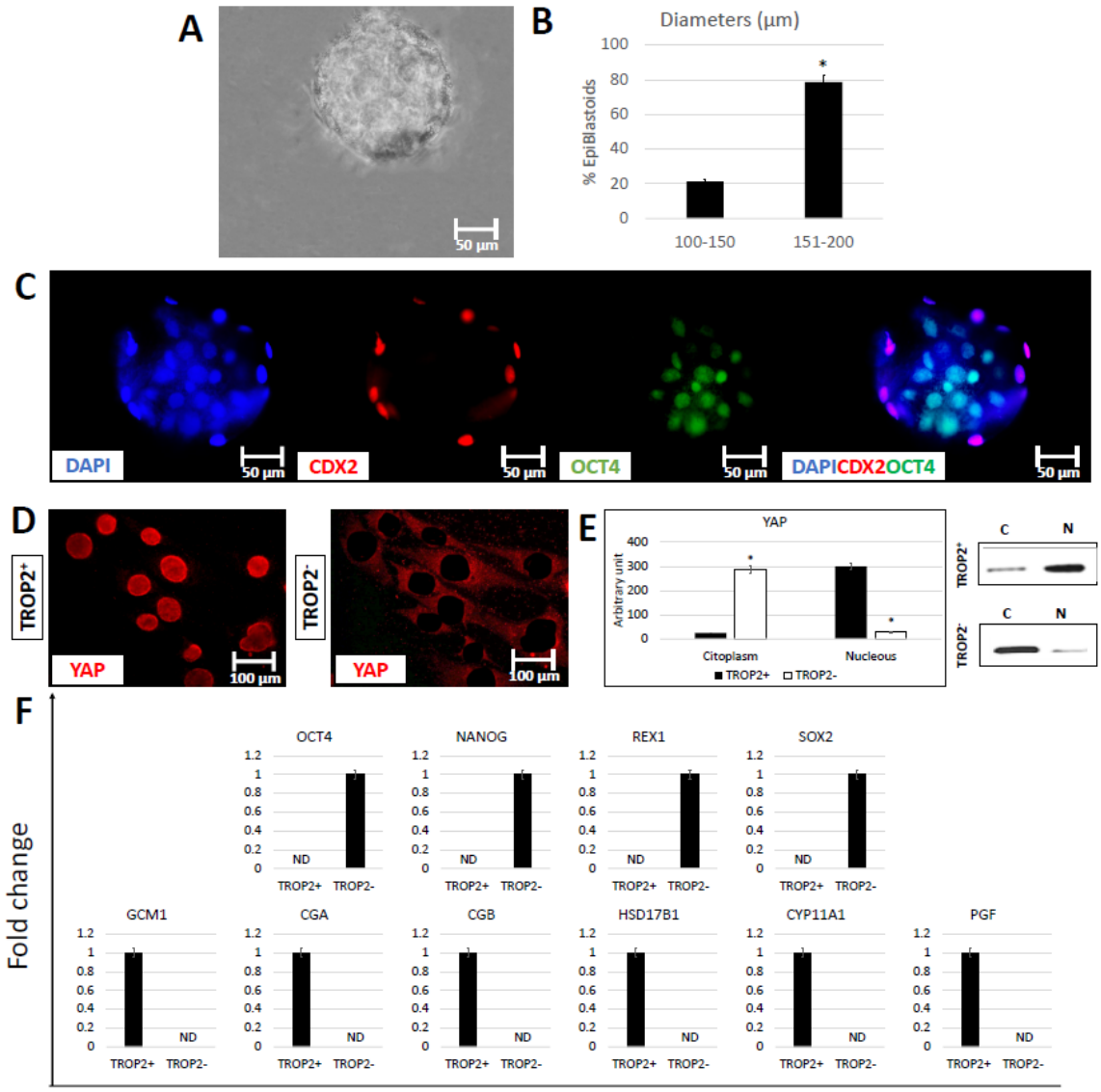


**Figure 3.** *Production of epiBlastoids by assembling TR-like cells and ICM-like spheroids.* ICM-like organoids co-cultured with TR-like cells into micro-bioreactors for 48 hours and, subsequently, into AggreWells for 5 days, self-assemble in epiBlastoids (A). Rates of epiBlasoids displaying diameters ranging from 100 to 150 and from 151 to 200 µm (B). Immunostaining shows CDX2$^{+}$ cells (red) localize in out layer of the epiBlastoids, while OCT4$^{+}$ cells (green) in the inner compartment. Nuclei are stained in blue (scale bars 50 µm; C). YAP protein is confined in the nuclear compartment in TROP2$^{+}$, while it is excluded from the nucleus and shifts to the cytoplasm in TROP2$^{-}$ cells (D). Densitometric analysis of western blots for YAP protein in cytoplasm (C) and nucleus (N) of TROP2$^{+}$ and TROP2$^{-}$ cells. The values (arbitrary units) are reported as relative

optical density of the bands normalized to GAPDH. *Superscripts denote significant differences ($P < 0.05$). Representative western blots for the two cell compartments of each cell type are also shown (E). Transcription levels for pluripotency- (OCT4, NANOG, REX1, SOX2), fibroblasts (VIM, THY1), and TR- (GCM1, CGA, CGB, HSD17B1, CYP11A1, and PGF) related genes in $TROP2^{+}$ and $TROP2^{-}$ cells. Gene expression values are reported with the highest expression set to 1 and all others relative to this. (F).

**Discussion**

The possibility to successfully recreate in vitro blastocyst-like structures using embryonic stem cells (ESCs) or induced pluripotent stem cells (iPSCs) has been recently demonstrated both in the mouse [33–36] and the human [7–12]. In the present manuscript we describe a novel method that combines, for the first time, the use of chemical stimuli and mechanical cues to generate in vitro 3D spherical structures phenotypically similar to natural embryos.

More in detail, in the first step, we induce a high permissivity window in adult dermal fibroblasts isolated from human healthy individuals, using 5-aza-CR which has been previously demonstrated to reactivate pluripotency-related genes [37–40], to induces a global DNA hypomethylation [16–23, 26, 41–50] and to modulate ten-eleven translocation (TET) gene transcription [23]. In agreement with this, in the present work, adult dermal fibroblasts exposed to 5-aza-CR for 18 hours lost their typical elongated morphology and acquired a round or oval shape, with larger nuclei and granular, vacuolated cytoplasm. These morphological changes closely resemble those previously identified in ESCs [51, 52] and iPSCs [53], suggesting the acquisition of features distinctive of a high plasticity phenotype. This was accompanied also by the onset of the main pluripotency-related gene transcription, namely OCT4, NANOG, REX1 and SOX2, which were originally undetectable in untreated fibroblasts (T0), and by a significant down-regulation of the fibroblast-related markers VIM and THY1, further supporting previously published reports that described 5-aza-CR ability to induce a pluripotent-like phenotype

hypomethylation [16–23, 26, 41–50]. Taking advantage of the acquired high permissivity window, cells were readdressed towards the TR lineage, using an induction cocktail containing BMP4 in combination with activin/nodal and FGF2 signalling inhibitors. This differentiation medium has been previously shown to drive cells towards the TR phenotype in both human [54–63] and pig [14, 15], with the acquisition of a tight adherent epithelial morphology, round shape and nuclei, as well as well-defined borders. Consistent with this, the obtained TR-like cells showed active transcription for the TR mature markers GCM1, CGA, CGB, HSD17B1, CYP11A1 and PGF, indicating the activation of the main molecular pathways distinctive of the newly acquired phenotype.

In the second step, we combined epigenetic and mechanosensing-related stimuli to generate ICM-like spheroids. To this purpose, erased adult dermal fibroblasts were encapsulated into PTFE micro-bioreactors to promote 3D cell rearrangement and boost pluripotency. Beside the morphological changes induced by exposure to 5-aza-CR, previously shown to be related to high plasticity (REF), the use of the PTFE micro-bioreactors allowed cells to self-assemble and form multicellular spheroids, displaying a uniform size geometry. This well fits with previous observations indicating that the use of micro-bioreactors efficiently encourages 3D cell aggregation [64, 65], which, in turn, has the ability to support the induction of a pluripotent state and to boost its maintenance [16]. In agreement with this, the generated ICM-like spheroids actively and steadily transcribed for the pluripotency-related genes OCT4, NANOG, REX1, and SOX2 and down-regulated VIM and THY1 genes.

In the third and last step of the protocol, we co-cultured TR-like cells with ICM-like spheroids in the PTFE micro-bioreactor for 2 days, to favour the formation of a single 3D spherical structure, composed by the two cell components. We subsequently transferred the newly generated aggregates into microwells and cultured them in a commercially available medium for further 5 days, to encourage epiBlastoid formation. Encapsulation of two different cell types has been previously reported by Jara et al. who applied this approach for the production of pancreatic islet-

like structures in vitro [66]. These Authors described encapsulation ability to stabilize 3D cell aggregation, maintain differentiation, and support functional activities. In the present manuscript, upon these specific culture conditions, TR-like cells and ICM-like spheroids were able to organize into structures with uniform round shape displaying a diameter raging from 100 μm to 200 μm. In particular, morphometric analysis demonstrated that 78.67% of the spheroids exhibited a diameter ranging from 150 to 200 μm, with only 21.33% from 100 to150 μm. These results well fit with the average reported values of natural blastocysts that measure 175 - 211 μm and with the parameters and criteria reported in Table 3 and currently used to define human blastoid models. In addition, immunostaining studies demonstrated $CDX2^+$ cells externally localized, to surround the epiblastoid, and $OCT4^+$ cells closely assembled within them, showing that our protocol induced cells to spontaneously organize into spheroid complexes displaying TR-like cells homogenously distributed in the outer layer of the structures and ICM-like aggregates confined to the internal compartment. Consistent with this, sorting of epiBlastoid-derived cell suspensions, using the surface TR marker TROP2, led to the obtainment of two distinct cell populations: one consisting of $TROP2^+$ cells and another containing $TROP2^-$ cells. The first cell type actively transcribed for GCM1, CGA, CGB, HSD17B1, CYP11A1, and PGF genes, indicating that $TROP2^+$ cells maintained a transcription pattern typical of TR cells. In addition, $TROP2^+$ cells displayed a distinct compartmentalization of YAP which was mainly accumulated in the nucleus. Consistent with this, several studies reported the direct involvement of the Hippo pathway in the blastocyst formation, highlighting the key role played by the TEAD4/WWTR1/YAP1 complex in promoting CDX2 expression during outside cell maturation to TR (Anani et al., 2014; Cao et al., 2015; Cockburn et al., 2013; Hirate et al., 2013; Kono et al., 2014; Leung and Zernicka-Goetz, 2013; Lorthongpanich et al., 2013; Menchero et al., 2019; Nishioka et al., 2009; Posfai et al., 2017; Rayon et al., 2014; Shi et al., 2017; Yagi et al., 2007; Yu et al., 2016). On the other hand, and in line with this, $TROP2^-$ cells showed cytoplasmic retention of YAP and expressed the pluripotency-related genes OCT4, NANOG, REX1 and SOX2.

Altogether, the procedure here described allows for an efficient in vitro generation of human epiBlastoids, starting from easily accessible adult dermal fibroblasts and avoiding the use of techniques that required retroviral gene transfection. Considering that the access to human embryo is subjected to tight regulation around the globe due to ethical concerns, the production of epiBlastoid models may overcome some and could find useful application in the assisted reproduction field, for the identification of the most adequate culture conditions and/or for peri- and early post-implantation investigations. In addition, the use of 3D micro-bioreactors may also represent a notable breakthrough in culture system technologies applied to reproduction and may constitute an advantageous micro-environment for long-term culture of blastoids, gastruloids or organoids.

**References**


1. Aitken, R. J., Beaconsfield, R., & Ginsburg, J. (1979). ORIGIN AND FORMATION OF THE PLACENTA. *Placenta*, 152–163. https://doi.org/10.1016/B978-0-08-024435-8.50025-0
2. Schulz, L., Ezashi, T., Das, P., Westfall, S., Livingston, K., & Roberts, R. (2009). HUMAN EMBRYONIC STEM CELLS AS MODELS FOR TROPHOBLAST DIFFERENTIATION Introduction: the trophoblast lineage and its emergence, *29*, 1–12. https://doi.org/10.1016/j.placenta.2007.10.009
3. Sheridan, M. A., Fernando, R. C., Gardner, L., Hollinshead, M. S., Burton, G. J., Moffett, A., & Turco, M. Y. (2020). Establishment and differentiation of long-term trophoblast organoid cultures from the human placenta. *Nature Protocols*, *15*(10), 3441–3463. https://doi.org/10.1038/s41596-020-0381-x
4. Rossant, J., & Cross, J. C. (2001, July). Placental development: Lessons from mouse mutants. *Nature Reviews Genetics*. Nature Publishing Group. https://doi.org/10.1038/35080570
5. Romito, A., & Cobellis, G. (2016). Pluripotent Stem Cells: Current Understanding and Future Directions. *Stem Cells Int*, *2016*, 9451492. https://doi.org/10.1155/2016/9451492
6. Daoud, A. M. P., Popovic, M., Dondorp, W. J., Bustos, M. T., Bredenoord, A. L., de Sousa Lopes, S. M. C., … Heindryckx, B. (2020). Modelling human embryogenesis: embryo-like structures spark ethical and policy debate. *Human reproduction update*, *26*(6), 779–798. https://doi.org/10.1093/HUMUPD/DMAA027
7. Fan, Y., Min, Z., Alsolami, S., Ma, Z., Zhang, E., Chen, W., … Yu, Y. (2021). Generation of human blastocyst-like structures from pluripotent stem cells. *Cell Discovery 2021 7:1*, *7*(1), 1–14. https://doi.org/10.1038/s41421-021-00316-8
8. Liu, X., Tan, J. P., Schröder, J., Aberkane, A., Ouyang, J. F., Mohenska, M., … Polo, J. M. (2021). Modelling human blastocysts by reprogramming fibroblasts into iBlastoids. *Nature 2021 591:7851*, *591*(7851), 627–632. https://doi.org/10.1038/s41586-021-03372-y

9. Yanagida, A., Spindlow, D., Nichols, J., Dattani, A., Smith, A., & Guo, G. (2021). Naive stem cell blastocyst model captures human embryo lineage segregation. *Cell Stem Cell*, *28*(6), 1016-1022.e4. https://doi.org/10.1016/J.STEM.2021.04.031

10. Sozen, B., Jorgensen, V., Weatherbee, B. A. T., Chen, S., Zhu, M., & Zernicka-Goetz, M. (2021). Reconstructing aspects of human embryogenesis with pluripotent stem cells. *Nature Communications 2021 12:1*, *12*(1), 1–13. https://doi.org/10.1038/s41467-021-25853-4

11. Yu, L., Wei, Y., Duan, J., Schmitz, D. A., Sakurai, M., Wang, L., … Wu, J. (2021). Blastocyst-like structures generated from human pluripotent stem cells. *Nature 2021 591:7851*, *591*(7851), 620–626. https://doi.org/10.1038/s41586-021-03356-y

12. Kagawa, H., Javali, A., Khoei, H. H., Sommer, T. M., Sestini, G., Novatchkova, M., … Rivron, N. (2021). Human blastoids model blastocyst development and implantation. *Nature 2021 601:7894*, *601*(7894), 600–605. https://doi.org/10.1038/s41586-021-04267-8

13. Kagawa, H., Javali, A., Khoei, H. H., Sommer, T. M., Sestini, G., Novatchkova, M., … Rivron, N. (2022). Protocol for Human Blastoids Modeling Blastocyst Development and Implantation. *Journal of visualized experiments : JoVE*, *2022*(186). https://doi.org/10.3791/63388

14. Arcuri, S., Gandolfi, F., Somigliana, E., & Brevini, T. A. L. (2021). A Two-Step Protocol to Erase Human Skin Fibroblasts and Convert Them into Trophoblast-like Cells. *Methods in molecular biology (Clifton, N.J.)*, *2273*, 151–158. https://doi.org/10.1007/978-1-0716-1246-0_10

15. Arcuri, S., Pennarossa, G., Gandolfi, F., & Brevini, T. A. L. (2021). Generation of Trophoblast-Like Cells From Hypomethylated Porcine Adult Dermal Fibroblasts. *Frontiers in veterinary science*, *8*. https://doi.org/10.3389/FVETS.2021.706106

16. Pennarossa, G., Manzoni, E. F. M., Ledda, S., deEguileor, M., Gandolfi, F., & Brevini, T. A. L. (2019). Use of a PTFE Micro-Bioreactor to Promote 3D Cell Rearrangement and Maintain High Plasticity in Epigenetically Erased Fibroblasts. *Stem cell reviews and reports*, *15*(1), 82–92. https://doi.org/10.1007/S12015-018-9862-5

17. Pennarossa, G., Ledda, S., Arcuri, S., Gandolfi, F., & Brevini, T. A. L. (2020). A Two-Step Strategy that Combines Epigenetic Modification and Biomechanical Cues to Generate Mammalian Pluripotent Cells. *Journal of visualized experiments : JoVE*, *2020*(162). https://doi.org/10.3791/61655

18. Pennarossa, G., Maffei, S., Campagnol, M., Tarantini, L., Gandolfi, F., & Brevini, T. A. L. A. L. T. A. L. (2013). Brief demethylation step allows the conversion of adult human skin fibroblasts into insulin-secreting cells. *Proceedings of the National Academy of Sciences of the United States of America*, *110*(22), 8948–53. https://doi.org/10.1073/pnas.1220637110

19. Pennarossa, G., Maffei, S., Campagnol, M., Rahman, M. M., Brevini, T. A. L., & Gandolfi, F. (2014). Reprogramming of Pig Dermal Fibroblast into Insulin Secreting Cells by a Brief Exposure to 5-aza-cytidine. *Stem Cell Reviews and Reports*, *10*(1). https://doi.org/10.1007/s12015-013-9477-9

20. Brevini, T. A. L., Pennarossa, G., Rahman, M. M., Paffoni, A., Antonini, S., Ragni, G., … Gandolfi, F. (2014). Morphological and Molecular Changes of Human Granulosa Cells Exposed to 5-Azacytidine and Addressed Toward Muscular Differentiation. *Stem Cell Reviews and Reports*, *10*(5). https://doi.org/10.1007/s12015-014-9521-4

21. Brevini, T. A. L., Pennarossa, G., Acocella, F., Brizzola, S., Zenobi, A., & Gandolfi, F. (2016). Epigenetic conversion of adult dog skin fibroblasts into insulin-secreting cells. *Veterinary Journal*, *211*. https://doi.org/10.1016/j.tvjl.2016.02.014

22. Pennarossa, G., Santoro, R., Manzoni, E. F. M., Pesce, M., Gandolfi, F., & Brevini, T. A. L. (2018). Epigenetic Erasing and Pancreatic Differentiation of Dermal Fibroblasts into Insulin-Producing Cells

are Boosted by the Use of Low-Stiffness Substrate. *Stem cell reviews and reports*, *14*(3), 398–411. https://doi.org/10.1007/s12015-017-9799-0

23. Manzoni, E. F. M., Pennarossa, G., DeEguileor, M., Tettamanti, G., Gandolfi, F., & Brevini, T. A. L. (2016). 5-azacytidine affects TET2 and histone transcription and reshapes morphology of human skin fibroblasts. *Scientific Reports*, *6*(April), 37017. https://doi.org/10.1038/srep37017

24. Pennarossa, G., Manzoni, E. F. M., Ledda, S., DeEguileor, M., Gandolfi, F., & Brevini, T. A. L. (2019). Use of a PTFE Micro-Bioreactor to Promote 3D Cell Rearrangement and Maintain High Plasticity in Epigenetically Erased Fibroblasts. *Stem Cell Reviews and Reports*, *15*(1), 82–92. https://doi.org/10.1007/s12015-018-9862-5

25. Pennarossa, G., Ledda, S., Arcuri, S., Gandolfi, F., & Brevini, T. A. L. (2020). A Two-Step Strategy that Combines Epigenetic Modification and Biomechanical Cues to Generate Mammalian Pluripotent Cells. *Journal of visualized experiments : JoVE*, (162). https://doi.org/10.3791/61655

26. Brevini, T. A. L., Pennarossa, G., Maffei, S., Zenobi, A., & Gandolfi, F. (2016). Epigenetic conversion as a safe and simple method to obtain insulinsecreting cells from adult skin fibroblasts. *Journal of Visualized Experiments*, *2016*(109). https://doi.org/10.3791/53880

27. Brevini, T. A. L., Pennarossa, G., Attanasio, L., Vanelli, A., Gasparrini, B., & Gandolfi, F. (2010). Culture Conditions and Signalling Networks Promoting the Establishment of Cell Lines from Parthenogenetic and Biparental Pig Embryos. *Stem Cell Reviews and Reports*, *6*(3), 484–495. https://doi.org/10.1007/s12015-010-9153-2

28. Brevini, T. A. L., Pennarossa, G., Maffei, S., & Gandolfi, F. (2012). Pluripotency network in porcine embryos and derived cell lines. *Reproduction in Domestic Animals*, *47*(SUPPL.4), 86–91. https://doi.org/10.1111/j.1439-0531.2012.02060.x

29. Pennarossa, G., Maffei, S., Campagnol, M., Rahman, M. M., Brevini, T. A. L., & Gandolfi, F. (2014). Reprogramming of Pig Dermal Fibroblast into Insulin Secreting Cells by a Brief Exposure to 5-aza-cytidine. *Stem Cell Reviews and Reports*, *10*(1), 31–43. https://doi.org/10.1007/s12015-013-9477-9

30. Amita, M., Adachi, K., Alexenko, A. P., Sinha, S., Schust, D. J., Schulz, L. C., … Ezashi, T. (2013). Complete and unidirectional conversion of human embryonic stem cells to trophoblast by BMP4. *Proceedings of the National Academy of Sciences of the United States of America*, *110*(13). https://doi.org/10.1073/pnas.1303094110

31. Arcuri, S., Pennarossa, G., Gandolfi, F., & Brevini, T. A. L. (2021). Generation of Trophoblast-Like Cells From Hypomethylated Porcine Adult Dermal Fibroblasts. *Frontiers in Veterinary Science*, *8*(July), 1–10. https://doi.org/10.3389/fvets.2021.706106

32. Pennarossa, G., Ledda, S., Arcuri, S., Gandolfi, F., & Brevini, T. A. L. (2020). A Two-Step Strategy that Combines Epigenetic Modification and Biomechanical Cues to Generate Mammalian Pluripotent Cells. *Journal of visualized experiments : JoVE*, (162), 1–22. https://doi.org/10.3791/61655

33. Rivron, N. C., Frias-Aldeguer, J., Vrij, E. J., Boisset, J.-C., Korving, J., Vivié, J., … Geijsen, N. (2018). Blastocyst-like structures generated solely from stem cells. *Nature*, *557*(7703), 106–111. https://doi.org/10.1038/s41586-018-0051-0

34. Sozen, B., Cox, A. L., de Jonghe, J., Bao, M., Hollfelder, F., Glover, D. M., & Zernicka-Goetz, M. (2019). Self-Organization of Mouse Stem Cells into an Extended Potential Blastoid. *Developmental Cell*, *51*(6), 698-712.e8. https://doi.org/10.1016/j.devcel.2019.11.014

35. Kime, C., Kiyonari, H., Ohtsuka, S., Kohbayashi, E., Asahi, M., Yamanaka, S., … Tomoda, K. (2019). Induced 2C Expression and Implantation-Competent Blastocyst-like Cysts from Primed Pluripotent Stem Cells. *Stem Cell Reports*, *13*(3), 485. https://doi.org/10.1016/J.STEMCR.2019.07.011

36. Li, R., Zhong, C., Yu, Y., Liu, H., Sakurai, M., Yu, L., … Izpisua Belmonte, J. C. (2019). Generation of Blastocyst-like Structures from Mouse Embryonic and Adult Cell Cultures. *Cell*, *179*(3), 687-702.e18. https://doi.org/10.1016/J.CELL.2019.09.029

37. Taylor, S. M., & Jones, P. A. (1979). Multiple new phenotypes induced in 10T1/2 and 3T3 cells treated with 5-azacytidine. *Cell*, *17*(4), 771–779. https://doi.org/0092-8674(79)90317-9 [pii]

38. Jones, P. A. (1985). Effects of 5-azacytidine and its 2′-deoxyderivative on cell differentiation and DNA methylation. *Pharmacology & therapeutics*, *28*(1), 17–27. https://doi.org/10.1016/0163-7258(85)90080-4

39. Jones, P. A. (1985). Altering gene expression with 5-azacytidine. *Cell*, *40*(3), 485–486. https://doi.org/0092-8674(85)90192-8 [pii]

40. Glover, T. W., Coyle-Morris, J., Pearce-Birge, L., Berger, C., & Gemmill, R. M. (1986). DNA demethylation induced by 5-azacytidine does not affect fragile X expression. *Am J Hum Genet*, *38*(3), 309–318. Retrieved from http://www.ncbi.nlm.nih.gov/entrez/query.fcgi?cmd=Retrieve&db=PubMed&dopt=Citation&list_uids=2420174

41. Palii, S. S., van Emburgh, B. O., Sankpal, U. T., Brown, K. D., & Robertson, K. D. (2008). DNA methylation inhibitor 5-Aza-2′-deoxycytidine induces reversible genome-wide DNA damage that is distinctly influenced by DNA methyltransferases 1 and 3B. *Molecular and cellular biology*, *28*(2), 752–71. https://doi.org/10.1128/MCB.01799-07

42. Brevini, T. A. L., Pennarossa, G., Maffei, S., & Gandolfi, F. (2015). Phenotype switching through epigenetic conversion. *Reproduction, Fertility and Development*, *27*(5). https://doi.org/10.1071/RD14246

43. Pennarossa, G., Zenobi, A., Gandolfi, C. E. E., Manzoni, E. F. M., Gandolfi, F., & Brevini, T. A. L. (2015). Erase and Rewind: Epigenetic Conversion of Cell Fate. *Stem Cell Rev*, *12*(2). https://doi.org/10.1007/s12015-015-9637-1

44. Brevini, T., Manzoni, E., & Gandolfi, F. (2018). Methylation mechanisms and biomechanical effectors controlling cell fate. *Reprod Fertil Dev*, *30*, 64–72.

45. Brevini, T. A. L., Pennarossa, G., Manzoni, E. F. M., & Gandolfi, F. (2018). Safety and Efficacy of Epigenetically Converted Human Fibroblasts Into Insulin-Secreting Cells: A Preclinical Study (pp. 151–162). Springer, Cham. https://doi.org/10.1007/5584_2018_172

46. Tan, S. J., Fang, J. Y., Wu, Y., Yang, Z., Liang, G., & Han, B. (2015). Muscle tissue engineering and regeneration through epigenetic reprogramming and scaffold manipulation. *Scientific reports*, *5*, 16333. https://doi.org/10.1038/srep16333

47. Mirakhori, F., Zeynali, B., Kiani, S., & Baharvand, H. (2015). Brief azacytidine step allows the conversion of suspension human fibroblasts into neural progenitor-like cells. *Cell journal*, *17*(1), 153–8. https://doi.org/10.22074/cellj.2015.522

48. Mirakhori, F., Zeynali, B., Rassouli, H., Salekdeh, G. H., & Baharvand, H. (2015). Direct conversion of human fibroblasts into dopaminergic neural progenitor-like cells using TAT-mediated protein transduction of recombinant factors. *Biochem Biophys Res Commun*, *459*(4), 655–661. https://doi.org/10.1016/j.bbrc.2015.02.166

49. Chandrakanthan, V., Yeola, A., Kwan, J. C., Oliver, R. A., Qiao, Q., Kang, Y. C., … Pimanda, J. E. (2016). PDGF-AB and 5-Azacytidine induce conversion of somatic cells into tissue-regenerative multipotent stem cells. *Proceedings of the National Academy of Sciences of the United States of America*, *113*(16), E2306-15. https://doi.org/10.1073/pnas.1518244113

50. Diomede, F., Zini, N., Pizzicannella, J., Merciaro, I., Pizzicannella, G., D'Orazio, M., … Trubiani, O. (2018). 5-Aza exposure improves reprogramming process through embryoid body formation in human gingival stem cells. *Frontiers in Genetics*, *9*(OCT). https://doi.org/10.3389/fgene.2018.00419

51. Niwa, H. (2007). How is pluripotency determined and maintained? *Development*, *134*(4), 635–646. Retrieved from http://www.ncbi.nlm.nih.gov/entrez/query.fcgi?cmd=Retrieve&db=PubMed&dopt=Citation&list_uids=17215298

52. Lai, D., Wang, Y., Sun, J., Chen, Y., Li, T., Wu, Y., … Wei, C. (2015). Derivation and characterization of human embryonic stem cells on human amnion epithelial cells. *Sci Rep*, *5*, 10014. https://doi.org/10.1038/srep10014

53. Courtot, A. M., Magniez, A., Oudrhiri, N., Feraud, O., Bacci, J., Gobbo, E., … Bennaceur-Griscelli, A. (2014). Morphological analysis of human induced pluripotent stem cells during induced differentiation and reverse programming. *Biores Open Access*, *3*(5), 206–216. https://doi.org/10.1089/biores.2014.0028

54. Sudheer, S., Bhushan, R., Fauler, B., Lehrach, H., & Adjaye, J. (2012). FGF inhibition directs BMP4-mediated differentiation of human embryonic stem cells to syncytiotrophoblast. *Stem Cells and Development*, *21*(16), 2987–3000. https://doi.org/10.1089/scd.2012.0099

55. Amita, M., Adachi, K., Alexenko, A. P., Sinha, S., Schust, D. J., Schulz, L. C., … Ezashi, T. (2013). Complete and unidirectional conversion of human embryonic stem cells to trophoblast by BMP4. *Proceedings of the National Academy of Sciences of the United States of America*, *110*(13). https://doi.org/10.1073/pnas.1303094110

56. Lee, Y. L., Fong, S. W., Chen, A. C. H., Li, T., Yue, C., Lee, C. L., … Lee, K. F. (2015). Establishment of a novel human embryonic stem cell-derived trophoblastic spheroid implantation model. *Human Reproduction*, *30*(11), 2614–2626. https://doi.org/10.1093/humrep/dev223

57. Yang, Y., Adachi, K., Sheridan, M. A., Alexenko, A. P., Schust, D. J., Schulz, L. C., … Roberts, R. M. (2015). Heightened potency of human pluripotent stem cell lines created by transient BMP4 exposure. *Proceedings of the National Academy of Sciences of the United States of America*, *112*(18), E2337–E2346. https://doi.org/10.1073/pnas.1504778112

58. Yabe, S., Alexenko, A. P., Amita, M., Yang, Y., Schust, D. J., Sadovsky, Y., … Roberts, R. M. (2016). Comparison of syncytiotrophoblast generated from human embryonic stem cells and from term placentas. *Proceedings of the National Academy of Sciences of the United States of America*, *113*(19), E2598–E2607. https://doi.org/10.1073/pnas.1601630113

59. Jain, A., Ezashi, T., Roberts, R. M., & Tuteja, G. (2017). Deciphering transcriptional regulation in human embryonic stem cells specified towards a trophoblast fate. *Scientific Reports*, *7*(1). https://doi.org/10.1038/s41598-017-17614-5

60. Koel, M., Võsa, U., Krjutškov, K., Einarsdottir, E., Kere, J., Tapanainen, J., … Salumets, A. (2017). Optimizing bone morphogenic protein 4-mediated human embryonic stem cell differentiation into trophoblast-like cells using fibroblast growth factor 2 and transforming growth factor-β/activin/nodal signalling inhibition. *Reproductive BioMedicine Online*, *35*(3), 253–263. https://doi.org/10.1016/j.rbmo.2017.06.003

61. Roberts, R. M., Ezashi, T., Sheridan, M. A., & Yang, Y. (2018). Specification of trophoblast from embryonic stem cells exposed to BMP4†. *Biology of Reproduction*, *99*(1), 212–224. https://doi.org/10.1093/biolre/ioy070

62. Sheridan, M. A., Yang, Y., Jain, A., Lyons, A. S., Yang, P., Brahmasani, S. R., … Michael Roberts, R. (2019). Early onset preeclampsia in a model for human placental trophoblast. *Proceedings of the*

*National Academy of Sciences of the United States of America*, *116*(10), 4336–4345. https://doi.org/10.1073/pnas.1816150116

63. Karvas, R. M., McInturf, S., Zhou, J., Ezashi, T., Schust, D. J., Roberts, R. M., & Schulz, L. C. (2020). Use of a human embryonic stem cell model to discover GABRP, WFDC2, VTCN1 and ACTC1 as markers of early first trimester human trophoblast. *Molecular Human Reproduction*, *26*(6), 425–440. https://doi.org/10.1093/molehr/gaaa029

64. Sarvi, F., Arbatan, T., Chan, P. P. Y., & Shen, W. A. (2013). A novel technique for the formation of embryoid bodies inside liquid marbles. *RSC Advances*, *3*, 14501–14508. https://doi.org/10.1039/C3RA40364E

65. Vadivelu, R. K., Kamble, H., Munaz, A., & Nguyen, N. T. (2017). Liquid marbles as bioreactors for the study of three-dimensional cell interactions. *Biomedical Microdevices*, *19*(2). https://doi.org/10.1007/s10544-017-0171-6

66. Jara, C., Oyarzun-Ampuero, F., Carrión, F., González-Echeverría, E., Cappelli, C., & Caviedes, P. (2020). Microencapsulation of cellular aggregates composed of differentiated insulin and glucagon-producing cells from human mesenchymal stem cells derived from adipose tissue. *Diabetology & Metabolic Syndrome*, *12*(1), 66. https://doi.org/10.1186/S13098-020-00573-9

**Table 3. Summary of the parameters and criteria to define blastocyst-like in vitro model.**

| Starting cell population | Induction molecules | Time(days) | Diameter (µm) | Cell lineages | Reference |
|---|---|---|---|---|---|
| **Human blastocyst** | **n.a.** | **5-7 days** | **175 - 211** | **EPI-, TE-, and PE-like cells** | **n.a.** |
| Embryonic Stem Cells | **Trophoblast**: PD0325901, A83-01, SB590885, WH-4-023, IM-12, CHIR99021, SB431542, recombinant human LIF, EGF, L-ascorbic acid, and VPA. **Hypoblast**: bFGF, Activin A, and CHIR99021. | 6.5-11.5 days | 50 - 319 | EPI-, TE-, and HYPO-like cells | Leqian Yu & al. 2021 |
| | PD0325901, A83-01 | 3-4 days | 100 - 400 | Not reported | Ayaka Yanagida & al. 2021 |
| | CHIR99021, Y27632, BMP4, FGF2, and A83-01. | 5-6 days | Not reported | Not reported | Berna Sozen & al. 2021 |
| | PD0325901, A83-01, LPA, Lif, Y-27632 | 3-4 days | 150 - 250 | TE-, EPI-, and PE- like cells | Harunobu Kagawa & al. 2022 |
| Induced Pluripotent Stem cells | CHIR99021, A83-01, SB431542, valproic acid, EGF, BMP4 | 6 days | 107 - 216 | EPI-, TE-, and PE-like cells | Xiaodong Liu & al. 2021 |
| | PD0325901, A83-01 | 3-4 days | 100 - 400 | Not reported | Ayaka Yanagida & al. 2021 |
| | **Trophoblast**: BMP4, Y-27632. **PSCs** : LIF, CHIR99021, (S)-(+)-Dimethindene maleate, minocycline hydrochloride, IWR endo-1 and Y-27632. **IVC**: β-estradiol, progesterone. | 5-6 days | 150 - 260 | TE-, EPI-, and PE- like cells | Yong Fan & al. 2021 |
| | PD0325901, A83-01, LPA, LIF, Y-27632 | 3-4 days | 150 - 250 | TE-, EPI-, and PE- like cells | Harunobu Kagawa & al. 2022 |

# 8. Annex I: List of abbreviations

| | |
|---|---|
| 2D | Two dimensions |
| 3D | Three dimensions |
| 5-aza-CR | 5-Azacytidine |
| AGEs | Advanced Glycation End-products |
| ATP | Adenosine triphosphate |
| DNA | Deoxyribonucleic acid |
| ECM | Extracellular matrix |
| EMT | Epithelial to Mesenchymal Transition |
| ESCs | Embryonic Stem Cells |
| EVs | Extracellular Vesicles |
| GAGs | Glycosaminoglycans |
| miRNAs | Micro RNA |
| MMPs | Metalloproteinases |
| OKSM | Oct3/4, Klf4, Sox2 and cMyc |
| PGA | 3-Phosphoglyceric acid |
| PLA | Polylactic acid |
| PLGA | Polylactic-co-glycolic acid |
| PLLA | Poly-L-lactic acid |
| ROS | Reactive Oxygen Species |
| SCNT | Somatic Cell Nuclear Transfer |
| SD | Sodium Deoxycholate |
| SDS | Sodium Dodecyl Sulfate |

# 9. Acknowledgements

I started my PhD during the Covid-19 pandemic, a period which presented numerous challenges and uncertainties. Nonetheless, it is almost done. I would therefore like to assert my deepest gratitude to the exceptional people who have supported and guided me throughout this transformation journey, despite the many unexpected obstacles that have arisen.

First and foremost, I would like to express my gratitude to Professor Georgia Pennarossa, my supervisor, and Professor Tiziana Brevini, my co-supervisor, for guiding me throughout my doctoral studies, reviewing my progresses and offering invaluable advice. Additionally, Professor Fulvio Gandolfi must be mentioned who took his time to generously sharing his extensive academic knowledge with me.

A particular thank to Dr. Sharon Arcuri who supported me since my master studies. My gratitude goes also to Dr. Rolando Pasquariello, for his precious suggestions and must be extended to Dr. Nicole Verdile and Dr. Federica Camin for being always there for discussions about anything I was unsure on.

My deepest gratefulness goes to all the students I have worked with: Dorotea Salemi, Anna Cartelli, Laura Sichenze, Joshua Grana, Marco Bianchi, Angelica Magni, Arianna Zancuoghi, Riccardo Sorrentino, Magda Cappellato, Martina Gerli, Martina Bianchini, Gaia Shari Bosco, Carola Leone e Noemi Rebosio.

Special thanks to my friends for making the past three years much more enjoyable and keeping me sane.

Last, but most important, I want to thank my family for always being 'here', I love you.